

THÈSE

Pour obtenir le grade de

DOCTEUR DE L'UNIVERSITÉ DE GRENOBLE

Spécialité : **Nanophysique**

Arrêté ministériel : 7 août 2006

Présentée par

Oleksii SHEVTSOV

Thèse dirigée par **Xavier WAIN TAL**

préparée au sein du **Service de Physique Statistique, Magnétisme et Supraconductivité**
et de l'**Ecole doctorale de Physique de Grenoble**

Contribution à la théorie du transport quantique: isolants topologiques à base de graphène et phénomènes à fréquence finie

Thèse soutenue publiquement le **26 Octobre 2012**,
devant le jury composé de :

Frank HEKKING

Université Joseph Fourier, Président

Mark GOERBIG

Université Paris-Sud, Rapporteur

Christophe MORA

Ecole Normale Supérieure, Rapporteur

Vincent BOUCHIAT

Institut Néel, Examineur

Fabio PISTOLESI

Université Bordeaux 1, Examineur

Stephan ROCHE

Catalan Institute of Nanotechnology, Examineur

Xavier WAIN TAL

CEA Grenoble, Directeur de thèse



Contents

Acknowledgements	5
Summary of thesis	6
Résumé de thèse	17
I Non-equilibrium quantum transport at the nanoscale	29
1 Introduction	33
1.1 Regimes of electron transport	33
1.2 Approaches to electron transport	35
2 Stationary electron transport	37
2.1 Scattering matrix approach	37
2.1.1 Scattering matrix and the Landauer-Büttiker formula	38
2.2 Green's function approach	42
2.2.1 Definition of a retarded Green's function	43
2.2.2 Integrating out the leads: self-energy	44
2.2.3 Meir-Wingreen formula for current	45
2.2.4 The KNIT package	46
2.3 Summary	48
3 Dynamical electron transport at finite frequency	50
3.1 Definition of the problem	51
3.2 Scattering matrix theory of finite-frequency electron transport	52
3.2.1 Response to an external perturbation	53
3.2.2 Response to an internal perturbation	55
3.2.3 The total response	56
3.3 Green's function theory of the AC electron transport: the cookbook	58
3.3.1 Response to an external perturbation	59

3.3.2	Response to an internal perturbation	60
3.3.3	The total response	62
3.4	Applications	64
3.4.1	Technical details on the numerical integration	64
3.4.2	Quantum Point Contact	66
3.4.3	Screening	70
3.4.4	Mach-Zehnder interferometer	71
4	The Green's function formalism at finite frequency	76
4.1	Time dependent NEGF formalism in a nut shell	76
4.1.1	Dyson equation	77
4.1.2	Integrating out the electrodes	78
4.1.3	Expression for the current	79
4.2	Effect of a periodic potential	80
4.3	Perturbation in the device region	81
4.3.1	Limit of a small perturbation amplitude	82
4.3.2	Adiabatic limit and beyond	83
4.4	Perturbation in the leads	84
4.4.1	Equation of motion	84
4.4.2	Limit of a small perturbation amplitude	85
4.4.3	Adiabatic limit and beyond	87
4.5	Conclusions	88
II	Quantum transport in a graphene-based topological insulator	89
5	Introduction to the physics of graphene	92
5.1	Crystal lattice and band structure	92
5.2	Low-energy (Dirac) effective description	98
5.3	Graphene ribbons	101
5.3.1	Armchair ribbons	101
5.3.2	Zigzag ribbons	103
6	Quantum Hall effect in graphene	107
6.1	Graphene in a strong magnetic field	107
6.2	QH effect in graphene ribbons	111
7	Graphene with spin-orbit coupling	114
7.1	Spin-orbit interaction in graphene	115

7.1.1	Intra-atomic SO interaction	115
7.1.2	Effects of curvature	117
7.1.3	Effect of an electric field	118
7.1.4	Low-energy expressions for SO interactions	118
7.2	Topological insulator in graphene: Kane-Mele model	120
7.2.1	Topologically protected edge modes	122
7.2.2	\mathbb{Z}_2 topological order	126
8	Topological insulating phase in functionalized graphene	130
8.1	Initial proposal	131
8.1.1	The setup	131
8.1.2	Numerical DFT simulations and effective TB description	132
8.1.3	Relation between the Kane-Mele model and adatoms' effective model	135
8.1.4	Transport properties of graphene with randomly distributed adatoms	136
8.2	Quantum spin Hall phase induced by randomly deposited adatoms	138
8.2.1	Parametric study of the QSH phase	139
8.2.2	Application to enhanced thermopower	146
8.2.3	Conclusions	148
9	From QH to QSH effect in graphene	149
9.1	Band structure	150
9.2	Topological order	153
9.3	Transport signatures	155
9.3.1	Ballistic regime	155
9.3.2	Effects of disorder	158
9.4	Topological heterojunction	160
9.5	Conclusions	163
	Perspectives and future work	165
A	General results for AC observables given in Section 3.3	167
A.1	External perturbation	167
A.2	Internal perturbation	170
B	Magnetic field in multi-terminal calculations	171
	Publication list	173
	Bibliography	174

Acknowledgements

First of all I would like to express my gratitude to my supervisor, Xavier Waintal, whose guidance and support have made this thesis possible. In 2009 we both moved to Grenoble, a very beautiful and lively town in the heart of the French Alps, looking forward to new challenges and achievements. The three years I have spent in the theory group at the Institute for Nanoscience and Cryogenics (CEA Grenoble) were a great opportunity to discover a very active, stimulating and encouraging research environment among very talented and successful people. I am also very thankful to Vitaly Golovach, with whom I shared an office during the first two years of my PhD. Endless discussions with him helped a lot in understanding and interpreting the results obtained in my calculations. I am grateful to the postdocs in our group – Pierre Carmier, Christoph Groth, and Cyril Petitjean – with whom I enjoyed working on our joint projects. It was a useful experience which showed me the importance and spirit of teamwork. Special thanks go to Benoit Gaury, with whom I share my office when writing this thesis. When he came to our group, I was barely able to say something in French. Numerous conversations and discussions with him helped to improve a lot my spoken and written French, which, I believe, is a valuable and important skill one needs to acquire living in France.

I also want to thank Dr. Mark Goerbig and Dr. Christophe Mora for taking their time to review this manuscript, and Dr. Fabio Pistolesi, Dr. Vincent Bouchiat, Dr. Stephan Roche and Prof. Frank Hekking for accepting to be the jury members on my thesis defense.

Finally, I wish to thank my parents, Serhii Shevtsov and Valentyna Shevtsova, and my better half, Anastasiia Tsarenko, for their love and patience. This work would not have been possible without their endless support.

Summary of thesis

The thesis which follows after this summary consists of two parts. The first part is devoted to the theoretical study of a problem of quantum electron transport in the presence of oscillating in time perturbations (AC bias, AC gate voltage, etc.). The second part concerns peculiar transport signatures caused by the presence of spin-orbit interaction in graphene with and without external magnetic field applied perpendicular to its plane. Let us briefly review below the key points of the thesis.

Part I

Problem statement and objectives

Demands of a rapidly changing computer engineering market necessitate the use of advanced theoretical approaches developed in physics. Nowadays, simulations of quantum transport in nanodevices has become more than just a tool to describe theoretical models. In the first part of this thesis we address the problem of quantum electronic transport in presence of varying in time fields. One can think, for example, of a device with an AC bias applied or a gate with oscillating voltage placed on top. So far, this problem has not got considerable attention and commonly used simulations are done for the case of stationary electrochemical potential and/or temperature gradients.

Pioneer works made in this direction were written by M. Büttiker and co-workers using the scattering matrix formalism [1, 2, 3, 4, 5, 6, 7]. Though, the general scheme of tackling the problem of dynamical (AC) transport was formulated, it was rather an important qualitative step than a practical prescription. Another set of works, taking an alternative path, are based on (non-equilibrium) Green's functions and are mainly due to the group of H. Guo and a few others [8, 9, 10, 11, 12, 13, 14, 15, 16, 17, 18, 19, 20, 21]. This method is very powerful (and is actually used in this thesis), however no general framework existed so far, which could be served as a recipe to solve problems arising from the presence of various oscillating perturbations.

In this thesis we attempt to cover this gap and formulate a set of practical rules and steps one needs to follow in order to attack this problem. We develop a systematic approach

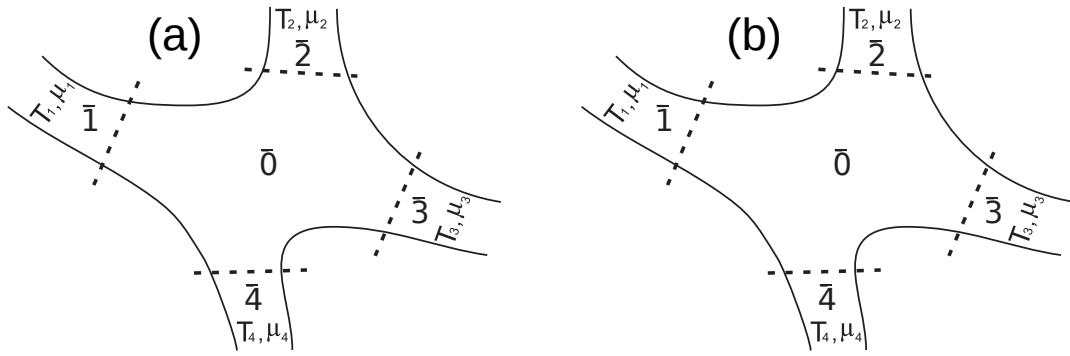


Figure 1: Multiterminal system with $M = 4$ leads influenced by an external (a) or an internal (b) perturbation. Red shaded region represents the part of the system affected by the perturbation.

that expresses finite frequency observables in terms of the stationary Green's function of the system, i.e. the natural output of most DC numerical codes. Our framework allows to extend the simulations capabilities of existing codes to a large class of observables including, for instance, AC conductance, quantum capacitance, quantum pumping, spin pumping or photo-assisted shot noise. The theory is based on the Keldysh formalism and we provide explicit links with the alternative scattering approach.

Considering two types of perturbations, external (in the leads) or internal (inside the device region), see Fig. 1, we derive a systematic expansion of any (AC) observable in powers of perturbation amplitude or in powers of modulation frequency (adiabatic limit). In the former, we develop a set of diagrammatic rules allowing to calculate a contribution of arbitrary order (and interpret it in terms of a series of photon absorption/emission processes), while in the latter we derive the adiabatic limit and explain how to calculate systematic corrections to it. Below we demonstrate how our formalism applies to calculation of the AC (linear) conductance and compare it to the scattering approach.

AC conductance: scattering approach

In order to calculate the AC conductance of a multiterminal system, we consider first an AC bias applied to one of the contacts, say β ($\beta = \bar{1}$ on Fig. 1a). It means that the electrochemical potential in lead β is oscillating as $\mu_\beta(t) = \mu + eV_{ac} \cos \omega t$, where μ is the equilibrium chemical potential (we assume it to be the same in all leads for simplicity – no DC bias). Then, there will be time-dependent currents generated in all the contacts in response to this perturbation. Each of these currents contains various harmonics,

$$I_\alpha(t) = \text{Re} \sum_{l=0}^{\infty} I_\alpha(l\omega) e^{-il\omega t}. \quad (1)$$

However if one is interested in the (linear) AC conductance, this means that the sought quantity is $\Upsilon_{\alpha\beta}(\omega) \equiv dI_{\alpha}(\omega)/(dV_{ac})$. Büttiker and co-workers have found that this quantity can be expressed in terms of an equilibrium scattering matrix $S_{\alpha\beta}(E)$. At low frequencies it reads [1, 5, 6],

$$\Upsilon_{\alpha\beta}^e(\omega) = \Upsilon_{\alpha\beta}^e(0) - i\omega e \frac{dN_{\alpha\beta}}{dV_{ac}}, \quad (2)$$

where $\Upsilon_{\alpha\beta}^e(0)$ is the stationary conductance matrix element, and the quantity

$$\frac{dN_{\alpha\beta}}{dV_{ac}} = -\frac{e}{4\pi i} \int dE \left(-\frac{\partial f}{\partial E} \right) \text{Tr} \left[S_{\alpha\beta}^{\dagger} \frac{dS_{\alpha\beta}(E)}{dE} - \frac{dS_{\alpha\beta}^{\dagger}(E)}{dE} S_{\alpha\beta}(E) \right] \quad (3)$$

is the density of particles emitted at contact α as a consequence of perturbing the electrochemical potential in lead β . Here $f(E)$ is a Fermi function and the superscript e is added to emphasize that this is the response function to an *external* perturbation.

There are two major requirements which must be satisfied in order for the theory to be correct: current conservation (Kirchhoff's law) and gauge invariance, which imply that,

$$\sum_{\alpha=1}^M \Upsilon_{\alpha\beta}(\omega) = \sum_{\beta=1}^M \Upsilon_{\alpha\beta}(\omega) = 0. \quad (4)$$

Equation (2) does not meet these requirements, which means that it cannot describe the full response of the system to the AC bias. Indeed, the contribution which is still missing comes from a displacement current. It is instructive to consider a continuity equation,

$$\sum_{\alpha=1}^M \Upsilon_{\alpha\beta}^e(\omega) - i\omega \frac{dQ(\omega)}{dV_{ac}} = 0, \quad (5)$$

where $Q(\omega)$ is a Fourier transform of the total charge in the scattering region $\bar{0}$ (see Fig. 1). The fact that elements of the conductance matrix (2) do not add up to zero signifies that there is a non-zero density of injected charge oscillating inside the scattering region. In reality this charge density cannot pileup because the systems adjusts so that to restore its charge neutrality. In our case it means that we have to consider the (oscillating) potential $U(\mathbf{r}, \omega)$ created by the injected charge, which modifies currents in all the contacts. This contribution is the displacement current and it refers to the case of *internal* perturbation, depicted on Fig. 1b. In terms of the scattering matrix this contribution is given by [1, 5, 6],

$$\frac{dI_{\alpha}^i(\omega)}{dV_{ac}} = ie\omega \int d^3\mathbf{r} \frac{\delta N_{\alpha}}{\delta U(\mathbf{r})} \frac{dU(\mathbf{r}, \omega)}{dV_{ac}}, \quad (6)$$

where the superscript i stands for *internal* and the quantity

$$\frac{\delta N_{\alpha}}{\delta U(\mathbf{r})} = \frac{1}{4\pi i} \int dE \left(-\frac{\partial f}{\partial E} \right) \sum_{\gamma} \text{Tr} \left[S_{\alpha\gamma}^{\dagger}(E) \left(\frac{\delta S_{\alpha\gamma}(E)}{\delta U(\mathbf{r})} \right) - \left(\frac{\delta S_{\alpha\gamma}^{\dagger}(E)}{\delta U(\mathbf{r})} \right) S_{\alpha\gamma}(E) \right] \quad (7)$$

is the density of particles, that are emitted at contact α if we perturb the scalar potential locally at point \mathbf{r} (in the scattering region $\bar{0}$). The induced oscillating potential profile is calculated from the Poisson equation [1, 6],

$$\Delta \frac{dU(\mathbf{r}, \omega, \beta)}{dV_{ac}} = -\frac{e}{\epsilon} \left[\frac{dn(\mathbf{r}, \beta)}{dV_{ac}} + \int d^3\mathbf{r}' \Pi(\mathbf{r}, \mathbf{r}') \frac{dU(\mathbf{r}', \omega, \beta)}{dV_{ac}} \right], \quad (8)$$

where $\Pi(\mathbf{r}, \mathbf{r}')$ is the so-called Lindhard function determining the change of the electron density at point \mathbf{r} in response to a perturbation at point \mathbf{r}' . This function has to be calculated separately and cannot be in general expressed via a scattering matrix. The first quantity in the brackets in Eq.(8) is the density of injected charge as a consequence of oscillating electrochemical potential in lead β , which is given by [1, 6],

$$\frac{dn(\mathbf{r}, \beta)}{dV_{ac}} = \frac{1}{4\pi i} \int dE \left(-\frac{\partial f}{\partial E} \right) \sum_{\alpha} \text{Tr} \left[S_{\alpha\beta}^{\dagger}(E) \left(\frac{\delta S_{\alpha\beta}(E)}{\delta U(\mathbf{r})} \right) - \left(\frac{\delta S_{\alpha\beta}^{\dagger}(E)}{\delta U(\mathbf{r})} \right) S_{\alpha\beta}(E) \right]. \quad (9)$$

Finally, putting all together, the full AC conductance satisfying Eq.(4) reads,

$$\Upsilon_{\alpha\beta}(\omega) = \Upsilon_{\alpha\beta}^e(\omega) + \frac{dI_{\alpha}^i(\omega)}{dV_{ac}}. \quad (10)$$

As one can clearly see, the scattering approach has a few weak sides. First of all, the internal response (6) and the induced charge density (9), necessary to calculate the full response function (10), depend on a functional derivative of the scattering matrix with respect to the scalar potential profile in the system, which cannot be found in general. Second, the Lindhard function, entering the Poisson equation (8), is an unknown function of coordinates and one has to make additional assumptions to do any calculation. Third, the theory was built relying on smallness of both the perturbation amplitude and the perturbation frequency. Nevertheless, the scattering theory presented above is an important step in understanding the main aspects of finite frequency phenomena in electron transport, though it does not give a general prescription how to do calculations in practice.

Our theory: Green's function approach

In this thesis, making use of the Keldysh formalism, we were able to express *any* AC observable in terms of stationary Green's functions, which are a raw output of a variety of numerical codes existing on a market [22]. Thus, being intrinsically adapted for numerical simulations, our theory can be used to calculate the AC conductance, for example, of a system with arbitrary shape and number of contacts.

Let us give expressions for the quantities needed to calculate the AC conductance. First of all, we note that in our approach the system (see Fig. 1) is described by a quadratic tight-binding

Hamiltonian,

$$\hat{\mathbf{H}} = \sum_{n,m} \mathbf{H}_{nm} c_n^\dagger c_m, \quad (11)$$

where c_n^\dagger (c_n) is a usual creation (destruction) operator on site n . We start again from the response to the external AC bias in lead β . Then, the corresponding response function is given by

$$\Upsilon_{\alpha\beta}^e(\omega) = \frac{e^2}{h} \int dE \text{Tr} \left[\Gamma_\alpha \mathcal{G}_2 \Gamma_\beta \mathcal{G}_0^\dagger - i\delta_{\alpha,\beta} (\mathcal{G}_2 - \mathcal{G}_0^\dagger) \Gamma_\alpha \right] \frac{f(E) - f(E + \hbar\omega)}{\hbar\omega}, \quad (12)$$

with $\Gamma_\alpha = \text{Im}(\Sigma_\alpha^r)$, where Σ_α^r is the (retarded) self-energy of lead α , and with the (stationary) Green's function defined as

$$\mathcal{G}_l(E) \equiv \left(E + \frac{\hbar\omega l}{2} - \mathbf{H}_{00} - \sum_{\alpha=1}^M \Sigma_\alpha^r \right)^{-1}. \quad (13)$$

Here \mathbf{H}_{00} is the scattering region sub-block of the full Hamiltonian matrix. Equations (12) and (13), as well as other expressions given below, are written for the sake of simplicity in the wide-band limit (self-energies of the leads are assumed independent of energy). General expressions can be found in the first part of the thesis and in the corresponding Appendix.

As was pointed out in the previous section, Eq.(12) does not describe the full response of the system. So, we have to include the displacement part of the current, which in terms of Green's functions has the form,

$$\frac{dI_\alpha^i(\omega)}{dV_{ac}} = \sum_j \frac{dI_\alpha(\omega)}{dV_{jj}} \frac{dU(j, \omega)}{dV_{ac}}, \quad (14)$$

where $U(j, \omega)$ is a discretized version of the induced potential $U(\mathbf{r}, \omega)$, and the quantity

$$\frac{dI_\alpha(\omega)}{dV_{jj}} = \frac{ie^2}{h} \int dE (f(E) - f(E + \hbar\omega)) \left[\mathcal{G}_0^\dagger \Gamma_\alpha \mathcal{G}_2 \right]_{jj}, \quad (15)$$

describes a current response in lead α in consequence of the local perturbation at site j . In order to complete the theory it is necessary to give expressions for the induced charge density and the Lindhard function, which enter the Poisson equation (8), determining the potential $U(j, \omega)$. Again, these quantities are conveniently expressed via the *stationary* Green's functions as,

$$\frac{dn(j, \beta)}{dV_{ac}} = \frac{e}{h\omega} \int dE (f(E) - f(E + \hbar\omega)) \left[\mathcal{G}_2 \Gamma_\beta \mathcal{G}_0^\dagger \right]_{jj}, \quad (16)$$

$$\begin{aligned} \Pi(\omega, j, j') = & -\frac{ie}{2\pi} \int dE \left\{ (f(E) - f(E + \hbar\omega)) \left[\mathcal{G}_2 \right]_{jj'} \left[\mathcal{G}_0^\dagger \right]_{j'j} \right. \\ & \left. + f(E + \hbar\omega) \left[\mathcal{G}_2^\dagger \right]_{jj'} \left[\mathcal{G}_0^\dagger \right]_{j'j} - f(E) \left[\mathcal{G}_2 \right]_{jj'} \left[\mathcal{G}_0 \right]_{j'j} \right\}. \end{aligned} \quad (17)$$

From this short demonstration one can immediately see the advantages of the Green's function approach. The quantities which were inaccessible in general (like functional derivative of a scattering matrix) or even undefined (Lindhard function) in the scattering theory are expressed in terms of Green's functions. Another advantage is that the Green's function (13) as well as leads self-energies are a raw output of many numerical codes based on a recursive algorithm, which makes our formalism a practical (numerical) tool.

In practice, however, one often combines the two approaches by solving simple toy models with the help of the scattering theory and then using these results to get insight into numerical simulations performed with Green's functions. Therefore, these methods complement each other and constitute a complete theoretical tool for investigating finite-frequency phenomena.

Part II

Problem statement and objectives

Graphene, a one-atom thick planar sheet of carbon atoms, is a hot topic nowadays and a lot of researchers believe that its unique properties can be used to make a revolution in the nanoelectronic device engineering. Some of the main features which made it famous are: (i) linear spectrum of low-energy excitations described by a massless relativistic Dirac equation; (ii) very high carrier mobility; (iii) anomalous quantization of quantum Hall steps in the transverse part of conductivity tensor, which can be observed at room temperatures.

In the second part of the thesis we studied influence of spin-orbital effects on electronic and transport properties of graphene. In seminal works by C. L. Kane and E. J. Mele [23, 24] it was found that a special type of spin-orbit interaction (which preserves a S_z component of spin) is capable of inducing a topological order in graphene. The latter results in appearance of a bulk energy gap with gapless (spin-filtered) excitations on the boundaries of a finite graphene structure, which are robust to a large class of perturbations and disorder. This property of the edge states relies on presence of a time-reversal symmetry, which forbids backscattering. Another interesting property of the edge states is that at a given sample boundary spin-up and spin-down electrons counterpropagate and thus support net spin current with no net charge current at the same time, see Fig. 3a. The latter feature has got a name Quantum Spin Hall (QSH) effect. Though the Kane-Mele model supports a variety of interesting effects, it has not been realized in reality yet. The reason for this is the fact that spin-orbit interaction in pristine graphene is too small [25] to be observed experimentally. In this thesis we elaborate a recent proposal how to overcome this issue and propose a way to see a transition between two (topologically) different quantum Hall (QH) and quantum spin Hall phases in the same setup. The latter is a unique situation being possible owing to the relativistic spectrum of graphene.

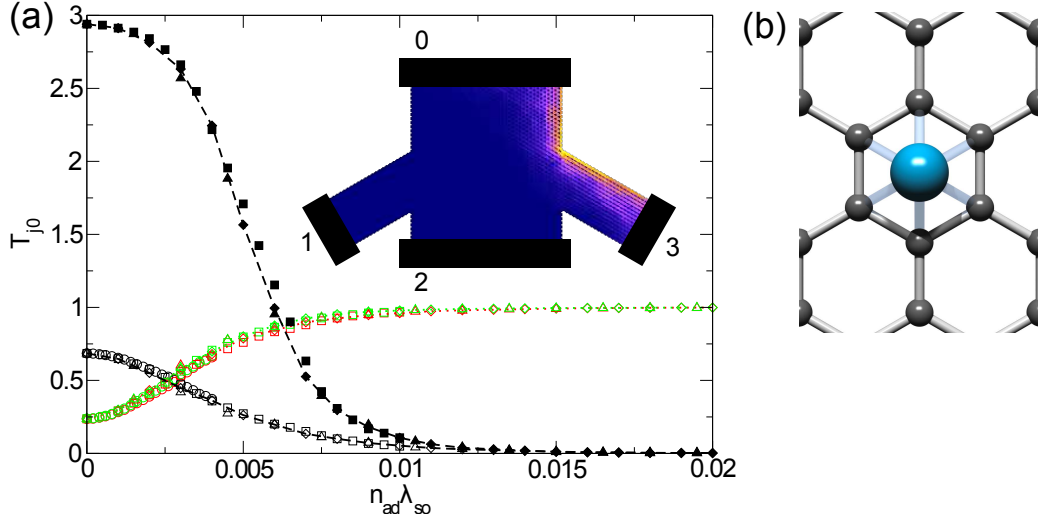


Figure 2: (a): Upper inset: schematic of our setup, a 4-terminal graphene cross with armchair edges. The different colors correspond to an actual calculation of the current density for spin-up electrons upon injection from contact 0. The existence of an edge state is manifest. Main figure: Scaling of the transmissions T_{j0} from contact 0 for various couplings λ_{so} and adatom densities n_{ad} , plotted as a function of the effective SO coupling strength $\lambda_{\text{so}}^{\text{eff}} = \lambda_{\text{so}} n_{\text{ad}}$. Dashed (black) lines correspond to “longitudinal” transmission T_{20} and dotted lines correspond to “Hall” transmissions T_{10} (red) and T_{30} (green). The two sets of curves correspond to an energy $E = 0$ (open symbols), and $E = 0.05$ (filled symbols). Different symbol shapes correspond to different values of SO coupling. (b): View from top of an adatom (blue circle) residing on a graphene’s surface.

Quantum spin Hall phase in graphene

As was mentioned above, the work presented in this thesis was motivated by a recent proposal to enhance the spin-orbit interaction in graphene by depositing heavy atoms (with strong intra-atomic spin-orbit interaction: In or Tl, for example) on its surface [26], see Fig. 2b. We elaborated further this idea and studied in details the experimentally relevant case of random distribution of the adatoms. Our findings can be summarized as follows: (i) even when the distribution of adatoms is arbitrary, a perfectly homogeneous QSH phase (described by the Kane-Mele model) emerges with a spin-orbit coupling constant renormalized by a density of adatoms; (ii) varying the density of adatoms allows for controlling the spin-orbit energy gap and the width of the edge states, which might potentially be used for efficient thermopower generation with a tunable target temperature (see Sec. 8.2.2 for details) [27]. On Fig. 2 we present an example of calculation of DC transmission coefficients between the contacts of a 4-terminal graphene cross. Varying the strength of spin-orbit coupling λ_{so} and/or adatom density

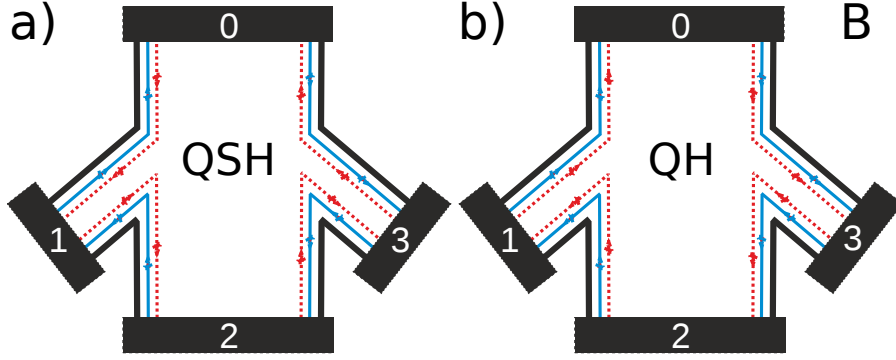


Figure 3: Cartoon of a 4-terminal conductor in a) QSH phase and b) QH phase. Blue solid and red dashed lines represent edge states for spin-up and spin-down electrons, respectively.

n_{ad} , we plot transmission amplitudes as a function of the effective parameter $\lambda_{\text{eff}} = n_{\text{ad}}\lambda_{\text{so}}$ assuming the current is injected at lead 0. One can see that the results are perfectly rescaled and the Hall transmissions T_{10} and T_{30} tend to unity, while the direct transmission T_{20} gets exponentially suppressed, as the effective parameter λ_{eff} increases. This is a signature of the emerging QSH phase characterized by the spin-filtered edge states, see Fig. 3a. We tested its robustness to various types of disorder and found it extremely stable with no signature of the spatial inhomogeneities of the adatom configuration (see Sec. 8.2 for details). Moreover, a simple rescaling of the spin-orbit coupling parameter allows us to account for the behavior of the inhomogeneous system using a homogeneous model introduced by Kane and Mele [23, 24].

Transition between quantum Hall and quantum spin Hall phases

The second part of our work concerns the behavior of the QSH phase in graphene (induced by adatoms, for example) in presence of a strong magnetic field applied perpendicular to graphene's surface. It is not obvious what exactly is going to happen because the presence of a magnetic field implies that the time-reversal symmetry protecting the edge states is explicitly broken. Consider a 4-terminal graphene cross for two situations: (i) in a QSH phase ($\lambda_{\text{so}} \neq 0$, $B = 0$, see Fig. 3a); and (ii) in a QH phase ($\lambda_{\text{so}} = 0$, $B \neq 0$, see Fig. 3b). In strong enough magnetic fields one expects to see the picture corresponding to the QH phase. However, in order to go from QSH edge states to QH edge states one has to reverse the direction of motion of one of the spin species, referred to as “unhappy” spin below (red dashed lines on Fig. 3). In our work, we studied in details how this transition happens.

In order to get an insight into this problem, we performed band structure calculations for three different cases: the two mentioned above, and applying both spin-orbit coupling and magnetic field together (see Fig. 4). The band structures of a graphene ribbon in the QSH and QH phases are quite different. In the QH phase, the perpendicular magnetic field gives rise

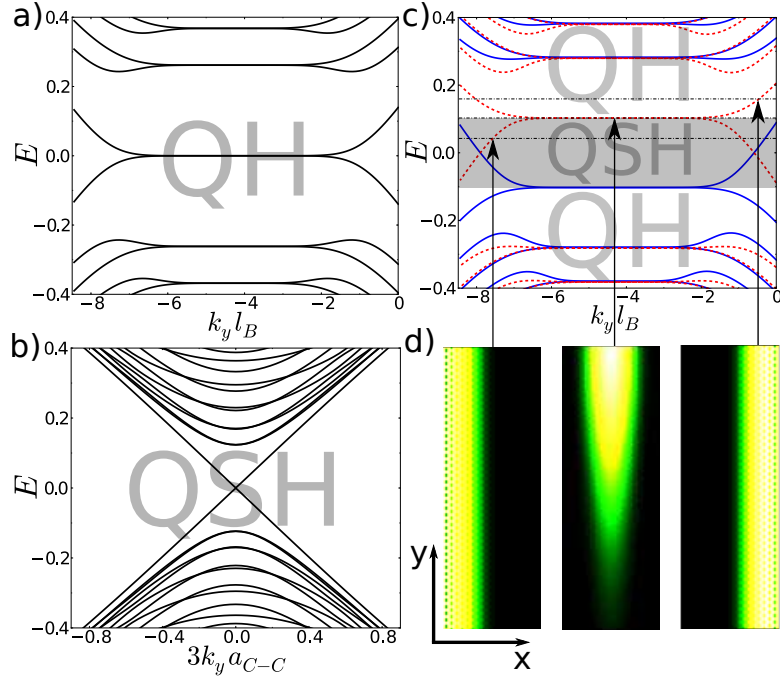


Figure 4: Band structure of a (semi-metallic armchair) graphene ribbon in the **a)** QH and **b)** QSH phase. When both magnetic field and SO coupling are present **c)**, the resulting band structure leads to a QSH phase for $|E_F| < \Delta_{so}$ (shaded region) and a QH phase for $|E_F| > \Delta_{so}$. Compared to the pure QH and QSH cases, the spin degeneracy is lifted (blue thick and red dashed lines), which is particularly prominent in the lowest band which consists of spin-polarized branches at $E = \pm\Delta_{so}$. As the Fermi energy crosses the SO gap, the localization of the “unhappy” spin (red dashed) shifts from one edge to the other, while it is fully localized in the bulk when $E_F = \Delta_{so}$. This is illustrated in the corresponding current-density plots **d)**. On the other hand, the “happy” spin (thick blue) gets increasingly localized on the same edge as the Fermi energy crosses the transition region (not shown).

to Landau levels $\epsilon_n = \pm(\hbar v_F/l_B)\sqrt{2|n|}$, with $l_B = \sqrt{\hbar/(eB)}$, which become dispersive close to the edges of the graphene ribbon (Fig. 4a). When the Fermi level is placed between two of these Landau levels, transport is characterized by spin-degenerate edge states as in Fig. 3b, which propagate in a direction imposed by the sign of the magnetic field. In the QSH phase, the band structure consists of hyperbolic bands above the QSH gap, $\Delta_{so} = 3\sqrt{3}\lambda_{so}$, and a pair of linearly dispersing ones below it (Fig. 4b). These linear bands correspond to spin-polarized states, localized at the edges of the graphene ribbon (see Section 7.2). When both magnetic field and spin-orbit coupling are present, the band structure can be summarized in very simple terms (see Fig. 4c): for Fermi energies inside the spin-orbit gap $|E_F| < \Delta_{so}$ (shaded region), the system is in the QSH phase, with opposite spin channels on a given edge propagating in

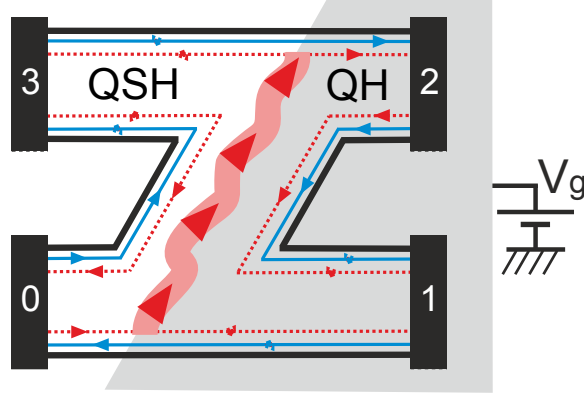


Figure 5: Topological heterojunction, with QSH edge states on the left and QH edge states on the right. This junction can be experimentally achieved by applying a top gate (grey shaded region) on the right half of the sample. While one of the spin species (thick blue) can propagate through this junction, the other one (red dashed) cannot and therefore gives rise to a chiral state, localized at the interface between QH and QSH phases, which connects both edges.

opposite directions, while for energies $|E_F| > \Delta_{\text{so}}$, the system is in the QH phase, with opposite spin channels on a given edge propagating in the same direction. Hence for a given value of Δ_{so} , the transition between the two phases is governed solely by the Fermi energy and does not depend at all on the value of the magnetic field (neglecting Zeeman splitting, which is very small in graphene). This quite remarkable result is a direct consequence of the existence in graphene of a B -independent zero-energy Landau level: as soon as $\Delta_{\text{so}} \neq 0$, the spin degeneracy of the zero-energy Landau level is lifted, as opposed to all other Landau levels which remain spin degenerate [28]. This lifting leads to a QSH phase in the corresponding spin-orbit gap.

In order to check these arguments, we performed a transmission calculation in a 4-terminal Z-shaped setup schematically depicted on Fig. 5. We placed a top gate on the right half of the sample, which controlled the position of the Fermi level locally there. By an appropriate choice of gate voltage V_g it is possible to make a heterojunction between the QH and QSH phases. The “unhappy” spin (red dashed line) being injected from lead 0 cannot penetrate the QH phase region and thus creates a chiral state at the interface between two phase. The results of the corresponding calculations are given on Fig. 6. While the Fermi energy in the right half remains below the value of Δ_{so} , transport characteristics remain unaffected by the gate (left inset of Fig. 6). However, as soon as the Fermi energy in the right half crosses the QSH gap, it gives rise to a QSH-QH junction characterized by a topological state at its interface (see right inset of Fig. 6). This chiral state propagates along the interface until it reaches the opposite edge, and then gets partially transmitted in lead 2, partially transmitted in lead 3, with proportions which depend on the microscopic details of the model (Fermi energies, the

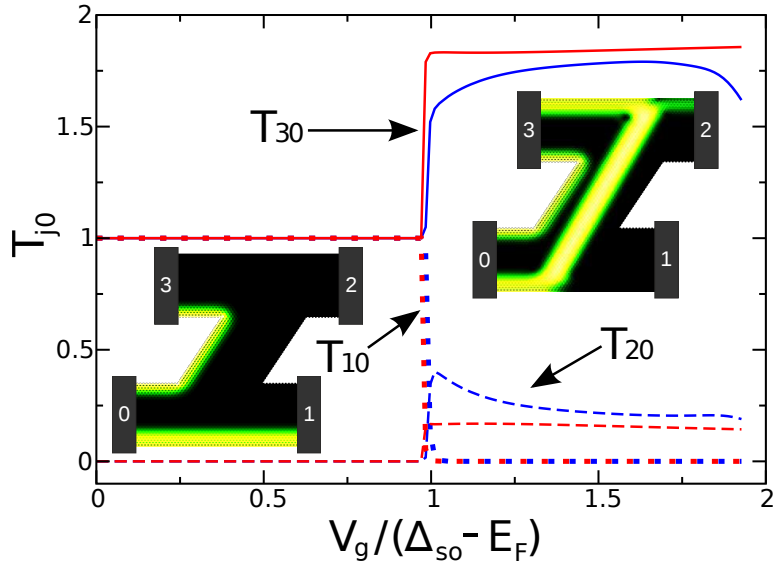


Figure 6: Heterostructure in a 4 terminal Z-shape sample as depicted in Fig. 5. Transmission probabilities from lead 0, where the current is injected, to outgoing leads 1 (dotted lines), 2 (dashed lines) and 3 (full lines) as a function of the top gate voltage V_g . When $V_g < (\Delta_{so} - E_F)$, such that left and right regions are in the QSH phase, current is perfectly transmitted by the QSH edge states, as shown in the current-density plot in the left inset. When V_g is high enough ($V_g > (\Delta_{so} - E_F)$) that the right part of the sample enters the QH phase, a QSH-QH junction is created, which is characterized by a chiral state propagating along the interface. This is illustrated in the current-density plot shown in the right inset. The red curves correspond to an abrupt voltage change across the junction region while the blue curves correspond to a smooth transition.

length of the interface, the smoothness of the potential step, the amount of disorder, etc.). This system constitutes a very efficient spin-polarized charge-current switching mechanism, as the current in lead 1 (respectively 2) can be reversibly switched from one (respectively zero) to zero (respectively non-zero) while simultaneously being spin-polarized (see Fig. 6).

In summary, we showed that the transition between QSH and QH phases in graphene is independent of the value of the magnetic field (neglecting the weak effect of Zeeman splitting) and can be crossed simply by tuning the value of the Fermi energy across the spin-orbit gap. This unique property owes to existence of the zero-energy Landau level ($n = 0$) in graphene. In a heterojunction, one of the spin species gives rise to a chiral state propagating along the interface between QSH and QH phases. The nature of this special state is a fascinating issue which is still to be investigated. The tunable transition between the QSH and QH topological phases could serve as a spin-polarized charge-current switch with potentially extremely high, topologically protected, on/off ratios.

Résumé de thèse

La thèse à la suite de ce résumé est constituée de deux parties. La première est dédiée à l'étude du transport électronique quantique en présence de perturbations oscillantes dans le temps (tension AC, tension de grille AC, etc.). La seconde partie traite des signatures particulières du transport résultant de la présence d'un couplage spin-orbite dans le graphène avec ou sans l'application d'un champ magnétique extérieur transverse. Nous passons brièvement en revue les points clés de la thèse dans ce qui suit.

Partie I

Etablissement du problème et objectifs

Les évolutions rapides du marché de l'ingénierie informatique forcent le recours à des approches théoriques avancées en physique. Aujourd'hui les simulations de transport quantique dans les objets de tailles nanoscopiques sont devenues bien plus qu'un outil d'illustration des modèles théoriques. Dans la première partie de cette thèse nous traitons du transport électronique quantique en présence de perturbations dépendantes du temps. On peut penser, par exemple, à un objet sur lequel est appliquée une tension AC ou bien une tension de grille. Jusqu'à présent ce problème n'a pas retenu une grande attention et les simulations sont communément réalisées pour des potentiels électrochimiques et/ou des gradients de température stationnaires.

Les premiers travaux empruntant cette voie ont été écrits par M. Büttiker et ses collaborateurs en ayant recours au formalisme des matrices de diffusion [1, 2, 3, 4, 5, 6, 7]. Malgré une volonté affichée de s'attaquer au problème du transport AC, les résultats ont constitué davantage en un profond saut qualitatif qu'en un progrès à usage pratique. D'autres travaux majoritairement dus au groupe de H. Guo et à quelques autres [8, 9, 10, 11, 12, 13, 14, 15, 16, 17, 18, 19, 20, 21] prennent un chemin différent en usant des fonctions de Green hors équilibre. Ce formalisme (utilisé dans cette thèse) est très puissant, cependant jusqu'à maintenant il manquait un cadre théorique lui permettant d'être utilisé comme une recette dans l'étude de problèmes faisant intervenir différents types de perturbations oscillantes.

Dans cette thèse nous comblons cette lacune. Nous formulons un ensemble de règles pra-

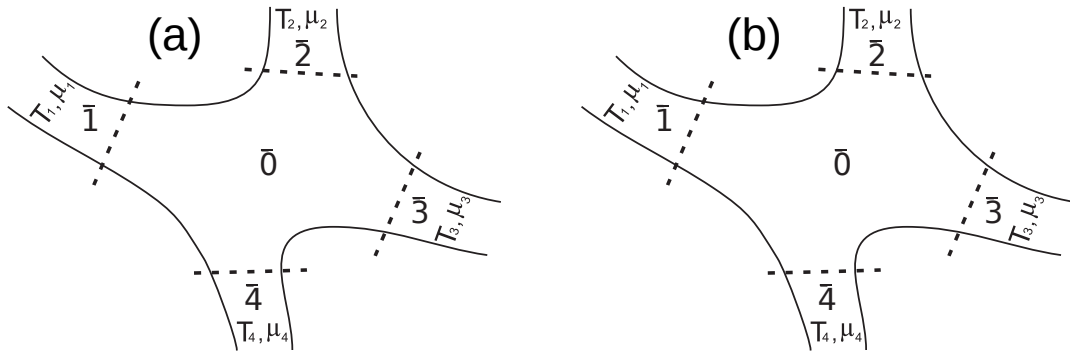


Figure 7: Système multi-terminal avec $M = 4$ contacts sur lequel est appliqué une perturbation externe (a) ou interne (b). La région en rouge représente la partie du système affectée par la perturbation.

tiques et d'étapes à suivre pour le traitement de ce problème. Nous développons une approche systématique pour exprimer des observables à fréquence finie en termes de fonctions de Green stationnaires du système, c'est-à-dire des quantités calculées par la majorité des codes numériques DC. Notre formalisme permet d'étendre les possibilités des codes existants à une large variété d'observables telles que la conductance AC, la capacité quantiques, le pompage quantique, le pompage de spin ou encore le bruit de grenaille photo-assisté. La théorie est basée sur le formalisme de Keldysh et nous présentons des liens explicites avec le formalisme alternatif des matrices de diffusion.

Nous considérons deux types de perturbations: externe (dans les contacts) ou interne (à l'intérieur de la région centrale du système), voir Fig. 7. Nous dérivons alors un développement systématique de n'importe quelle observable (AC) en puissance de l'amplitude de la perturbation ou en puissance de la fréquence (limite adiabatique). Pour le premier développement nous proposons un ensemble de règles diagrammatiques permettant le calcul de la contribution d'un ordre quelconque et son interprétation par une série de processus d'absorption/émission de photons. Pour le second nous dérivons la limite adiabatique et nous expliquons comment y apporter des corrections systématiques.

Nous allons maintenant démontrer comment notre formalisme s'applique au calcul de la conductance (AC) et le comparons à l'approche des matrices de diffusion.

Conductance AC : approche des matrices de diffusion

Afin de calculer la conductance AC d'un système multi-terminal, on considère d'abord une tension AC appliquée à l'un des contacts, prenons le contact β ($\beta = \bar{1}$ on Fig. 7a). Ceci implique que le potentiel électrochimique du contact β oscille de la façon suivante $\mu_\beta(t) = \mu + eV_{ac} \cos \omega t$, où μ est le potentiel chimique à l'équilibre (on suppose que c'est le même dans tous les contacts,

aucune tension DC n'est appliquée). Des courants dépendants du temps sont alors générés dans tous les contacts en réponse à la perturbation. Chacun de ces courants contient diverses harmoniques,

$$I_\alpha(t) = \text{Re} \sum_{l=0}^{\infty} I_\alpha(l\omega) e^{-il\omega t}. \quad (18)$$

Cependant si l'on est intéressé par la conductance AC (linéaire), cela implique que la quantité recherchée est $\Upsilon_{\alpha\beta}(\omega) \equiv dI_\alpha(\omega)/(dV_{ac})$. Büttiker et ses collaborateurs ont trouvé que celle-ci peut-être exprimée en termes de matrices de diffusion à l'équilibre $S_{\alpha\beta}(E)$. A basse fréquence elle s'écrit [1, 5, 6],

$$\Upsilon_{\alpha\beta}^e(\omega) = \Upsilon_{\alpha\beta}^e(0) - i\omega e \frac{dN_{\alpha\beta}}{dV_{ac}}, \quad (19)$$

où $\Upsilon_{\alpha\beta}^e(0)$ est l'élément de matrice de la conductance stationnaire, et la quantité

$$\frac{dN_{\alpha\beta}}{dV_{ac}} = -\frac{e}{4\pi i} \int dE \left(-\frac{\partial f}{\partial E} \right) \text{Tr} \left[S_{\alpha\beta}^\dagger \frac{dS_{\alpha\beta}(E)}{dE} - \frac{dS_{\alpha\beta}^\dagger(E)}{dE} S_{\alpha\beta}(E) \right] \quad (20)$$

est la densité de particules émises du contact α en réponse à la variation du potentiel électrochimique du contact β . Ici $f(E)$ est une fonction de Fermi et l'exposant e est ajouté pour souligner que c'est la fonction de réponse à une perturbation *externe*.

La théorie doit satisfaire deux conditions afin d'être correcte: la conservation du courant (loi de Kirchhoff) et l'invariance de jauge, ce qui implique que,

$$\sum_{\alpha=1}^M \Upsilon_{\alpha\beta}(\omega) = \sum_{\beta=1}^M \Upsilon_{\alpha\beta}(\omega) = 0. \quad (21)$$

L'équation (19) ne remplit pas ces conditions ce qui signifie qu'elle ne peut pas décrire la réponse totale du système à la perturbation AC. En effet la contribution manquante vient d'un courant de déplacement. Considérons l'équation de continuité suivante,

$$\sum_{\alpha=1}^M \Upsilon_{\alpha\beta}^e(\omega) - i\omega \frac{dQ(\omega)}{dV_{ac}} = 0, \quad (22)$$

où $Q(\omega)$ est la transformée de Fourier de la charge total dans la région $\bar{0}$ (voir Fig. 7). Le fait que la somme des éléments de la matrice de conductance (19) ne s'annule pas signifie qu'il y a une densité non nulle de charge injectée oscillant à l'intérieur de la région centrale. En réalité cette densité de charge ne peut pas s'accumuler parce que le système s'ajuste de façon à restaurer sa neutralité électrique. Dans notre cas cela signifie que nous devons considérer le potentiel oscillant $U(\mathbf{r}, \omega)$ créé par la charge injectée, ce qui modifie les courants dans tous les contacts. Cette contribution est le courant de déplacement et elle est assimilable à une perturbation interne décrite en Fig. 7b. En termes de matrices de diffusion elle est donnée par [1, 5, 6],

$$\frac{dI_{\alpha}^i(\omega)}{dV_{ac}} = ie\omega \int d^3\mathbf{r} \frac{\delta N_{\alpha}}{\delta U(\mathbf{r})} \frac{dU(\mathbf{r}, \omega)}{dV_{ac}}, \quad (23)$$

où l'exposant i signifie *interne*, et la quantité

$$\frac{\delta N_{\alpha}}{\delta U(\mathbf{r})} = \frac{1}{4\pi i} \int dE \left(-\frac{\partial f}{\partial E} \right) \sum_{\gamma} \text{Tr} \left[S_{\alpha\gamma}^{\dagger}(E) \left(\frac{\delta S_{\alpha\gamma}(E)}{\delta U(\mathbf{r})} \right) - \left(\frac{\delta S_{\alpha\gamma}^{\dagger}(E)}{\delta U(\mathbf{r})} \right) S_{\alpha\gamma}(E) \right] \quad (24)$$

est la densité de particules émises au contact α si l'on perturbe le potentiel scalaire localement au point \mathbf{r} (dans la région centrale $\bar{0}$). Le profil du potentiel oscillant induit est calculé par l'équation de Poisson [1, 6],

$$\Delta \frac{dU(\mathbf{r}, \omega, \beta)}{dV_{ac}} = -\frac{e}{\epsilon} \left[\frac{dn(\mathbf{r}, \beta)}{dV_{ac}} + \int d^3\mathbf{r}' \Pi(\mathbf{r}, \mathbf{r}') \frac{dU(\mathbf{r}', \omega, \beta)}{dV_{ac}} \right], \quad (25)$$

où $\Pi(\mathbf{r}, \mathbf{r}')$ est la fonction de Lindhard déterminant le changement de densité électronique au point \mathbf{r} en réponse à une perturbation au point \mathbf{r}' . Cette fonction doit être calculée séparément et ne peut pas en général être exprimée via des matrices de diffusion. La première quantité entre les parenthèses de l'équation (25) est la densité de charge injectée par l'oscillation du potentiel électrochimique du contact β , et est donnée par [1, 6],

$$\frac{dn(\mathbf{r}, \beta)}{dV_{ac}} = \frac{1}{4\pi i} \int dE \left(-\frac{\partial f}{\partial E} \right) \sum_{\alpha} \text{Tr} \left[S_{\alpha\beta}^{\dagger}(E) \left(\frac{\delta S_{\alpha\beta}(E)}{\delta U(\mathbf{r})} \right) - \left(\frac{\delta S_{\alpha\beta}^{\dagger}(E)}{\delta U(\mathbf{r})} \right) S_{\alpha\beta}(E) \right]. \quad (26)$$

Enfin, en rassemblant ces résultats la conductance AC complète satisfaisant l'équation (21) s'écrit,

$$\Upsilon_{\alpha\beta}(\omega) = \Upsilon_{\alpha\beta}^e(\omega) + \frac{dI_{\alpha}^i(\omega)}{dV_{ac}}. \quad (27)$$

Comme on peut clairement le voir, l'approche par matrice de diffusion a quelques faiblesses. Premièrement la réponse interne (23) et la densité de charge induite (26), nécessaires au calcul de la fonction de réponse complète (27), dépendent d'une dérivée fonctionnelle de la matrice de diffusion par rapport au profil du potentiel scalaire dans le système, qui ne peut pas être trouvé en général. Deuxièmement, la fonction de Lindhard, présente dans l'équation de Poisson (25), est une fonction inconnue des coordonnées et nécessite des hypothèses supplémentaires pour être calculée. Troisièmement, la théorie a été construite en reposant sur le faible ordre de grandeur de l'amplitude de la perturbation et de sa fréquence. La théorie de la diffusion présentée ci-dessus ne fournit pas de guide général pour faire des calculs en pratique. Néanmoins elle est une étape qualitative importante pour la compréhension des aspects principaux des phénomènes à fréquence finie dans le transport électronique.

Notre théorie: l'approche par fonctions de Green

Dans cette thèse, nous avons utilisé le formalisme de Keldysh afin d'exprimer *n'importe quelle* observable AC en termes de fonctions de Green. Ces dernières représentent le résultat brut d'une grande variété de codes numériques existants [22]. Ainsi, étant intrinsèquement adaptée pour les simulations numériques, notre théorie peut être utilisée, par exemple, pour le calcul de la conductance AC d'un système ayant une forme et un nombre de contacts arbitraires.

Nous donnons maintenant des expressions pour les quantités utiles au calcul de la conductance AC. Tout d'abord on remarque que dans notre approche le système (voir Fig. 7) est décrit par un Hamiltonien de liaisons fortes quadratique,

$$\hat{\mathbf{H}} = \sum_{n,m} \mathbf{H}_{nm} c_n^\dagger c_m, \quad (28)$$

où c_n^\dagger (c_n) est l'opérateur usuel de création (d'annihilation) au site n . On commence par la réponse à une tension externe AC imposée au contact β . Alors la fonction de réponse correspondante est donnée par

$$\Upsilon_{\alpha\beta}^e(\omega) = \frac{e^2}{h} \int dE \text{Tr} \left[\Gamma_\alpha \mathcal{G}_2 \Gamma_\beta \mathcal{G}_0^\dagger - i\delta_{\alpha,\beta} (\mathcal{G}_2 - \mathcal{G}_0^\dagger) \Gamma_\alpha \right] \frac{f(E) - f(E + \hbar\omega)}{\hbar\omega}, \quad (29)$$

avec $\Gamma_\alpha = \text{Im}(\Sigma_\alpha^r)$, où Σ_α^r est la self-énergie (retardée) du contact α , et avec la fonction de Green (stationnaire) définie par

$$\mathcal{G}_l(E) \equiv \left(E + \frac{\hbar\omega l}{2} - \mathbf{H}_{00} - \sum_{\alpha=1}^M \Sigma_\alpha^r \right)^{-1}. \quad (30)$$

Ici \mathbf{H}_{00} est le sous-bloc de la matrice de l'Hamiltonien complet correspondant à la région centrale. Les équations (29) et (30), ainsi que d'autres expressions données ci-après, sont écrites par souci de simplicité dans l'approximation de la large bande (les self-énergies des contacts sont supposées indépendantes de l'énergie). Les expressions générales peuvent être trouvées dans la première partie du manuscrit et dans l'annexe correspondant.

Comme cela a été souligné dans la partie précédente, l'équation (29) ne décrit pas la réponse totale du système. Ainsi nous devons inclure le courant de déplacement qui en termes de fonctions de Green prend la forme,

$$\frac{dI_\alpha^i(\omega)}{dV_{ac}} = \sum_j \frac{dI_\alpha(\omega)}{dV_{jj}} \frac{dU(j, \omega)}{dV_{ac}}, \quad (31)$$

où $U(j, \omega)$ est une version discrétisée du potentiel induit $U(\mathbf{r}, \omega)$, et la quantité

$$\frac{dI_\alpha(\omega)}{dV_{jj}} = \frac{ie^2}{h} \int dE (f(E) - f(E + \hbar\omega)) \left[\mathcal{G}_0^\dagger \Gamma_\alpha \mathcal{G}_2 \right]_{jj}, \quad (32)$$

décrit un courant de réponse au contact α correspondant à une perturbation locale au site j . Afin de compléter la théorie il est nécessaire de donner les expressions de la densité de charge induite et de la fonction de Lindhard qui entrent dans l'équation de Poisson (25). Ces grandeurs déterminent alors le potentiel $U(j, \omega)$. Encore une fois ces dernières sont exprimées via les fonctions de Green *stationnaires* comme suit,

$$\frac{dn(j, \beta)}{dV_{ac}} = \frac{e}{\hbar\omega} \int dE (f(E) - f(E + \hbar\omega)) [\mathcal{G}_2 \Gamma_\beta \mathcal{G}_0^\dagger]_{jj}, \quad (33)$$

$$\begin{aligned} \Pi(\omega, j, j') = -\frac{ie}{2\pi} \int dE \left\{ (f(E) - f(E + \hbar\omega)) [\mathcal{G}_2]_{jj'} [\mathcal{G}_0^\dagger]_{j'j} \right. \\ \left. + f(E + \hbar\omega) [\mathcal{G}_2^\dagger]_{jj'} [\mathcal{G}_0^\dagger]_{j'j} - f(E) [\mathcal{G}_2]_{jj'} [\mathcal{G}_0]_{j'j} \right\}. \end{aligned} \quad (34)$$

De par cette courte démonstration nous pouvons immédiatement voir les avantages de l'approche par fonctions de Green. Les quantités qui sont en général inaccessibles (comme la dérivée fonctionnelle de la matrice de diffusion) ou même non définies (comme la fonction de Lindhard) dans la théorie de la diffusion sont ici exprimées en termes de fonctions de Green. Un autre avantage est que la fonction de Green (30) ainsi que les self-énergies des contacts sont le résultat brut de nombreux codes numériques basés sur un algorithme récursif. Cela fait de notre formalisme un outil (numérique) pratique.

Cependant, en pratique on combine les deux approches en résolvant des modèles simples à l'aide de la théorie de la diffusion et on utilise ces résultats pour comprendre les simulations numériques réalisées avec les fonctions de Green. En conséquence, ces méthodes se complètent l'une l'autre et forment un outil théorique pour étudier les phénomènes à fréquence finie.

Partie II

Etablissement du problème et objectifs

Le graphène, cette feuille plane d'atomes de carbone d'épaisseur atomique, est aujourd'hui un sujet bouillonnant et de nombreux chercheurs estiment que ses propriétés peuvent être utilisées pour révolutionner la micro/nano électronique. Les principales caractéristiques qui ont rendues ce matériau célèbre sont: (i) un spectre linéaire d'excitations à basse énergie décrit par l'équation de Dirac relativiste sans masse; (ii) une mobilité des porteurs très élevée; (iii) quantification anormale de l'effet Hall dans la partie transverse du tenseur de conductivité pouvant être observée à température ambiante.

Dans la seconde partie de la thèse nous avons étudié l'influence du couplage spin-orbite sur les propriétés électroniques et de transport dans le graphène. Il a été trouvé par C. L. Kane et

E. J. Mele, dans des travaux qui ont fait date [23, 24], qu'un type particulier d'interaction spin-orbite (qui préserve la composante S_z du spin) est capable d'induire un ordre topologique dans le graphène. Cet ordre fait apparaître un gap dans le spectre d'excitations se trouvant à l'intérieur du matériau, et des excitations sans gap (filtrées par le spin) aux bords d'une structure finie de graphène. Ces états de bord sont robustes vis-à-vis d'une large gamme de perturbations et au désordre. Cela est dû à la présence d'une symétrie par renversement du temps qui interdit toute rétrodiffusion. Une autre propriété intéressante de ces états est qu'à un bord d'un échantillon donné les spins up et les spins down se propagent en sens opposés. Ainsi on a un courant de spin sans courant de charge, voir Fig. 9a. Ce phénomène s'appelle l'effet Hall quantique de spin (QSH). Bien que de nombreux effets intéressants sortent du modèle de Kane et Mele aucune réalisation concrète n'a encore vu le jour. Une raison pour cela est que le couplage spin-orbite dans le graphène natif est trop faible [25] pour être observé expérimentalement. Dans cette thèse nous détaillons une proposition récente permettant de surmonter cet écueil. Nous proposons un moyen d'observer dans une seule expérience une transition entre les phases topologiquement différentes d'effet Hall quantique (QH) et d'effet Hall quantique de spin. Cela est rendu possible grâce au spectre relativiste du graphène.

Phase de Hall quantique de spin dans le graphène

Comme indiqué au-dessus, le travail présenté dans cette thèse a été motivé par une proposition récente visant à accroître le couplage spin-orbite dans le graphène. Ce résultat est obtenu après le dépôt d'atomes lourds (avec une forte interaction spin-orbite intra-atomique: In ou Tl par exemple) en surface [26], voir Fig. 8b. Nos conclusions se résument ainsi: (i) même lorsque la distribution d'atomes ajoutés est arbitraire, une phase QSH parfaitement homogène (décrite par le modèle de Kane-Mele) émerge avec une constante de couplage spin-orbite renormalisée par la densité d'atomes ajoutés; (ii) varier la densité d'atomes ajoutés autorise le contrôle du gap d'énergie créé par le couplage spin-orbite et la largeur des états de bord, ce qui pourrait permettre la création d'un thermocouple efficace à température ajustable (voir Sec. 8.2.2 pour les détails) [27]. En Fig. 8 nous présentons un exemple de calcul DC de coefficients de transmission entre les contacts d'une croix de graphène à quatre terminaux. On varie la force du couplage spin-orbite λ_{so} et/ou la densité d'atomes ajoutés n_{ad} et on trace les amplitudes de transmission en fonction du paramètre effectif $\lambda_{eff} = n_{ad}\lambda_{so}$ en supposant que le courant est injecté au terminal 0. On peut voir que les résultats se tracent très bien en fonction du paramètre effectif et que les transmissions de Hall T_{10} et T_{30} tendent vers l'unité, alors que la transmission directe T_{20} disparaît exponentiellement à mesure que le paramètre effectif λ_{eff} augmente. C'est une signature de la phase QSH qui émerge, caractérisée par les états de bords filtrés en spin, voir Fig. 9a. Nous avons testé sa robustesse à divers types de désordre et l'avons trouvée extrêmement stable sans signe de l'inhomogénéité spatiale de la configuration d'atomes

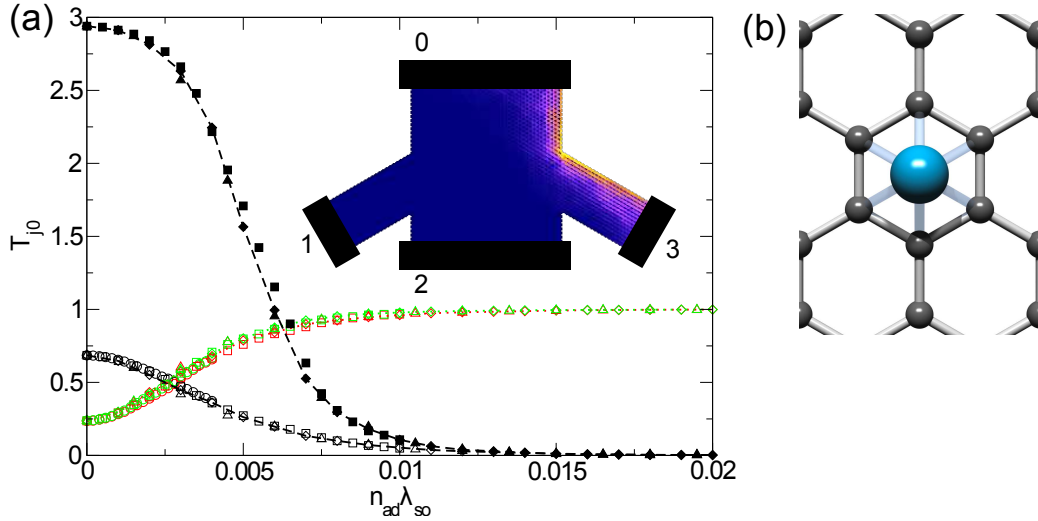


Figure 8: (a): Insert en haut: schéma de notre dispositif, une croix de graphène à quatre terminaux avec des bords de type fauteuil. Les différentes couleurs correspondent à un calcul de la densité de courant pour les électrons de spin up après injection au contact 0. L'existence d'un état de bord est manifeste. Figure principale: tracé de la transmission T_{j0} à partir du contact 0 pour plusieurs couplages λ_{so} et densités d'atomes ajoutés n_{ad} , en fonction du couplage spin-orbite effectif $\lambda_{so}^{eff} = \lambda_{so} n_{ad}$. Les courbes en tirets noirs correspondent à la transmission "longitudinale" T_{20} et les courbes en pointillés correspondent aux transmissions de "Hall" T_{10} (rouge) et T_{30} (vert). Les deux groupes de courbes correspondent à aux énergies $E = 0$ (symboles vides), et $E = 0.05$ (symboles pleins). Les différentes formes de symboles correspondent à différentes valeurs de couplage spin-orbite. (b): Vue de dessus d'un atome ajouté (cercle bleu) à un plan de graphène.

ajoutés (voir Sec. 8.2 pour les détails). De plus un simple changement d'échelle du paramètre de couplage spin-orbite permet d'expliquer le comportement du système inhomogène en utilisant le modèle homogène introduit par Kane et Mele [23, 24].

Transition entre les phases de Hall quantique et quantique de spin

La seconde partie de notre travail traite du comportement de la phase QSH dans le graphène (induite par l'ajout d'atomes par exemple) en présence d'un fort champ magnétique appliqué perpendiculairement au plan de ce dernier. Ce qui va se produire n'est pas évident parce que la présence d'un champ magnétique brise explicitement la symétrie par renversement du temps qui protège les états de bord. Considérons une croix de graphène à quatre terminaux dans les deux situations suivantes: (i) dans une phase QSH ($\lambda_{so} \neq 0$, $B = 0$, voir Fig. 9a); et (ii) dans une phase QH ($\lambda_{so} = 0$, $B \neq 0$, voir Fig. 9b). Pour un champ magnétique suffisamment fort on

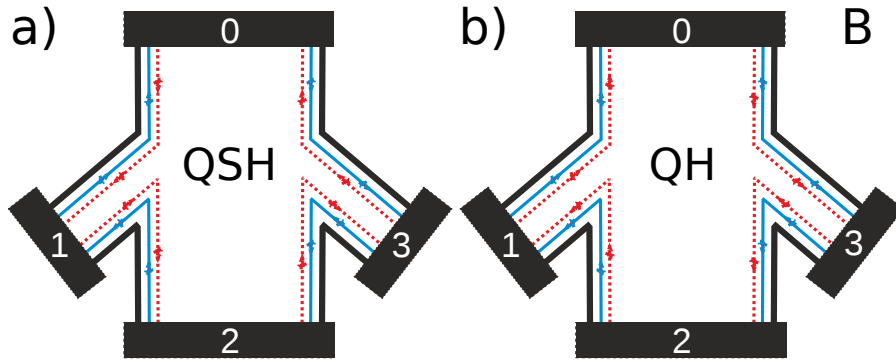


Figure 9: Schéma d'un conducteur à quatre terminaux en a) phase QSH et en b) phase QH. Les traits bleus solides et rouges en tirets représentent les états de bord pour les électrons de spins up et down respectivement.

s'attend à voir le schéma correspondant à la phase QH. Cependant, pour passer des états de bord de type QSH à ceux de type QH, on doit inverser le sens de propagation d'une des deux espèces de spin. On appellera celle-ci spin "insatisfait" dans la suite (lignes en tirets rouges en Fig. 9). Dans notre travail, nous avons étudié cette transition en détails.

Afin de développer l'intuition sur ce problème nous avons effectué des calculs de structures de bandes dans trois cas différents: les deux cas décrits ci-dessus ainsi que le cas où l'on applique ensemble un couplage spin-orbite et un champ magnétique (voir Fig. 10). La structure de bandes d'un ruban de graphène dans la phase QSH est assez différente de celle calculée en phase QH. Dans la phase QH le champ magnétique transverse donne lieu à l'apparition de niveaux de Landau $\epsilon_n = \pm(\hbar v_F/l_B)\sqrt{2|n|}$, avec $l_B = \sqrt{\hbar/(eB)}$, qui deviennent dispersifs proche des bords du ruban (Fig. 10a). Lorsque le niveau de Fermi est placé entre deux niveaux de Landau, le transport est caractérisé par des états de bords dégénérés en spin, comme indiqué en Fig. 9b, qui se propagent dans un sens imposé par le signe du champ magnétique. Dans la phase QSH, la structure de bande consiste en des bandes hyperboliques au-dessus du gap QSH, $\Delta_{so} = 3\sqrt{3}\lambda_{so}$, et une paire de bandes dispersives en-dessous (Fig. 10b). Ces bandes linéaires correspondent à des états polarisés en spin localisés aux bords du ruban de graphène (voir Section 7.2). Lorsque sont présents à la fois le champ magnétique et le couplage spin-orbite, la structure de bande se résume en des termes simples (voir Fig. 10c). Pour des énergies de Fermi à l'intérieur du gap spin-orbite telles que $|E_F| < \Delta_{so}$ (région ombragée), le système est dans la phase QSH avec des canaux de spins opposés se propageant en sens inverses. Pour des énergies telles que $|E_F| > \Delta_{so}$, le système est dans la phase QH avec des canaux de spins opposés se propageant sur un bord donné dans le même sens. Ainsi pour une valeur donnée de Δ_{so} , la transition entre les phases est gouvernée uniquement par l'énergie de Fermi et ne dépend pas du tout de la valeur du champ magnétique (en négligeant la levée de dégénérescence Zeeman, très faible dans

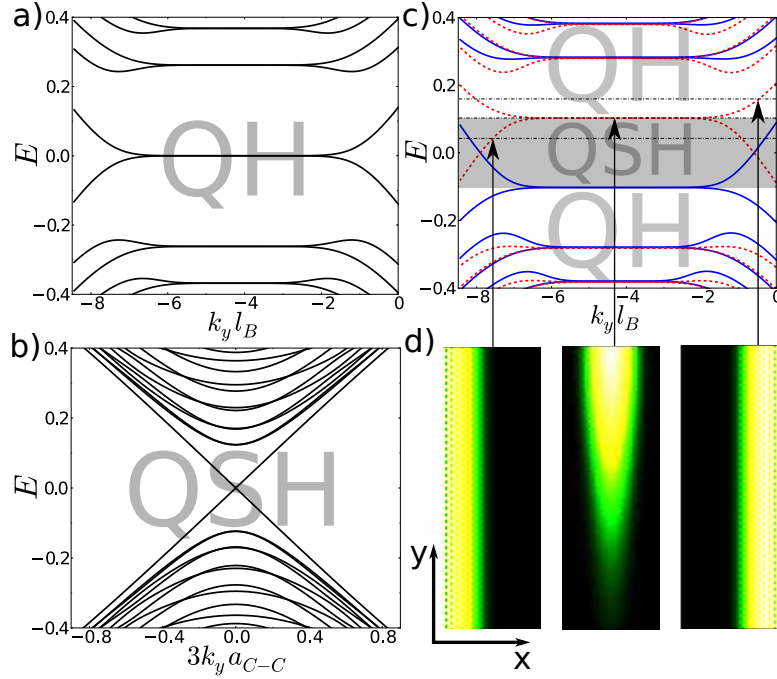


Figure 10: Structure de bandes d'un ruban de graphène (fauteuil semi-métallique) en **a)** phase QH et en **b)** phase QSH. Lorsque sont présents à la fois le champ magnétique et le couplage spin-orbite **c)**, la structure de bandes résultante conduit à une phase QSH pour $|E_F| < \Delta_{so}$ (région ombragée), et à une phase QH pour $|E_F| > \Delta_{so}$. En comparaison avec les cas QH et QSH purs, la dégénérescence en spin est levée (lignes bleues épaisses et tirets rouges). Cela est particulièrement visible dans la bande la plus basse qui consiste en des branches polarisées en spin à $E = \pm \Delta_{so}$. A mesure que l'énergie de Fermi traverse le gap spin-orbite, la localisation du spin "insatisfait" (tirets rouges) se déplace d'un bord à un autre, tandis qu'il est complètement localisé à l'intérieur du système quand $E_F = \Delta_{so}$. Ceci est illustré dans les tracés de densité de courant en **d)**. D'autre part le spin "satisfait" (bleu épais) devient de plus en plus localisé sur le même bord à mesure que l'énergie de Fermi traverse la région de transition (non présentée).

le graphène). Ce résultat assez remarquable est une conséquence directe de l'existence dans le graphène d'un niveau de Landau à énergie nulle indépendant du champ magnétique: dès que $\Delta_{so} \neq 0$ la dégénérescence en spin du niveau de Landau à énergie nulle est levée, contrairement aux autres niveaux de Landau qui restent dégénérés en spin [28]. Cette levée de dégénérescence conduit à une phase QSH dans le gap spin-orbite correspondant.

In order to check these arguments, we performed a transmission calculation in a 4-terminal Z-shaped setup schematically depicted on Fig. 11. We placed a top gate on the right half of the sample, which controlled the position of the Fermi level locally there. By an appropriate choice of gate voltage V_g it is possible to make a heterojunction between the QH and QSH phases. The

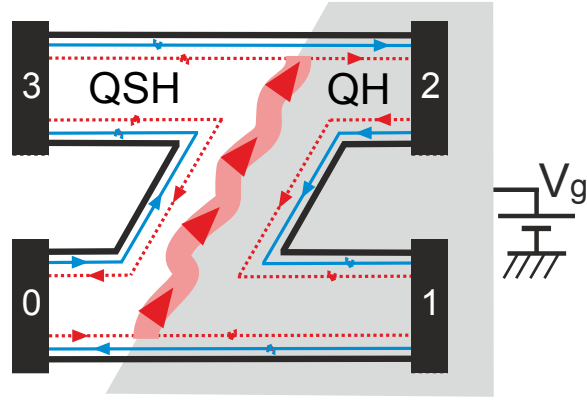


Figure 11: Hétérojonction topologique avec des états de bord QSH sur la gauche et des états de bord QH sur la droite. Cette jonction peut être réalisée expérimentalement en appliquant une grille au-dessus de la partie droite de l'échantillon (zone grisée). Tandis qu'un type de spin (bleu épais) peut se propager à travers la jonction, l'autre ne le peut pas et donne lieu à un état chiral localisé à l'interface entre les phases QSH et QH connectant les deux bords du système.

“unhappy” spin (red dashed line) being injected from lead 0 cannot penetrate the QH phase region and thus creates a chiral state at the interface between two phase. The results of the corresponding calculations are given on Fig. 12.

Afin de vérifier ces arguments nous avons réalisé un calcul de transmission dans un système en forme de Z à quatre terminaux schématisé en Fig. 11. Nous avons placé une grille au-dessus de la moitié droite de l'échantillon, celle-ci contrôlant la position du niveau de Fermi localement. Il est possible de faire une hétérojonction entre les phases QH et QSH par un choix approprié de la tension de grille V_g . Le spin “insatisfait” (ligne en tirets rouges) injecté au contact 0 ne peut pas pénétrer la région QH et crée ainsi un état chiral à l'interface entre les deux phases. Les résultats des calculs sont donnés en Fig. 12. Tant que l'énergie de Fermi dans la partie droite reste inférieure à la valeur de Δ_{so} , les caractéristiques du transport restent non affectées par la grille (insert de gauche en Fig. 12) Cependant, dès que l'énergie de Fermi de la partie droite croise le gap QSH il apparaît une jonction QSH-QH caractérisée par un état topologique à l'interface (voir insert de droite en Fig. 12). Cet état chiral se propage le long de l'interface jusqu'au bord opposé, puis est partiellement transmis dans les contacts 2 et 3 en des proportions qui dépendent des détails microscopiques du modèle (énergies de Fermi, longueur de l'interface, aspect plus ou moins lisse de la marche de potentiel, quantité de désordre, etc.). Ce système constitue un commutateur très efficace de courant de charges polarisé en spin. En effet le courant au contact 1 (respectivement 2) peut passer de un (respectivement zéro) à zéro (respectivement une valeur non nulle) tout en étant polarisé en spin simultanément (voir Fig. 12).

En résumé, nous avons montré que la transition entre les phases QSH et QH dans le graphène

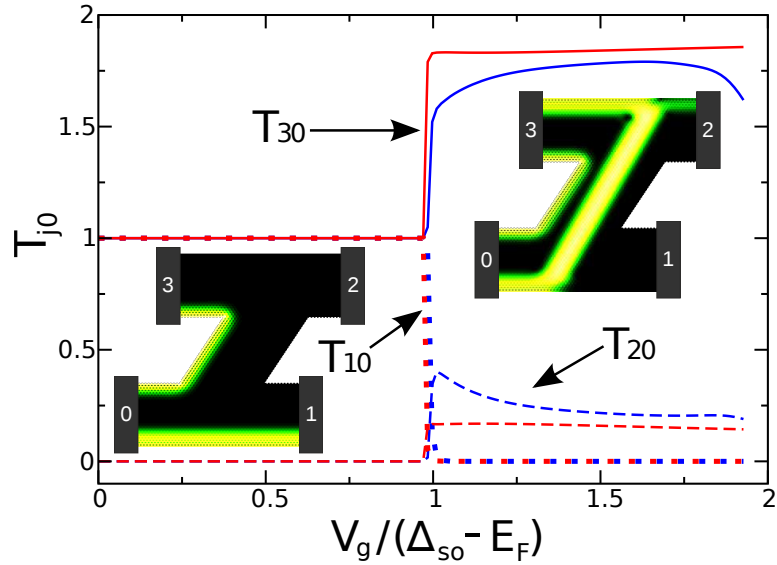


Figure 12: Hétérostructure dans un système en forme de Z à quatre terminaux comme décrit en Fig. 11. Probabilités de transmission du contact 0, d'où le courant est injecté, aux contacts 1 (courbes en pointillés), 2 (courbes en tirets) et 3 (lignes pleines) en fonction de la tension de grille V_g . Lorsque $V_g < (\Delta_{so} - E_F)$, de sorte que les régions gauche et droite sont en phase QSH, le courant est parfaitement transmis par les états de bord QSH comme indiqué par le tracé de densité de courant dans l'insert à gauche. Lorsque V_g est suffisamment grand ($V_g > (\Delta_{so} - E_F)$), de sorte que la partie droite entre dans une phase QH, une jonction QSH-QH est créée et est caractérisée par un état chiral se propageant le long de l'interface. Ceci est illustré par le graphe de densité de courant en insert à droite. Les courbes rouges correspondent à un changement de tension abrupte à travers la jonction, tandis que les courbes bleues correspondent à une transition douce.

est indépendante de la valeur du champ magnétique (en négligeant le faible effet de la levée de dégénérescence Zeeman), et qu'elle peut être franchie simplement en ajustant l'énergie de Fermi à l'intérieur du gap spin-orbite. Cette propriété unique est permise par l'existence de niveaux de Landau d'énergie nulle ($n = 0$) dans le graphène. Dans une hétérojonction un type de spin provoque l'apparition d'un état chiral le long de l'interface entre les phases QSH et QH. La nature de cet état particulier est une question fascinante qui reste encore à étudier. La transition ajustable entre les phases topologiques QSH et QH pourrait servir de commutateur de courant de charges polarisé en spin avec potentiellement de très bons ratios on/off protégés topologiquement.

Part I

Non-equilibrium quantum transport at the nanoscale

Rapidly changing market of electronic devices sets up a lot of challenges for the manufacturing and design technologies. Modern computers are built on integrated circuits which allow for more than 2.5 billion components put on a single chip. Gordon Moore in 1965 formulated a hypothesis, now called *Moore's law*, which says that the number of transistors squeezed on a single integrated circuit doubles every two years. Of course there is a natural limitation to this trend, which is the atomic scale. But before we reach this limit, we face another complication. As the density of integrated circuits continues to increase, there is a resulting need to shrink the dimensions of the individual devices of which they are comprised, see Fig. 13. As semiconduc-

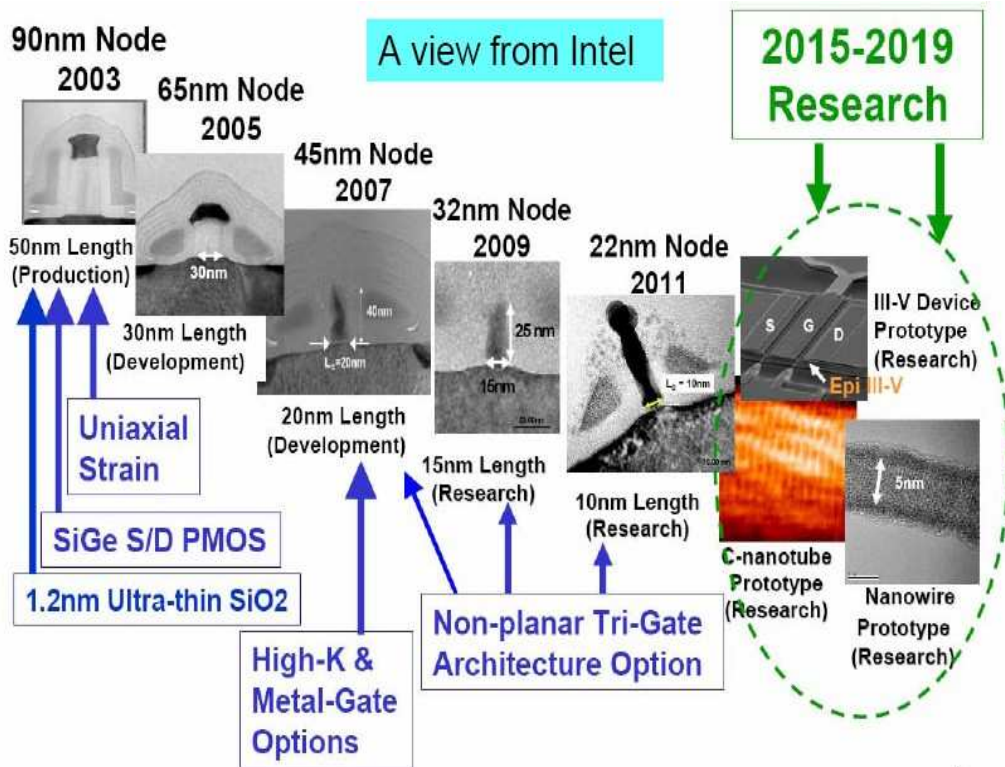


Figure 13: Scaling of successive generations of MOSFETs into the nanoscale regime and emerging nanoelectronic devices.

tor feature sizes shrink into the nanometer scale regime, device behavior becomes increasingly complicated as new physical phenomena at short dimensions occur, and limitations in material properties are reached. At this stage classical circuit theory is not capable to describe physics of nanoscale devices and quantum effects like tunnelling, size quantization, interference, and correlations become important. Microscopic details of shape and atomic structure play a crucial role in understanding the physical phenomena. All this motivates active searches for both alternative materials (graphene, for example) and innovative manufacturing technologies. On the theory side, quantum transport at the nanoscale has already become a mature branch of

condensed matter physics. Impetuous increase of computer power resources conjugated with the progress in device fabrication, stimulated development of powerful numerical techniques, like Quantum Monte Carlo, Dynamical Mean Field Theory, Numerical Renormalization Group, etc. These methods are now standard and in some cases are the only ones, which capture and reproduce behavior of nanoscale samples (Kondo effect, for example).

In this part of the thesis, we will present a general framework for calculating transport properties of small conductors out of equilibrium. In our case, ingredients which drive a system out of equilibrium are finite (stationary) bias and/or time-dependent perturbation (AC bias, oscillating gate voltage, time-dependent magnetic field, etc.). Since the case of time-independent bias is a well established and solved problem, particular emphasis of this work is on dynamical effects due to time-dependent fields.

There are two complementary approaches to coherent quantum transport, namely the scattering matrix and Non Equilibrium Green's function (NEGF) formalisms. Let us consider that our physical setup consists of (semi-infinite) leads and a scattering region. Within the scattering matrix approach we do not take into account internal details of the scattering region and treat it as a "black box". One searches for a solution in the basis of the leads, which play a role of waveguides, as a combination of incoming and outgoing waves. In contrast to this, NEGF approach considers all the details of the scattering region, while the leads play a role of boundary conditions. The scattering matrix approach allows for analytical solutions but for a very limited range of problems, where physical system has a regular shape. When it comes to numerical calculations, this method is more involved than its alternatives. On the contrary, NEGF approach is completely general and can be applied to a system of arbitrary geometry and with an arbitrary number of leads. This is because NEGF is more numerically oriented and turns out to be very powerful for simulations of nanoscale devices. The only necessary ingredient in this theory is a knowledge of equilibrium (retarded) Green's function. However it is not an issue because there exist very fast and efficient recursive techniques [29, 30, 22], which give everything we need as a standard output.

In our work we elaborate a NEGF-based theory of quantum transport in presence of finite frequency oscillating perturbations. In the literature there exist some pieces of information regarding this problem, but as far as we know, a general theory has not been built yet. We attempt to provide a rather general and simple framework to generalize existing results and give recipes for calculating new observables (photon-assisted shot noise, charge and spin pumping, etc.). Such a framework has been built within the scattering matrix formalism by M. Büttiker in the early 90's [1, 2, 3, 4, 5, 6, 7]. But, as we mentioned before, it is limited to regular system shapes and low frequencies. We generalize the results obtained by Büttiker and express all the quantities in terms of (stationary) Green's functions, which are obtained as a standard output of efficient numerical codes [29, 30, 22].

This part of the thesis is organised as follows. In Chapter 1 we briefly discuss the main characteristic length scales which govern the behavior of electrons' motion in conductors. Then, we define various physical regimes of electron transport, which are observed at certain relations between these length scales. This Chapter ends with a discussion of theoretical approaches used for describing electron transport at different levels of complexity. Chapter 2 is devoted to the overview of the problem of stationary (DC) electron transport in the presence of electrochemical potential (and/or temperature) gradients. Here we consider two complementary approaches to this problem: scattering matrix (or Landauer-Büttiker) theory and the (non-equilibrium) Green's function theory. In Chapter 3 we define the problem of electron transfer in the presence of oscillating in time (AC) perturbations. Section 3.2 is dedicated to the review of the scattering matrix formalism, developed by M. Büttiker and co-workers, for tackling this problem and discuss its main weak sides for practical use. Then follows Section 3.3, where we summarize the main practical results of our (alternative) approach based on the knowledge of *stationary* Green's functions. Namely, in the form of a short "cookbook" we present a rather long list of AC observables, each of which (such as AC conductance or photocurrent) is related to the integral (over energy) of the trace of a product of stationary (DC) Green's functions. In Section 3.4 we provide some technical details explaining how to evaluate the energy integrals in practice, and, as an application of our theory, consider two examples of calculating the AC conductance: a quantum point contact and a Mach-Zehnder interferometer in the quantum Hall regime.

Finally, the full machinery used to derive the expressions of Section 3.3 is developed in Chapter 4. It provides a set of simple rules allowing to derive any new expression beyond those given explicitly in this thesis. Section 4.1 briefly introduces the necessary notations and main results of the Keldysh formalism. Section 4.2 focuses on the particular case where the perturbation is periodic in time. We then proceed with developing systematic perturbative expansions around two distinct limits: first we provide a diagrammatic technique to expand the results in powers of the amplitude of the perturbation. Second, we expand around the adiabatic limit where the frequency of the AC perturbation is very small. These expansions are presented in Section 4.3 (perturbation applied inside the system) and Section 4.4 (perturbation in the electrodes). Section 4.5 concludes this Chapter and the first part of the thesis.

Chapter 1

Introduction

In this chapter we will give a general idea of the possible transport regimes in small conductors. Introducing the main length scales, such as the *Fermi wavelength* λ_F , *elastic mean free path* l_e , *localization length* ξ , and *phase coherence length* l_ϕ , we can distinguish between different behaviors (or regimes) of a physical system, from a purely ballistic to diffusive and even localized depending on how these scales compare to the system dimensions. For example, in the coherent ballistic regime, electrons experience no scattering on a disorder behaving like electromagnetic waves in a waveguide and analogues to most optical phenomena can be observed [31, 32, 33, 34, 35, 36, 37, 38, 39, 40]. In this case, the geometry of a sample plays very important role as the only possible scattering process occurs at the boundaries. In the diffusive regime, electrons undergo a lot of random scatterings on impurities and imperfections of a lattice performing a random walk while travelling through the sample. This case brings us to a classical limit, when leading order effects are given by the Drude model. However, if system sizes are smaller than the phase coherence length, traces of quantum interference can be observed as corrections to the classical picture. These include weak localization and antilocalization corrections and universal conductance fluctuations. Even more, when phase coherence is preserved but disorder in a system is quite strong, one can see the very intriguing phenomenon of Anderson localization, when the resistance of the sample grows exponentially with its length demonstrating strongly non-Ohmic behavior.

Finally, we will also briefly discuss a hierarchy of approaches to the problem of electron transport and see which of them are applicable in certain transport regimes.

1.1 Regimes of electron transport

In this thesis we are primarily interested in two-dimensional or quasi one-dimensional conductors. So, let us consider a conductor of length L and width W connected to two electron reservoirs. Electronic motion inside the conductor strongly depends on the relation between

the conductor dimensions and characteristic length scales, which are defined by the microscopic processes occurring when an electron traverses from the left reservoir to the right one. Thus, one can discriminate between several transport regimes (see below). Now we are going to define the characteristic length scales of the system and discuss how various relations between them affect the electron dynamics.

In the absence of a magnetic field there are four major length scales which govern the electron motion through the system. First of all, it is the wavelength of an electron, λ_F , which is also called Fermi wavelength since at low temperature only electrons close to the Fermi surface contribute to all physical observables. Another aspect which introduces an important length scale is the fact that real samples always contain disorder: impurities or lattice imperfections. Then, we can introduce the average length travelled by the electron between two successive scatterings, the (elastic) mean free path, l_e , where the subscript means that the scattering is *elastic* and can only change the direction of electron momentum without changing its energy (disorder is static). Another important length scale is called phase relaxation length l_ϕ . This length characterizes processes which randomize the phase of the electronic wave. These include inelastic scattering with dynamic quasiparticles, like phonons for example, and collisions between electrons. The former lead to energy relaxation and by this destroy information about the initial electron phase, while the latter do not change the total momentum of the electronic subsystem but destroy the phase coherence of individual carriers. So, l_ϕ is the average distance an electron travels before losing its phase coherence. It should be noted that impurities can also lead to phase breaking processes provided they have an internal degree of freedom (spin, for example) which can change a state of the impurity in the scattering process. Finally, if the conductor maintains phase coherence (its size is smaller than l_ϕ), then in the presence of disorder interference caused by multiple scattering events may lead to an exponential localization of the electron wave function on a scale ξ called the localization length. This scale becomes important when the conductor length becomes comparable to it.

Having defined the main length scales we can discuss the transport regimes which arise from the competition between the former. One of the smallest scales is the Fermi wavelength λ_F . If we assume that electrons occupy the states within a Fermi sphere up to some maximal momentum k_F , then in 2D we have $\lambda_F = 2\pi/k_F = \sqrt{2\pi/n}$, where n is the electron density. In metals because of a high electron density we typically have $\lambda_F \sim 1\text{\AA}$, however in semiconductors it can be up to a few hundreds of nanometers (for example, $\lambda_F = 35\text{ nm}$ for electron density $n \simeq 5 \times 10^{11}/\text{cm}^2$). In this thesis we are interested in quantum effects on the electron transport resulting from an interference of phase coherent electrons. This branch of condensed matter physics is called *mesoscopic* physics. So, in what follows we implicitly assume that the conductors under interest are phase coherent, i.e. $L, W < l_\phi$. One should note that this is a typical case in low temperature experiments as phase breaking processes become considerably suppressed at high temperatures,

where $l_\phi \propto T^{-p}$ ($p > 0$). On the other hand if we deal with a system of a size bigger than l_ϕ , we can divide it into coherent subparts, inside of which the transport is coherent, and then simply apply a law of adding resistors in parallel and/or in series to find the resistance of the whole sample. So, in order to classify various regimes, we will use $\mathcal{L} = \min(L, W, l_\phi)$. It is also important to remember that the localization length $\xi \gg l_e$ because multiple electron scatterings are needed to produce a localized state of an electron. For example, in a quasi one-dimensional wire of finite width, we typically have $\xi/l_e \simeq 2W/\lambda_F$.

Ballistic regime ($\mathcal{L} \ll l_e \ll \xi$). Here we can neglect the disorder effects and the resistance does not depend on the sample length as in the case of Ohm's law. The resistance comes from the contact resistance due to connection to the reservoirs. A particle propagates through the conductor bouncing off the boundaries.

Diffusive regime ($l_e \ll \mathcal{L} \ll \xi$). An electron when travelling through the conductor undergoes a big number of (elastic) scatterings relaxing the momentum and its motion resembles a random walk. The leading order contribution to the resistance is given by the Drude model, while interference effects (like weak localization (WL) or universal conductance fluctuations (UCF)) give corrections to it. The resistance thus (to leading order) grows linearly with length recovering the Ohm's law.

Localized regime ($l_e \ll \xi \ll \mathcal{L}$). In this case as a consequence of both a strong disorder and a destructive interference the electron wave function is exponentially localized in space. Then, as was shown by Anderson [41], the resistance demonstrates strongly non-Ohmic behavior and grows exponentially with the conductor length.

In this thesis we mainly focused on the applications of our theory to ballistic samples at low temperature. However, it is straightforward to extend it to a broader class of systems because the formalism developed is rather general.

1.2 Approaches to electron transport

In this small section we will briefly mention various theoretical approaches to the problem of electron transport. We summarize them in a table in the order of increasing complexity, see Fig. 1.1. Semiclassical approaches, like drift-diffusion equations or Boltzmann equation, can be used to describe satisfactory effects happening on a level of the Drude model, i.e. they do not take into account interference effects. These can be used to describe leading order effects in the diffusive regime. If one wants to look at the interference corrections or describe the ballistic or localized regime, it is necessary to use one of the quantum approaches.

In this thesis we will use the Green's function approach, more specifically the Keldysh non-equilibrium Green's function (NEGF) formalism [43, 44, 45, 46, 47], which is rather general and can be applied at least in principle to any transport regime. We will explicitly neglect the

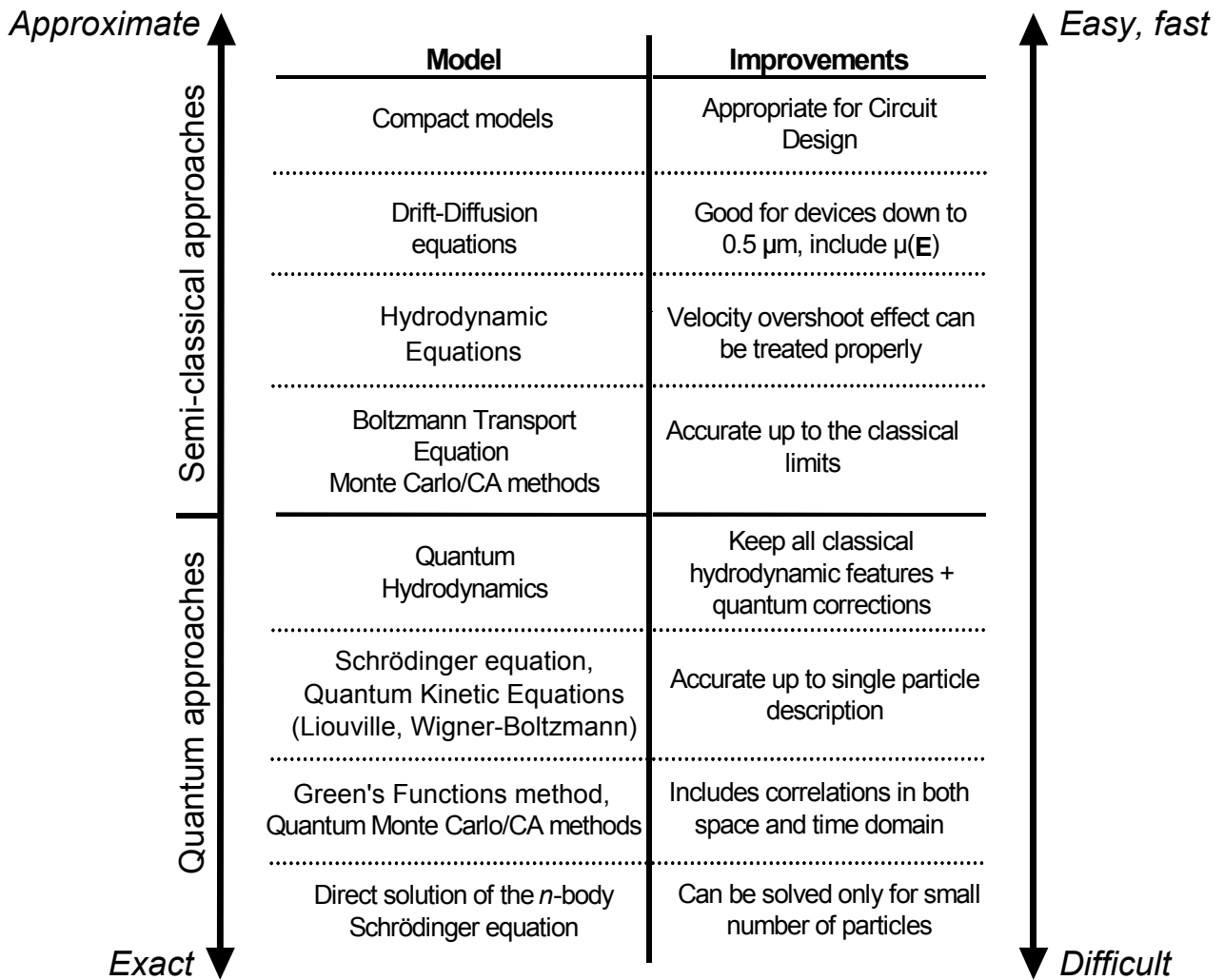


Figure 1.1: Hierarchy of approaches to the electron transport. Adapted from [42].

electron-electron interactions and thus the theory developed in the thesis is accurate up to a one-particle approach. Applied to ballistic transport problems, it is equivalent to an alternative scattering matrix formalism [48, 49, 50, 51, 45], which is basically a solution to a one-particle Schrödinger equation.

In the next chapter we will review these two approaches and their application to a stationary (DC) electron transport.

Chapter 2

Stationary electron transport

In this chapter we address the problem of stationary electron transport. It is a common situation for a case when various subparts of a system are in a local thermal equilibrium. Then, gradients of temperature or electrochemical potential give rise to a directed flux of heat or charge in the system according to laws of thermodynamics. This problem is rather old and has been described at different levels by the approaches from Fig. 1.1. However for a particular case of phase coherent systems, there are two major approaches which will be discussed in the two subsequent sections: scattering matrix approach and the Green's function approach. They rely on two distinct but complementary points of view on the problem. Imagine a mesoscopic system connected to multiple semi-infinite leads, see Fig. 2.1.

Within the scattering formalism we search for reflected and transmitted electronic waves in the leads resulting from scattering of an incident wave on the sample. By doing this it is not required to know any information about the sample itself, we treat it as a black box which only reacts in response to the incoming waves in the form of the scattered ones.

On the other hand, with the Green's function approach one takes a different point of view. By "integrating out" the leads, the otherwise infinite problem gets reduced to the size of the sample. Thus, one takes into account all the microscopic details of the mesoscopic sample while the effect of the leads enters the formalism through the so-called self-energies, which play a role of boundary conditions.

Each of these methods has its advantages and weak sides as we will see below. However in most cases they are equivalent and give the same results, while the choice between one method or the other depends on convenience and a specific problem at hand.

2.1 Scattering matrix approach

This section is devoted to a method, which proved to be very useful in describing small coherent conductors in a ballistic regime. Its main ingredient is a knowledge of the so-called scattering

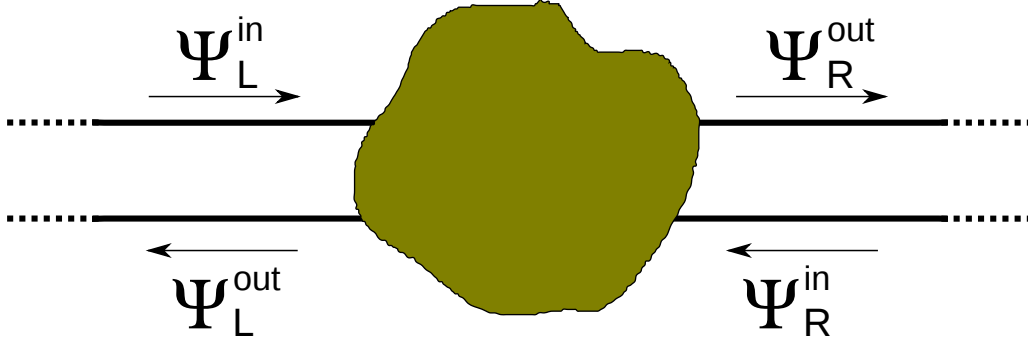


Figure 2.1: Mesoscopic sample connected to two semi-infinite ideal leads. By arrows we denote incoming and outgoing waves in the left and right contacts.

matrix and it is essentially a rather general solution to a Schrödinger equation. Below we will introduce the scattering matrix and discuss the main idea and advantage of describing electron transport in terms of this quantity.

2.1.1 Scattering matrix and the Landauer-Büttiker formula

Imagine that we have a mesoscopic system connected to external reservoirs via perfect leads, see Fig. 2.1. Under perfect leads we imply semi-infinite contacts of a regular shape with a translational symmetry. In the scattering approach we do not care about the internal details of the sample and we treat it as a "black box". On the other hand, what is important is to know the system response to an incoming electron wave. So, we are normally working in the basis of the leads and are searching for transmitted and reflected waves inside them resulting from the incident wave scattering on the mesoscopic system. One can thus classify the waves in the whole system into two categories: "incoming" and "outgoing" with respect to the mesoscopic sample. It is instructive to consider a simple case when the leads on Fig. 2.1 are one-dimensional and described by a simple Schrödinger equation,

$$-\frac{\hbar^2}{2m} \frac{d^2}{dx^2} \Psi(x) = E\Psi(x). \quad (2.1)$$

Let's also assume that the mesoscopic system to which they are connected is just a piece of the same one-dimensional lead. So, the whole system is just an infinite one-dimensional wire. Now consider a small bias V applied between the leads. We are interested in the conductance of such a structure. It is well-known that because of the Pauli principle only electrons near the Fermi surface contribute to the current. Then, the energy gain of the particles moving due to the applied bias is given by,

$$eV = \frac{1}{2}m(v_F + \delta v)^2 - \frac{1}{2}mv_F^2 = mv_F\delta v + \frac{1}{2}m(\delta v)^2. \quad (2.2)$$

If the bias is small, we can neglect the second term and find the current through the system as $I = en\delta v$, where $n = k_F/(2\pi)$ (spin not included) is the electron density in 1D. Thus, we obtain

$$I = e \frac{k_F}{\pi} \frac{eV}{mv_F} = \frac{e^2}{h} V, \quad (2.3)$$

where we have used $mv_F = \hbar k_F$. Then the conductance reads

$$G = \frac{I}{V} = \frac{e^2}{h}. \quad (2.4)$$

It is a rather important conclusion which tells us that the conductance of a one-dimensional wire without scatterers is a universal constant. We can generalize it on a case of a quasi one-dimensional wire of a finite width W . Then one has to solve a 2D Schrödinger equation with corresponding boundary conditions,

$$-\frac{\hbar^2}{2m} \left(\frac{d^2}{dx^2} + \frac{d^2}{dy^2} \right) \Psi(x, y) = E\Psi(x, y), \quad (2.5)$$

$$\Psi(x, y = 0) = \Psi(x, y = W) = 0. \quad (2.6)$$

This brings us to the concept of transverse channels or modes, since the wavenumber in y -direction gets quantized due to confinement. Thus, the eigenvalue problem leads to the solution of the form,

$$\Phi_n^\pm(x, y) = C \sin(q_n y) e^{\pm i k_x x}, \quad E = \frac{\hbar^2}{2m} (k_x^2 + q_n^2), \quad (2.7)$$

$$q_n = \frac{n\pi}{W}, \quad n = 1 \dots N, \quad (2.8)$$

where the maximal number of channels $N = \text{int}(kW/\pi)$, $k = \sqrt{2mE}/\hbar$. If we deal with a perfect wire, i.e. if there is no disorder in it which might cause backscattering and mode-mixing, then each transverse channel at a given integer n is independent of the others and completely equivalent to the one-dimensional wire discussed above. In this case the conductance at a given energy is simply given by the number of open transverse modes times the conductance quantum (2.4). One should note that the normalization constant C in Eq.(2.7) is chosen so that each channel carried unit flux and thus contributed a single conductance quantum to the overall conductance of the wire.

Now we are prepared to discuss a general case of arbitrary system connected to ideal leads, Fig. 2.1. In order to describe a response of a mesoscopic system to the incident waves, we can write down the electronic wave function at each side of the system in the form,

$$\Psi_L(x, y) = \Psi_L^{in} + \Psi_L^{out} = \sum_{n=1}^{N_L} [c_{n,L}^{in} \Phi_n^+(x, y) + c_{n,L}^{out} \Phi_n^-(x, y)], \quad (2.9)$$

$$\Psi_R(x, y) = \Psi_R^{in} + \Psi_R^{out} = \sum_{n=1}^{N_R} [c_{n,R}^{in} \Phi_n^-(x, y) + c_{n,R}^{out} \Phi_n^+(x, y)]. \quad (2.10)$$

Here the concept of the scattering matrix is introduced. It is a matrix, which provides a relation between the coefficients $c_{n,L/R}^{in}$ of the incoming waves and the coefficients $c_{n,L/R}^{out}$ of the outgoing ones. If we introduce vectors $\mathbf{c}^{in/out} = \left(c_{1,L}^{in/out}, \dots, c_{N_L,L}^{in/out}, c_{1,R}^{in/out}, \dots, c_{N_R,R}^{in/out} \right)^T$, then one can write

$$\mathbf{c}^{out} = S\mathbf{c}^{in}, \quad (2.11)$$

where S is a $N_T \times N_T$ ($N_T = N_L + N_R$ – total number of modes) scattering matrix, which can be conveniently decomposed into sub-blocks as

$$S = \begin{pmatrix} r & t' \\ t & r' \end{pmatrix}. \quad (2.12)$$

Here, if we imagine a wave incident on the system from the left, the $N_L \times N_L$ matrix r describes the reflected wave exiting through the left lead, and the $N_R \times N_R$ matrix t describes the transmitted wave in the right lead. Similarly, r' and t' describe reflection and transmission for waves coming from the right lead.

Now we consider main properties of the scattering matrix. First of all, current conservation leads to the conclusion that S is unitary. Indeed, the flux incoming on the system must be equal to the outgoing flux,

$$\mathbf{c}^{in\dagger} \mathbf{c}^{in} = \mathbf{c}^{out\dagger} \mathbf{c}^{out}. \quad (2.13)$$

Then, using the definition (2.11), we come to

$$S^\dagger S = S S^\dagger = \mathbf{1}. \quad (2.14)$$

Another useful property of the scattering matrix is the Onsager reciprocity relation, which holds irrespectively of a system under consideration in the presence of local thermal equilibrium at small bias (linear regime). When the system is in the external magnetic field B , then under reversing the field direction scattering matrix gets transposed

$$[S]_{-B} = [S^T]_B. \quad (2.15)$$

Though Onsager relations are rather general and may be derived from the thermodynamic arguments, one can demonstrate that Eq.(2.15) holds from a very simple consideration [45]. In the presence of a magnetic field, using the minimal coupling substitution ($-i\hbar\nabla \rightarrow -i\hbar\nabla + e\mathbf{A}$, where $[\nabla \times \mathbf{A}] = \mathbf{B}$) in the Schrödinger equation it straightforward to find that $[\Psi^*(x, y)]_{-B} = [\Psi(x, y)]_B$ [45]. In other words, if we know a solution for the magnetic field B , it is enough to take its complex conjugate to find the solution at $-B$. But taking complex conjugate transforms incoming waves into outgoing ones and vice versa (see Eq.(2.7)). Therefore, we can write

$$(\mathbf{c}^{in})^* = [S]_{-B} (\mathbf{c}^{out})^*. \quad (2.16)$$

Then, combining Eq.(2.16) with the definition (2.11) one finds

$$[S^*]_{-B} = [S^{-1}]_B. \quad (2.17)$$

Finally, the unitarity condition (2.14) ensures that $S^{-1} = S^\dagger$, which immediately yields Eq.(2.15).

The scattering matrix formalism is useful for studying electron transport in coherent systems because as soon as we know the scattering matrix of a problem, we can directly find the conductance between any pair of the leads connected to a mesoscopic system using the Landauer-Büttiker approach [48, 49, 50, 51, 45]. Within this approach, if we have a mesoscopic sample connected to M semi-infinite leads, then the current flowing *into* the lead α can be found from

$$I_\alpha = \frac{e}{h} \int dE \sum_{\beta=1}^M [T_{\alpha\beta} f_\beta(E) - T_{\beta\alpha}(E) f_\alpha(E)], \quad (2.18)$$

where $T_{\alpha\beta}$ is a transmission coefficient from lead β to lead α at a given energy, $f_\alpha(E)$ is a Fermi-Dirac distribution in lead α , and $e > 0$ is the elementary charge. Since we expect to see no net current at (global) equilibrium ($f_\alpha(E) \equiv f(E)$ for $\alpha = 1, \dots, M$) we deduce that

$$\sum_{\beta=1}^M T_{\alpha\beta}(E) = \sum_{\beta=1}^M T_{\beta\alpha}(E) = N_\alpha(E), \quad (2.19)$$

where $N_\alpha(E)$ is the number of open channels in the lead α . The last equality is a simple sum rule which follows from the fact that we perform a summation of transmissions over all recipient electrodes provided we inject particles through the lead α . Therefore since we assume ideal semi-infinite leads, this quantity is simply given by the number of open modes in the source lead at energy E (see discussion after Eq.(2.7)) [45]. Exploiting these properties we finally get

$$I_\alpha = \frac{e}{h} \int dE \sum_{\beta=1}^M T_{\alpha\beta}(E) [f_\beta(E) - f_\alpha(E)] = -\frac{e}{h} \int dE \sum_{\beta=1}^M [N_\alpha(E) \delta_{\alpha\beta} - T_{\alpha\beta}(E)] f_\beta(E). \quad (2.20)$$

If we imagine that the bias applied between the contacts is small, then the current can be expressed via the conductance matrix as¹

$$I_\alpha = \sum_{\beta=1}^M \bar{\Upsilon}_{\alpha\beta} (V_\beta - V_\alpha) = \sum_{\beta=1}^M \Upsilon_{\alpha\beta} V_\beta, \quad (2.21)$$

$$\bar{\Upsilon}_{\alpha\beta} = \frac{e^2}{h} \int dE T_{\alpha\beta}(E) \left(-\frac{\partial f}{\partial E} \right), \quad (2.22)$$

$$\Upsilon_{\alpha\beta} = -\frac{e^2}{h} \int dE [N_\alpha(E) \delta_{\alpha\beta} - T_{\alpha\beta}(E)] \left(-\frac{\partial f}{\partial E} \right). \quad (2.23)$$

¹We use $\Upsilon_{\alpha\beta}$ instead of $G_{\alpha\beta}$ to clearly distinguish the conductance matrix from various types of Green's functions introduced in the thesis.

As one can see the only ingredient necessary to find the transport properties of a multiterminal system is the matrix of transmission coefficients between the contacts. The point is that it is directly related to the scattering matrix via

$$T_{\alpha\beta}(E) = \sum_{n \in \alpha} \sum_{m \in \beta} \tau_{nm}(E), \quad \tau_{nm}(E) = |S_{nm}(E)|^2, \quad (2.24)$$

where the double summation runs over all open channels in the "source" lead β and all open channels in the "drain" α ; $\tau_{nm}(E)$ is a transmission probability between the mode m in lead β and the mode n in lead α .

Onsager relation (2.15) for the scattering matrix leads to the following symmetry of the conductance matrix elements,

$$[\Upsilon_{\alpha\beta}]_B = [\Upsilon_{\beta\alpha}]_{-B}. \quad (2.25)$$

In the end, we note that in a case when a mesoscopic sample can be decomposed into several parts, for each of which we know a scattering matrix, the scattering matrix for the whole system can be easily found by combining the scattering matrices of the individual parts [45]. By doing this one takes into account all Feynman paths consisting of all possible successive reflections/transmissions between the parts of the system before the wave gets finally transmitted or reflected into the contacts.

To conclude, it is necessary to say that the scattering approach considered in this section is particularly useful when it is possible to do the calculation of a scattering matrix analytically since the results are very intuitive and allow for a simple physical interpretation. However when a system has a nonregular shape, disorder, or when it is necessary to consider various types of particle-particle interactions, this approach is not efficient in practice. In this case a standard method to choose is based on Green's functions. We will discuss it in the next section.

2.2 Green's function approach

In this section we recall the main idea behind the use of the so-called Green's functions in describing stationary electron transport in multiterminal devices. The main advantage of this method is that it is rather general, can be fairly easily extended to take into account multiple ingredients (like disorder, electric and magnetic fields, electron-phonon and electron-electron interactions, etc.), and is much more numerically oriented than the scattering approach described in the previous section. The latter feature is very important since, at present, the computer power resources available are enough to simulate realistic devices in a couple of hours or days. This stimulated a big progress in this direction and nowadays computer-assisted science is a mature field of research.

2.2.1 Definition of a retarded Green's function

Let us start with a definition of a typical model system. Imagine a system which consists of a central part, which we will call a *scattering* or *device region*, connected to M semi-infinite leads, see Fig. 2.2. The leads are assumed to have a translational symmetry so that one can

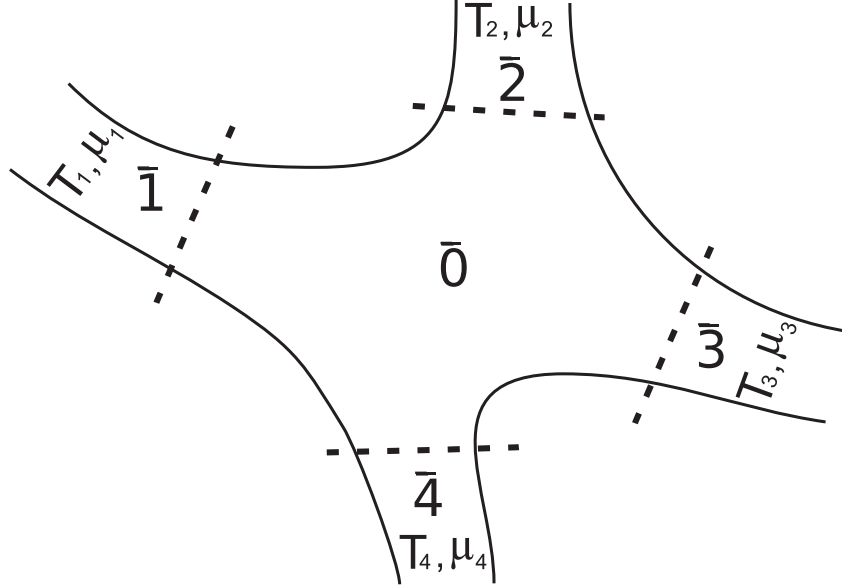


Figure 2.2: Sketch of a multi terminal mesoscopic system connected to $M = 4$ leads. Numbers with a bar on top denote the parts of our system, i.e. $\bar{0}$ for the device region and $\bar{1} \dots \bar{4}$ for the leads.

single out a unit layer in each of them, which is infinitely repeated. The system in total is kept out of equilibrium (but in a stationary state) by assuming a local thermal equilibrium in the contacts with fixed temperatures and chemical potentials. The goal is to find currents flowing through the contacts in response to the gradients of chemical potential and/or temperature.

In order to simulate such a device it is common to use a tight-binding model with a Hamiltonian

$$\hat{\mathbf{H}} = \sum_{n,m} \mathbf{H}_{nm} c_n^\dagger c_m, \quad (2.26)$$

where c_n^\dagger (c_n) is a usual creation (destruction) operator on site n . The site index n is very generic and includes all the degrees of freedom present in the system (spatial, momentum, spin, electron/hole, orbital, etc.). This kind of Hamiltonian can be obtained in various ways, via a discretization of a usual Schrödinger equation on a lattice or by using an appropriate localized basis set (Wannier functions) in a procedure of the second quantization. In any case Eq.(2.26) is the most general form of the model Hamiltonian if one neglects interactions between the particles. Then, in terms of the (infinite) \mathbf{H} matrix the retarded Green's function can be

defined as

$$\mathcal{G}(E) = (E + i\epsilon - \mathbf{H})^{-1}, \quad (2.27)$$

where ϵ is an infinitely small positive number. This is one of the two basic quantities one needs to know to solve a stationary transport problem. One should note that even if we defined the retarded Green's function in Eq. (2.27), it is impossible to find an inverse of the infinite matrix. To resolve this issue, there is one important step in this formalism, namely integrating out the leads. We will outline it further.

2.2.2 Integrating out the leads: self-energy

We will enumerate different parts of the system by numbers with a bar on top: $\bar{0}$ for the device region and $\bar{1}, \dots, \bar{M}$ for the leads (see Fig. 2.2). For convenience it is useful to introduce a notation $A_{\bar{m}\bar{m}'}$, which refers to the corresponding sub-block of the full infinite matrix A . Let us split the full Hamiltonian matrix as follows

$$\mathbf{H} = \mathcal{H} + \mathbf{V} = \begin{pmatrix} \mathbf{H}_{\bar{0}\bar{0}} & 0 & 0 & \dots & 0 \\ 0 & \mathbf{H}_{\bar{1}\bar{1}} & 0 & \dots & 0 \\ 0 & 0 & \ddots & \dots & 0 \\ 0 & 0 & 0 & \dots & \mathbf{H}_{\bar{M}\bar{M}} \end{pmatrix} + \begin{pmatrix} 0 & \mathbf{H}_{\bar{0}\bar{1}} & \dots & \mathbf{H}_{\bar{0}\bar{M}} \\ \mathbf{H}_{\bar{1}\bar{0}} & 0 & \dots & 0 \\ \vdots & 0 & \dots & 0 \\ \mathbf{H}_{\bar{M}\bar{0}} & 0 & \dots & 0 \end{pmatrix}, \quad (2.28)$$

where \mathcal{H} consists of the Hamiltonian matrices of the device region and the leads when they are decoupled, and \mathbf{V} is the coupling between them. If we define the Green's function calculated via Eq.(2.27) with \mathcal{H} as g , then we can write

$$(E - \mathbf{H}) \mathcal{G}(E) = \mathbf{1}, \quad (2.29)$$

$$(E - \mathcal{H}) g(E) = \mathbf{1}, \quad (2.30)$$

where $\mathbf{1}$ is a unit matrix. Now inserting the splitting (2.28) into Eq.(2.29) and using Eq.(2.30) we come to the Dyson equation,

$$\mathcal{G} = g + g\mathbf{V}\mathcal{G}. \quad (2.31)$$

Since we are interested in a current flowing through the device, we need to calculate explicitly the $\mathcal{G}_{\bar{0}\bar{0}}$ sub-block of the full Green's function. This can be done using the Dyson equation (2.31). Thus, one obtains for the retarded Green's function inside the device region

$$\mathcal{G}_{\bar{0}\bar{0}}(E) = \left(E - \mathbf{H}_{\bar{0}\bar{0}} - \sum_{m=1}^M \Sigma^r(m; E) \right)^{-1}, \quad (2.32)$$

where $\mathbf{H}_{\bar{0}\bar{0}}$ is the Hamiltonian matrix projected inside the device region (see Fig. 2.2) and $\Sigma^r(m; E)$ is the (retarded) self-energy due to the presence of the lead m . The latter is given by,

$$\Sigma^r(m; E) = \mathbf{H}_{\bar{0}\bar{m}}(E + i\epsilon - \mathbf{H}_{\bar{m}\bar{m}})^{-1}\mathbf{H}_{\bar{m}\bar{0}}. \quad (2.33)$$

In contrast to the general definition (2.27), the quantities in equations (2.32) and (2.33) are finite size matrices. As we will see below, knowledge of these quantities is all we need to calculate the DC conductance of a mesoscopic system.

2.2.3 Meir-Wingreen formula for current

As soon as one knows the retarded Green's function of the device and self-energies of the leads, it is possible to make use of the Landauer formalism outlined in the previous chapter. Thus, it is necessary to find an expression for the transmission matrix $T_{mm'}(E)$ between any pair of contacts (see Eq.(2.20)). Since initially we assumed the leads to be kept at different temperatures and chemical potentials, the problem of electron transport is essentially non equilibrium. In order to treat it properly one has to apply the non equilibrium Green's function (NEGF) formalism [43, 46, 47]. This is the central method used in the thesis and it will be addressed in the subsequent chapters. What one has to know for the moment is that using NEGF it is quite straightforward to show that any element of the transmission matrix can be expressed via $\mathcal{G}_{\bar{0}\bar{0}}(E)$ and $\Sigma^r(m; E)$. Then we can finally write down the Meir-Wingreen formula for the current [52, 45],

$$I_m = \frac{e}{h} \int dE \sum_{m'=1}^M (f_{m'} - f_m) \text{Tr} \left[\mathcal{G}_{\bar{0}\bar{0}} \Gamma_{m'} \mathcal{G}_{\bar{0}\bar{0}}^\dagger \Gamma_m \right], \quad (2.34)$$

where the Fermi function $f_m(E) = 1/(e^{-(E-\mu_m)/kT_m} + 1)$, and we have introduced a standard broadening matrix

$$\Gamma_m(E) = i \left[\Sigma^r(m; E) - \Sigma^{r\dagger}(m; E) \right]. \quad (2.35)$$

At small bias we can express the current via the conductance matrix (as in Eq.(2.21))²,

$$I_m = \sum_{m'} \bar{\Upsilon}_{mm'} (V_{m'} - V_m) = \sum_{m'} \Upsilon_{mm'} V_{m'}, \quad (2.36)$$

$$\bar{\Upsilon}_{mm'} = \frac{e^2}{h} \int dE \left(-\frac{\partial f}{\partial E} \right) \text{Tr} \left[\mathcal{G}_{\bar{0}\bar{0}} \Gamma_{m'} \mathcal{G}_{\bar{0}\bar{0}}^\dagger \Gamma_m \right], \quad (2.37)$$

$$\Upsilon_{mm'} = \frac{e^2}{h} \int dE \left(-\frac{\partial f}{\partial E} \right) \text{Tr} \left[\mathcal{G}_{\bar{0}\bar{0}} \Gamma_{m'} \mathcal{G}_{\bar{0}\bar{0}}^\dagger \Gamma_m - i \delta_{mm'} \left(\mathcal{G}_{\bar{0}\bar{0}} - \mathcal{G}_{\bar{0}\bar{0}}^\dagger \right) \Gamma_m \right]. \quad (2.38)$$

As we pointed out in the beginning of this section, the Green's function formalism is a powerful numerical tool. Indeed, equations (2.32) and (2.33) are the typical raw output of, say, recursive Green's function techniques [29, 30, 53, 22, 54, 55]. So, a calculation of conductance or current noise is a trivial task with such tools at hand. In the next paragraph we will briefly

²In order to write Eq.(2.38) we used the relation: $\mathcal{G}_{\bar{0}\bar{0}} - \mathcal{G}_{\bar{0}\bar{0}}^\dagger = \mathcal{G}_{\bar{0}\bar{0}}^> - \mathcal{G}_{\bar{0}\bar{0}}^< = -i \sum_{m'} \mathcal{G}_{\bar{0}\bar{0}} \Gamma_{m'} \mathcal{G}_{\bar{0}\bar{0}}^\dagger$, where $\mathcal{G}_{\bar{0}\bar{0}}^<$ and $\mathcal{G}_{\bar{0}\bar{0}}^>$ are the lesser and greater Green's functions inside the device region (see Section 4.1).

review one of them based on a "knitting algorithm" developed in Ref.[22]. This package called KNIT³ was used to perform all the numerical calculations presented in this thesis.

2.2.4 The KNIT package

KNIT is a numerical tool for solving tight-binding problems with quadratic Hamiltonians as in Eq.(2.26). It implements an attempt to make a solver which would not depend on a problem geometry or topology. All earlier existing codes were written for specific problems with a concrete geometry and thus had to be considerably modified in order to adapt to different problems. First great advantage of KNIT is that one can build a system site by site (just like one knits some clothes) and thus simulate any geometry, which makes this package rather flexible. Second advantage is that KNIT is a library compatible with a Python scripting language. The latter is quite spread in the scientific community because of its simplicity but yet powerful capabilities.

The input of a typical KNIT calculation is a quantum system connected to semi-infinite periodic electrodes, as on Fig. 2.2. In practice, one has to provide a tight-binding model that describes the finite quantum region of interest as well as a description of the electrodes. For the latter it is necessary to provide a tight-binding model for a unit layer and the inter-layer coupling, which defines the direction in which this layer should be repeatedly translated to form an electrode. The bare output of KNIT are various elements of the retarded Green's function of the system (device region) and the self-energies of all leads. This is enough to calculate a variety of observables, like conductance, current noise, (local) density of states, density of particles on a given site of the system, current density maps, etc. KNIT calculates any sub-block of the Green's function matrix on demand:

- a) between the leads-system interface sites (to study global transport properties of the system, such as conductance, shot noise, etc.)
- b) at a given site inside the system (to study single particle density)
- c) between neighbouring sites inside the system (to study local current density and build current density maps)

For b) and c) KNIT calculates both a retarded and lesser (see Chapter 4.1) Green's functions of the system.

It is instructive to consider a very simple example of a KNIT script, which creates a two terminal system and calculates its conductance as a function of energy. On Fig. 2.3 one can see a 20 lines piece of code which does it. Let us discuss in details various parts of this script:

1. First, the hopping matrix \mathbf{t} , the on-site energy matrix \mathbf{V} , and the energy E at which transport through our mesoscopic system is studied are defined in lines 1-3;

³For more details, visit <http://inac.cea.fr/Pisp/xavier.waintal/KNIT.php>.

```

1. t=knit.scalarM(1.)
2. V=knit.scalarM(0.)
3. E=-0.5
4. MyA=knit.rectangle([8,4],[0,3],t,v)
5. MyB=knit.rectangle([3,7],[5,0],t,v)
6. MyA.collider(MyB)
7.
8. interface_contact1=knit.rectangle([1,4],[0,3],t,v)
9. interface_contact2=knit.rectangle([3,1],[5,0],t,v)
10. lead1=knit.unreservoirN(interface_contact1,t)
11. lead2=knit.unreservoirN(interface_contact2,t)
12.
13. MySystemWithLeads=knit.systemtotal(MyA,lead1)
14. MySystemWithLeads.addlead(lead2)
15. system.visu2D(MySystemWithLeads, s+".MySystem")
16.
17. for i in range(10):
18.     E=(float(i)/10)*2.-1.99
19.     G_MATRIX=obs.conductance_matrix(MySystemWithLeads,E)
20.     print E,G_MATRIX[1,0]

```

Annotations in the image:

- Hopping matrix (points to line 1)
- On-site energy matrix (points to line 2)
- Size of the block: 8x4 (points to line 4)
- Position of the block: x=0; y=3 (points to line 4)
- Gluing B on top of A (points to line 6)
- Interface parts as rectangular blocks... (points to line 8)
- System with 1 lead (points to line 13)
- Adding the second lead (points to line 14)
- Visualization (points to line 15)
- Calculation... (points to line 19)
- Printing results on the screen (points to line 20)

Figure 2.3: Python script, which uses KNIT to construct a simple two terminal system and calculate its conductance as a function of energy.

2. Second, in lines 4-6 we build rectangular blocks A and B and construct a system of a required geometry by "gluing" them together, as illustrated in Fig. 2.4a;
3. In lines 8-11 the interface contacts (unit layers) of the leads are created and then infinitely repeated (with the inter-layer coupling t) to form the leads themselves;
4. Then, we create the total system (see Fig. 2.4b) by attaching the leads to a system defined in the step 2 (lines 13-14), and plot it, saving the image in *.eps, and *.pdf files (line 15);
5. Finally, we make a loop on 10 different values of energy E , calculate the conductance matrix of the constructed system at these values and print the results on the screen, see Fig. 2.5.

We note that in the last step, the conductance matrix was calculated with a predefined function `obs.conductance_matrix`, which implements exactly Eq.(2.38). This was just a simple example of a DC conductance calculation for a system in two dimensions. Of course, one can imagine more practical applications of this tool as has been done in Refs.[22, 56, 57, 58, 59, 27, 60]. And, in principle, any physical problem which may be modeled by a quadratic tight-binding Hamiltonian can be solved using KNIT⁴.

⁴An improved version of the KNIT package, called "kwant", is now being finished in the group of X. Waintal.

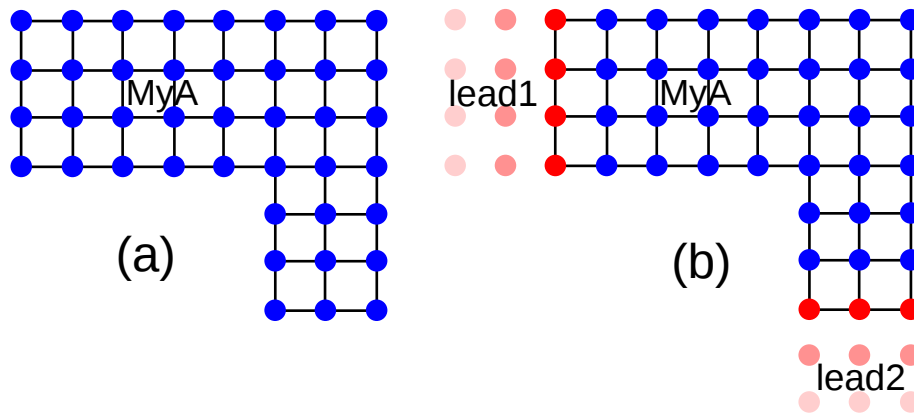


Figure 2.4: (a): System MyA constructed by gluing two rectangular blocks together. (b): Total system with attached leads. Red fading out circles are used to depict semi-infinite leads.

```
File Edit View Terminal Tabs Help
7. We calculate the conductance as a function of energy E.
-1.99 1.24439060882
-1.79 1.61769940517
-1.59 1.55317980007
-1.39 1.18915814162
-1.19 1.93435916102
-0.99 1.96142900593
-0.79 1.95987879756
-0.59 1.93926989872
-0.39 2.66000035396
-0.19 2.97249061447
irina@Linux-desktop:~/Work/svn_knit/trunk/tutorialpys
```

Figure 2.5: Results of a conductance calculation for MyA printed on a user's screen.

2.3 Summary

We have considered two complementary approaches to the coherent quantum electron transport: scattering matrix formalism and the Green's function formalism. They implement different points of view on the problem. The scattering approach is based on the idea of arbitrary system connected to semi-infinite ideal contacts. Then one looks for the asymptotic wave solutions generated in the contacts as a result of scattering of the incident wave on the system. This theory relies on the knowledge of the scattering matrix, which provides a relation between the amplitudes of the incoming and outgoing waves in the system. Provided this quantity is known, one can get access to such observables as the linear conductance or current noise, for example. The main advantage of this method is its simplicity and intuitive interpretation of the results. However, though it is very general, only the simplest models can be solved explicitly.

It implements a much more efficient algorithm for finding the Green's functions and self-energies and thus demonstrates much better performance. For more details, please contact: xavier.waintal@cea.fr.

In the cases when it is impossible to find an analytical answer and numerical simulations are needed, the alternative, Green's function, method turns out to be much more powerful. In contrast to the scattering approach, it takes into account all the microscopic details of the system while the presence of the leads enters the formalism via the self-energies. The basic object one needs to know is the (retarded) Green's function. Though in some trivial cases it is possible to make analytical calculations with this approach, it is perfectly designed for numerical simulations. The latter is its main advantage since systems of arbitrarily complex shape with such ingredients as disorder, external fields and various types of interactions can be, in principle, considered.

Chapter 3

Dynamical electron transport at finite frequency

In this chapter we will consider a problem of a non-equilibrium electron transport in the presence of oscillating in time perturbations, as, for example, AC bias, AC gate voltage, time-dependent magnetic field, etc. This problem is not completely new and obtained considerable attention in early 90's in the group of M. Büttiker. The theory was built from the scattering matrix point of view for the case of small low-frequency perturbations. Later, in the beginning of the first decade of the 21st century, the interest to this problem was revived in the pioneer works by H. Guo and a few others [8, 9, 10, 11, 12, 13, 14, 15, 16, 17, 18, 19, 20, 21]. This time the theory was based on the NEGF formalism. However, even after these attempts there was no general framework of how to address a transport problem with time-periodic fields. Pieces of the results derived so far are diffused in literature and lack generality, which makes them hardly usable for a wider community of researchers. On the other hand, there is a new tide of interest to this problem from an experimental point of view nowadays. This stimulated us to try to generalize the results of both scattering and Green's function approaches and give general practical recipes to the wide community of researchers familiar with stationary problems discussed in the previous chapter.

In the beginning of the chapter we define the problem and discuss four important limits which will be elaborated further. Next, a brief review of the scattering matrix-based results will be given. Then, we will present (without derivation) a "dictionary" of the results obtained with the help of our theory in the wide-band limit (see below). Finally, to conclude this chapter we discuss technical aspects of the calculations based on our formalism and three model examples for the dynamical (AC) conductance in a nanowire, a quantum point contact, and a Mach-Zehnder electronic interferometer.

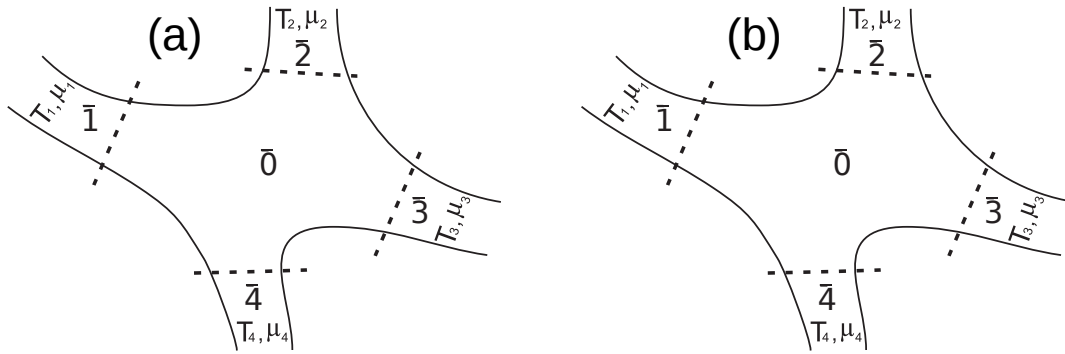


Figure 3.1: Multiterminal system with $M = 4$ leads influenced by an external (a) or an internal (b) perturbation. Red shaded region represents the part of the system affected by the perturbation.

3.1 Definition of the problem

We consider a general multiterminal system consisting of a scattering region (central part) and semi-infinite leads (see Fig. 3.1). The latter are kept at local thermal equilibrium with corresponding temperatures and chemical potentials. We assume now that a time-dependent perturbation (AC bias or AC gate voltage, for example) is applied to the system. General form of the perturbation we consider takes the form

$$\hat{\mathbf{W}} = [\cos \omega t] \sum_{nm} \mathbf{W}_{nm} c_n^\dagger c_m, \quad (3.1)$$

where \mathbf{W} is a rather arbitrary (Hermitian) matrix. Obviously, there are two distinct ways to affect our system: by perturbing the scattering region $\bar{0}$ or the contacts $\bar{1} \dots \bar{M}$. Though Eq.(3.1) is rather generic and may describe many types of excitations, we will, for concreteness, specify the form of matrix \mathbf{W} for these two cases.

Imagine that the perturbation is applied to *one* of the contacts (see Fig. 3.1a), however the generalization to arbitrary number of contacts is straightforward. Then, we will assume that

$$\mathbf{W} = eV_{ac} 1_{\bar{m}'}, \quad (3.2)$$

where $1_{\bar{m}'}$ is the identity matrix inside the contact \bar{m}' . This is the case of an AC bias, though one could in principle always find a basis in which \mathbf{W} is diagonal. Various physical observables, which can be calculated in this case will be given in the next sections. Formally we call them a response to an *external* perturbation.

For the complementary case of a perturbation applied to the device region (see Fig. 3.1b), we will consider

$$\mathbf{W} = eV_{ac} \mathbf{W}_{\bar{0}\bar{0}}, \quad (3.3)$$

where the matrix block $\mathbf{W}_{\bar{0}\bar{0}}$ can take an arbitrary form inside the device region, allowing one to include many types of perturbation such as electric gates (when $\mathbf{W}_{\bar{0}\bar{0}}$ is a unity matrix for the perturbed region), for example. This case will be referred to as a response to an *internal* perturbation.

As we will see below, there are two important limits for each of the two cases. Namely, one can either assume that the amplitude eV_{ac} of the perturbation is much smaller than all other energy scales while the frequency ω is arbitrary and vice versa. In the first limit, we will do a systematic expansion in powers of amplitude while in the second one (adiabatic) – in powers of frequency.

Before moving directly to the results of our theory, we are going to review in the next section the alternative theory developed by Büttiker and co-workers [7] based on the scattering approach. Afterwards, the two approaches will be compared.

3.2 Scattering matrix theory of finite-frequency electron transport

In order to understand why the presence of oscillating potentials complicates the theory, let us first discuss the stationary case. Imagine there is no time-dependent perturbation, $V_{ac} = 0$. Then we already know that at small bias the current is given by Eq.(2.21). One can immediately make two important conclusions. First, due to the current conservation, the sum of the currents in all electrodes should be equal to zero. In other words, this is simply the Kirchhoff's law. Second, the system must be gauge invariant meaning that any constant shift of *all* chemical potentials in the leads has no effect on the current. As a consequence of these two properties we find that the rows and columns of a conductance matrix must add up to zero,

$$\sum_{\alpha=1}^M \Upsilon_{\alpha\beta} = \sum_{\beta=1}^M \Upsilon_{\alpha\beta} = 0. \quad (3.4)$$

Any physically correct theory of stationary transport has to satisfy these relations [61]. Like in Section 2.1, we use here Greek letters instead of Latin letters to enumerate leads in order to avoid confusion with the transverse channels numbers.

Now let us come back to the non-stationary case ($V_{ac} \neq 0$). Our starting point will be a situation when electrochemical potentials in the electrodes may oscillate, i.e. the case of *external* perturbation. Then, at not too high frequencies the system under interest remains locally charge neutral at all times [5]. Thus, we expect that current conservation and gauge invariance must all also be satisfied in this case. If we express the current at electrode α as

$$I_{\alpha}(\omega) = \sum_{\beta} \Upsilon_{\alpha\beta}(\omega)V_{\beta}(\omega), \quad (3.5)$$

then the dynamical conductance matrix elements must also satisfy Eq.(3.4). We remind that according to our convention, an external perturbation is given by equations (3.1) and (3.2). Therefore, we conclude that $V_\beta(\omega) = V_{ac}$ if lead β is affected by the perturbation, and $V_\beta(\omega) = 0$ otherwise.

3.2.1 Response to an external perturbation

As was first found by Büttiker [1, 5, 6, 7], if we calculate a response to an *external* perturbation only (assuming for simplicity that there was no bias in the system before applying the perturbation), then the AC conductance elements read

$$\Upsilon_{\alpha\beta}^e(\omega) \equiv \frac{dI_\alpha^e(\omega)}{dV_{ac}} = -\frac{e^2}{h} \int dE \text{Tr} \left[\mathbf{1}_\alpha \delta_{\alpha\beta} - S_{\alpha\beta}^\dagger(E) S_{\alpha\beta}(E + \hbar\omega) \right] \frac{f(E) - f(E + \hbar\omega)}{\hbar\omega}, \quad (3.6)$$

where $f(E)$ is a Fermi function (equal in all leads at zero DC bias), $S(E)$ is a stationary scattering matrix, and trace is taken over the transverse channels. The unit matrix $\mathbf{1}_\alpha$ has dimensions equal to the number of transverse channels below the Fermi level in lead α . The idea behind is rather simple: according to the (first order) time-dependent perturbation theory [62], a particle with energy E when travelling in the presence of a time-dependent perturbation can be promoted to energies $E \pm \hbar\omega$ by gaining/losing a modulation quantum. This intuitive picture will be used below to interpret various terms in the retarded Green's function (see Chapter 4).

As the theory was initially built for the low-frequency limit, it is enough to take into account the leading in frequency term in the expansion of Eq.(3.6)

$$\Upsilon_{\alpha\beta}^e(\omega) = \Upsilon_{\alpha\beta}^e(0) - i\omega e \frac{dN_{\alpha\beta}}{dV_{ac}}, \quad (3.7)$$

where $\Upsilon_{\alpha\beta}^e(0)$ is the stationary conductance matrix element (2.23), and the quantity

$$\frac{dN_{\alpha\beta}}{dV_{ac}} = -\frac{e}{4\pi i} \int dE \left(-\frac{\partial f}{\partial E} \right) \text{Tr} \left[S_{\alpha\beta}^\dagger \frac{dS_{\alpha\beta}(E)}{dE} - \frac{dS_{\alpha\beta}^\dagger(E)}{dE} S_{\alpha\beta}(E) \right] \quad (3.8)$$

is the density of particles emitted at contact α as a consequence of perturbing the electrochemical potential in lead β . The first term in the right-hand side of Eq.(3.7) describes a purely adiabatic response, when the current follows the slow oscillation of the potential. At the same time the second term is the correction to it which contributes to the non-adiabatic component of the current oscillating out of phase with the voltage¹. We will see below, that departure from adiabaticity results in polarization of the device, which produces displacement currents. Now, if one takes a sum of elements in the columns or rows of the conductance matrix (3.7), it turns

¹The current at frequency ω as a function of time is given by: $I_\alpha(\omega, t) = \text{Re} [\Upsilon_{\alpha\beta}(\omega) e^{-i\omega t}] V_{ac}$.

out that it does not vanish. The elements of the adiabatic part, $\Upsilon_{\alpha\beta}^e(0)$, add up to zero and it is the second term in the right-hand side of Eq.(3.7), which violates Eq.(3.4). At the first glance one could think that the theory is completely wrong because Eq.(3.4) are the general requirements to be satisfied. However, in fact, it only means that there is an essential ingredient missing.

To understand it better, we propose to consider a system of equations of classical electrodynamics:

$$\mathbf{j} = \mathbf{j}_p + \frac{\partial \mathbf{D}}{\partial t}, \quad (3.9)$$

$$\mathbf{D} = \epsilon \mathbf{E}, \quad \mathbf{E} = -\nabla \phi(\mathbf{r}), \quad (3.10)$$

$$\text{div} \mathbf{D} = \rho, \quad (3.11)$$

$$\text{div} \mathbf{j}_p + \frac{\partial \rho}{\partial t} = 0. \quad (3.12)$$

Here, \mathbf{E} and \mathbf{D} are the electric field and the electric induction, \mathbf{j} and \mathbf{j}_p are the full current density and particle current density, while ρ and $\phi(\mathbf{r})$ are the density of electric charge and the scalar potential, respectively. For systems of finite size these equations must also be supplemented by the appropriate boundary conditions. Eq.(3.9) tells us that in the presence of time-dependent fields the total current density is a sum of the density of moving charges (particle current) and the displacement current. The latter originates either due to changing in time electric field or because of a time-dependent polarization of a material. The effect of polarization is incorporated into the permittivity ϵ (in linear materials). If we substitute Eq.(3.9) to Eq.(3.12) and use Eq.(3.11), one readily sees that

$$\text{div} \mathbf{j} = 0, \quad (3.13)$$

which means that the total current density has neither sources nor sinks and is therefore conserved. On the other hand, in accordance with the continuity equation (3.12), the particle current density \mathbf{j}_p alone is not necessarily divergenceless and is thus not conserved in general. To avoid confusion one has to remember that the experimentally measurable quantity is the total current, so the fact that the particle current alone is not conserved is irrelevant. Equations (3.10) and (3.11) combined together lead to the Poisson equation, which represents electron-electron interactions. It is crucial to ensure the conservation of the total current. Thus, if one wants to build a description which might be relevant for experiments, it is necessary to include interactions at least at some mean-field level. We will show a simple scheme to do it below. Finally, it is worth saying that in the stationary limit we neglect the terms containing time derivatives in equations (3.9) and (3.12) and deduce that conservation of the particle density automatically guarantees conservation of the total current density.

From this rather long discussion we have to learn that in the stationary case it is enough to calculate the particle currents in all the contacts of the system to verify that they add up to zero.

So, when searching for the stationary linear conductance matrix, one does not need to know the actual potential profile in the system (but for non-linear effects in the I-V characteristics it becomes important, see Ref.[63]), only the global difference of chemical potentials plays a role. However, when time-dependent fields are present, besides the particle current one has to take into account the displacement part as well. And only the sum of the two when added up for all contacts vanishes. What we found above in Eq.(3.7) is the *particle part* of the total current. In order to understand what is the displacement part, we come back to our multiterminal system (Fig. 3.1) and write down the continuity equation for it,

$$\sum_{\alpha=1}^M I_{\alpha}(t) + \frac{dQ}{dt} = 0, \quad (3.14)$$

where $Q(t)$ is a total charge in the scattering region $\bar{0}$. The fact that the particle currents do not add up to zero in this context means that there is a varying in time charge piled up in the device region. Indeed, performing a Fourier transform in this equation, and then taking a derivative with respect to the oscillating voltage in the perturbed lead, $V_{\beta}(\omega) \equiv V_{ac}$, we finally get

$$\sum_{\alpha=1}^M \Upsilon_{\alpha\beta}^e(\omega) - i\omega \frac{dQ(\omega)}{dV_{ac}} = 0. \quad (3.15)$$

Then, since $\sum_{\alpha} \Upsilon_{\alpha\beta}^e(0) = 0$, the role of the second term in the right-hand side of Eq.(3.7) becomes obvious. If the system cannot respond adiabatically to the oscillation of the chemical potential, then the non-adiabatic part of the current creates an extra charge density oscillating with frequency ω in the device region (charge entering the leads out of phase relative to the AC bias leaves in the scattering region a charge of opposite sign, polarizing the system). It would not be an issue if electrons were non-interacting in reality and can in principle be considered as a toy model. But they do interact and to complete our description we note that the oscillating charge inside the device creates an oscillating voltage, which this time is *internal* according to our classification (see Fig. 3.1b). Thus, one needs to calculate the response to it as well.

3.2.2 Response to an internal perturbation

Since the *internal* oscillating potential $U(\mathbf{r}, t)$ is induced, according to the discussion above, by the initially applied external potential of the form (3.2), it will in general have a form of Eq.(3.3). In this paragraph we use a continuous coordinate \mathbf{r} instead of site indices to describe the spatial dependence of the induced time-dependent potential. Then, Büttiker and co-workers found [1, 5, 6] that the current response in a contact α due to the internal perturbation is given by,

$$\frac{dI_{\alpha}^i(\omega)}{dV_{ac}} = ie\omega \int d^3\mathbf{r} \frac{\delta N_{\alpha}}{\delta U(\mathbf{r})} \frac{dU(\mathbf{r}, \omega)}{dV_{ac}}, \quad (3.16)$$

where the superscript i stands for *internal* and the quantity

$$\frac{\delta N_\alpha}{\delta U(\mathbf{r})} = \sum_\beta \frac{\delta N_{\alpha\beta}}{\delta U(\mathbf{r})} = \frac{1}{4\pi i} \int dE \left(-\frac{\partial f}{\partial E} \right) \sum_\beta \text{Tr} \left[S_{\alpha\beta}^\dagger(E) \left(\frac{\delta S_{\alpha\beta}(E)}{\delta U(\mathbf{r})} \right) - \left(\frac{\delta S_{\alpha\beta}^\dagger(E)}{\delta U(\mathbf{r})} \right) S_{\alpha\beta}(E) \right] \quad (3.17)$$

is the density of particles, that are emitted at contact α if we perturb the scalar potential profile locally at point \mathbf{r} (in the device region $\bar{0}$). It is closely related to Eq.(3.8) summed over the source leads, β , because if we perturb all the points in the device region, it is equivalent to simultaneously perturbing all the contacts instead (with the potential of the opposite sign). In the original works [1, 5, 6] the quantity (3.17) was given the name **emissivity**. Like Eq.(3.7), formula (3.16) holds when the frequency of the perturbation is low. In this case one can say that a particle traversing the system experiences the instantaneous potential and thus Eq.(3.17) is written in a quasi-stationary limit via the functional derivatives $\delta S_{\alpha\beta}(E)/(\delta U(\mathbf{r}))$ of the (stationary) scattering matrix with respect to the (stationary) scalar potential in the system.

3.2.3 The total response

As we have obtained both the response to the external AC bias (particle conductance) in Eq.(3.7) and the induced internal potential (displacement conductance), Eq.(3.16), we can write down the total dynamical conductance, which satisfies properties (3.4) as

$$\Upsilon_{\alpha\beta}(\omega) = \Upsilon_{\alpha\beta}^e(\omega) + \frac{dI_\alpha^i(\omega)}{dV_{ac}}. \quad (3.18)$$

The only element of the "puzzle" which is still missing is how to find the induced potential $dU(\mathbf{r}, \omega)/(dV_{ac})$, which is necessary to determine the displacement term. However, this issue can be resolved since we are interested in low frequencies so that this quantity can be found in the quasi-stationary approximation. In this case, the potential we are searching for has to be calculated from the Poisson equation² [1, 6],

$$\Delta \frac{dU(\mathbf{r}, \omega, \beta)}{dV_{ac}} = -\frac{e}{\epsilon} \left[\frac{dn(\mathbf{r}, \beta)}{dV_{ac}} + \int d^3\mathbf{r}' \Pi(\mathbf{r}, \mathbf{r}') \frac{dU(\mathbf{r}', \omega, \beta)}{dV_{ac}} \right], \quad (3.19)$$

where the right-hand side is the density of charge at point \mathbf{r} which consists of two parts. The first term in the brackets is the density of particles injected inside the device at point \mathbf{r} as a consequence of the external perturbation in lead β . This density induces the internal potential we are looking for, which in turn additionally changes the density of particles at \mathbf{r} as described by the second term in the brackets. The so-called Lindhard function $\Pi(\mathbf{r}, \mathbf{r}')$ provides a density response at point \mathbf{r} due to a potential change at point \mathbf{r}' . It cannot be calculated in general

²We add an additional lead index to the potential $U(\mathbf{r}, \omega, \beta)$ to show that it is induced by the external perturbation of lead β .

within the scattering approach, so one needs to do it separately [1, 64]. Büttiker and co-workers have found [1, 6, 63] that the density of particles induced at point \mathbf{r} by the perturbation of lead β can be also expressed via the functional derivative of the scattering matrix and thus it is closely related to the emissivity (see Eq.(3.17)),

$$\begin{aligned} \frac{dn(\mathbf{r}, \beta)}{dV_{ac}} &= \sum_{\alpha} \frac{\delta N_{\alpha\beta}}{\delta U(\mathbf{r})} \\ &= \frac{1}{4\pi i} \int dE \left(-\frac{\partial f}{\partial E} \right) \sum_{\alpha} \text{Tr} \left[S_{\alpha\beta}^{\dagger}(E) \left(\frac{\delta S_{\alpha\beta}(E)}{\delta U(\mathbf{r})} \right) - \left(\frac{\delta S_{\alpha\beta}^{\dagger}(E)}{\delta U(\mathbf{r})} \right) S_{\alpha\beta}(E) \right]. \end{aligned} \quad (3.20)$$

Indeed, if one uses the Onsager reciprocal relation (2.15), it is straightforward to see that for a non-zero magnetic field B ,

$$\left[\frac{dn(\mathbf{r}, \beta)}{dV_{ac}} \right]_B = \left[\frac{\delta N_{\beta}}{\delta U(\mathbf{r})} \right]_{-B}. \quad (3.21)$$

In fact, in the original papers the quantity in the left-hand side was given the name **injectivity**.

We complete our discussion of the scattering theory of dynamical quantum transport by a simple particular case, where one does not have to solve Eq.(3.19) to find the induced potential and therefore one can manage without knowledge of the Lindhard function. Let us assume that we have a system made of a good metal which effectively screens any charge accumulation over a Thomas-Fermi screening length. In this approximation, if we argue that the injected charge due to varying in time potential in the contact β induces the internal potential $U(\mathbf{r}, \omega, \beta)$, then in turn this internal potential generates a density, which compensates completely the injected charge [5],

$$\frac{dn(\mathbf{r}, \beta)}{dV_{ac}} dV_{ac} - \sum_{\alpha} \frac{\delta N_{\alpha}}{\delta U(\mathbf{r})} dU(\mathbf{r}, \omega, \beta) = 0. \quad (3.22)$$

Then, in the absence of a magnetic field using equation (3.21) we find

$$\frac{dU(\mathbf{r}, \omega, \beta)}{dV_{ac}} = \left[\frac{\delta N_{\beta}/(\delta U(\mathbf{r}))}{\sum_{\alpha} \delta N_{\alpha}/(\delta U(\mathbf{r}))} \right]_{B=0}. \quad (3.23)$$

This result can be used in Eq.(3.16) to find the full dynamic conductance matrix (3.18). Then, taking into account the fact that perturbing all the points inside the device is equivalent to perturbing the contacts instead (see discussion after Eq.(3.17)), one can explicitly see that Eq.(3.4) is satisfied, i.e. the total current is conserved and gauge invariant.

To summarize, in this section we have recalled the scattering matrix theory of AC electron transport and found the *formal* expression for the dynamical conductance. Even though the theory is in principle complete, it is inapplicable to most physical problems except for the simplest ones, like, for example, a single level between the contacts [2, 4, 5]. Indeed, as we have seen from the discussion above, to find the full dynamical response of the system, one needs to calculate the functional derivative of the scattering matrix with respect to the change

in the potential profile. Besides, one has to calculate somehow the Lindhard function as well. Nevertheless, the theory is quite intuitive and may be served to give an insight into essential points one has to pay attention to in order to build a physically correct theory of AC quantum transport with the help of other theoretical approaches. In the next section we will see how this problem can be solved using the NEGF formalism.

3.3 Green's function theory of the AC electron transport: the cookbook

In this section we are going to present without derivation³ the main formulas one needs to know in order to solve a problem of the quantum transport at finite frequency with the help of Green's functions. We already saw in the previous section how this can be done in the framework of the scattering theory and what follows below is the alternative approach. It might be of great interest to the experimentalists and theorists familiar with the stationary problem of electron transport because we express all the (AC) observables in terms of the stationary (DC) Green's functions (see Section 2.2). And since the stationary problem is very well understood and many numerical tools for solving it exist on the market, our theory makes it possible to extend their capabilities to the AC regime.

The section is organised as follows. We start from a discussion of the response to the external perturbation as we did in the previous section. Then, we present the expressions one has to know to calculate the response to the internal perturbation – necessary ingredient in the current-conserving theory. In the end we give an expression for the total response and provide a self-consistent scheme which has to be employed in order to do the full calculation. Finally, we briefly discuss how the results presented in this section can be related to the scattering approach considered in the previous section.

Before we start, let us make several remarks. (i) As we have seen in the Section 2.2, in the Green's function formalism the observables (electric current, for example) are typically expressed via the Green's function of the device region, $\mathcal{G}_{\bar{0}\bar{0}}$. So, in order to present the results in a compact and convenient way, for the rest of the thesis we introduce a notation,

$$\mathcal{G}_l(E) \equiv \mathcal{G}_{\bar{0}\bar{0}}\left(E + \frac{\hbar\omega l}{2}\right). \quad (3.24)$$

(ii) The expressions presented in this section are given in the so-called **wide-band limit (WBL)**, where the energy dependence of the electrodes (retarded self-energies) is neglected. This is a situation relevant for massive metallic contacts with a high density of states. The most general (but cumbersome) expressions without this approximation are given in Appendix A.

³The formalism necessary to derive the results of this section will be given in the next chapter.

3.3.1 Response to an external perturbation

Let us start with the case when *one* of the contacts, say m' , is affected by the time-dependent perturbation of the form given in equations (3.1) and (3.2). We assume for simplicity that before applying it, there was no (DC) bias in the system, so that all chemical potentials in the leads are equal. We are going to give a list of observables which comprise the response of the system to such a perturbation.

The first important observable is the current $I_m(t)$ flowing through contact m . It can be decomposed according to different harmonics of the perturbation as

$$I_m(t) = \text{Re} \sum_{l=0}^{\infty} I_m(l\omega) e^{-il\omega t}. \quad (3.25)$$

Then, the AC conductance matrix [7, 9] can be written as follows (compare with Eq.(3.6)):

$$\Upsilon_{mm'}^e(\omega) \equiv \frac{dI_m(l\omega)}{dV_{ac}} = \frac{e^2}{h} \int dE \text{Tr} \left[\Gamma_m \mathcal{G}_2 \Gamma_{m'} \mathcal{G}_0^\dagger - i\delta_{m,m'} \left(\mathcal{G}_2 - \mathcal{G}_0^\dagger \right) \Gamma_m \right] \frac{f(E) - f(E + \hbar\omega)}{\hbar\omega}, \quad (3.26)$$

where we added the superscript e to emphasize that this is the response function to an *external* perturbation. Note that at small frequency (adiabatic limit) it simply reduces to the Meir-Wingreen formula⁴ (2.38).

If we consider a zero-frequency component of the current, i.e. the effect of rectification, we find that in the WBL it vanishes:

$$\frac{d^2 I_m(0\omega)}{dV_{ac}^2} = 0. \quad (3.27)$$

However this is not the case in general, as seen in Eq.(A.4) in Appendix A. This qualitative difference calls for one important remark. Suppose that the "electrodes" are made of two parts: a very wide metallic part (WBL is justified) followed by a narrower region (WBL breaks down) which is itself connected to the device region. At the quantum mechanical level, the position of the leads is totally arbitrary and simply corresponds to which degrees of freedom are integrated out. Therefore at this level, the physics is unaffected by the position (in the wide region or in the narrower one) where one chooses to divide the total system into the device region and the leads. The fact that Eq.(A.4) gives a non zero result (leads are in the narrower region) or a vanishing one (leads are in the wide region, where the WBL applies) therefore indicates that the difference between the two cases takes place at the statistical physics level, i.e. upon assuming that the electrodes always remain at thermal equilibrium. The correct choice between the two above mentioned possibilities depends on the inelastic mean free path: when almost no inelastic collisions take place in the narrower region, the electrodes should be considered to be in the

⁴One should remember that there are two common ways to write down the current in terms of the conductance matrix, see Eq.(2.21). They are related: $\Upsilon_{mm'} = \bar{\Upsilon}_{mm'} - (\sum_{m''} \bar{\Upsilon}_{mm''}) \delta_{mm'}$.

wide region and the rectification effect vanishes. At higher temperature, the inelastic mean free path decreases, and the narrower region eventually becomes thermalized, which leads to a non zero rectification effect.

Another interesting limit is the adiabatic limit when the frequency ω is very small while the amplitude of the perturbation V_{ac} can remain arbitrarily large. To zeroth order in $\hbar\omega$, the current (for $m \neq m'$) is simply given by a trivial extension of the DC result (see also Eq.(3.26)),

$$I_m^{ad}(t) = \frac{e}{h} \int dE \left(-\frac{\partial f}{\partial E} \right) \text{Tr} \left[\mathcal{G}_0 \Gamma_{m'} \mathcal{G}_0^\dagger \Gamma_m \right] eV_{ac} \cos \omega t. \quad (3.28)$$

This expression is linear in V_{ac} in the WBL. However, in general (see Eq.(A.5)) adiabatic current contains *all* higher orders in amplitude as well. More interestingly, the first correction to adiabaticity reads,

$$\delta I_m^{ad}(t) = \frac{ie\omega}{4\pi} \int dE \left(-\frac{\partial f}{\partial E} \right) \text{Tr} \left[\mathcal{G}_0 \Gamma_{m'} \frac{\partial \mathcal{G}_0^\dagger}{\partial E} \Gamma_m - \frac{\partial \mathcal{G}_0}{\partial E} \Gamma_{m'} \mathcal{G}_0^\dagger \Gamma_m \right] eV_{ac} \sin \omega t. \quad (3.29)$$

Note that while the adiabatic current follows exactly the slow changes of voltage, the correction to it is out of phase.

Another important observable, which we need to construct the current-conserving theory, is the electronic density $n(i, t) = \langle c_i^\dagger(t) c_i(t) \rangle$ on site i whose decomposition in harmonics reads

$$n(i, t) = n_{eq}(i) + \text{Re} \sum_{l=0}^{\infty} n(i, l\omega, m') e^{-il\omega t}, \quad (3.30)$$

where $n_{eq}(i)$ is the stationary density in the absence of the time dependent potential. We refer to the response function $dn(i, l\omega, m')/dV_{ac}$ as the generalized injectivity. It is a straightforward generalization of the injectivity defined in Refs.[1, 6, 20] at small frequency (see Eq.(3.20)), and can be expressed as

$$\frac{dn(i, l\omega, m')}{dV_{ac}} = \frac{e}{h\omega} \int dE (f(E) - f(E + \hbar\omega)) \left[\mathcal{G}_2 \Gamma_{m'} \mathcal{G}_0^\dagger \right]_{ii}. \quad (3.31)$$

This is the extra density injected into the device region at site i in consequence of the finite-frequency perturbation. Since the system *overall* has to stay charge neutral, it is allowed to have only dipoles in the system. As we saw in the previous section, in order to tackle this problem one has to take into account the displacement part of the current as well. The injected dynamical charge creates an oscillating *internal* potential, which in turn modifies currents in the contacts. So, we move on to discuss the response to an internal perturbation.

3.3.2 Response to an internal perturbation

We assume now a perturbation of the form given by equations (3.1) and (3.3) affecting the device region. For the moment, let us suppose that the leads are kept at equilibrium with

the chemical potentials equal. We will combine the responses to both the external and the internal perturbations afterwards. Keeping in mind the expansion (3.25) of the current in various harmonics, we give a list of some useful observables.

First, the linear in V_{ac} current response in the lead m is given by the expression (compare with Eq.(3.16)),

$$\frac{dI_m(1\omega)}{dV_{ac}} = \frac{ie^2}{h} \int dE (f(E) - f(E + \hbar\omega)) \text{Tr} \left[\mathcal{G}_0^\dagger \Gamma_m \mathcal{G}_2 W \right], \quad (3.32)$$

where $W \equiv \mathbf{W}_{00}$ (see Eq.(3.3)). One has to specify the distribution W of the internal potential to calculate this quantity.

Second, let us consider the rectification effect, i.e. the zero-frequency component of the current. Obviously, it contains only even orders in V_{ac} (because sign of V_{ac} is just a phase shift in Eq.(3.1)). Thus, the leading order contribution reads,

$$\begin{aligned} \frac{d^2 I_m(0\omega)}{dV_{ac}^2} = \frac{e^3}{4h} \int dE \left\{ (f(E) - f(E + \hbar\omega)) \text{Tr} \left[\mathcal{G}_0 W \mathcal{G}_2 \Gamma \mathcal{G}_2^\dagger W \mathcal{G}_0^\dagger \Gamma_m \right] \right. \\ \left. - (f(E - \hbar\omega) - f(E)) \text{Tr} \left[\mathcal{G}_0 W \mathcal{G}_{-2} \Gamma \mathcal{G}_{-2}^\dagger W \mathcal{G}_0^\dagger \Gamma_m \right] \right\}, \quad (3.33) \end{aligned}$$

where $\Gamma = \sum_m \Gamma_m$ is the sum of the broadening matrices of all leads.

Another quantity one might be interested in is the generation of the second harmonics of the current, which is (to the leading order in V_{ac}) given by

$$\begin{aligned} \frac{d^2 I_m(2\omega)}{dV_{ac}^2} = \frac{ie^3}{2h} \int dE \left\{ (f(E) - f(E + \hbar\omega)) \text{Tr} \left[\mathcal{G}_2 W \mathcal{G}_0^\dagger W \mathcal{G}_{-2}^\dagger \Gamma_m \right] \right. \\ \left. + (f(E - \hbar\omega) - f(E)) \text{Tr} \left[\mathcal{G}_2 W \mathcal{G}_0 W \mathcal{G}_{-2}^\dagger \Gamma_m \right] \right\}. \quad (3.34) \end{aligned}$$

Let us consider a particularly interesting case of the current generated upon perturbing the onsite potential on site i (i.e. $\mathbf{W}_{kl} = eV_{ii}\delta_{ik}\delta_{il}$ in Eq.(3.1)). We will call the AC response function for this case the (generalized) emissivity [1, 6, 20] and it reads (see Eq.(3.32)),

$$\frac{dI_m(1\omega)}{dV_{ii}} = \frac{ie^2}{h} \int dE (f(E) - f(E + \hbar\omega)) \left[\mathcal{G}_0^\dagger \Gamma_m \mathcal{G}_2 \right]_{ii}. \quad (3.35)$$

Note that the emissivity (3.17) defined by Büttiker has a meaning of the number of particles (rather than the current) being emitted into the lead m as a consequence of an internal perturbation. Thus, to come back to the original definition one has to multiply Eq.(3.35) on both sides by $1/(ie\omega)^5$. Then its relation to the introduced above injectivity, Eq.(3.31), will become obvious.

⁵Consider the continuity equation: $\sum_m I_m(t) + dQ/(dt) = 0$. In our case we have an internal perturbation

Finally, we introduce the frequency-dependent Lindhard function [1, 6, 20] that relates a change of density on site j to the onsite energy perturbation on site j' ,

$$\begin{aligned} \Pi(1\omega, j, j') \equiv \frac{dn(j, 1\omega)}{dV_{j'j'}} = -\frac{ie}{2\pi} \int dE \left\{ (f(E) - f(E + \hbar\omega)) [\mathcal{G}_2]_{jj'} [\mathcal{G}_0^\dagger]_{j'j} \right. \\ \left. + f(E + \hbar\omega) [\mathcal{G}_2^\dagger]_{jj'} [\mathcal{G}_0]_{j'j} - f(E) [\mathcal{G}_2]_{jj'} [\mathcal{G}_0]_{j'j} \right\}, \end{aligned} \quad (3.36)$$

where we implied an expansion similar to Eq.(3.30) for the electronic density on site j . It is worth saying that this expression is general and does not rely on the WBL.

3.3.3 The total response

Now we have all the ingredients to discuss the total response of the system. First, like in the scattering approach, let us assume that we apply an external perturbation. As a result, we obtain the dynamical conductance matrix $\Upsilon_{mm'}^e(\omega)$, which for the interacting system cannot be considered as a full response since it violates the current conservation and the gauge invariance,

$$\sum_m \Upsilon_{mm'}^e \neq 0 \quad \sum_{m'} \Upsilon_{mm'}^e \neq 0. \quad (3.37)$$

It means that there is a dynamical charge pileup in the device region (which must be screened by other parts of the system via capacitances, for example, to restore charge neutrality). This charge induces the internal potential, $U(\mathbf{r}, 1\omega, m')$ ⁶, of the same frequency, which in turn creates additional (displacement) currents in the contacts. In order to have a result which satisfies current conservation and is gauge invariant at the same time, we have to consider the two contributions together yielding the full AC current response in the leads as,

$$\Upsilon_{mm'}(\omega) = \Upsilon_{mm'}^e(\omega) + \int d^3\mathbf{r} \frac{\delta I_m(1\omega)}{\delta U(\mathbf{r})} \frac{dU(\mathbf{r}, 1\omega, m')}{dV_{ac}}, \quad (3.38)$$

where we exploited Eq.(3.35) to right the second term on the right-hand side, and wrote formally the continuous variable \mathbf{r} instead of the site index to compare this result to Eq.(3.18).

Finally, one has to solve the Poisson equation in order to find the induced potential distribution (see also Eq.(3.19)),

$$\Delta \frac{dU(\mathbf{r}, 1\omega, m')}{dV_{ac}} = -\frac{e}{\epsilon} \left[\frac{dn(\mathbf{r}, 1\omega, m')}{dV_{ac}} + \int d^3\mathbf{r}' \Pi(1\omega, \mathbf{r}, \mathbf{r}') \frac{dU(\mathbf{r}', 1\omega, m')}{dV_{ac}} \right], \quad (3.39)$$

and, as a result, the charge Q in the device region is partitioned between the leads. Assuming, that we know the partition, $Q(t) = \sum_m q_m(t)$, we may write $I_m(t) = -dq_m/(dt)$. Then, doing an expansion in harmonics for the current, Eq.(3.25), and the charge $q_m(t) = en_m(t)$ (similar to Eq.(3.30)) we arrive to: $I_m(\omega) = i\omega en_m(\omega)$. Then, the emissivity defined by Büttiker is $dn_m(\omega)/(dV_{ii}) = (1/(ie\omega))dI_m(\omega)/(dV_{ii})$.

⁶We add the additional lead index m' , which signifies that this potential is induced by the external perturbation of lead m' .

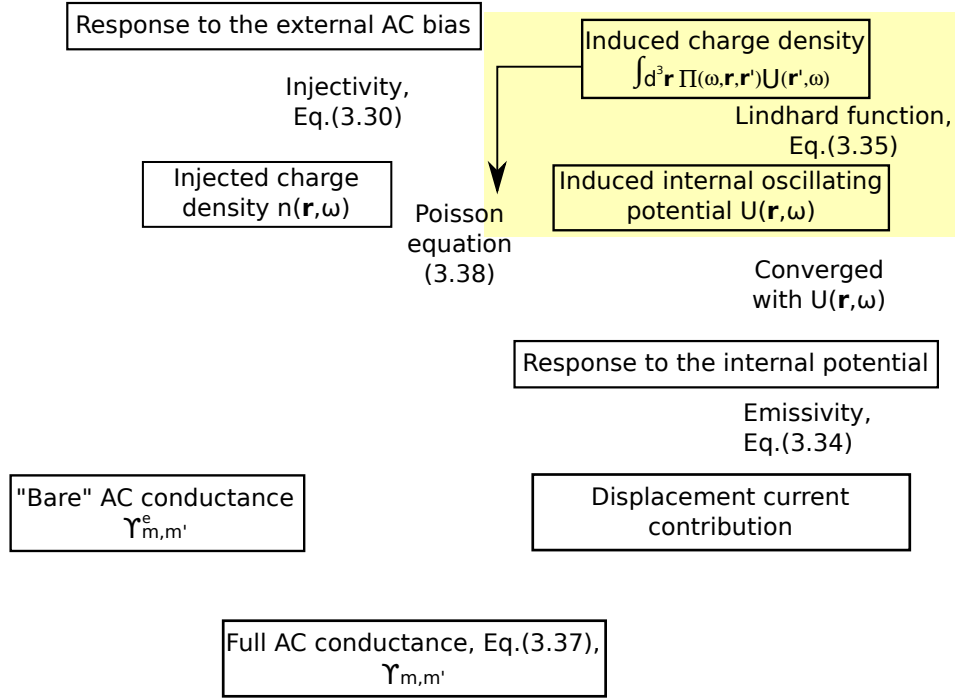


Figure 3.2: General scheme for calculating the full AC conductance matrix. Yellow shaded region denotes the Poisson equation self-consistent loop for evaluating the induced internal potential.

where ϵ is the dielectric constant, and we used equations (3.31) and (3.36).

Let us now summarize the obtained results. On Fig. 3.2 we depict the general scheme one has to follow to find the full dynamical (AC) conductance of a multiterminal system, which satisfies two fundamental properties: current conservation and gauge invariance. First, starting from the response to the external potential, one calculates the "bare" conductance matrix $\Upsilon_{mm'}^e(\omega)$, Eq.(3.26), and at the same time finds the extra charge density injected into the device, Eq.(3.31). Second, one has to solve the Poisson equation (3.39) self-consistently (yellow shaded region on Fig. 3.2) to find the distribution of the internal potential induced by the injected charge. As soon as it is done, one proceeds by evaluating the internal response to this potential and finds the displacement current (using the emissivity (3.35)), which together with the external response yields the full conductance matrix (3.38).

To conclude, we have found analogs to all the expressions entering the Büttiker's theory of the dynamical AC transport⁷, described in Section 3.2. The advantage of our approach

⁷In the WBL, the equivalent expressions in the scattering formalism are simply obtained by using the *formal* substitution: $\sqrt{\Gamma_n} \mathcal{G}_0 \sqrt{\Gamma_m} \rightarrow -i S_{nm}(E) - i \mathbf{1} \delta_{nm}$, which immediately yields Eq.(3.6). This is known as the Fisher-Lee relation [65, 45]. Finding a mapping between the two formalisms beyond the WBL requires solving the scattering problem in presence of the oscillating field via the Floquet approach. For more details on this approach and its relation to the NEGF see Ref.[66].

is that these quantities can be easily calculated because they are expressed in terms of the stationary Green's functions and self-energies. In contrast to this, the scattering formulas involve functional derivatives of the scattering matrix with respect to the scalar potential in the system, which cannot be found in general. Therefore, existing numerical tools, like the KNIT package mentioned in Sec. 2.2.4, by using the Green's function theory presented above, can be directly extended to provide access to the dynamical AC observables.

3.4 Applications

In this section we apply the formalism presented in the previous section on three practical examples: the AC conductance of a simple one dimensional chain, a quantum point contact (QPC) and an electronic Mach-Zehnder (MZ) interferometer in the quantum Hall regime. These examples, of increasing complexity, are chosen to illustrate how the numerical calculations can be performed in practice and how the AC physics can provide insights absent in DC. The stationary Green's function \mathcal{G}_l at the root of the AC expressions was obtained with the knitting algorithm described in Ref.[22].

3.4.1 Technical details on the numerical integration

We start with the AC conductance of a simple one dimensional chain described by the Hamiltonian,

$$H = 2 - \sum_{n=-\infty}^{\infty} \left(c_{n+1}^\dagger c_n + h.c. \right) \quad (3.40)$$

(the constant 2 serves to offset the bottom of the band to $E = 0$). The device region is of size L so that we suppose that the system stays in thermal equilibrium for $n \leq 0$ (left lead, region $\bar{1}$) and $n > L$ (right lead, region $\bar{2}$). We consider the AC conductance, which is given by Eq.(A.1). It can be written as the sum of three terms,

$$\Upsilon_{21}(\omega) = -\frac{e^2}{h} \int \frac{dE}{\hbar\omega} \text{Tr} [(f(E) - f(E + \hbar\omega)) A_{21}^{ar} - f(E)A_{21}^{rr} + f(E + \hbar\omega)A_{21}^{aa}], \quad (3.41)$$

with

$$A_{21}^{ar} = \text{Tr} \left[\Lambda_2^{ar}(E; E + \hbar\omega) \mathcal{G}_2 \Lambda_1^{ra}(E + \hbar\omega; E) \mathcal{G}_0^\dagger \right], \quad (3.42)$$

$$A_{21}^{rr} = \text{Tr} \left[\Lambda_2^{rr}(E; E + \hbar\omega) \mathcal{G}_2 \Lambda_1^{rr}(E + \hbar\omega; E) \mathcal{G}_0 \right], \quad (3.43)$$

$$A_{21}^{aa} = \text{Tr} \left[\Lambda_2^{aa}(E; E + \hbar\omega) \mathcal{G}_2^\dagger \Lambda_1^{aa}(E + \hbar\omega; E) \mathcal{G}_0^\dagger \right], \quad (3.44)$$

where

$$\Lambda_m^{cb}(E; E') = \Sigma^c(m; E) - \Sigma^b(m; E'). \quad (3.45)$$

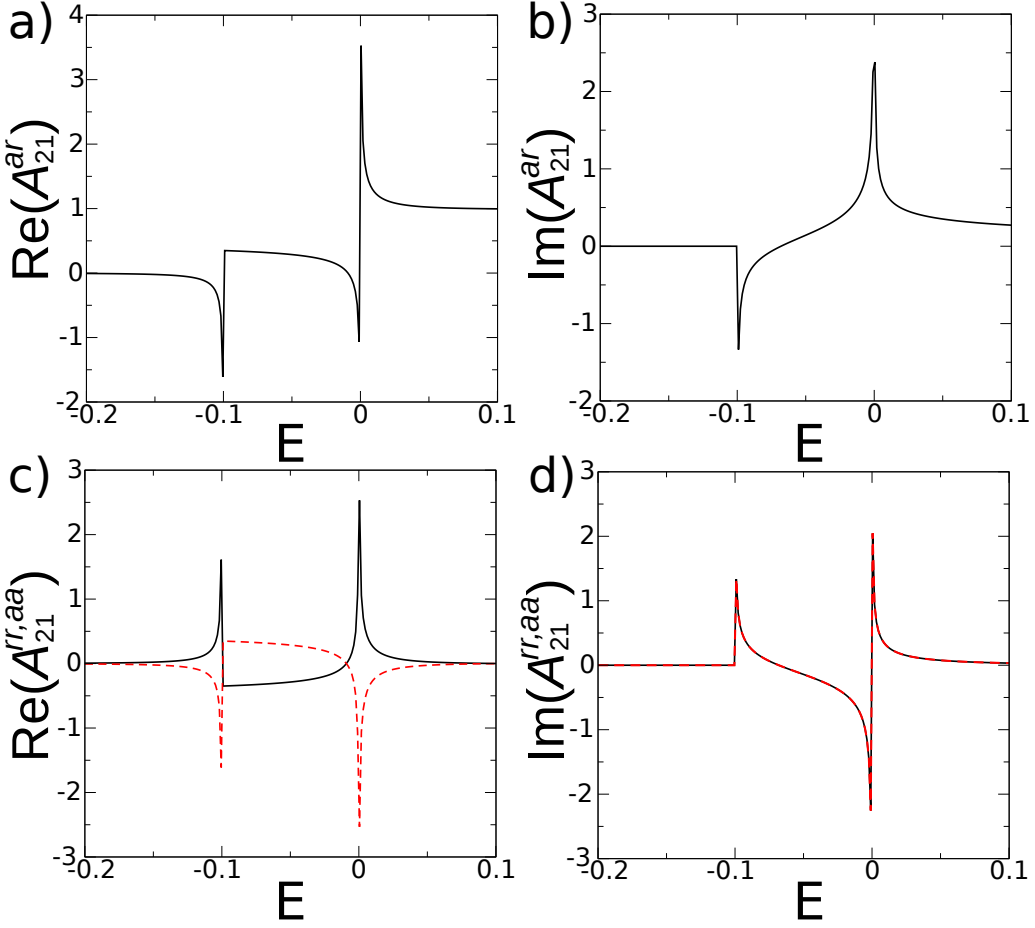


Figure 3.3: Real (left panels) and imaginary (right panels) parts of the integrands appearing in Eq.(3.41) as a function of energy close to the band edge $E = 0$. The frequency was chosen to be $\hbar\omega = 0.1$. There are pronounced peaks at energies $E = 0$ and $E = -\hbar\omega$. Upper panels: A_{21}^{ar} . Lower panels: A_{21}^{rr} (black solid line) and A_{21}^{aa} (red dashed line).

(here $c, b \in \{a, r\}$ stands for the retarded or advanced self energy). The three terms (3.42), (3.43) and (3.44) are direct outputs of recursive Green's function like techniques so that the main numerical difficulty lies in the evaluation of the integral over energies.

For a single site $L = 1$ device, the (onsite) Green's function of the system can be easily obtained [67],

$$\mathcal{G}_0(E) = \begin{cases} -\frac{1}{\sqrt{(E-2)^2-4}}, & \text{for } E \leq 0, \\ \frac{1}{i\sqrt{4-(E-2)^2}}, & \text{for } |E| < 4, \\ \frac{1}{\sqrt{(E-2)^2-4}}, & \text{for } E \geq 4. \end{cases} \quad (3.46)$$

We find that it contains square root singularities $1/\sqrt{E - E_0}$ which appear on the edges of the band (or more generally in quasi 1D system, whenever there is an opening/closing of a new

conducting channel). Typical plots of the integrands are shown in Fig. 3.3. These singularities are integrable but may require a very fine discretization mesh. In practice, we find that advanced integration routines, such as QUAD which is used in this thesis [68] can handle these singularities properly. Alternatively, one can locate and remove them by proper changes of the integration variable [69].

The AC conductance of the one dimensional wire is shown in Fig. 3.4 for two lengths $L = 40$ and $L = 200$. We find that the calculation performed keeping only the "WBL-like" term A_{21}^{ar} (this is the only surviving term in the WBL) in Eq.(3.41), is equivalent to using Eq.(3.6), derived within the scattering approach [7], in the large L limit. In order to compare the two approaches, we integrated numerically (assuming zero temperature) Eq.(3.6) using the actual dispersion relation of the Hamiltonian (3.40), $E(k) = 2 - 2 \cos k$, and $S_{21} = \exp(ikL)$ (perfect transmission). To understand why both formalisms coincide when $L \rightarrow \infty$, note that terms A_{21}^{rr} and A_{21}^{aa} typically oscillate as $\exp[\pm i(k(E + \hbar\omega) + k(E))L] \propto \exp[\pm 2ik_F L]$ (k_F : Fermi momentum) so they quickly vanish when $k_F L \gg 1$ and only the (WBL) term $A_{21}^{ar} \propto \exp[i(k(E + \hbar\omega) - k(E))L]$ remains (in agreement with Refs.[7, 61] where the fast oscillating terms are neglected in the derivation of the current operator).

3.4.2 Quantum Point Contact

We continue with a quasi one-dimensional wire of width W and length L connected to two reservoirs. AC bias is applied to the source lead (S) and we are interested in the current response in the drain (D), see Fig. 3.5. The Hamiltonian is the direct extension of Eq.(3.40) to the quasi 1D geometry. The dispersion relation for this discrete model is (in units of the hopping constant)

$$E_n(k) = \epsilon_n + 2 - 2 \cos k, \quad (3.47)$$

which corresponds, in the continuum limit, $k \rightarrow 0$, to

$$E_n(k) = \epsilon_n + k^2, \quad (3.48)$$

where the transverse energy $\epsilon_n = 2 - 2 \cos(n\pi/(W + 1))$, $n = 1 \dots W$, and k is the longitudinal momentum. The integer n defines the quantized values of the transverse momentum and thereby enumerates the conducting channels.

We focus on the regime where only the first ($n = 1$) channel is open and use the corresponding transverse energy ϵ_1 as our reference energy. In the scattering matrix approach, the system is described by its transmission matrix $S_{DS}(E) = \exp(ikL)$: a wave packet is entirely transmitted and only acquires a (energy dependent) phase. Then, equation (3.6) reads

$$\Upsilon_{DS} = \frac{e^2}{h} \int_{E_F - \hbar\omega}^{E_F} \frac{dE}{\hbar\omega} \exp\{iL[k(E + \hbar\omega) - k(E)]\}. \quad (3.49)$$

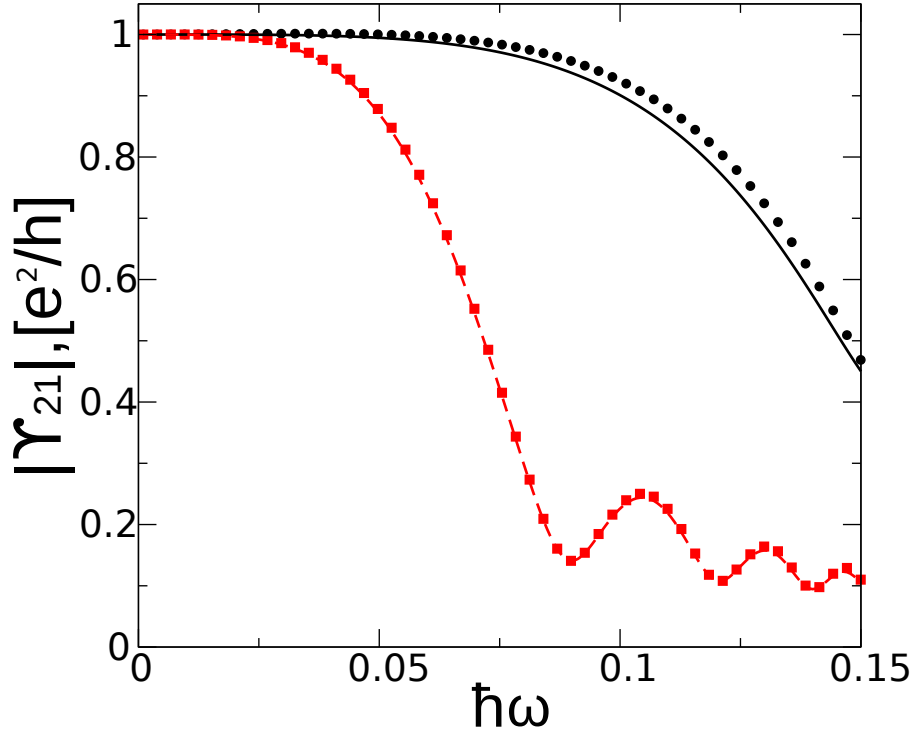


Figure 3.4: Absolute value of the AC left-to-right conductance for the one-dimensional wire of length $L = 40$ (black circles) and $L = 200$ (red rectangles). Symbols: numerical calculation with the Green's function formalism, Eq.(3.41) (keeping only the A_{21}^{gr} term), lines: scattering approach Eq.(3.6) (see text for details). We find a visible difference between the two approaches for the small size $L = 40$ that disappears when L increases. Fermi energy is $E_F = 0.17$.

In the continuum limit, when $\hbar\omega \ll E_F$ it can be further simplified using Eq.(3.48) into

$$\Upsilon_{DS} = \frac{e^2}{h} e^{i\omega\tau} \frac{\sin\left(\frac{\hbar\omega^2\tau}{4E_F}\right)}{\left(\frac{\hbar\omega^2\tau}{4E_F}\right)}, \quad (3.50)$$

where $\tau = L/v_F$ is the time of flight from the source lead to the drain (see lower inset on Fig. 3.5). From this simple calculation we notice that the AC conductance gives access to two characteristic time (or energy) scales of the system. Indeed, the numerical results of Fig. 3.5 indicate that the absolute value of the AC conductance and its phase can be very well described by this simple scaling law up to moderately large frequencies. The scaling parameters arising in this case allow for the extraction of the time of flight and the longitudinal Fermi energy. We note that, as the Fermi energy E_F and thus the velocity v_F that enter the previous expression are counted from ϵ_1 (i.e. they are in fact the longitudinal Fermi energy and velocity), one can actually slow down the electrons to bring these times and energy scales into an experimentally accessible window (GHz range).

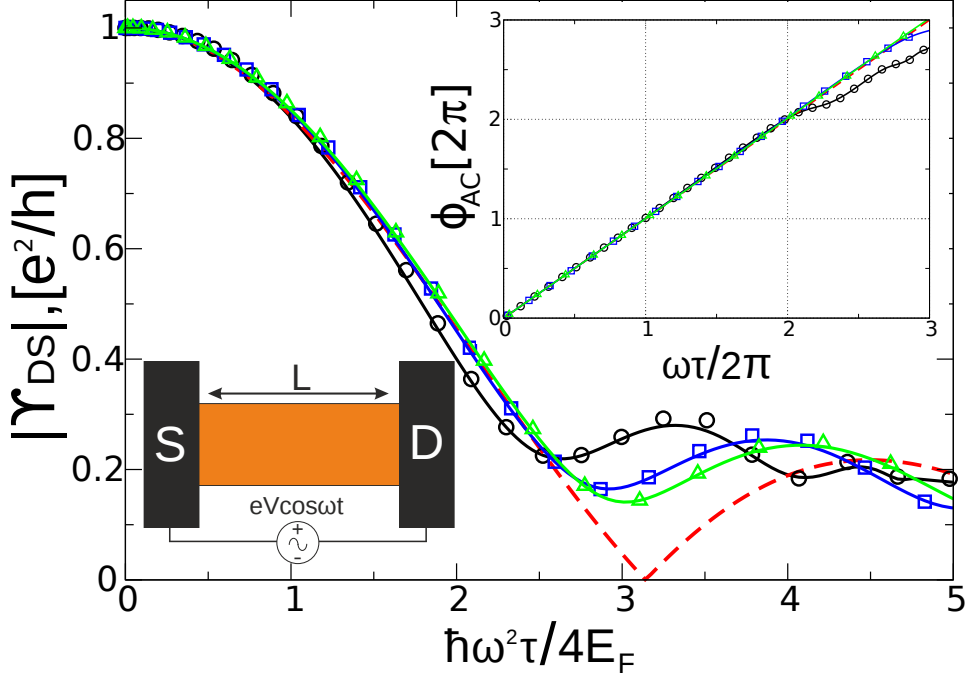


Figure 3.5: Rescaled amplitude and phase (upper inset) of the two terminal AC conductance $\Upsilon_{DS} = |\Upsilon_{DS}|e^{i\phi_{AC}}$ for a quasi one-dimensional wire of width $W = 10$. Lower inset: schematic picture of the setup. Fermi energy is chosen to have only one propagating mode. The parameters are: $E_F = 0.68\epsilon_2$, $L = 100$ (black circles), $E_F = 0.79\epsilon_2$, $L = 150$ (blue rectangles), $E_F = 0.79\epsilon_2$, $L = 200$ (green triangles), where ϵ_2 is the energy of the second mode opening (see Eq.(3.47)). Different symbols correspond to the numerical integration of Eq.(3.41), while the lines are calculated with the help of Eq.(3.49) exploiting the full tight-binding dispersion relation (3.47). Red dashed line is the analytical fit using Eq.(3.50). All the lengths are in units of the lattice constant.

A practical way to implement an effective quasi-one dimensional wire is through a quantum point contact (QPC) formed by confining an electron gas with electrostatic gates placed on top of a semiconducting heterostructure. We use the following model for the electric potential (see lower inset of Fig. 3.6a for a color plot of the potential seen by the electrons),

$$V(x, y) = V_g \Phi_x(x - x_0) \Phi_y(y - y_0),$$

$$\Phi_x(x) = \frac{1}{2} \left[\tanh \left(\frac{x + \eta_x}{\xi_x} \right) + \tanh \left(-\frac{x - \eta_x}{\xi_x} \right) \right], \quad (3.51)$$

$$\Phi_y(y) = \frac{1}{2} \left[2 - \tanh \left(\frac{y + \eta_y}{\xi_y} \right) - \tanh \left(-\frac{y - \eta_y}{\xi_y} \right) \right], \quad (3.52)$$

where the parameters ξ_x, ξ_y control the steepness of the potential (they are chosen so that to suppress backscattering – adiabatic regime), and (x_0, y_0) determines the position of the center of

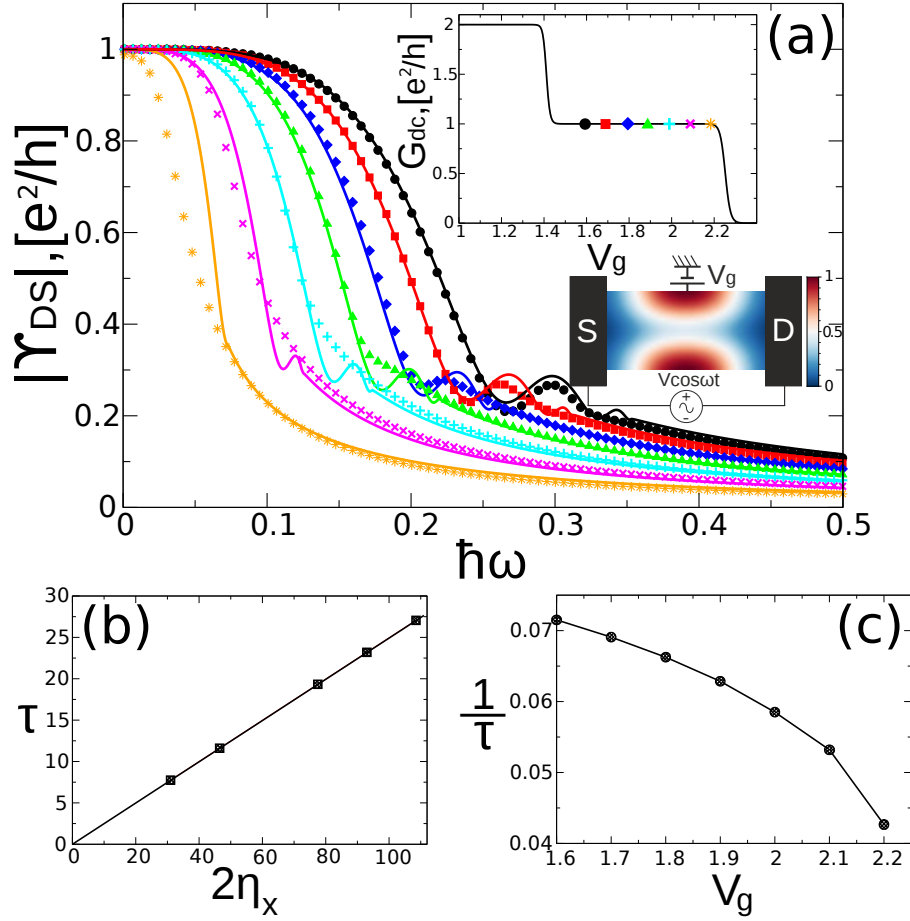


Figure 3.6: Quantum Point Contact. (a) Absolute value of the AC conductance as a function of driving frequency for different values of V_g depicted on the upper inset. Upper inset: dc conductance as a function of V_g . The lower inset represents actual potential profile in the device forming the QPC. (b),(c) Extracted time of flight as a function of QPC length, $2\eta_x$, (see Eq.(3.51)) and V_g , respectively. Fermi energy in the calculations was $E_F = 1.2$ providing 4 open channels in the leads, while only one being transmitted through the QPC. Other parameters: $\xi_x = \eta_x/2$, $\xi_y = 3\eta_y/2$, and $\eta_y = 2$.

the QPC. The effective length (width) of the QPC is $2\eta_x$ ($2\eta_y$). In this case the dispersion relation in the gated region may be considered similar to Eq.(3.49) except that now the transverse energy ϵ_n is determined not only by the width, but also depends on the parameters of the QPC (η_y, ξ_y, V_g , etc.). In our calculations we controlled the value of V_g (keeping other parameters fixed) to have only one open channel (at a given E_F) in the gated region (see upper inset on Fig. 3.6a). The results of the numerical simulations of the AC conductance for this system are given in Fig. 3.6. Fig. 3.6a shows the absolute value of the AC conductance as a function of the driving frequency. Different symbols are calculated numerically via Eq.(3.41) for different

values of the gate voltage V_g (hence of the effective longitudinal velocities), as shown in the upper inset. The fitting lines are obtained from the scattering matrix formalism, Eq.(3.49), making use of the dispersion relation (3.47). Again, the transverse energy of the open mode, $\epsilon_1(\eta_y, \xi_y, V_g, \dots)$, was chosen as the energy reference. Comparing the two approaches, we see that the closer we are to the edge of the propagating mode (various symbols on the upper inset of Fig. 3.6a), the worse is the fit given by Eq.(3.49). This is due to the fact that the scattering matrix formula is applicable when the Fermi velocity is a smooth slowly varying function of energy[61], which breaks down near the band bottom ($E_F \approx \epsilon_1$).

From the slope of the phase of the AC conductance ($\phi = \omega\tau$, curves similar to the inset of Fig. 3.5, not shown) we can extract the effective time of flight τ of the electrons through the QPC, see Figs. 3.6b,c. We find that τ scales linearly with the QPC length $2\eta_x$ (ballistic transport) while it increases as we tune V_g towards the closing of the propagating mode (the velocity vanishes when the mode becomes evanescent, $E_F < \epsilon_1$).

3.4.3 Screening

Note that the above calculations did not take screening into account. We presented only the results referring to the particle part of the current omitting the displacement part. As was already discussed in Sec. 3.2, this is correct as soon as one considers the non-interacting electrons.

Consider now the case of a quasi one-dimensional wire discussed above. In order to account for the interactions, at least in the simplest approximation, one could assume that the induced charge density inside the wire, which is to be screened, creates a *homogeneous* oscillating potential. Then, if we replace our setup by the one depicted on Fig. 3.7 (assuming there is a metallic top gate at some distance from the wire), it is possible to find the displacement part as a function of a single parameter C – capacitance between the wire and the gate. It was done in Refs.[2, 7] and the result for the AC conductance matrix reads (see also Eq.(3.38))

$$\Upsilon_{nm}^{\text{scr}}(\omega) = \Upsilon_{nm}(\omega) - \frac{\sum_k \Upsilon_{nk}(\omega) \sum_l \Upsilon_{lm}(\omega)}{\sum_{kl} \Upsilon_{kl}(\omega) - i\omega C}, \quad (3.53)$$

where $\Upsilon_{nm}(\omega)$ is the particle current contribution (3.26). Examining this expression one can single out two limiting cases: (i) $C = \infty$, which corresponds to the non-interacting case discussed above (see Fig. 3.5); and (ii) $C = 0$, which refers to the case of infinitely strong interaction between electrons, forbidding any charge accumulation in the wire. These cases are compared on Fig. 3.7, where we plot real (upper plot) and imaginary (lower plot) parts of the source-to-drain conductance for the non-interacting (blue) and the strongly interacting (red) cases. One can see that even in the presence of screening there are still oscillations in the source-to-drain conductance with a period characterized by the time of flight (just as in the non-interacting case, see Eq.(3.50)), which allow for the measurement of the latter [2].

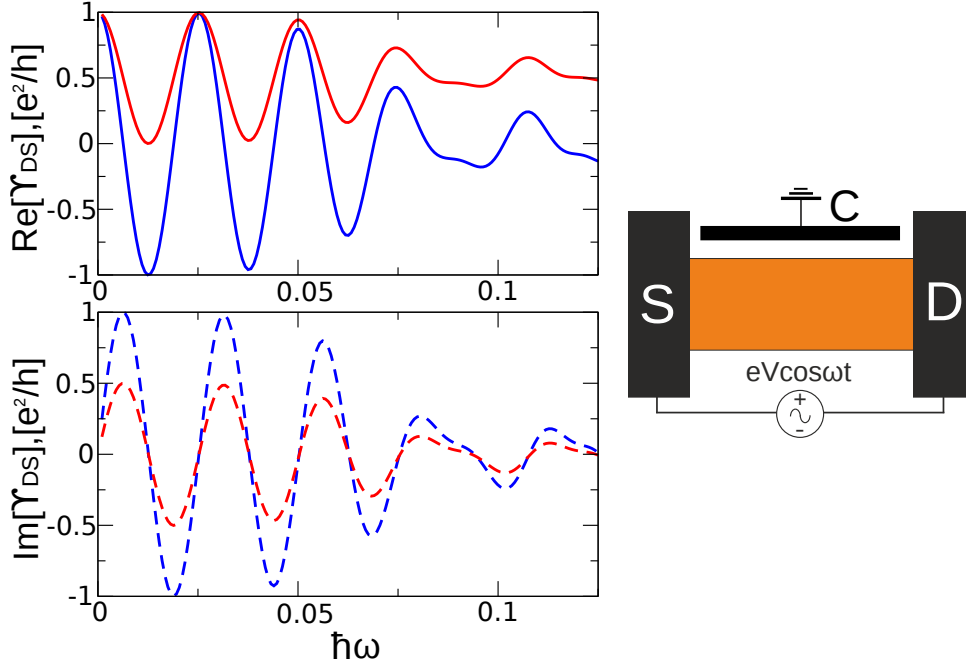


Figure 3.7: Real (upper plot) and imaginary (lower plot) parts of the source-to-drain conductance for two limiting cases: non-interacting electrons ($C = \infty$ in Eq.(3.53)) – blue lines; and strongly interacting electrons ($C = 0$ in Eq.(3.53)) – red lines. On the right side of the figure: schematic picture of a setup used to obtain Eq.(3.53).

Situation becomes more complicated if we consider the case of a point contact. The advantage of the quasi one-dimensional wire is that we dealt with a perfectly transmitting channel. Contrary to this, in order to correctly describe the interacting limit for a QPC, it is necessary to take into account both transmitted and reflected waves [70, 71, 72]. Then, it turns out that the real and imaginary parts of the source-to-drain conductance also oscillate with frequency, however the oscillation period is different compared to the non-interacting case (see Fig. 3.6) [71, 72]. In fact, it is determined by the mean time of flight of the open (transmitted) channels and a contribution coming from the closed (reflected) channels. Moreover, in order to find the displacement conductance at least in the crudest approximation, one needs minimum two capacitances C_1 and C_2 at each side of the QPC [7, 70]. This is still a subject of subsequent research.

3.4.4 Mach-Zehnder interferometer

We close this section with a discussion of the AC response of an electronic MZ interferometer in the quantum Hall regime [31, 32, 33, 34, 35, 36, 37, 73]. The setup consists of the two-dimensional electron gas confined in a finite geometry, connected to three reservoirs: source

(S), drain (D) and internal drain (D'). Fig. 3.8a presents the sample together with a schematic of the two interfering edge states. The additional electrode (D') is necessary to avoid multiple

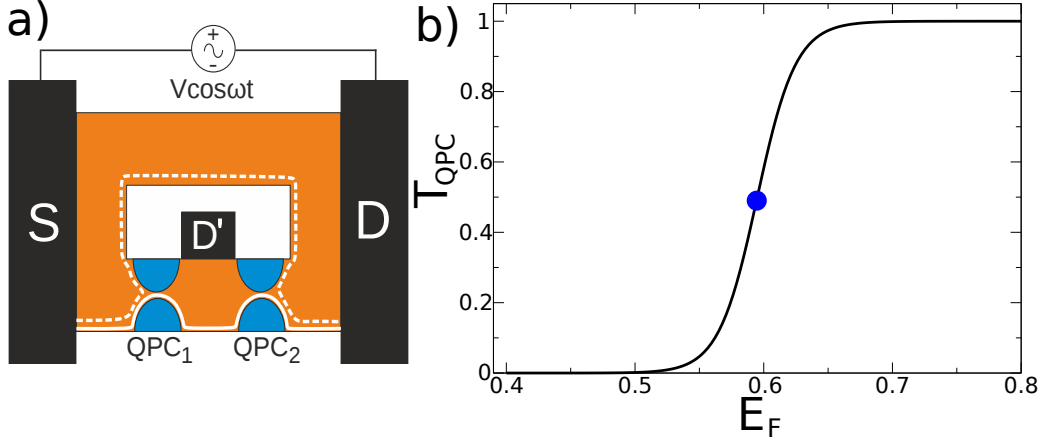


Figure 3.8: Mach-Zehnder interferometer. (a) Cartoon of the system with the interfering paths represented by the solid and dashed white lines. Length of the sample $L = 80$, width of the system $W = W_h + 22$, where W_h is the width of the hole. The system is in the quantum Hall regime at filling factor $\nu = 1$. The two QPCs were chosen to be semi-transparent $T_{1,2} = \frac{1}{2}$. (b) Transmission characteristics of the QPCs. The blue dot corresponds to the Fermi energy at which QPC is half transparent.

loops of the electron edge states and the corresponding Fabry-Perot physics. The system is put in a strong magnetic field driving the system into the quantum Hall regime. We considered the case with a filling factor $\nu = 1$ (single edge channel). The QPCs are defined by two pairs of gates in the lower arm of the interferometer and play a role of the beam splitters. The interfering paths are shown by the solid and dashed lines on Fig. 3.8a. We put an additional Aharonov-Bohm (AB) flux φ_{AB} through the hole of the interferometer that allows to change the relative phase between the paths without changing the edge states. We calculated the AC conductance as a function of the AB flux φ_{AB} and frequency ω as shown in Fig. 3.9.

We start with simple analytical considerations using the scattering matrix approach. Let us assume, for simplicity, that both QPCs are characterized by energy independent transmission probabilities $T_{1,2}$ (and corresponding reflection probabilities are $R_{1,2} = 1 - T_{1,2}$). We describe the QPCs by their scattering matrices, which can be parametrized as follows

$$\begin{pmatrix} i\sqrt{R_k} & \sqrt{T_k} \\ \sqrt{T_k} & i\sqrt{R_k} \end{pmatrix}, \quad k = 1, 2. \quad (3.54)$$

The source-to-drain transmission amplitude S_{DS} then consists of the contributions from two paths, path a (solid line on Fig. 3.8a) which is a consequence of two sequential transmissions

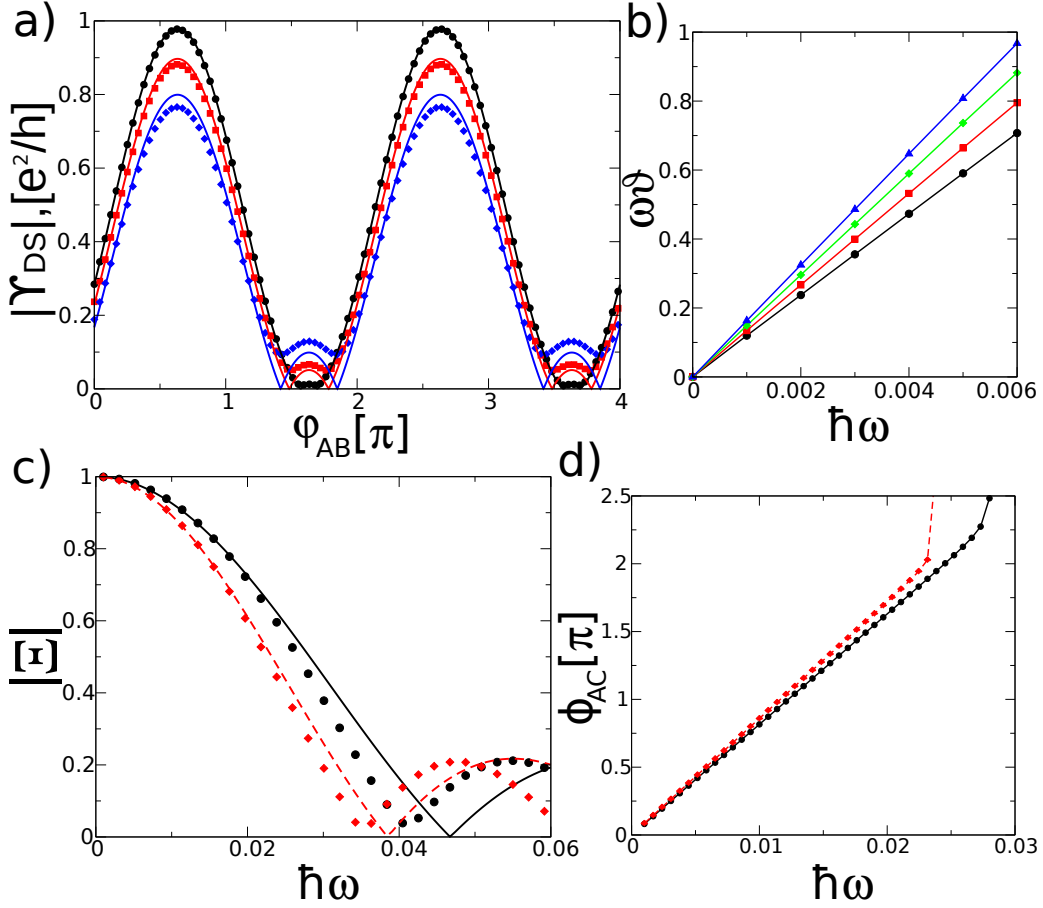


Figure 3.9: Mach-Zehnder interferometer. (a) AB oscillations of AC conductance as a function of magnetic flux through the hole. Black circles, red rectangles, and blue diamonds correspond to the driving frequency $\hbar\omega = 0.003, 0.007, 0.01$ respectively. Width of the hole $W_h = 45$. (b) $\omega\tau$ as a function of frequency for different values of W_h extracted with Eq.(3.60) (see text for details). From bottom up $W_h = 30, 35, 40, 45$. (c) Function $|\Xi(\omega)|$, see Eq.(3.62), as a function of frequency. Black circles and red diamonds correspond to $W_h = 35, 45$ respectively. (d) Respective phase of the AC conductance $\phi_{AC} = \omega\tau$ as a function of frequency. In plots (a) and (c) all the symbols were calculated with the Green's function formalism, Eq.(3.41), modeling the QPCs with Eq.(3.51). The connecting lines are the corresponding analytical fits, Eq.(3.60), with parameters calculated from the Green's function-based numerics.

through the QPCs and path b (dashed line) arising from sequential reflections

$$S_{DS}(E) = \sqrt{T_1 T_2} e^{i\psi_a(E)} - \sqrt{R_1 R_2} e^{i\psi_b(E)}. \quad (3.55)$$

Traversing either path, an electron acquires a phase $\psi_{a,b}$. The phase itself contains two contributions, the AB phase caused by the magnetic flux through the hole and a dynamical phase of

the propagating plain wave along the path,

$$\psi_x(E) = k(E)L_x + \varphi_x, \quad x = \{a, b\}, \quad (3.56)$$

$$\varphi_{AB} = \varphi_b - \varphi_a, \quad (3.57)$$

where k is the longitudinal wave number of the edge state and L_x is a length of the corresponding path. In order to calculate the AC conductance we need to specify the energy dependence of the phase factors in Eq.(3.55). We note that by varying energy we modify only the dynamical part of the phase, while the AB flux is unaffected. Thus, we make the following ansatz

$$\psi_x(E) \approx \psi_x(E_F) + \lambda_x(E - E_F), \quad (3.58)$$

$$\lambda_x = L_x \frac{\partial k}{\partial E}(E_F), \quad x = \{a, b\}. \quad (3.59)$$

Actual value of $\psi_x(E_F)$ and λ_x depends on the boundary conditions defining the geometry of the setup. Assuming we know the edge state dispersion relation, we can relate the latter to the group velocity of the edge state v_g at the Fermi level via $\lambda_x = L_x/(\hbar v_g)$.

At this stage we are prepared to calculate the AC conductance with equations (3.6), (3.55), and (3.58). The scattering formula is valid when $\hbar\omega \ll E_F$ and we will use it to carry out the integration in energy. Let's assume, for simplicity, that the QPCs are tuned to half transparency $T_{1,2} = 1/2$. Then, after a straightforward calculation we obtain

$$\Upsilon_{DS}(\omega, \varphi_{AB}) = \frac{1}{2} e^{i\omega\tau} \left[\cos \frac{\omega\vartheta}{2} - \frac{\sin \frac{\omega\vartheta}{2}}{\frac{\omega\vartheta}{2}} \cos(\psi_b(E_F) - \psi_a(E_F)) \right], \quad (3.60)$$

$$\tau = \frac{L_b + L_a}{2v_g}, \quad \vartheta = \frac{L_b - L_a}{v_g}. \quad (3.61)$$

We have two time scales naturally appeared, namely the average time of flight τ and the relative time ϑ , coming from the asymmetry between the paths.

Now we turn to our numerical results (see Fig. 3.9) and compare them to the simple formula (3.60). On Fig. 3.8b we plot the DC characteristics of the QPCs considered in our modelling. The Fermi level is fixed at a half transparency value. We remind that in order to obtain Eq.(3.60) we assumed that the transmission characteristics of the QPCs are energy independent. However, as one can see from Fig. 3.8b, in our sample detuning from the assumed value becomes important for $\hbar\omega \simeq 0.01$ and is of the order $\Delta T_{1,2} \simeq 0.15$. Next, Fig. 3.9a represents the plots of the AB oscillations of the AC conductance as a function of flux for three different values of driving frequency. Symbols of different types on the Figure represent the Green's function based calculation, Eq.(3.41), while the solid lines are corresponding fits according to Eq.(3.60). This fit is obtained as follows: (i) we perform a DC calculation (which corresponds to $\omega \rightarrow 0$ in Eq.(3.60)) and find $\phi_0 \equiv \arccos(\Upsilon_{DS}(0, \pi) - \Upsilon_{DS}(0, 0))$, which corresponds to the phase offset at zero flux $\varphi_{AB} = 0$, see Fig.(3.9)a; (ii) we compute the phase $\omega\vartheta = 2 \arccos |\Upsilon_{DS}(\omega, \pi) + \Upsilon_{DS}(\omega, 0)|$ at

small ω ; (iii) finally, we plot Eq.(3.60) using the extracted ϑ and $\psi_b(E_F) - \psi_a(E_F) = \phi_0 + \varphi_{AB}$. We see that this formula describes quite well the numerical data, especially at low frequencies. However when the driving frequency is increased deviation of the numerical data from the fit becomes more pronounced. A more detailed analysis shows that these deviations can be accounted for by including the quadratic term in energy, which we have neglected in Eq.(3.58). In Fig. 3.9b we plot the extracted $\omega\vartheta$ as a function of driving frequency. Various plots correspond to the samples with a different width of the hole in the interferometer. Varying this width, we modify the length of the upper path (dashed line in Fig. 3.8a). Extracting the corresponding slopes, i.e. ϑ , for each sample, we are able to calculate the velocity of the edge state v_g owing to Eq.(3.61). For the parameters chosen in our calculation, $B \simeq 20\text{T}$ and the lattice constant $a_0 \simeq 1\text{nm}$, we have obtained the velocity $v_g \simeq 0.7a_0t\hbar^{-1}$ (which corresponds to $v_g \simeq 10^6\text{m/s}$), where $t = \hbar^2/(2ma_0^2)$ is a hopping parameter of the tight-binding model [45] used to simulate the setup, m -effective mass.

In Figs. 3.9c,d we present the AC conductance calculations as a function of frequency. On Fig. 3.9c, using the source-to-drain conductance $\Upsilon_{DS}(\omega, \varphi_{AB})$, we plot the function

$$\Xi(\omega) = \left| \frac{\Upsilon_{DS}(\omega, \pi) - \Upsilon_{DS}(\omega, 0)}{\Upsilon_{DS}(0, \pi) - \Upsilon_{DS}(0, 0)} \right|, \quad (3.62)$$

which for a simple case of Eq.(3.60) reduces to $\sin(\omega\vartheta/2)/(\omega\vartheta/2)$. Again, the symbols correspond to the Green's function calculations, while the lines are given by the analytical fit, Eq.(3.60), using the calculated before values of $\omega\vartheta$ (see Fig. 3.9b). Black circles and red diamonds represent calculations with various values of the hole width (allowing to change the length difference between the paths). We notice that for the frequencies $\hbar\omega \lesssim 0.02$, the numerical data is very well fit by Eq.(3.60), while at higher values of $\hbar\omega$ this is no longer true. There are two reasons for this. First, at high enough frequencies detuning of the QPCs from the half transparency value becomes significant (see Fig. 3.8b) and we cannot neglect the energy dependence of the transmission/reflection amplitudes. Second, due to the dispersion of the edge state, there is always a contribution from the quadratic term neglected in the expansion (3.58), which becomes important at high frequencies.

Finally, we plot the frequency dependence of the phase of the AC conductance (see Fig. 3.9d) varying the hole width in order to extract the second time scale, τ according to Eq.(3.60). We find again the value of the group velocity $v_g \simeq 0.72a_0t\hbar^{-1}$, which is consistent with the previous result.

To conclude, we have analyzed the AC response of the MZ electronic interferometer and found that the non-equilibrium dynamics makes it possible to address the internal time scales of the setup via transport measurements.

Chapter 4

The Green's function formalism at finite frequency

In this chapter we provide the details necessary to derive the expressions given in Section 3.3 and Appendix A as well as systematic tools to derive other observables. The formalism developed in this chapter is based on the Non Equilibrium Green's Function formalism (NEGF). In Section 4.1 we briefly review its time-dependent version [13, 14, 8, 11] and define the main quantity we are interested in – electric current – in terms of Green's functions. Then, in Section 4.2 we explain how to take advantage of the fact the perturbation is periodic in time and introduce the form of Fourier transform we use to transform various quantities from time to energy domain. In Sections 4.3 and 4.4 we consider the cases of internal and external perturbations, respectively. For each of them we investigate two limiting cases: limit of small perturbation amplitude (eV_{ac}) and the adiabatic limit ($\omega \rightarrow 0$). In the former we develop a systematic expansion of the (retarded) Green's function in powers of eV_{ac} and give the corresponding Feynman rules to construct arbitrary order correction (any diagram can be interpreted as a sequence of photon absorption/emission processes). In the latter we introduce generating functions, which are convenient quantities to work with when the frequency of the perturbation is small. Any observable can be expressed in terms of them (as the adiabatic current and the correction to it, see Appendix A).

4.1 Time dependent NEGF formalism in a nut shell

Our starting point is a general time-dependent quadratic Hamiltonian for our system:

$$\hat{\mathbf{H}}(t) = \sum_{n,m} \mathbf{H}_{nm}(t) c_n^\dagger c_m. \quad (4.1)$$

We do not include electron-electron interactions besides some mean field treatment as was discussed in Sec. 3.3.3.

The basic objects that will be manipulated in this chapter are various sorts of Green's Functions (GFs). The retarded $\mathfrak{G}_{nm}^r(t, t')$, advanced $\mathfrak{G}_{nm}^a(t, t')$, lesser $\mathfrak{G}_{nm}^<(t, t')$ and greater $\mathfrak{G}_{nm}^>(t, t')$ Green's functions are defined as,

$$\mathfrak{G}_{nm}^r(t, t') = -\frac{i}{\hbar}\theta(t-t')\langle\{c_n(t), c_m^\dagger(t')\}\rangle, \quad (4.2)$$

$$\mathfrak{G}_{nm}^a(t, t') = \frac{i}{\hbar}\theta(t'-t)\langle\{c_n(t), c_m^\dagger(t')\}\rangle, \quad (4.3)$$

$$\mathfrak{G}_{nm}^<(t, t') = \frac{i}{\hbar}\langle c_m^\dagger(t'), c_n(t) \rangle, \quad (4.4)$$

$$\mathfrak{G}_{nm}^>(t, t') = -\frac{i}{\hbar}\langle c_n(t), c_m^\dagger(t') \rangle. \quad (4.5)$$

where $c_n^\dagger(t)$ ($c_n(t)$) corresponds to c_n^\dagger (c_n) in the Heisenberg representation. The retarded and lesser/greater GFs satisfy the following equations of motion [46, 47],

$$\left(i\hbar\frac{\partial}{\partial t} - \mathbf{H}(t)\right)\mathfrak{G}^r(t, t') = \delta(t-t'), \quad (4.6)$$

$$\left(i\hbar\frac{\partial}{\partial t} - \mathbf{H}(t)\right)\mathfrak{G}^\kappa(t, t') = 0, \quad \kappa = <, >. \quad (4.7)$$

Table 4.1 summarizes the various Green's functions introduced so far, as well as the one needed later for the AC formalism.

4.1.1 Dyson equation

It is often convenient to split the full Hamiltonian (4.1) into a sum of an "unperturbed part" \mathcal{H} and a perturbation $\mathcal{V}(t)$:

$$\mathbf{H} = \mathcal{H} + \mathcal{V}(t). \quad (4.8)$$

This splitting can (and will) be done in several different ways, dictated by convenience. For instance, \mathcal{V} can be a time-dependent potential, or a hopping element between the device and the leads, or a sum of the previous two, etc. Introducing $\mathfrak{g}^r(t, t')$ and $\mathfrak{g}^<(t, t')$, the unperturbed Green's functions associated to \mathcal{H} , one can derive the Dyson equations [52, 44, 46, 47], which relate the full GFs to the unperturbed ones. They read,

$$\mathfrak{G}^r = \mathfrak{g}^r + \mathfrak{g}^r * \mathcal{V} * \mathfrak{G}^r, \quad (4.9)$$

$$\mathfrak{G}^r = \mathfrak{g}^r + \mathfrak{G}^r * \mathcal{V} * \mathfrak{g}^r. \quad (4.10)$$

$$\mathfrak{G}^\kappa = \mathfrak{g}^\kappa + \mathfrak{g}^r * \mathcal{V} * \mathfrak{G}^\kappa + \mathfrak{g}^\kappa * \mathcal{V} * \mathfrak{G}^a, \quad \kappa = <, >, \quad (4.11)$$

$$\mathfrak{G}^\kappa = \mathfrak{g}^\kappa + \mathfrak{G}^r * \mathcal{V} * \mathfrak{g}^\kappa + \mathfrak{G}^\kappa * \mathcal{V} * \mathfrak{g}^a, \quad \kappa = <, >, \quad (4.12)$$

where the symbol $*$ stands for convolution with respect to time and matrix product with respect to the site indices:

$$(A * B)_{ij}(t, t') = \sum_k \int dt'' A_{ik}(t, t'') B_{kj}(t'', t'), \quad (4.13)$$

Table 4.1: Summary of notations.

Type of GF ^a	Description
$\mathfrak{g}^\kappa(t, t')$	GF of the system when the leads and the scattering region are decoupled, see Eq.(4.8).
$g^\kappa(t, t')$	GF of the device sub-block for a system with decoupled leads. $g^\kappa(t, t') \equiv \mathfrak{g}_{00}^\kappa(t, t')$
$\mathfrak{G}^\kappa(t, t')$	GF of the system described by the full Hamiltonian (4.1).
$G^\kappa(t, t')$	GF of the device sub-block, see Eq.(4.16). $G^\kappa(t, t') \equiv \mathfrak{G}_{00}^\kappa(t, t')$
$G_l^\kappa(E)$	GF of the device sub-block with l photons emitted/absorbed, see Eq.(4.29).
$G_l^{(n)}(E)$	n -th order in V_{ac} of the device sub-block GF with l photons emitted/absorbed, see Eq.(4.38).
$\mathcal{G}_l(E)$	Retarded <i>equilibrium</i> GF of the system at energy $E + \frac{\hbar\omega l}{2}$, see Eqs.(2.32) and (3.24).

^a $\kappa = r, a, <, >$

and \mathcal{V} should be understood as $\delta(t - t')\mathcal{V}(t)$ in a convolution.

4.1.2 Integrating out the electrodes

From now on we restrict $\mathcal{V}(t)$ to the matrix elements that couple the leads to the system plus (possibly) a time dependent potential in the device region. Then from Eqs.(4.9) and (4.11) one arrives at

$$G^r = g^r + g^r * (\Sigma^r + V) * G^r, \quad (4.14)$$

and

$$G^\kappa = g^\kappa + g^r * V * G^\kappa + g^r * \Sigma^r * G^\kappa + g^r * \Sigma^\kappa * G^a + g^\kappa * V * G^a + g^\kappa * \Sigma^a * G^a, \quad \kappa = <, >, \quad (4.15)$$

where we have introduced special notations for the $(\bar{0}\bar{0})$ device sub-block (see Fig. 2.2),

$$H \equiv \mathcal{H}_{\bar{0}\bar{0}}, \quad V = \mathcal{V}_{\bar{0}\bar{0}}, \quad G^\kappa \equiv \mathfrak{G}_{\bar{0}\bar{0}}^\kappa, \quad g^\kappa \equiv \mathfrak{g}_{\bar{0}\bar{0}}^\kappa, \quad \dots \quad (4.16)$$

and also the self-energies Σ^κ defined as

$$\begin{aligned}\Sigma^\kappa(m) &= \mathcal{V}_{\bar{0}\bar{m}} * \mathfrak{g}_{\bar{m}\bar{m}}^\kappa * \mathcal{V}_{\bar{m}\bar{0}}, \\ \Sigma^\kappa &= \sum_{m=1}^M \Sigma^\kappa(m), \quad \kappa = r, a, <, > .\end{aligned}\quad (4.17)$$

Utilizing Eq.(4.6), equation (4.14) can be rewritten in terms of an effective equation of motion,

$$\left(i\hbar\frac{\partial}{\partial t} - H\right) G^r(t, t') - (\Sigma^r + V) * G^r = \delta(t - t'), \quad (4.18)$$

while the lesser and greater GFs (4.15) with the help of Eqs.(4.6)-(4.7) and (4.18) are simplified to,

$$G^\kappa = G^r * \Sigma^\kappa * G^a, \quad \kappa = <, > . \quad (4.19)$$

In the absence of time-dependent perturbations in the Hamiltonian (4.8), the Fourier transform of the self-energies $\Sigma^<(m)$ and $\Sigma^>(m)$ are given by the fluctuation-dissipation theorem which results in [45, 46, 47],

$$\Sigma^<(m; E) = if_m(E)\Gamma_m(E), \quad (4.20)$$

$$\Sigma^>(m; E) = -i(1 - f_m(E))\Gamma_m(E), \quad (4.21)$$

with Γ_m defined in Eq.(2.35).

4.1.3 Expression for the current

The current associated with the m -th lead is found using the approach of [52, 13, 14, 44], i.e. calculating the change of the number of particles in the lead due to connection with the device region and thereby with other leads too. So, the expression for the current reads

$$I_m = -e\left\langle\frac{d\hat{N}_m}{dt}\right\rangle, \quad \hat{N}_m = \sum_{\alpha\in\bar{m}} c_\alpha^\dagger(t)c_\alpha(t). \quad (4.22)$$

Taking into account the definition (4.4), Eq.(4.22) transforms into

$$I_m(t) = e\sum_{\substack{i\in\bar{0}, \\ \alpha\in\bar{m}}} (\mathcal{V}_{\alpha i}(t)\mathfrak{G}_{i\alpha}^<(t, t) - \mathcal{V}_{i\alpha}(t)\mathfrak{G}_{\alpha i}^<(t, t)). \quad (4.23)$$

Let us introduce auxiliary quantity,

$$J(m; t, t') = e\sum_{\substack{i\in\bar{0}, \\ \alpha\in\bar{m}}} (\mathcal{V}_{\alpha i}(t')\mathfrak{G}_{i\alpha}^<(t, t') - \mathcal{V}_{i\alpha}(t)\mathfrak{G}_{\alpha i}^<(t, t')) \equiv e\text{Tr}(\mathfrak{G}_{\bar{0}\bar{m}}^<* \mathcal{V}_{\bar{m}\bar{0}} - \mathcal{V}_{\bar{0}\bar{m}} * \mathfrak{G}_{\bar{m}\bar{0}}^<). \quad (4.24)$$

Exploiting Eqs.(4.11) and (4.12), one can get

$$\mathfrak{G}_{\bar{m}\bar{0}}^{\leq} = \mathfrak{g}_{\bar{m}\bar{m}}^r * \mathcal{V}_{\bar{m}\bar{0}} * \mathfrak{G}_{00}^{\leq} + \mathfrak{g}_{\bar{m}\bar{m}}^{\leq} * \mathcal{V}_{\bar{m}\bar{0}} * \mathfrak{G}_{00}^a, \quad (4.25)$$

$$\mathfrak{G}_{0\bar{m}}^{\leq} = \mathfrak{G}_{00}^r * \mathcal{V}_{0\bar{m}} * \mathfrak{g}_{\bar{m}\bar{m}}^{\leq} + \mathfrak{G}_{00}^{\leq} * \mathcal{V}_{0\bar{m}} * \mathfrak{g}_{\bar{m}\bar{m}}^a. \quad (4.26)$$

Substituting expressions (4.25) and (4.26) into Eq.(4.24), we come to

$$J(m; t, t') = e \text{Tr} (G^r * \Sigma^{\leq}(m) + G^{\leq} * \Sigma^a(m) - \Sigma^r(m) * G^{\leq} - \Sigma^{\leq}(m) * G^a). \quad (4.27)$$

Having this, we can easily find our expression for the current, since

$$I_m(t) = J(m; t, t). \quad (4.28)$$

4.2 Effect of a periodic potential

We now use explicitly the fact that the perturbation (3.1) is periodic in time. We introduce the Wigner coordinates $\{\tau = t - t', T = (t + t')/2\}$ and notice that the GF is periodic in T , $G^r(\tau, T) \rightarrow G^r(\tau, T + 2\pi/\omega)$. Thus it is possible to expand the GF into a Fourier series with respect to T and into a Fourier integral with respect to τ

$$G^r(\tau, T) = \int \frac{dE}{2\pi\hbar} \sum_{l=-\infty}^{\infty} e^{-\frac{i}{\hbar}E\tau} e^{-i\omega l T} G_l^r(E). \quad (4.29)$$

We will use extensively the fact that when $C(t, t') = A * B$ is a convolution of two quantities, one gets,

$$C_l(E) = \sum_{l_1+l_2=l} A_{l_1}(E + \frac{\hbar\omega l_2}{2}) B_{l_2}(E - \frac{\hbar\omega l_1}{2}). \quad (4.30)$$

For instance, the currents reads,

$$I_m(t) = \int \frac{dE}{2\pi\hbar} \sum_{l=-\infty}^{\infty} e^{-i\omega l t} J_l(m; E), \quad (4.31)$$

where using Eq.(4.30) for each term in Eq.(4.27) we arrive at

$$J_l(m; E) = e \sum_{l_1+l_2=l} \text{Tr} \left[G_{l_1}^r(E + \frac{\hbar\omega l_2}{2}) \Sigma_{l_2}^{\leq}(m; E - \frac{\hbar\omega l_1}{2}) + G_{l_1}^{\leq}(E + \frac{\hbar\omega l_2}{2}) \Sigma_{l_2}^a(m; E - \frac{\hbar\omega l_1}{2}) \right. \\ \left. - \Sigma_{l_1}^r(m; E + \frac{\hbar\omega l_2}{2}) G_{l_2}^{\leq}(E - \frac{\hbar\omega l_1}{2}) - \Sigma_{l_1}^{\leq}(m; E + \frac{\hbar\omega l_2}{2}) G_{l_2}^a(E - \frac{\hbar\omega l_1}{2}) \right]. \quad (4.32)$$

This is the main starting point of all the subsequent derivations. We still have to supplement it by three equations. First, using Eqs.(4.19) and (4.30) it is straightforward to find

$$G_l^<(E) = \sum_{m'=1}^M \sum_{l_1+l_2+l_3=l} G_{l_1}^r(E + \frac{\hbar\omega l_2}{2} + \frac{\hbar\omega l_3}{2}).$$

$$\Sigma_{l_2}^<(m'; E - \frac{\hbar\omega l_1}{2} + \frac{\hbar\omega l_3}{2}) G_{l_3}^a(E - \frac{\hbar\omega l_1}{2} - \frac{\hbar\omega l_2}{2}). \quad (4.33)$$

Second, if we consider the definition of the advanced and the retarded GFs and a symmetry of the transformation (4.29), we easily get

$$G_l^a(E) = [G_{-l}^r(E)]^\dagger. \quad (4.34)$$

Finally, with the two previous expressions and Eq.(4.32) one can deduce

$$J_l(m; E) = [J_{-l}(m; E)]^\dagger. \quad (4.35)$$

In the next sections we develop a systematic way to calculate the current (4.31), i.e. to express the GF elements $G_l^r(E)$ in terms of known quantities. We consider two types of perturbations: internal perturbation (in the device region) and external perturbation (in the contacts).

4.3 Perturbation in the device region

In this section we consider the case when the perturbation is applied inside the scattering region. Therefore we assume that the leads are at local thermal equilibrium and unaffected by the perturbation. This implies that V in Eq.(4.18) is given by Eqs.(3.1) and (3.3). Performing the transformation (4.29) in the Eq.(4.18) we get

$$\left(E + \frac{\hbar\omega l}{2} - H - \Sigma^r(E + \frac{\hbar\omega l}{2})\right) G_l^r(E) - eV_{ac} \frac{W}{2} G_{l-1}^r(E - \frac{\hbar\omega}{2}) - eV_{ac} \frac{W}{2} G_{l+1}^r(E + \frac{\hbar\omega}{2}) = \delta_{l,0}. \quad (4.36)$$

or equivalently,

$$G_l^r(E) - eV_{ac} \mathcal{G}_l(E) \frac{W}{2} \left(G_{l-1}^r(E - \frac{\hbar\omega}{2}) + G_{l+1}^r(E + \frac{\hbar\omega}{2})\right) = \delta_{l,0} \mathcal{G}_0(E). \quad (4.37)$$

In the two following paragraphs we explore two complementary limits: small perturbation amplitude (eV_{ac}) and adiabatic limit ($\omega \rightarrow 0$).

4.3.1 Limit of a small perturbation amplitude

Let us assume that the perturbation amplitude is much smaller than all characteristic energy scales in the system, e.g. hopping constant between sites. Then we can solve Eq.(4.36) iteratively in powers of eV_{ac} . The solution takes form

$$G_l^r(E) = \sum_{n=0}^{\infty} (eV_{ac})^n G_l^{(n)}(E), \quad (4.38)$$

$$G_l^{(n)}(E) = \mathcal{G}_l(E) \frac{W}{2} \left(G_{l-1}^{(n-1)}(E - \frac{\hbar\omega}{2}) + G_{l+1}^{(n-1)}(E + \frac{\hbar\omega}{2}) \right), \quad (4.39)$$

for $n \geq 1$ and

$$G_l^{(0)}(E) = \delta_{l,0} \mathcal{G}_l(E). \quad (4.40)$$

This equation can be solved iteratively. It is instructive to write down explicitly the first and second order contributions,

$$G_l^{(1)}(E) = \delta_{l,1} \mathcal{G}_1(E) \frac{W}{2} \mathcal{G}_{-1}(E) + \delta_{l,-1} \mathcal{G}_{-1}(E) \frac{W}{2} \mathcal{G}_1(E), \quad (4.41)$$

$$G_l^{(2)}(E) = \delta_{l,2} \mathcal{G}_2(E) \frac{W}{2} \mathcal{G}_0(E) \frac{W}{2} \mathcal{G}_{-2}(E) + \delta_{l,-2} \mathcal{G}_{-2}(E) \frac{W}{2} \mathcal{G}_0(E) \frac{W}{2} \mathcal{G}_2(E) \\ + \delta_{l,0} \left(\mathcal{G}_0(E) \frac{W}{2} \mathcal{G}_{-2}(E) \frac{W}{2} \mathcal{G}_0(E) + \mathcal{G}_0(E) \frac{W}{2} \mathcal{G}_2(E) \frac{W}{2} \mathcal{G}_0(E) \right). \quad (4.42)$$

The structure of the two previous equations suggests the following simple diagrammatic representation of an arbitrary order contribution (see Fig. 4.1). The diagrams are made by horizontal propagating lines $[\mathcal{G}_l(E)]$ separated by "photon absorption/emission" vertical wavy lines $[W/2]$. In order to build $G_l^{(n)}(E)$ one has to remember the following "Feynman rules",

- To get the contributions of order n , draw n wavy lines pointing up or down in all possible configurations (there are 2^n diagrams).
- Each diagram of order n gives a contribution to $G_l^{(n)}(E)$ where l is the difference between the number of up wavy lines and down wavy lines.
- Read the diagram from left to right. Starting from $\mathcal{G}_l(E)$, each wavy line corresponds to a factor $W/2$ followed by another $\mathcal{G}_{l'}(E)$ with l' decreased by 2 (up wavy line, a "photon" is emitted) or increased by 2 (down wavy line, "photon" absorbed). Repeat until the end of the diagram.

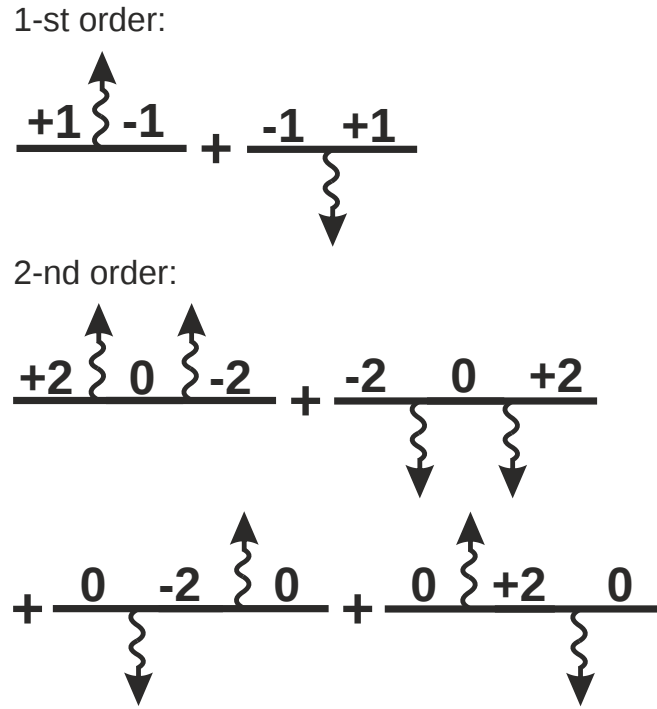


Figure 4.1: First and second order diagrams. Numbers over the straight lines correspond to the index l for \mathcal{G}_l . Direction of the wavy line tells us whether the absorption or emission of a photon takes place. Each diagram corresponds directly to one term in Eqs.(4.41)-(4.42).

4.3.2 Adiabatic limit and beyond

We now turn to a very different limit where the driving frequency (and not the amplitude) is the small parameter of the problem. When the perturbation varies slowly the system follows adiabatically. We introduce the generating function F as,

$$F(z, E) \equiv \sum_{l=-\infty}^{\infty} z^l G_l(E + \frac{\hbar\omega l}{2}). \quad (4.43)$$

A closed equation for F can be obtained by expanding the self energy,

$$\Sigma^r(E + \hbar\omega l) = \Sigma^r(E) + \sum_{n=1}^{\infty} \frac{1}{n!} (\hbar\omega l)^n \frac{\partial^n \Sigma^r}{\partial E^n}. \quad (4.44)$$

Assuming that we work around the wide band limit and using Eq.(4.36) (evaluated at energy $E + \hbar\omega l/2$), we obtain up to first order in the derivative of $\Sigma^r(E)$,

$$F + \hbar\omega z F_{ad} \left[1 - \frac{\partial \Sigma^r}{\partial E} \right] \frac{\partial F}{\partial z} = F_{ad} \quad (4.45)$$

with

$$F_{ad} = \frac{1}{E - H - \Sigma^r(E) - eV_{ac} \frac{W}{2} \left(z + \frac{1}{z} \right)}. \quad (4.46)$$

Note that F_{ad} corresponds to the adiabatic limit: when one evaluates F for a given time T (see Eq.(4.29)), $F_{ad}(e^{-i\omega T}, E)$ corresponds to the stationary retarded Green's function at energy E for the potential at time T , i.e. assuming that at a given time T , the potential varies so slowly that it can be considered as constant. Higher order terms can be obtained straightforwardly and correspond to higher derivatives of F . For instance, to second order, one should add the following to the left hand side of Eq.(4.45)

$$-\frac{(\hbar\omega)^2}{2}F_{ad}(z)\frac{\partial^2\Sigma^r}{\partial E^2}\left[z^2\frac{\partial^2 F}{\partial z^2}+z\frac{\partial F}{\partial z}\right]. \quad (4.47)$$

Equation (4.45) allows for a systematic calculation of F (and therefore the G_l), for instance by expanding it in powers of $\hbar\omega$. To first order we get,

$$F(e^{-i\omega T}) = F_{ad}(e^{-i\omega T}) - i\hbar F_{ad}(e^{-i\omega T})\left[1 - \frac{\partial\Sigma^r}{\partial E}\right]\frac{\partial F_{ad}}{\partial T}. \quad (4.48)$$

And higher orders are obtained straightforwardly. We emphasize that in the adiabatic limit the processes contain a (arbitrary) large number of absorbed/emitted photons, hence the role of the generating function which reflects the idea of working in an instantaneous basis being "natural" in this case¹. The resulting observables (the adiabatic current and the correction to it) are given in the cookbook section 3.3 and in Appendix A.

4.4 Perturbation in the leads

The formalism developed above can be extended to homogeneous perturbations in the leads. The algebra is very similar with one notable exception: multiple absorption/emission processes are now allowed. We suppose (for definiteness) that a bias voltage $V_{ac}\cos\omega t$ is applied to lead \bar{m}' , see Eq.(3.2).

4.4.1 Equation of motion

It is convenient to change the basis in the lead affected by the perturbation in order to move to a frame where the lead is stationary. The AC voltage then gives rise to a time-dependent phase factor in the coupling matrix between the lead and the device. This is easily seen with the help of the unitary transformation

$$\hat{U} = \exp\left[\frac{i}{\hbar}\int_0^t dt' eV_{ac}\cos(\omega t')\hat{N}\right], \hat{N} = \sum_{i\in\sigma_m} c_\alpha^\dagger c_\alpha. \quad (4.49)$$

¹Note that if instead of Wigner coordinates in Eq.(4.29) we use $T = t$ and $\tau = t - t'$ (see Ref.[66] and references therein), then Eq.(4.43) is transformed as: $F(z, E) = \sum_{l=-\infty}^{\infty} z^l G_l(E)$. If we take $z = \exp(-i\omega T)$ and compare this to Eq.(4.29), we see that the generating function is nothing else than a Fourier transform of the Green's function with respect to the time difference τ only.

The Hamiltonian after the transformation refers to the old one,

$$\mathbf{H}' = \hat{U} \mathbf{H} \hat{U}^\dagger - i\hbar \hat{U} \frac{\partial \hat{U}^\dagger}{\partial t}.$$

Then, it consists of

$$\mathbf{H}'(t) = \mathcal{H} + \mathcal{V}(t), \quad (4.50)$$

where \mathcal{H} is the Hamiltonian of the leads and device (when they are decoupled) and,

$$\mathcal{V}(t) = \sum_{m=1}^M \sum_{\alpha \in \bar{m}, i \in \bar{0}} (\mathcal{V}_{\alpha i} e^{\frac{ieV_{ac}}{\hbar\omega} \sin \omega t} c_\alpha^\dagger c_i + \mathcal{V}_{i\alpha} e^{-\frac{ieV_{ac}}{\hbar\omega} \sin \omega t} c_i^\dagger c_\alpha) \quad (4.51)$$

is the *new* coupling between them. By doing this change of basis we are back to the situation where the leads are kept at (local) thermal equilibrium, whereas the effect of the perturbation is completely transferred to the coupling matrix between the latter and the scattering region. As a result, the self energies of lead \bar{m}' now acquire an additional phase factor,

$$\Sigma^\kappa(m'; t, t') = \Sigma^\kappa(m'; t - t') e^{-\frac{ieV_{ac}}{\hbar\omega} (\sin \omega t - \sin \omega t')}, \quad \kappa = r, a, <, \quad (4.52)$$

where $\Sigma^\kappa(m'; t - t')$ is the equilibrium self-energy (in the absence of the AC field). Expanding the phase factor in Eq.(4.52) in terms of Bessel functions,

$$e^{-\frac{ieV_{ac}}{\hbar\omega} \sin \omega t} = \sum_{n=-\infty}^{+\infty} J_n \left(\frac{eV_{ac}}{\hbar\omega} \right) e^{-i\omega n t},$$

the transformation (4.29) applied to the (perturbed) self-energy (4.52) gives

$$\Sigma_l^\kappa(m'; E) = \sum_{n=-\infty}^{\infty} J_{l+n} \left(\frac{eV_{ac}}{\hbar\omega} \right) J_n \left(\frac{eV_{ac}}{\hbar\omega} \right) \Sigma^\kappa \left(m'; E - \frac{\hbar\omega l}{2} - \hbar\omega n \right). \quad (4.53)$$

Finally, the equation of motion has the form

$$\begin{aligned} & \left(E + \frac{\hbar\omega l}{2} - H - \sum_{m \neq m'}^M \Sigma^r(m; E + \frac{\hbar\omega l}{2}) \right) G_l^r(E) \\ & - \sum_{l_1=-\infty}^{\infty} \Sigma_{l_1}^r \left(m'; E + \frac{\hbar\omega}{2} (l - l_1) \right) G_{l-l_1}^r \left(E - \frac{\hbar\omega l_1}{2} \right) = \delta_{l,0}. \end{aligned} \quad (4.54)$$

This equation is the starting point for the approximation schemes considered below.

4.4.2 Limit of a small perturbation amplitude

Let us now expand $G_l^r(E)$ in powers of $(eV_{ac}/\hbar\omega) \ll 1$,

$$G_l^r(E) = \sum_{n=0}^{\infty} \left(\frac{eV_{ac}}{\hbar\omega} \right)^n G_l^{(n)}(E). \quad (4.55)$$

The first order result can be obtained by a direct expansion of Eq.(4.53),

$$\begin{aligned} \Sigma_l^\kappa(m'; E) &= \Sigma^\kappa(m'; E)\delta_{l,0} + \frac{eV_{ac}}{2\hbar\omega} \left[\Sigma^\kappa(m'; E - \frac{\hbar\omega}{2}) - \Sigma^\kappa(m'; E + \frac{\hbar\omega}{2}) \right] \delta_{l,1} \\ &+ \frac{eV_{ac}}{2\hbar\omega} \left[\Sigma^\kappa(m'; E - \frac{\hbar\omega}{2}) - \Sigma^\kappa(m'; E + \frac{\hbar\omega}{2}) \right] \delta_{l,-1} + O(e^2V_{ac}^2), \quad \kappa = r, a, <, \end{aligned} \quad (4.56)$$

where we used the power series representation of Bessel functions. Utilizing the notation introduced in Eq.(3.45), we obtain

$$G_l^{(0)}(E) = \left(\frac{1}{2}\right)^0 \delta_{l,0} \mathcal{G}_0, \quad (4.57)$$

$$G_l^{(1)}(E) = \left(\frac{1}{2}\right)^1 \left[\delta_{l,-1} \mathcal{G}_{-1} \Lambda_{m'}^{rr} \left(E - \frac{\hbar\omega}{2}; E + \frac{\hbar\omega}{2}\right) \mathcal{G}_1 + \delta_{l,1} \mathcal{G}_1 \Lambda_{m'}^{rr} \left(E - \frac{\hbar\omega}{2}; E + \frac{\hbar\omega}{2}\right) \mathcal{G}_{-1} \right]. \quad (4.58)$$

which is similar to expressions (4.40) and (4.41).

In analogy with the case of internal perturbations, a systematic diagrammatic expansion can be constructed. The set of rules to obtain all the contributions to $G_l^{(n)}(E)$ is given by,

- Draw all diagrams with $1 \leq p \leq n$ wavy lines. Contrary to the previous case, the wavy lines now point both up *and* down (see Fig. 4.2, for example), reflecting the possibility of multiple absorption and emission processes. Each wavy line i is associated with two positive integers n_i^a and n_i^e ($n_i^e + n_i^a \geq 1$) that correspond to the two types of processes. We have

$$n = \sum_{i=1}^p (n_i^e + n_i^a), \quad (4.59)$$

$$l = \sum_{i=1}^p (n_i^e - n_i^a). \quad (4.60)$$

- Read the diagram from left to right. Starting from $\mathcal{G}_l(E)$, each wavy line corresponds to a factor $T_{n_i^a, n_i^e}^l$ (see below) followed by another $\mathcal{G}_{l'}(E)$ with $l' = l + 2(n_i^a - n_i^e)$ (n_i^e "photons" are emitted and n_i^a are absorbed). Repeat until the end of the diagram.
- The "vertex" is defined as

$$T_{n_i^a, n_i^e}^l = \frac{1}{2^{n_i^e + n_i^a}} \frac{1}{n_i^e! n_i^a!} \Delta_{m'}^{n_i^e + n_i^a} \left(E + \frac{\hbar\omega}{2} [l + n_i^a - n_i^e] \right), \quad (4.61)$$

with the matrix $\Delta_{m'}^q(E)$ given by

$$\Delta_{m'}^q(E) = \sum_{i=0}^{q-1} (-1)^i \binom{q-1}{i} \Lambda_{m'}^{rr} \left(E + (2i - q) \frac{\hbar\omega}{2}; E + (2i + 2 - q) \frac{\hbar\omega}{2} \right), \quad (4.62)$$

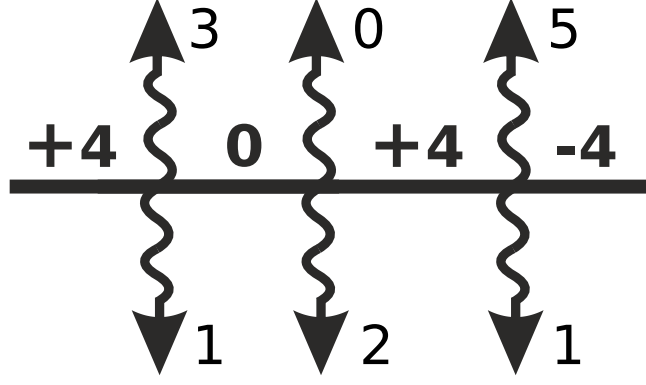


Figure 4.2: Example of a diagram that contributes to $G_4^{(12)}(E)$. Each diagram is characterized by the set of upper and lower numbers which correspond respectively to the number of emitted and absorbed photons. The numbers along the horizontal line are calculated from the diagrammatic rules.

where $\binom{q}{i}$ is the binomial coefficient. As an example, Fig. 4.2 corresponds to one contribution to the 12-th order with $l = 4$, namely $G_4^{(12)}(E)$. Using the above rules, this diagram gives,

$$G_4^{(12)}(E) = \mathcal{G}_4 T_{1,3}^4 \mathcal{G}_0 T_{2,0}^0 \mathcal{G}_4 T_{1,5}^4 \mathcal{G}_{-4}, \quad (4.63)$$

where, according to Eq.(4.61),

$$T_{1,3}^4 = \frac{1}{2^4 3!} [\Lambda_{m'}^{rr}(E - \hbar\omega; E) - 3\Lambda_{m'}^{rr}(E; E + \hbar\omega) + 3\Lambda_{m'}^{rr}(E + \hbar\omega; E + 2\hbar\omega) - \Lambda_{m'}^{rr}(E + 2\hbar\omega; E + 3\hbar\omega)], \quad (4.64)$$

$$T_{2,0}^0 = \frac{1}{2^2 2!} [\Lambda_{m'}^{rr}(E; E + \hbar\omega) - \Lambda_{m'}^{rr}(E + \hbar\omega; E + 2\hbar\omega)], \quad (4.65)$$

$$T_{1,5}^4 = \frac{1}{2^6 5!} [\Lambda_{m'}^{rr}(E - 3\hbar\omega; E - 2\hbar\omega) - 5\Lambda_{m'}^{rr}(E - 2\hbar\omega; E - \hbar\omega) + 10\Lambda_{m'}^{rr}(E - \hbar\omega; E) - 10\Lambda_{m'}^{rr}(E; E + \hbar\omega) + 5\Lambda_{m'}^{rr}(E + \hbar\omega; E + 2\hbar\omega) - \Lambda_{m'}^{rr}(E + 2\hbar\omega; E + 3\hbar\omega)]. \quad (4.66)$$

We see that in contrast to the case when the perturbation was inside the scattering region, multiple-photon absorption/emission processes are allowed. This fact can be also understood from the concept of the *sidebands* (with energy shifted with respect to the Fermi level by an amount $\pm n\hbar\omega$) which have been introduced in the context of AC scattering theory [12, 74, 17].

4.4.3 Adiabatic limit and beyond

Finally, we consider the adiabatic limit following a similar procedure to the one presented in Section 4.3.2. The procedure is very similar except for the expansion of the self energy of the

lead under AC perturbation. The general expansion of Eq.(4.53) reads,

$$\begin{aligned} \Sigma_{l_1}^r \left(m'; E + \frac{\hbar\omega}{2}(l - l_1) \right) &= \sum_{k=0}^{\infty} \frac{1}{k!} \left(\frac{\hbar\omega}{2} \right)^k \frac{\partial^k \Sigma^r(m'; E)}{\partial E^k} \\ &\times \sum_{n=-\infty}^{\infty} (l - 2l_1 - 2n)^k J_{l_1+n} \left(\frac{eV_{ac}}{\hbar\omega} \right) J_n \left(\frac{eV_{ac}}{\hbar\omega} \right). \end{aligned} \quad (4.67)$$

which, using the following two identities for Bessel functions,

$$\sum_{n=-\infty}^{\infty} J_{n+l}(x) J_n(x) = \delta_{l,0}, \quad (4.68)$$

$$\frac{2n}{x} J_n(x) = J_{n-1}(x) + J_{n+1}(x), \quad (4.69)$$

allows to obtain the self energy to any value of k . Restricting to first order, we get

$$\begin{aligned} \Sigma_{l_1}^r \left(m'; E + \frac{\hbar\omega}{2}(l - l_1) \right) &\approx \delta_{l_1,0} \left[\Sigma^r(m'; E) + \frac{\hbar\omega l}{2} \frac{\partial \Sigma^r(m'; E)}{\partial E} \right] \\ &- \frac{eV_{ac}}{2} (\delta_{l_1,1} + \delta_{l_1,-1}) \frac{\partial \Sigma^r(m'; E)}{\partial E}. \end{aligned} \quad (4.70)$$

This expansion corresponds to the wide-band limit ($k = 0$) [13, 9] and its first correction ($k = 1$). It is expected to be very accurate in metallic leads, for instance. At this level, we introduce again the generating function $F(z)$, Eq.(4.43), and obtain the same equation (4.45) as for the internal perturbation case provided one replaces W by $[-\partial \Sigma^r(m'; E)/\partial E]$. The corresponding results can hence be adapted to this case straightforwardly. Note that beyond this first order ($k \geq 2$ in Eq.(4.67)) a closed equation can also be obtained, but this simple replacement rule does not apply anymore.

4.5 Conclusions

Numerical simulations of quantum transport has become an ubiquitous tool for mesoscopic physics and are more and more commonly used to help the design of nanoelectronic devices. On the other hand there is a general trend of mesoscopic physics and microelectronics towards GHz or even higher frequencies, so that developing a general framework to tackle finite frequency transport is becoming of increasing importance. In this chapter we have developed the corresponding formalism allowing to derive a large set of formulas that express AC observables in terms of numerically accessible quantities. We provide systematic rules to construct other expressions that we did not give explicitly. Hence, our formalism can either be used as a recipe book for extending DC numerical tools to AC, or as a starting point for further developments.

Part II

Quantum transport in a graphene-based topological insulator

During the last decade both exotic states of matter and low-dimensional nanostructures gained considerable attention because of a big progress in device fabrication and characterization techniques. Small nano- and mesoscale structures are used to observe various quantum interference and many-body effects, which are invisible at the macroscale. Conventional quantum dots and nanowires as well as all commercial electronic devices are made of semiconducting materials, such as Si, Ge, GaAs, etc. However, a lot of effort has been put into discovering alternative materials which could open up new avenues in nanoelectronics.

In this part of the thesis we will discuss electronic and transport properties of a real two-dimensional material, graphene, which only recently was discovered experimentally [75, 76], though theoretical works existed long before it [77, 78, 79, 80]. In 2010 Nobel Prize in Physics was awarded to Andre Geim and Konstantin Novoselov from the University of Manchester (UK) "for groundbreaking experiments regarding the two-dimensional material graphene". Graphene is a mono-atomic layer of graphite. It owes its fascinating properties to its hexagonal lattice structure. In six corners of the Brillouin zone, the so-called K points, valence band and conduction band touch each other making graphene a zero gap semiconductor. It turns out that in the vicinity of the K points low-energy excitations in graphene are massless Dirac quasiparticles [76]. This feature made graphene a hot topic since its discovery, and now it is a mature branch of condensed matter research. The second feature which made it one of the leading subjects nowadays is the (anomalous) quantum Hall effect. In contrast to conventional two-dimensional electron gases (2DEG) in semiconducting heterostructures, where Landau level sequence is $\epsilon_n \propto (n + 1/2)$, Landau levels in graphene are not equidistant and do not have 1/2 offset, $\epsilon_n^{gr} \propto \pm\sqrt{n}$. Thus, Hall plateaus in graphene appear at half integer filling factors [76]. This is a direct consequence of relativistic nature of its low-energy excitations. At the same time, longitudinal conductivity has a phase shift π in the Shubnikov-de Haas oscillations compared to 2DEG, which is the manifestation of a non-zero Berry's phase [76].

Topological insulators (TIs) are materials which are insulating in the bulk but possess conducting states on their surfaces/edges depending on the dimensionality [81, 23, 24, 82, 83, 84]. These states at the boundaries are said to be protected by the time-reversal symmetry (TRS) preventing them from backscattering, which makes TIs particularly interesting. Existence of the metallic surface states is a consequence of a bulk band structure topology. They cannot be eliminated by any smooth perturbation of the Hamiltonian unless the TRS is broken. Whereas examples of three-dimensional TIs have been found to abound in Nature, two-dimensional systems having similar properties are so far limited to HgTe/CdTe heterostructures which only a few experimental groups in the world can synthesize.

In the following chapters we will see how properties of graphene are modified in the presence of spin-orbit (SO) interaction [25]. SO interaction is a tiny effect in pristine graphene, while it would open a way to much richer physical phenomena (such as the quantum spin Hall effect

[23], for example), if there was a way to substantially enhance it. There was a proposal for possible solution to this problem [26]. Namely, we will see that a certain type of heavy atoms when deposited on graphene's surface could give rise to a significant SO coupling.

It turns out that graphene might become a TI provided a large enough SO coupling is induced [24, 23]. In the topologically non-trivial phase graphene structure with edges possesses spin filtered edge states at its boundaries. At a given edge, there is a pair of states counter-propagating each other. Thus, there is no net charge current along the edge, but a non-zero spin current. This effect is called the quantum spin Hall effect in literature [23].

This part of the thesis is organized as follows. First, in Chapter 5 we give a general introduction to graphene. Starting from the crystal structure we build the simplest tight-binding model capturing its main properties. Further in this Chapter we derive a continuous effective model valid in the vicinity of K points. Finally, in Section 5.3 we recall briefly the main properties of graphene ribbons. Then, in Chapter 6 we discuss properties of graphene in a strong magnetic field. We derive the spectrum of Landau levels and then review main features of the quantum Hall effect in graphene ribbons. Chapter 7 is devoted to the effects of spin-orbital interactions in graphene. Starting from a microscopic model of SO coupling in pristine graphene, we recall the Kane-Mele model of the quantum spin Hall effect [23]. At the root of understanding the latter are the topological properties of graphene in the presence of SO interaction, which are discussed in the end of this Chapter. The material presented in the last two Chapters contains our original work, which was published in Refs.[27, 60]. More specifically, in Chapter 8 we review the proposal of Weeks *et al.* [26] to enhance the SO coupling in graphene by functionalizing it with a certain type of adatoms. This follows by a detailed discussion of experimentally relevant case of randomly deposited atoms on the graphene's surface. We find that the non-uniformly covered graphene can be mapped onto the fully covered case by simply renormalizing the strength of the SO interaction by the density of adatoms. In Chapter 9 we investigate the properties of the topological (quantum spin Hall) phase in graphene in the external magnetic field. One could think that the topological order is broken in this case, however we find that due to the relativistic nature of quasiparticles in graphene, one can observe features of both quantum Hall and quantum spin Hall effects by simply varying the Fermi level. Finally, we use this feature by investigating a heterojunction between the QH and QSH phases in a 4-terminal geometry. Here, one part of the system is kept in the QSH phase, while another one, thanks to the electric gate, can be in one of the two: QH or QSH. Whenever two distinct phases meet, there is a chiral state at the interface, which is quite similar to the interface states in the n - n' and n - p junctions in graphene. This Chapter (and the second part of the thesis) ends up with conclusions 9.5

Chapter 5

Introduction to the physics of graphene

In this chapter we'll give a general introduction to the physics of graphene. We will show that the peculiar lattice structure is responsible for the remarkable properties of this material. At first we will introduce a tight-binding model describing electronic properties of graphene. It turns out that the low-energy physics of graphene (in the vicinity of K points) is well described within the first nearest neighbors approximation. This is the case we are interested in. However it is necessary to take into account influence of up to the third nearest neighbors in the tight-binding Hamiltonian to get good agreement with *ab initio* simulations in other parts of the Brillouin zone. Secondly, we demonstrate that at low energies an effective continuous model can be introduced and quasiparticles in graphene are described by a massless Dirac equation with linear dispersion. At the end of this chapter we discuss electronic properties of graphene ribbons, quasi-one-dimensional strips of graphene.

5.1 Crystal lattice and band structure

In order to understand the crystallographic structure of graphene and carbon-based materials in general, it is useful to review the basic chemical bonding properties of carbon atoms. The carbon atom possesses 6 electrons, which, in the atomic ground state, are in the configuration $1s^2 2s^2 2p^2$, i.e. 2 electrons fill the inner shell 1s, which is close to the nucleus and which is irrelevant for chemical reactions, whereas 4 electrons occupy the outer shell of 2s and 2p orbitals. Because the 2p orbitals ($2p_x$, $2p_y$, and $2p_z$) are roughly 4 eV higher in energy than the 2s orbital, it is energetically favorable to put 2 electrons in the 2s orbital and only 2 of them in the 2p orbitals (see Fig. 5.1). It turns out, however, that in the presence of other atoms, such as e.g. H, O, or other C atoms, it is favorable to excite one electron from the 2s to the third 2p orbital, in order to form covalent bonds with the other atoms.

In the excited state, we therefore have four equivalent quantum-mechanical states, $|2s\rangle$, $|2p_x\rangle$, $|2p_y\rangle$, and $|2p_z\rangle$. A quantum-mechanical superposition of the state $|2s\rangle$ with n $|2p_j\rangle$

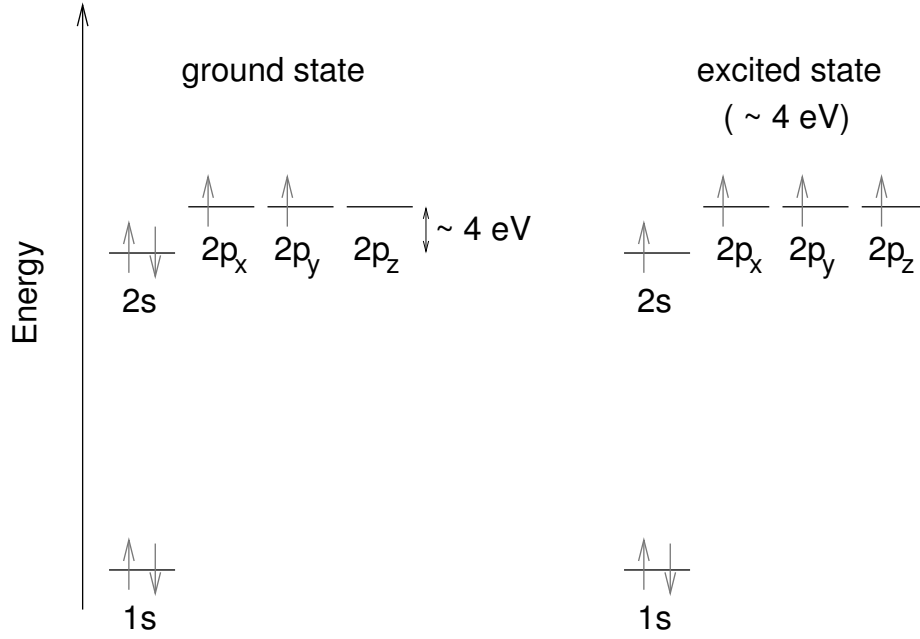


Figure 5.1: Electronic configurations for carbon in the ground state (left) and in the excited state (right). Adapted from [85].

states is called sp^n hybridization. The sp^1 hybridization plays, e.g., an important role in the context of organic chemistry (such as the formation of acetylene) and the sp^3 hybridization gives rise to the formation of diamonds, a particular 3D form of carbon. Here, however, we are interested in the planar sp^2 hybridization, which is the basic ingredient for the graphitic allotropes. In this case $|2s\rangle$ states hybridize with $|2p_x\rangle$ and $|2p_y\rangle$ forming the so-called σ bonds. They lie in one plane and are responsible for strong coupling between the neighboring carbon atoms. The non-hybridized $|2p_z\rangle$ orbitals lie in the perpendicular plane and give rise to the weak coupling between the σ -bonded layers. In literature this type of bonds is called π bonds.

Graphene is a two-dimensional one atom thick planar sheet of sp^2 -bonded carbon atoms densely packed in a honeycomb lattice, see Fig. 5.2. Since honeycomb lattice is not a Bravais lattice, it consists of two triangular Bravais lattices shifted with respect to each other. Primitive translation vectors on each sublattice are (see Fig. 5.2),

$$\mathbf{a}_1 = \sqrt{3}a_{c-c} \begin{pmatrix} 1 \\ 0 \end{pmatrix}, \quad \mathbf{a}_2 = \frac{\sqrt{3}a_{c-c}}{2} \begin{pmatrix} 1 \\ \sqrt{3} \end{pmatrix}. \quad (5.1)$$

The reciprocal space is spanned by the vectors

$$\mathbf{b}_1 = \frac{2\pi}{3a_{c-c}} \begin{pmatrix} \sqrt{3} \\ -1 \end{pmatrix}, \quad \mathbf{b}_2 = \frac{4\pi}{3a_{c-c}} \begin{pmatrix} 0 \\ 1 \end{pmatrix}. \quad (5.2)$$

Thus, an elementary cell of graphene consists of two nonequivalent atoms denoted as A and B in literature and referred to as *pseudospin*. It means that the wave function of a Bloch

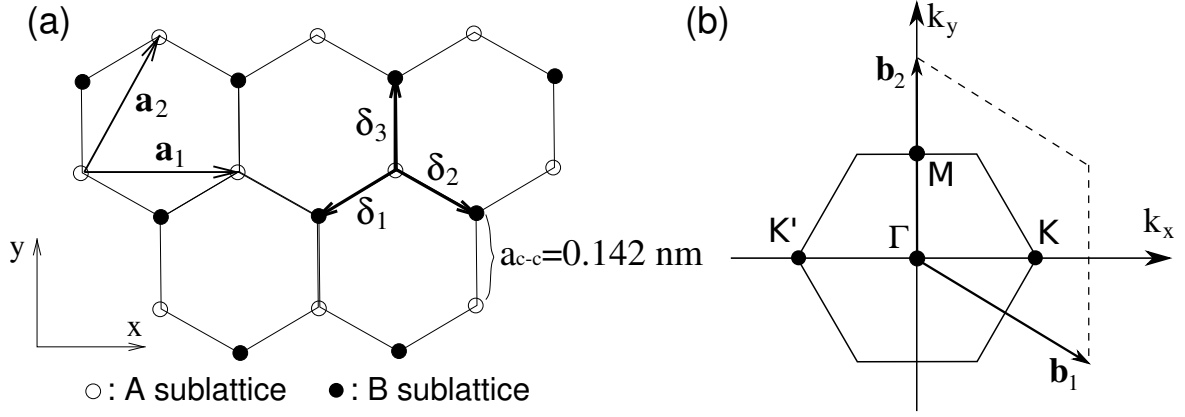


Figure 5.2: Honeycomb lattice and its Brillouin zone. (a): Lattice structure of graphene, made out of two interpenetrating triangular lattices (\mathbf{a}_1 and \mathbf{a}_2 are the lattice unit vectors; and δ_i , $i = 1, 2, 3$ are the nearest neighbor vectors); (b): corresponding Brillouin zone. \mathbf{b}_1 and \mathbf{b}_2 are reciprocal unit vectors. Big letters K, Γ, M denote high symmetry points in the Brillouin zone. The Dirac cones are located at the K and K' points, see Fig. 5.6.

electron is a spinor having two components. We also define the nearest neighbor vectors δ_i , which will be used further in this section,

$$\delta_1 = \frac{a_{c-c}}{2} \begin{pmatrix} -\sqrt{3} \\ -1 \end{pmatrix}, \quad \delta_2 = \frac{a_{c-c}}{2} \begin{pmatrix} \sqrt{3} \\ -1 \end{pmatrix}, \quad \delta_3 = a_{c-c} \begin{pmatrix} 0 \\ 1 \end{pmatrix}. \quad (5.3)$$

As was shown by first principles calculations [80], the energy bands coming from σ bonds lie much higher in energy than those from π bonds (see Fig. 5.3). This means that for energies $|E| \lesssim 3\text{eV}$ it is enough to take into account only π bonds, i.e. $|2p_z\rangle$ orbitals. They define completely the band structure and electronic properties of graphene. Thus, we will elaborate a tight-binding model on a honeycomb lattice with one orbital per site.

If $|\phi(\mathbf{r})\rangle$ is the normalized orbital $|2p_z\rangle$ wave function for an isolated carbon atom, then the wave function of graphene has the form

$$|\Psi\rangle = C_A|\psi_A\rangle + C_B|\psi_B\rangle, \quad (5.4)$$

where

$$|\psi_A\rangle = \frac{1}{N} \sum_A e^{i\mathbf{k}\cdot\mathbf{R}_A} |\phi(\mathbf{r} - \mathbf{R}_A)\rangle, \quad (5.5)$$

and

$$|\psi_B\rangle = \frac{1}{N} \sum_B e^{i\mathbf{k}\cdot\mathbf{R}_B} |\phi(\mathbf{r} - \mathbf{R}_B)\rangle. \quad (5.6)$$

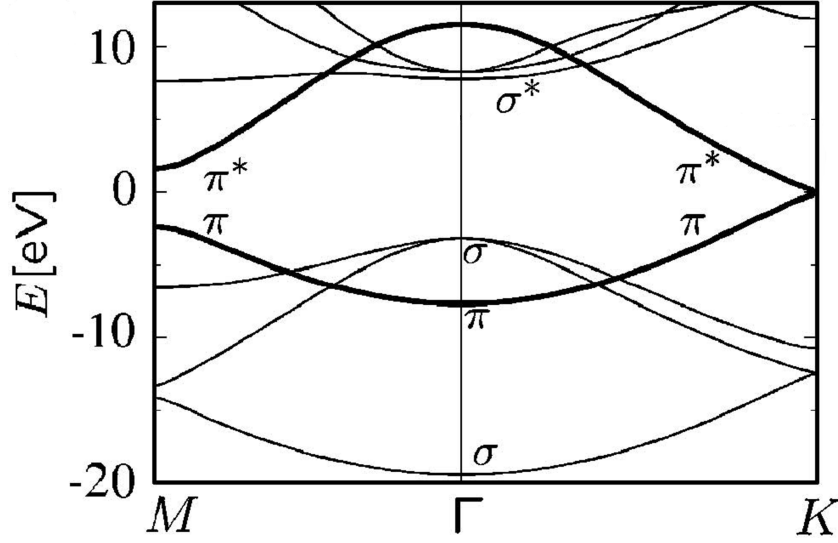


Figure 5.3: Band structure of graphene from *ab initio* calculations. One can clearly see that at low energies, electronic properties of graphene are determined by the π bands (thick lines). Adapted from [86].

The summations are performed over all lattice points belonging to A or B sublattices, N is the number of unit cells in a graphene sheet. Coefficients $C_{A,B}$ are to be determined from the Schrödinger equation for the full wave function,

$$H|\Psi\rangle = E|\Psi\rangle. \quad (5.7)$$

Carrying out a simple derivation, we come to the following secular equation [87, 88],

$$\begin{vmatrix} H_{AA}(\mathbf{k}) - E(\mathbf{k})S_{AA} & H_{AB}(\mathbf{k}) - E(\mathbf{k})S_{AB} \\ H_{AB}^*(\mathbf{k}) - E(\mathbf{k})S_{AB}^* & H_{AA}(\mathbf{k}) - E(\mathbf{k})S_{AA} \end{vmatrix} = 0, \quad (5.8)$$

where $H_{ij} = \langle \psi_i | H | \psi_j \rangle$ – Hamiltonian matrix elements, $S_{ij} = \langle \psi_i | \psi_j \rangle$ – elements of the overlap matrix. To write down Eq.(5.8) we have used the equivalence of the A and B atoms. Now this is time to make assumptions and approximations. The band structure of graphene has been studied extensively both within TB model and by means of *ab initio* simulations [77, 79, 86, 89, 87, 90]. The simplest model that works well at low energies is the first nearest neighbor tight-binding model. We will describe it here. Let us assume that the orbitals on neighboring sites weakly overlap and we can take into account only matrix elements of the Hamiltonian between the orbitals residing on the same lattice point or on the nearest surrounding (the smallest circle around atom 0 on Fig. 5.4). Another simplification we are going to use is to neglect the overlap matrix elements between A and B atoms, taking $S_{ij} = \delta_{i,j}$. Thus, the remaining

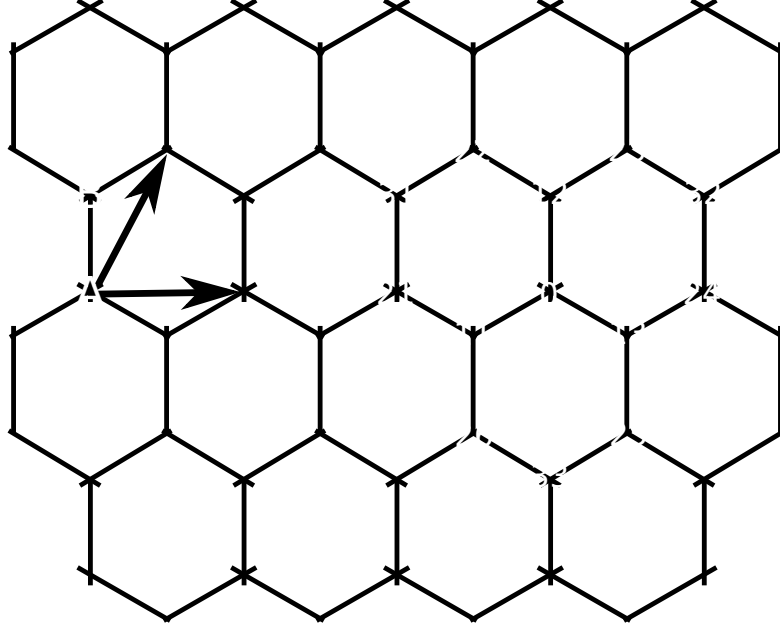


Figure 5.4: A piece of graphene. Arrows indicate the lattice unit vectors. Dashed circles are used to show the first, second and third coordination spheres of a carbon atom A_0 (denoted by 0 and belongs to the A sublattice). The atom A_0 is surrounded by three first nearest neighbors B_{1i} , six second nearest neighbors A_{2i} , and three third nearest neighbors B_{3i} .

non-zero parameters that we keep are the following,

$$H_{AB} = \frac{1}{N} \sum_{A,B} e^{i\mathbf{k}\cdot(\mathbf{R}_B-\mathbf{R}_A)} \langle \phi(\mathbf{r}-\mathbf{R}_A) | \mathbf{H} | \phi(\mathbf{r}-\mathbf{R}_B) \rangle = -t (e^{i\mathbf{k}\cdot\boldsymbol{\delta}_1} + e^{i\mathbf{k}\cdot\boldsymbol{\delta}_2} + e^{i\mathbf{k}\cdot\boldsymbol{\delta}_3}), \quad (5.9)$$

$$H_{AA} = \frac{1}{N} \sum_{A,A'} e^{i\mathbf{k}\cdot(\mathbf{R}_{A'}-\mathbf{R}_A)} \langle \phi(\mathbf{r}-\mathbf{R}_A) | \mathbf{H} | \phi(\mathbf{r}-\mathbf{R}_{A'}) \rangle = \epsilon, \quad (5.10)$$

where we have introduced the parameters ϵ and t defined as

$$\epsilon = \langle \phi(\mathbf{r}-\mathbf{R}_A) | \mathbf{H} | \phi(\mathbf{r}-\mathbf{R}_A) \rangle, \quad (5.11)$$

$$t = -\langle \phi(\mathbf{r}-\mathbf{R}_A) | \mathbf{H} | \phi(\mathbf{r}-\mathbf{R}_A-\boldsymbol{\delta}_i) \rangle, \quad i = 1, 2, 3. \quad (5.12)$$

Thus, the band structure of bulk graphene according to Eq.(5.8) is given by

$$E(\mathbf{k}) = \epsilon \pm t|f(\mathbf{k})|, \quad (5.13)$$

$$f(\mathbf{k}) = e^{i\mathbf{k}\cdot\boldsymbol{\delta}_1} + e^{i\mathbf{k}\cdot\boldsymbol{\delta}_2} + e^{i\mathbf{k}\cdot\boldsymbol{\delta}_3}. \quad (5.14)$$

Now we use the fact that $\boldsymbol{\delta}_2 - \boldsymbol{\delta}_1 = \mathbf{a}_1$ and $\boldsymbol{\delta}_3 - \boldsymbol{\delta}_1 = \mathbf{a}_2$ (see Fig. 5.4) to write down

$$E(\mathbf{k}) = \epsilon \pm t \sqrt{1 + 4 \cos \frac{\sqrt{3}a_{c-c}k_x}{2} \cos \frac{3a_{c-c}k_y}{2} + 4 \cos^2 \frac{\sqrt{3}a_{c-c}k_x}{2}}. \quad (5.15)$$

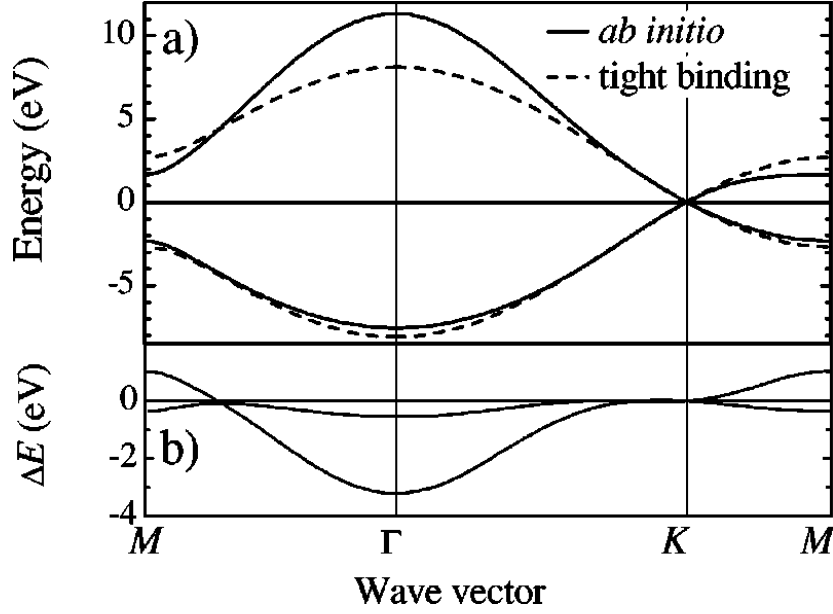


Figure 5.5: Ab initio and nearest-neighbor tight-binding dispersions of graphene. (a): The *ab initio* calculation of the graphene electronic bands is shown by the full lines. The dashed lines represent the tight-binding dispersion (5.15) with $\epsilon = 0$ and $t = 2.7$ eV. (b): Difference ΔE between the *ab initio* and tight-binding band structures. Adapted from [87].

Still we have to find the parameters ϵ and t . The way to find them is to do first principles calculations and then do a mapping of those results onto our simplified model at high symmetry points (K , M , Γ). Since we are interested in the low-energy properties, we do a mapping at the K point and the results of both *ab initio* and our effective descriptions are depicted on Fig. 5.5. Thus we find that $\epsilon = 0$ and $t = 2.7$ eV [87]. To summarize our findings it is convenient to write down the built above effective model in the second quantized form. So, the simplest model of graphene is defined by the nearest neighbor tight-binding Hamiltonian,

$$\hat{H} = -t \sum_{\substack{\langle i,j \rangle \\ i \neq j}} c_i^\dagger c_j, \quad (5.16)$$

where c_i and c_i^\dagger are creation and annihilation operators of an electron on a lattice site \mathbf{R}_i ($i = A$ or B); $\langle i, j \rangle$ means that the hopping is allowed only to the nearest neighbors (small circle around site 0 on Fig. 5.4). Now let us show the full tight-binding spectrum of graphene (5.15) in the first Brillouin zone, see Fig. 5.6. We notice that the spectrum is symmetric with respect to the plane $E = 0$, which is the Fermi level. There are six zero energy (K) points (only two of them are non-equivalent) in the Brillouin zone, where the valence and the conduction bands touch each other. Thus, graphene is a zero gap semiconductor, which is the reason of its fascinating properties. In the next section we will construct an effective continuous model of

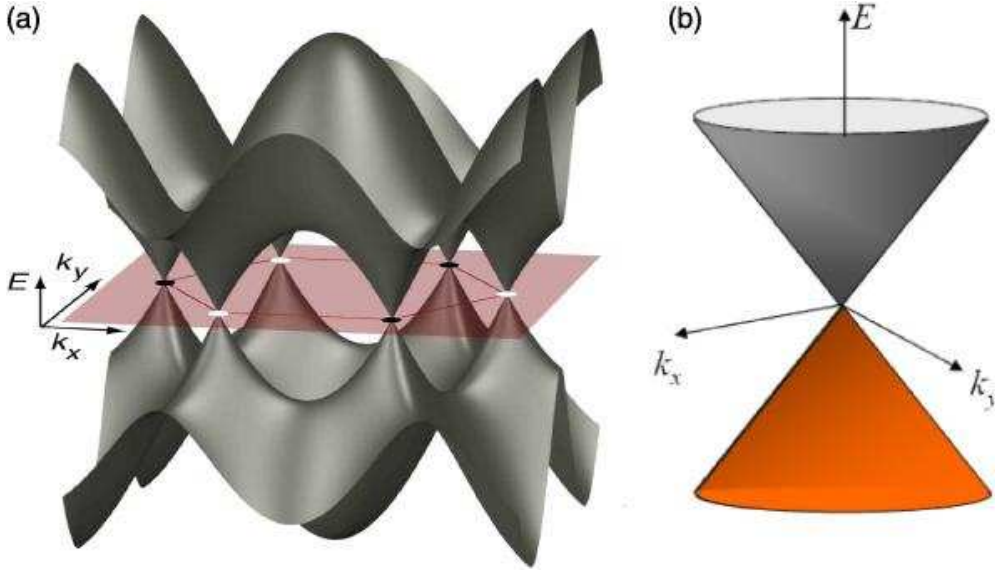


Figure 5.6: (a): Three-dimensional band structure of graphene, see Eq.(5.15). At six corners of the Brillouin zone (K points) the conduction band and the valence band touch each other. (b): Zoom into low energy dispersion at one of the K points shows the electron-hole symmetric Dirac cone structure. Adapted from [91]

graphene in the vicinity of its K points and show that it is described by a massless relativistic Dirac equation. Graphene gained its popularity during the last decade thanks to this feature.

In the derivation above we considered that the effects from overlapping between neighboring orbitals as well as the next nearest hopping are negligible. However if one wants to get a much better agreement with the *ab initio* results, it is necessary to consider the terms up to third nearest neighbors when constructing an effective tight-binding model as well as non-zero overlap between $|2p_z\rangle$ orbitals on different lattice points [87, 88, 92, 85]. In that case the spectrum loses the electron-hole symmetry and the chemical potential has a non-zero offset [92].

5.2 Low-energy (Dirac) effective description

Now we will build an effective model of graphene in the vicinity of zero-energy points. To do this, we first choose two non-equivalent K points that we will call K and K' in the following sections. Parts of the Brillouin zone around these points are called *valleys*. We will use this term further. They are defined as,

$$\mathbf{K} = \frac{4\pi}{3\sqrt{3}a_{c-c}} \begin{pmatrix} 1 \\ 0 \end{pmatrix}, \quad \mathbf{K}' = -\mathbf{K}. \quad (5.17)$$

Then, we expand the energy dispersion (5.15) (with $\epsilon = 0$) in the vicinity of K and K' making the substitution

$$\mathbf{k} = \pm \mathbf{K} + \mathbf{q}, \quad |q_{x,y}a_{c-c}| \ll 0. \quad (5.18)$$

Omitting straightforward steps, we write down the final result

$$E(\mathbf{q}) = \pm \hbar v_F \sqrt{q_x^2 + q_y^2}, \quad v_F = \frac{3a_{c-c}t}{2\hbar}. \quad (5.19)$$

The quantity v_F has a dimension of velocity and is called *Dirac velocity*. It is analogous to the speed of light in the relativistic Dirac spectrum, however it is estimated to be 300 times smaller [76]. Now we are going to find the effective Hamiltonian characterized by the spectrum (5.19).

From the previous section we know that the Hamiltonian matrix H_{ij} (see equations (5.9) and (5.10)) has the form,

$$\begin{pmatrix} 0 & -tf(\mathbf{k}) \\ -tf^*(\mathbf{k}) & 0 \end{pmatrix}, \quad (5.20)$$

where $f(\mathbf{k})$ is defined in Eq.(5.14). Now, we can do the expansion of it around K and K'. Utilizing Eq.(5.3) and keeping only linear terms in $q_{x,y}a_{c-c}$ brings us to [85]

$$f^\pm(\mathbf{q}) \simeq e^{\mp i \frac{2\pi}{3}} (1 + i\mathbf{q} \cdot \boldsymbol{\delta}_1) + e^{\pm i \frac{2\pi}{3}} (1 + i\mathbf{q} \cdot \boldsymbol{\delta}_2) + 1 + i\mathbf{q} \cdot \boldsymbol{\delta}_3 = -\frac{3a_{c-c}}{2} (\pm q_x - iq_y), \quad (5.21)$$

where upper (lower) sign corresponds to K (K'). Then, the Hamiltonian can be written as,

$$H(\mathbf{q}) = \hbar v_F (\xi q_x \sigma_x + q_y \sigma_y), \quad (5.22)$$

where $\xi = \pm$ is a valley index, distinguishes between K and K'; $\sigma_{x,y,z}$ are Pauli matrices,

$$\sigma_x = \begin{pmatrix} 0 & 1 \\ 1 & 0 \end{pmatrix}, \quad \sigma_y = \begin{pmatrix} 0 & -i \\ i & 0 \end{pmatrix}, \quad \sigma_z = \begin{pmatrix} 1 & 0 \\ 0 & -1 \end{pmatrix}. \quad (5.23)$$

If we quantize the expression (5.22) substituting $\hbar q_{x,y} \rightarrow \hat{p}_{x,y} = -i\hbar \partial_{x,y}$, we obtain the operator we were seeking for,

$$\hat{H} = v_F (\tau_z \sigma_x \hat{p}_x + \sigma_y \hat{p}_y), \quad (5.24)$$

where we have used another type of Pauli matrices $\tau_{x,y,z}$ to denote the valley degree of freedom, i.e. the two K points. It has a form of a Dirac equation for massless relativistic particles with linear dispersion relation (5.19).

In particle physics, one defines the helicity of a particle as the projection of its spin onto the direction of propagation (momentum) [93],

$$\eta_{\mathbf{q}} = \frac{\mathbf{q} \cdot \boldsymbol{\sigma}}{|\mathbf{q}|}, \quad (5.25)$$

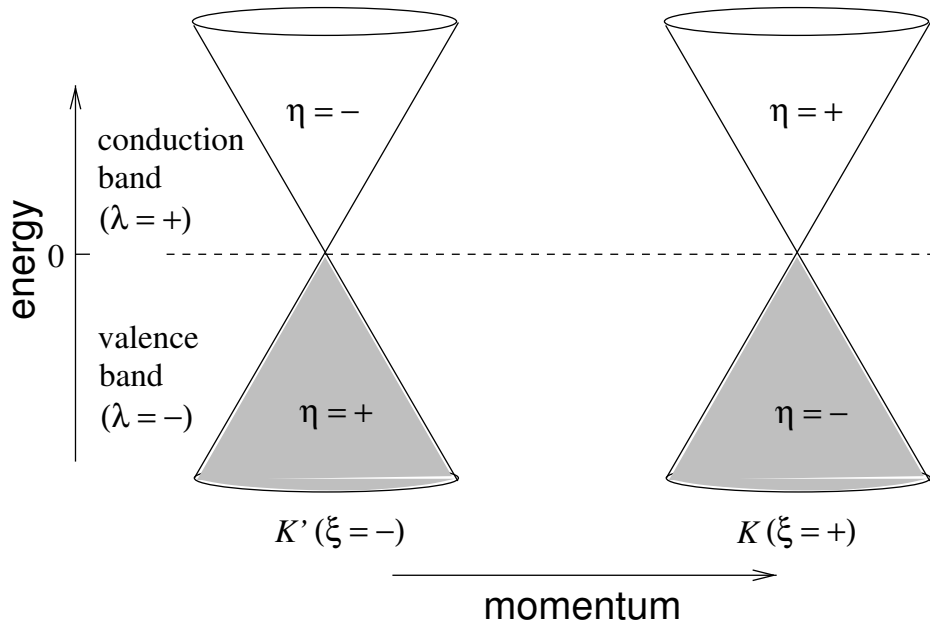


Figure 5.7: Relation between band index $\lambda = \xi\eta$, valley index ξ , and helicity η in graphene. Adapted from [85].

which is a Hermitian and unitary operator with the eigenvalues $\eta = \pm 1$, $\eta_{\mathbf{q}}|\eta = \pm\rangle = \pm|\eta = \pm\rangle$. Note that in our case the role of spin σ plays the pseudospin or a sublattice degree of freedom [85]. In the absence of a mass term, the helicity operator commutes with the Dirac Hamiltonian, and the helicity is therefore a good quantum number. The helicity is preserved in elastic scattering processes induced by impurity potentials that vary smoothly on the lattice scale. In this case, intervalley scattering is suppressed and the helicity is thus conserved [85], see Fig. 5.7. This effect gives rise to the absence of backscattering in graphene [94] and is at the origin of Klein tunneling, according to which a massless Dirac particle is fully transmitted, under normal incidence, through a high electrostatic barrier without being reflected [95].

In the end let us briefly discuss the corrections to our theory. When deriving equation (5.22), we kept only linear terms in the expansion of $f(\mathbf{k})$. Although most of the fundamental properties of graphene are captured within the effective model obtained at first order in the expansion, it might be useful to take into account second-order terms. These corrections include the next nearest neighbor hopping corrections and off-diagonal second-order contributions from the expansion of $f(\mathbf{k})$. The latter yield the so-called *trigonal warping*, which consists of an anisotropy in the energy dispersion around the Dirac points [85].

5.3 Graphene ribbons

In this section we discuss electronic properties of graphene ribbons, i.e. strips of graphene cut out of the 2D structure in a certain direction. In literature they commonly discuss two major types of edges, *armchair* and *zigzag* [96, 97, 92] (see Fig. 5.8). Any other type of edge can be thought of as a combination of those. In order to classify armchair graphene ribbons it is useful to characterize them by an integer M , counting the number of dimer lines (A-B pairs) along the width. Zigzag ribbons are characterized by the number N of zigzag lines (bold lines on Fig. 5.8b).

We will work in the continuous limit obtained in the previous section, though a full tight-binding description has been extensively studied in literature [97, 98, 89]. Band structure of the ribbons depends drastically on the type of the edge and on its width. We will see that zigzag ribbons are always semimetallic, i.e. they have no energy gap in their spectrum, while armchair ribbons can be both semiconducting and semimetallic. The latter is controlled by the width.

Let us formulate an eigenvalue problem to find the band structure and corresponding eigenstates of graphene ribbons. So, we have to solve the Schrödinger equation

$$H\Phi(\mathbf{r}) = E\Phi(\mathbf{r}), \quad (5.26)$$

where for clarity we write down explicitly the Hamiltonian (5.24) in the valley space,

$$H = -i\hbar v_F \begin{pmatrix} \sigma_x \partial_x + \sigma_y \partial_y & 0 \\ 0 & -\sigma_x \partial_x + \sigma_y \partial_y \end{pmatrix}, \quad (5.27)$$

and

$$\Phi(\mathbf{r}) = [\Phi_K(\mathbf{r}), \Phi_{K'}(\mathbf{r})]^T = [\Phi_A(\mathbf{r}), \Phi_B(\mathbf{r}), \Phi'_A(\mathbf{r}), \Phi'_B(\mathbf{r})]^T. \quad (5.28)$$

Here $\Phi_{K^{(\nu)}}$ is a spinor with two components $\Phi_{A,B}^{(\nu)}$ standing for scalar wavefunctions with different *pseudospin* or sublattice subscript, which is reminiscent of the initial tight-binding model (see Sec. 5.1). The total wavefunction containing the fast oscillations from the K-points is then

$$\Psi(\mathbf{r}) = \begin{pmatrix} \Psi_A(\mathbf{r}) \\ \Psi_B(\mathbf{r}) \end{pmatrix} = e^{i\mathbf{K}\cdot\mathbf{r}} \begin{pmatrix} \Phi_A(\mathbf{r}) \\ \Phi_B(\mathbf{r}) \end{pmatrix} + e^{i\mathbf{K}'\cdot\mathbf{r}} \begin{pmatrix} \Phi'_A(\mathbf{r}) \\ \Phi'_B(\mathbf{r}) \end{pmatrix}. \quad (5.29)$$

5.3.1 Armchair ribbons

We consider an armchair nanoribbon which is infinitely extended along the y-direction, see Fig. 5.8a. In order to find the band structure and wave functions we have to solve equation (5.26) supplemented by the appropriate boundary conditions. If we consider hard wall (or Dirichlet) boundary conditions we come to [97, 99]

$$\Psi(\mathbf{r}) = 0 \quad \text{for } x = 0 \text{ and } x = W. \quad (5.30)$$

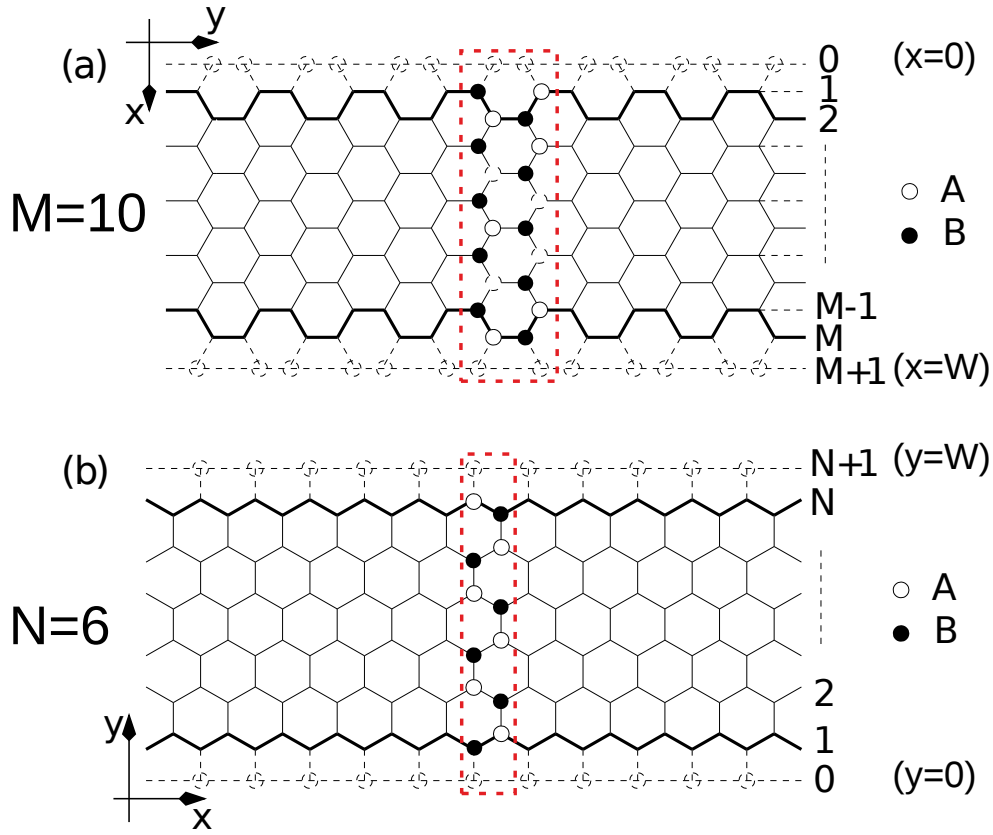


Figure 5.8: Sketch of graphene ribbons of width W with (a) armchair edges and (b) zigzag edges. M and N are integers characterizing the ribbon width. Row of non-existing atoms (dashed circles) with numbers 0 and (a) $M + 1$ and (b) $N + 1$ are shown to reflect corresponding boundary conditions. Red dashed rectangle represents a unit cell of the ribbon.

They follow from the corresponding hard wall boundary conditions of a discrete model. The wave function must vanish on the rows of non-existing atoms depicted by dashed lines on Fig. 5.8a. They contain atoms of both sublattices, which means that armchair boundary conditions (5.30) mix solutions from both valleys. Now we utilize the Bloch ansatz

$$\Phi(\mathbf{r}) = e^{ik_y y} \phi(x), \quad (5.31)$$

and obtain the equations

$$-i\hbar v_F (\partial_x + k_y) \phi_B(x) = E \phi_A(x), \quad (5.32)$$

$$-i\hbar v_F (\partial_x - k_y) \phi_A(x) = E \phi_B(x), \quad (5.33)$$

$$-i\hbar v_F (-\partial_x + k_y) \phi'_B(x) = E \phi'_A(x), \quad (5.34)$$

$$-i\hbar v_F (-\partial_x - k_y) \phi'_A(x) = E \phi'_B(x). \quad (5.35)$$

Grouping the first two and the last two equations together we find

$$(k_y^2 - \partial_x^2)\phi_B^{(j)}(x) = \left(\frac{E}{\hbar v_F}\right)^2 \phi_B^{(j)}(x). \quad (5.36)$$

We look for a solution as a combination of incoming and outgoing waves in the x -direction,

$$\phi_B(x) = Ae^{iq_n x} + Be^{-iq_n x}, \quad \phi_B'(x) = Ce^{iq_n x} + De^{-iq_n x}. \quad (5.37)$$

Thus we can deduce the band spectrum of a ribbon,

$$E = \pm \hbar v_F \sqrt{q_n^2 + k_y^2}, \quad (5.38)$$

where quantization of the transverse wave number q_n is found by satisfying the boundary conditions (5.30),

$$q_n = \frac{n\pi}{W} - K, \quad n \in \mathbb{Z} \quad (5.39)$$

Here $K = 4\pi/(3\sqrt{3}a_{c-c})$ is the x -component of K point. Therefore one has a semimetallic ribbon when there is a state $q_n = 0$. This happens when ribbon width satisfies the relation,

$$\frac{4W}{3\sqrt{3}a_{c-c}} \in \mathbb{N}. \quad (5.40)$$

For the eigenstates we find that $B = C = 0$ and $A = -D$. Using equations (5.32) and (5.34) to determine other components, we finally write (up to a normalization constant)

$$\phi(x) \propto \left[\frac{\hbar v_F(q_n - ik_y)}{E} e^{iq_n x}, e^{iq_n x}, -\frac{\hbar v_F(q_n - ik_y)}{E} e^{iq_n x}, -e^{iq_n x} \right]^T, \quad (5.41)$$

$$\Psi(\mathbf{r}) \propto e^{ik_y y} \sin[(q_n + K)x] \left[\frac{\hbar v_F(q_n - ik_y)}{E}, 1 \right]^T. \quad (5.42)$$

In the end of this paragraph we present a full tight-binding spectrum of armchair ribbons and the corresponding density of states [97], see Fig. 5.9. On this figure ribbons with $M = 4$ and $M = 30$ dimers are semiconducting and do not satisfy the condition (5.40), while $M = 5$ is semimetallic with a linearly dispersing mode at zero energy. In terms of the number M of dimer lines (see Fig. 5.8a), we say that the ribbon is semimetallic if $M = 3p - 1$ (p – integer) or semiconducting otherwise [97]. There is also an interesting feature on Fig. 5.9b, namely there are dispersionless modes at energies $E = \pm 1$.

5.3.2 Zigzag ribbons

Now we examine electronic properties of zigzag ribbons, Fig. 5.8b. From the figure we can deduce that the appropriate boundary conditions are

$$\Psi_A(y = 0) = \Psi_B(y = W) = 0, \quad (5.43)$$

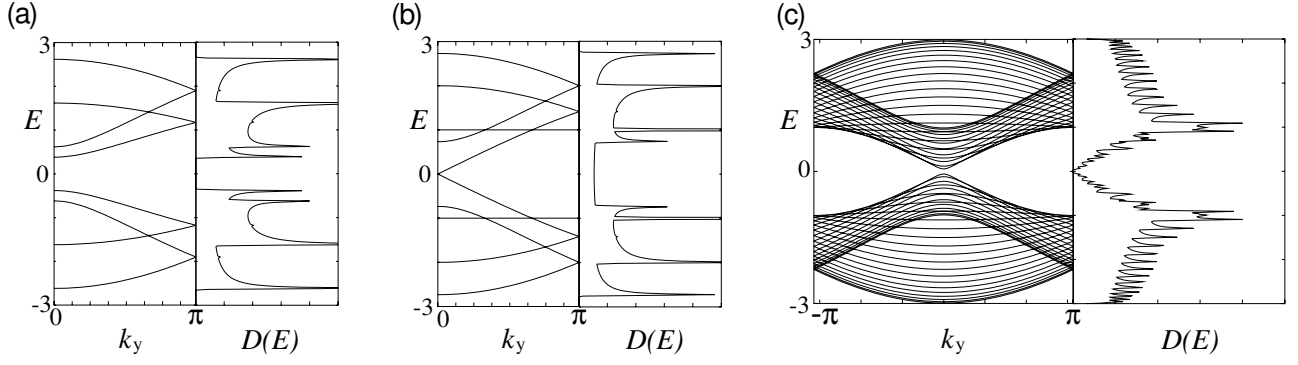


Figure 5.9: Energy band structure $E(k_y)$ and density of states $D(E)$ of armchair ribbons of various widths: (a) $M = 4$, (b): $M = 5$, and (c): $M = 30$. Energy is calculated in units of the hopping constant t , and the (dimensionless) wave number k_y is in units of $3a_{c-c}/2$ (see Eq.(5.15)). Adapted from [97].

which can be met satisfying the conditions [96, 92]

$$\Phi_A(y=0) = \Phi'_A(y=0) = \Phi_B(y=W) = \Phi'_B(y=W) = 0. \quad (5.44)$$

Zigzag ribbons have infinite length along x -direction, therefore we use the Bloch ansatz

$$\Phi(\mathbf{r}) = e^{ik_x x} \phi(y). \quad (5.45)$$

This leads to the Dirac equations

$$\hbar v_F(k_x - \partial_y)\phi_B(y) = E\phi_A(y), \quad (5.46)$$

$$\hbar v_F(k_x + \partial_y)\phi_A(y) = E\phi_B(y), \quad (5.47)$$

$$-\hbar v_F(k_x + \partial_y)\phi'_B(y) = E\phi'_A(y), \quad (5.48)$$

$$-\hbar v_F(k_x - \partial_y)\phi'_A(y) = E\phi'_B(y). \quad (5.49)$$

It enables us to find the equations for $\phi_A(y)$ and $\phi'_A(y)$,

$$(k_x^2 - \partial_y^2)\phi_A^{(l)}(y) = \left(\frac{E}{\hbar v_F}\right)^2 \phi_A^{(l)}(y). \quad (5.50)$$

We look for a solution in the form of plane waves by analogy with the case of armchair ribbons,

$$\phi_A = Ae^{izy} + Be^{-izy}, \quad \phi'_A = Ce^{izy} + De^{-izy}. \quad (5.51)$$

This yields the spectrum, $E = \pm \hbar v_F \sqrt{k_x^2 + z^2}$, where, as we will see further, z can be either real or imaginary. Boundary conditions at $y = 0$ imply that $B = -A$ and $D = -C$. Thus, we can see that the valleys are decoupled in zigzag ribbons, and equations (5.47) and (5.49) yield

$$\Phi_{K/K'} \propto e^{ik_x x} \left[\sin(zy), \frac{\hbar v_F(\xi k_x \sin(zy) + z \cos(zy))}{E} \right]^T, \quad (5.52)$$

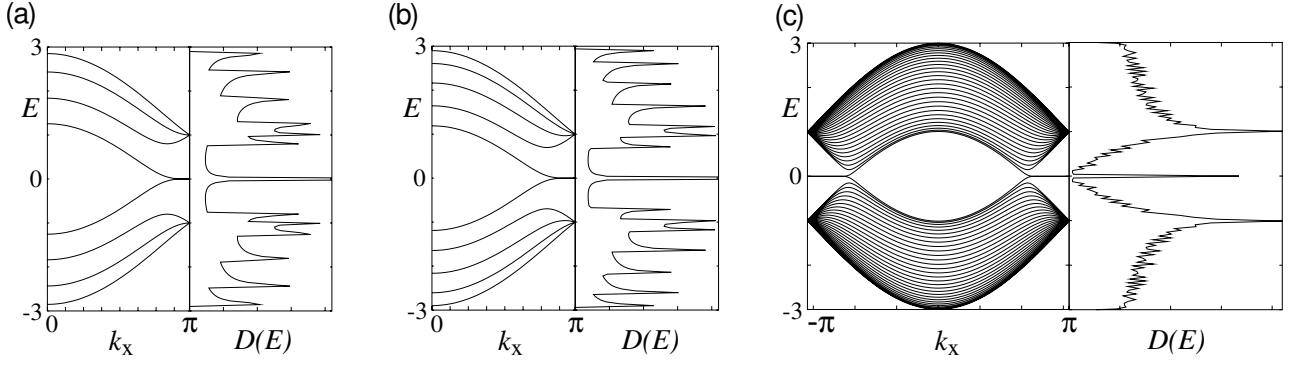


Figure 5.10: Energy band structure $E(k_x)$ and density of states $D(E)$ of zigzag ribbons of various widths: (a) $N = 4$, (b): $N = 5$, and (c): $N = 30$. Energy is calculated in units of the hopping constant t , and the (dimensionless) wave number k_x is in units of $\sqrt{3}a_{c-c}/2$ (see Eq.(5.15)). Adapted from [97].

where $\xi = +1$ in the valley of K point and $\xi = -1$ for the K' . The boundary conditions (5.44) for B parts of the wavefunction provide an equation that determines the allowed values for z ,

$$k_x = -\frac{\xi z}{\tan(zW)}. \quad (5.53)$$

Thus the transverse quantum number is coupled to the longitudinal momentum, as in 2DEG waveguides in the presence of a magnetic field. In order to write equation (5.52) in a symmetric way, we take a square of the quantization condition (5.53) and use the relation $k_x^2 = E^2/(\hbar v_F)^2 - z^2$ to obtain

$$\left(\frac{E}{\hbar v_F}\right)^2 = \frac{z^2}{\sin^2(zW)}. \quad (5.54)$$

Using equations (5.53) and (5.54) in equation (5.52) leads to

$$\Phi_{K/K'} \propto e^{ik_x x} [\sin(zy), s(z, E) \sin\{z(W - y)\}]^T \quad (5.55)$$

with $s(z, E) = \text{sign}[Ez/\sin(zW)]$. The transcendental equation (5.54) has real solutions $z \in \mathbb{R}$ only for $|E| \geq \hbar v_F/W$. These states correspond to bulk states: they are extended over the whole width of the ribbon. For $|E| < \hbar v_F/W$ there are only imaginary solutions $iz \in \mathbb{R}$, corresponding to the so-called edge states [96, 97], which are exponentially localized at the edges and live predominantly on one sublattice at each side, as can be seen from equation (5.55).

In order to see explicitly how the states in a zigzag ribbon divide into extended and localized we present a full tight-binding spectrum in the whole Brillouin zone and the corresponding density of states, see Fig. 5.10. We clearly see on Fig. 5.10c that for $|k_x| > 2\pi/3$ there are

flat bands at zero energy. They are dispersionless and correspond to the edge states mentioned above. They give a high peak in the density of states. Since zigzag edges do not mix valleys, as was pointed out above, we can see contributions from both K points in the spectrum. We can also notice that these peculiar edge states, which become dispersive at $|k_x| < 2\pi/3$, ensure that zigzag graphene ribbons are always semimetallic irrespective of their width [97].

Chapter 6

Quantum Hall effect in graphene

In this chapter we discuss general properties of graphene in presence of a strong magnetic field. It turns out that the honeycomb lattice structure of graphene leads to important consequences for spectrum and charge transfer when magnetic field is applied. We know that graphene at low energies is described by a massless Dirac equation. This fact singles out graphene if compared to conventional 2D electron gases (2DEG). Specifically, the quantum Hall (QH) effect in graphene demonstrates an unusual sequence of Hall plateaus occurring at half-integer filling factors in contrast to 2DEG. This is a direct consequence of a relativistic nature of low-energy excitations. Existence of such anomalous QH effect can be also viewed as a manifestation of a non-zero Berry phase π at each of the Dirac cones. One particular feature of the spectrum is the existence of a zero-energy Landau level (LL), which is independent of the value of a magnetic field and has occupancy twice smaller than any other LL. This zero-energy LL is responsible for half-integer filling factors in the QH measurements [76].

Besides bulk graphene, we will also briefly discuss the spectrum of armchair and zigzag nanoribbons in presence of a magnetic field.

6.1 Graphene in a strong magnetic field

In order to describe Dirac quasiparticles in graphene in the magnetic field one has to replace the canonical momentum \mathbf{p} by the gauge-invariant kinetic momentum

$$\mathbf{p} \rightarrow \mathbf{\Pi} = \mathbf{p} + e\mathbf{A}(\mathbf{r}), \quad (6.1)$$

where $\mathbf{A}(\mathbf{r})$ is the vector potential that generates the magnetic field $\mathbf{B} = \nabla \times \mathbf{A}(\mathbf{r})$. The kinetic momentum is proportional to the electron velocity \mathbf{v} , which must naturally be gauge invariant because it is a physical quantity. Note that throughout the text we use a gauge (see below), which ensures a uniform magnetic field $\mathbf{B} = B\mathbf{e}_z$ is perpendicular to the xy -plane of graphene.

Remember that we used a canonical quantization to obtain operator (5.24). According to this procedure the components of position operator $\hat{\mathbf{r}}$ and the associated canonical momentum $\hat{\mathbf{p}}$ satisfy the commutation relations $[\hat{x}, \hat{p}_x] = [\hat{y}, \hat{p}_y] = i\hbar$ and $[\hat{x}, \hat{y}] = [\hat{p}_x, \hat{p}_y] = [\hat{x}, \hat{p}_y] = [\hat{y}, \hat{p}_x] = 0$. As a consequence of these relations, the components of the kinetic momentum $\hat{\Pi}$ no longer commute. They satisfy the relation,

$$[\hat{\Pi}_x, \hat{\Pi}_y] = -ie\hbar \left(\frac{\partial A_y}{\partial x} - \frac{\partial A_x}{\partial y} \right) = -i \frac{\hbar^2}{l_B^2}, \quad (6.2)$$

where l_B – magnetic length, a length scale introduced by the magnetic field,

$$l_B = \frac{\hbar}{eB}. \quad (6.3)$$

For the quantum-mechanical solution of the Hamiltonian (5.24) after substitution (6.1), it is convenient to use the pair of conjugate operators $\hat{\Pi}_x$ and $\hat{\Pi}_y$ to introduce ladder operators in the same manner as in the quantum-mechanical treatment of the one-dimensional harmonic oscillator. These ladder operators play the role of a complex gauge-invariant momentum (or velocity), and they read [85],

$$\hat{a} = \frac{l_B}{\sqrt{2\hbar}}(\hat{\Pi}_x - i\hat{\Pi}_y), \quad \hat{a}^\dagger = \frac{l_B}{\sqrt{2\hbar}}(\hat{\Pi}_x + i\hat{\Pi}_y), \quad (6.4)$$

where we have chosen the appropriate normalization so as to obtain the usual commutation relation

$$[\hat{a}, \hat{a}^\dagger] = 1. \quad (6.5)$$

Now we invert the expressions (6.4),

$$\hat{\Pi}_x = \frac{\hbar}{\sqrt{2}l_B}(\hat{a} + \hat{a}^\dagger), \quad \hat{\Pi}_y = \frac{i\hbar}{\sqrt{2}l_B}(\hat{a} - \hat{a}^\dagger) \quad (6.6)$$

and plug Eq.(6.6) into our Dirac Hamiltonian. In terms of the ladder operators the Hamiltonian reads

$$\mathbf{H} = \begin{pmatrix} \mathbf{H}_K & 0 \\ 0 & \mathbf{H}_{K'} \end{pmatrix} \text{ with} \quad (6.7)$$

$$\mathbf{H}_K = \frac{\sqrt{2}\hbar v_F}{l_B} \begin{pmatrix} 0 & \hat{a} \\ \hat{a}^\dagger & 0 \end{pmatrix}, \quad \mathbf{H}_{K'} = -\frac{\sqrt{2}\hbar v_F}{l_B} \begin{pmatrix} 0 & \hat{a}^\dagger \\ \hat{a} & 0 \end{pmatrix}$$

for the states around K and K' points, respectively. One remarks the occurrence of a characteristic frequency

$$\omega_c = \frac{\sqrt{2}v_F}{l_B}, \quad (6.8)$$

which plays the role of the cyclotron frequency in the relativistic case. We look for a spinor solution for each K point,

$$\Phi_K(\mathbf{r}) = \begin{pmatrix} \Phi_A(\mathbf{r}) \\ \Phi_B(\mathbf{r}) \end{pmatrix}, \quad \Phi_{K'}(\mathbf{r}) = \begin{pmatrix} \Phi'_A(\mathbf{r}) \\ \Phi'_B(\mathbf{r}) \end{pmatrix}. \quad (6.9)$$

Thus we have to solve the system of equations,

$$\hbar\omega_c \hat{a} \Phi_B(\mathbf{r}) = E \Phi_A(\mathbf{r}) \quad \text{and} \quad \hbar\omega_c \hat{a}^\dagger \Phi_A(\mathbf{r}) = E \Phi_B(\mathbf{r}), \quad (6.10)$$

which yields

$$\hat{a}^\dagger \hat{a} \Phi_B(\mathbf{r}) = \left(\frac{E}{\hbar\omega_c} \right)^2 \Phi_B(\mathbf{r}) \quad (6.11)$$

for the second spinor component. One may therefore identify, up to a numerical factor, the second spinor component $\Phi_B(\mathbf{r})$ with the eigenstate $|n\rangle$ of the usual number operator $\hat{a}^\dagger \hat{a}$, with $\hat{a}^\dagger \hat{a} |n\rangle = n |n\rangle$ in terms of the integer $n \geq 0$. Furthermore, one observes that the spectrum is [78, 85]

$$E_{\lambda,n} = \lambda \hbar\omega_c \sqrt{n}, \quad (6.12)$$

where we have introduced another quantum number $\lambda = \pm 1$ to label states with positive and negative energies, respectively (it is analogous to the band index λ on Fig. 5.7 from the previous chapter). Equation (6.12) represents the relativistic LLs that disperse as $\lambda\sqrt{Bn}$ as a function of the magnetic field, unlike conventional 2DEGs, where LLs disperse linearly with B . As soon as we know the second component of the spinor, we can easily find the first one using Eq.(6.10) because of the usual equations for the ladder operators,

$$\hat{a}^\dagger |n\rangle = \sqrt{n+1} |n+1\rangle \quad \text{and} \quad \hat{a} |n\rangle = \sqrt{n} |n-1\rangle, \quad (6.13)$$

where the last one holds for $n > 0$. Knowing the solution for K point it is straightforward to find it for the K' point (see Eq.(6.7)). So, for any $n \neq 0$, we can write down

$$\Phi_K^n = \frac{1}{\sqrt{2}} \begin{pmatrix} \lambda |n-1\rangle \\ |n\rangle \end{pmatrix}, \quad \Phi_{K'}^n = \frac{1}{\sqrt{2}} \begin{pmatrix} |n\rangle \\ -\lambda |n-1\rangle \end{pmatrix}. \quad (6.14)$$

Special attention deserves the zero-energy ($n = 0$) LL because it stands out from the others. Indeed, when $n = 0$ the first (second) component in Φ_K ($\Phi_{K'}$) is zero because

$$\hat{a} |n=0\rangle = 0. \quad (6.15)$$

In this case we obtain the spinors,

$$\Phi_K^{n=0} = \frac{1}{\sqrt{2}} \begin{pmatrix} 0 \\ |n=0\rangle \end{pmatrix}, \quad \Phi_{K'}^{n=0} = \frac{1}{\sqrt{2}} \begin{pmatrix} |n=0\rangle \\ 0 \end{pmatrix}. \quad (6.16)$$

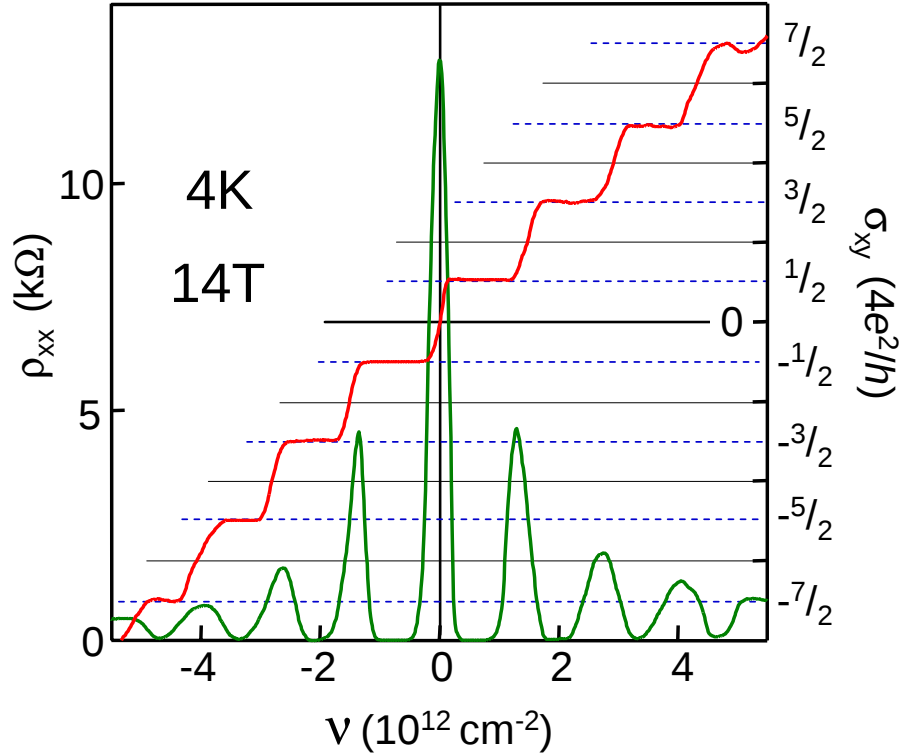


Figure 6.1: Quantum Hall effect in graphene as a function of charge-carrier concentration. The peak at $\nu = 0$ shows that in high magnetic fields there appears a LL at zero energy where no states exist in zero field. The field draws electronic states for this level from both conduction and valence bands [76, 92]. The dashed lines indicate plateaus in $\sigma_{xy} = \pm(4e^2/h)(n + 1/2)$. Adapted from [76].

This observation is rather important since only one component in each valley is non-vanishing, which means that the states in the zero-energy LL belong to sublattice A (B) for the K' (K) point. It implies that $|n = 0\rangle$ LL has an occupancy twice smaller than any other LL [76], which is responsible for the anomalies observed in the quantum Hall effect. This particular Landau level structure has been observed by many different experimental probes, from Shubnikov–de Haas oscillations in single layer graphene [76, 100] to infrared spectroscopy [101] and to scanning tunneling spectroscopy [102] on a graphite surface.

In order to see clearly why graphene spectrum is special compared to 2DEG, we present here the experimental data (see Fig. 6.1) obtained by Novoselov *et al.* in their seminal work [76]. The figure represents QH measurements in graphene. One can see a sequence of plateaus in the Hall conductivity occurring at *half-integer* filling factors. On top of that the degeneracy of all LLs is 4-fold (spin and valley degrees of freedom) in contrast with 2DEGs. In 2DEG, the QH plateaus occur at $\sigma_{xy}^{2DEG} = (2e^2/h)n$ ($n \geq 0$). Note however that from another perspective the fractional shift in the Hall conductivity of graphene can be viewed as the direct manifestation

of Berry's phase acquired by Dirac fermions moving in the magnetic field [76]. Indeed, if we use a quasiclassical quantization condition for closed orbits in reciprocal space, we obtain [91]

$$S(E) = \pi q_F^2 = \frac{2\pi eB}{\hbar} \left(n + \frac{1}{2} - \frac{\gamma}{2\pi} \right), \quad (6.17)$$

where $S(E)$ is a k -space surface enclosed by an orbit of energy E , q_F is the absolute value of the Fermi momentum; γ is a Berry's phase. The latter is a consequence of the band structure topology and manifests itself as a phase factor in a wave function if we change particle momentum around a loop in k -space. There is a simple way to see this. We already know (see Sec. 5.2) that for Dirac quasiparticles in graphene, helicity $\eta_{\mathbf{q}}$ is a good quantum number, meaning that for a fixed energy around K (or K') point, $\eta_{\mathbf{q}}$ is conserved. By definition it means that the quasiparticle pseudospin is linked to the axis determined by the electron momentum. Thus, rotation around a closed loop in k -space can be also viewed as a rotation of a pseudospin around z -axis. In this case the wave function is transformed as,

$$\Psi \rightarrow e^{2\pi \frac{i}{2} \sigma_z} \Psi = e^{i\pi} \Psi \quad (6.18)$$

and we deduce that the Berry phase is $\gamma = \pi$. This immediately gives our relativistic LL spectrum if we remember that $E = \lambda \hbar v_F q_F$ and use quantization rule (6.17). In 2DEG $\gamma = 0$ resulting in a usual 1/2 offset in the LL spectrum.

These experiments confirm the picture of relativistic quasiparticles responsible for the QH effect in graphene and make graphene special as a "playground" for investigating relativistic effects with simple room-temperature measurements.

6.2 QH effect in graphene ribbons

In this section we briefly discuss the electronic properties of graphene ribbons in a (strong) magnetic field. Each type of ribbons (zigzag and armchair) has a translation invariant direction. For the coordinate system chosen on Fig. 5.8, armchair ribbons possess translation symmetry in y -direction, while zigzag ribbons are invariant along x -axis. In the previous section we assumed that the magnetic field was applied perpendicular to the plane of the ribbons. We may use symmetries of the ribbons when choosing a gauge. Thus, it is convenient to use a Landau gauge of the form $\mathbf{A}(\mathbf{r}) = (0, Bx, 0)$ for *armchair* and $\mathbf{A}(\mathbf{r}) = (-By, 0, 0)$ for *zigzag* ribbons.

Having fixed the gauge it is straightforward to find an explicit form of the LL eigenstates $|n\rangle$. To do this, we write down explicitly the number operator $\hat{a}^\dagger \hat{a}$ and notice that it coincides exactly with the Hamiltonian for a harmonic oscillator if we use a Bloch ansatz

$$\Phi_B(\mathbf{r}) = e^{ik_x x} \phi_B(y) \text{ for zigzag,} \quad (6.19)$$

$$\Phi_B(\mathbf{r}) = e^{ik_y y} \phi_B(x) \text{ for armchair,} \quad (6.20)$$

and analogous expressions for Φ'_A . Then we come to the equation

$$\left[\frac{\partial^2}{\partial \xi^2} + \xi^2 \right] \phi_B = (\epsilon^2 + 1) \phi_B, \quad (6.21)$$

where $\epsilon = El_B/(\hbar v_F)$ and a dimensionless parameter $\xi = x/l_B + k_y l_B$ for armchair and $\xi = y/l_B - k_x l_B$ for zigzag. In the case of graphene (infinitely large ribbons), the relativistic LL spectrum is found from the condition $\epsilon^2 = 2n$ and the eigenstates are those of a harmonic oscillator,

$$\phi_n = \sqrt{\frac{1}{2^n n!}} e^{-\frac{\xi^2}{2}} H_n(\xi), \quad (6.22)$$

where $H_n(\xi)$ is a Hermite polynomial.

As we can see, the electron wave function is localized around $y_c = k_x l_B^2$ in zigzag and $x_c = -k_y l_B^2$ in armchair ribbons. Thus, if we plot the band structure (see Fig. 6.2), electron momentum also defines an actual position of this state in real space within the width of the ribbon. On Fig. 6.2 we plot typical band structure of graphene ribbons in presence of a magnetic field. As in the case without magnetic field, one can observe on Fig. 6.2b contribution from both valleys in a zigzag ribbon because they are decoupled in contrast to armchair ribbons. The flat parts of the spectrum correspond to the graphene LL quantization (6.12). For these values of the wave number, the electronic states are localized in the bulk of the ribbon. However, they become dispersive as we reach the ribbon edges ($k_y l_B = 0 \Leftrightarrow x = 0$ and $k_y l_B \simeq -8 \Leftrightarrow x = W$ on Fig. 6.2a, for example) [103, 104]. In this case each LL (except $n = 0$) contributes a pair of chiral edge states (propagating clockwise or counterclockwise depending on the magnetic field direction) on the boundaries of the ribbon. The peculiar zero-energy LL gives rise to only one edge channel. Indeed, if we fix the value of Fermi energy μ and do a measurement of left-to-right transmission we can see that the number of (right moving) edge states taking part in charge transfer is $2n + 1$, where n is the highest occupied LL ($n = 1$ on Fig. 6.2). Therefore, the Hall conductivity is given by

$$\sigma_{xy} = \frac{2e^2}{h} (2n + 1) = \frac{4e^2}{h} \left(n + \frac{1}{2} \right), \quad (6.23)$$

just like in the experiments (see Fig. 6.1) discussed above.

To calculate the band structures on Fig. 6.2, we use the tight-binding Hamiltonian,

$$H = t \sum_{\langle i,j \rangle} e^{i\phi_{ij}} c_i^\dagger c_j, \quad (6.24)$$

where in order to incorporate the magnetic field we utilize the Peierls phase $\phi_{ij} = (e/\hbar) \int_{\mathbf{r}_i}^{\mathbf{r}_j} \mathbf{A} \cdot d\mathbf{r}$ taking into account the contribution from the magnetic flux threading the lattice [45]. This approach remains valid as soon as the lattice spacing a_{c-c} and the magnetic length l_B satisfy $l_B \gg a_{c-c}$.

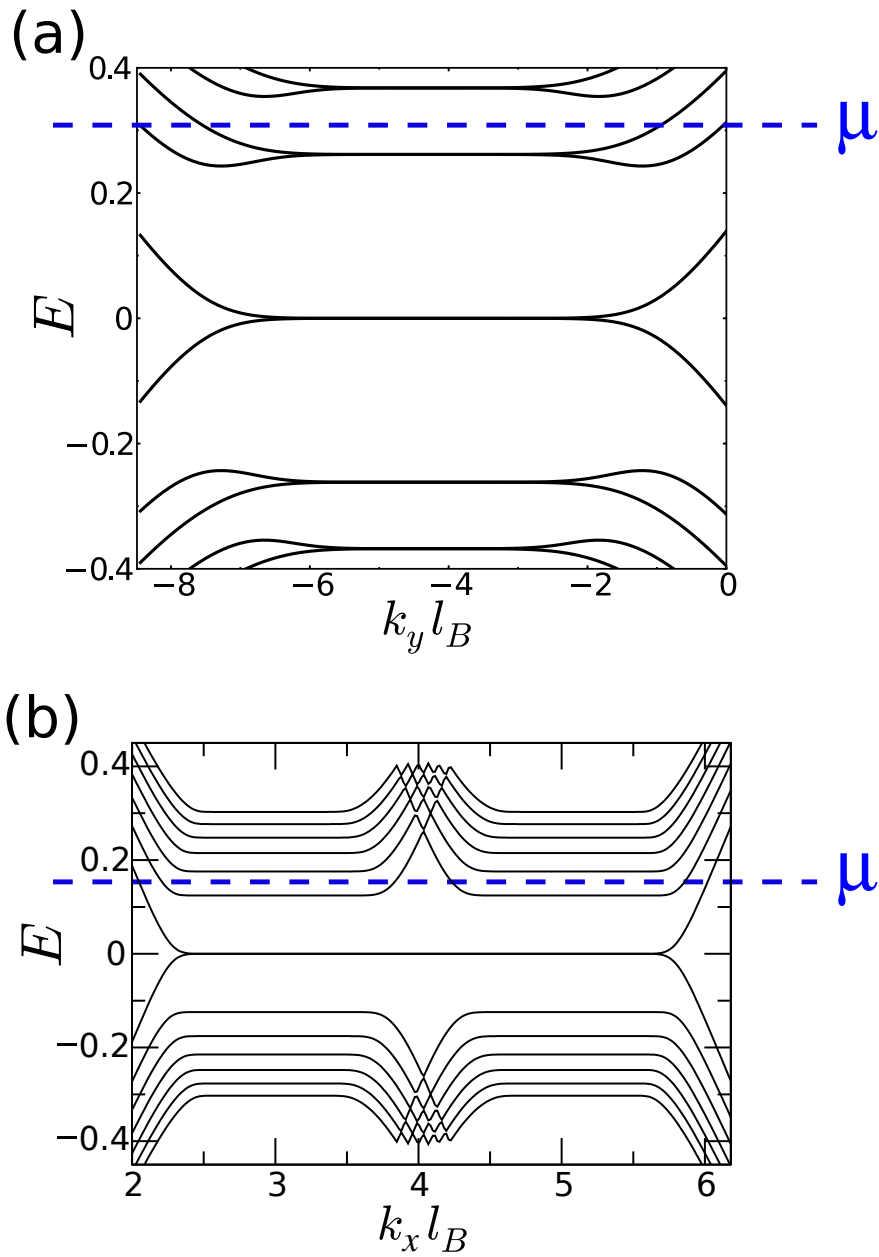


Figure 6.2: (a): Spectrum of an armchair graphene ribbon with $M = 80$ in a strong magnetic field, $l_B \simeq 8a_{c-c}$ (adapted from [60]). (b): Spectrum of a zigzag ribbon with $N = 400$ and a magnetic length $l_B \simeq 43a_{c-c}$ (adapted from [92]). For both ribbons we can see the LL sequence in the bulk of the ribbon (flat regions), while these states become dispersive at the edges. Blue dashed lines denote the position of a Fermi level μ . At the chosen value of μ the highest occupied LL in both ribbons is $n = 1$.

Chapter 7

Graphene with spin-orbit coupling

In this chapter we discuss the electronic and transport properties of graphene in the presence of spin-orbit (SO) interaction. There exist a lot of literature addressing this problem [105, 106, 25, 107, 108, 109]. Various types of SO coupling emerge as a consequence of interplay between intra-atomic SO coupling and the effects of curvature and/or external electric field [25]. However, SO interaction in graphene is supposed to be weak, due to the low atomic number $Z = 6$ of carbon. Indeed, though these effects are always present, estimates show that the SO interaction in graphene is too small to be visible and is therefore neglected in most theoretical works.

However, various interesting phenomena could emerge in its presence as, for example, a quantum spin Hall (QSH) effect [23]. In graphene, there are two general types of SO coupling, Rashba SO interaction which does not conserve z -projection of spin S_z , and intrinsic SO coupling – diagonal in spin space. Both terms when taken into account in graphene are responsible for a gap opening. However, they compete with each other, which can be understood as follows. Intrinsic SO coupling, $H_{int} = \Delta_{so}\sigma_z\tau_zs_z$ (here σ_z, τ_z, s_z are Pauli matrices describing the sublattice, valley, and spin degrees of freedom respectively), is responsible for the QSH effect as was argued in Refs.[23, 24]. It induces a “negative gap” for an electron with a given spin projection in one of two graphene valleys. And this is the reason of existence of a helical edge state on the boundary of a confined graphene structure with vacuum (trivial insulator), where the gap is assumed infinite positive, since the gap has to vanish if we traverse the boundary. If it happens we say that graphene is in a topologically non-trivial phase (or QSH phase, further). In contrast to this, Rashba SO coupling induces a trivial (positive) gap in graphene destroying the QSH phase [23, 24].

In the following section we will briefly review various types of SO interaction and corresponding mechanisms responsible for their existence. Then, we will discuss the model of the QSH effect proposed by Kane and Mele [23, 24] and present in a continuous limit expressions for the wave function and the spectrum of the edge states. Various types of graphene edges, like zigzag, armchair, or mixed and their influence on the QSH phase will also be discussed.

7.1 Spin-orbit interaction in graphene

There were numerous works on microscopic description of SO interaction in graphene [25, 106, 107]. Effective low-energy expressions both in tight-binding and continuous limits were obtained and we will briefly discuss them in this section. As we know from a microscopic description of graphene, electronic bands forming its band structure come from the outer shell electrons of carbon atoms and are of two types: σ and π [25]. The simplest model of graphene neglects σ bands as they exist at much higher energies (in absolute value) than the π bands (see Fig. 7.1). However, since we want to study the influence of SO interaction, which is a small relativistic correction to Hamiltonian, it is necessary to include both types of bands [25].

The orbitals corresponding to the σ bands of graphene are made by linear combinations of the $2s$, $2p_x$ and $2p_y$ atomic orbitals, whereas the orbitals of the π bands are just the p_z orbitals. We consider the following Hamiltonian [25]:

$$\mathcal{H} = \mathcal{H}_{\text{SO}} + \mathcal{H}_{\text{atom}} + \mathcal{H}_{\pi} + \mathcal{H}_{\sigma}, \quad (7.1)$$

where the atomic Hamiltonian in the absence of spin orbit coupling is:

$$\mathcal{H}_{\text{atom}} = \sum_{\kappa} \left(\epsilon_p \sum_{i=x,y,z; s'=\uparrow, \downarrow} c_{i s'}^{\kappa, \dagger} c_{i s'}^{\kappa} + \epsilon_s \sum_{s; s'=\uparrow, \downarrow} c_{s, s'}^{\kappa, \dagger} c_{s, s'}^{\kappa} \right). \quad (7.2)$$

where $\epsilon_{p,s}$ denote the atomic energy for the $2p$ and $2s$ atomic orbitals of carbon, the operators $c_{i; s'}^{\kappa}$ and $c_{s; s'}^{\kappa}$ refer to p_z, p_x, p_y and s atomic orbitals of atom κ respectively, and $s' = \uparrow, \downarrow$ denote the electronic spin. \mathcal{H}_{SO} refers to the atomic spin-orbit coupling occurring at the carbon atoms and the terms $\mathcal{H}_{\pi}, \mathcal{H}_{\sigma}$ describe the π and σ bands. We use the nearest neighbor hopping model between the p_z orbitals for \mathcal{H}_{π} , using one parameter $V_{pp\pi}$ (it is equivalent to t in Eq.(5.16)). The rest of the intra-atomic hoppings are the nearest neighbor interactions $V_{pp\sigma}, V_{sp\sigma}$ and $V_{ss\sigma}$ between the atomic orbitals s, p_x, p_y of the σ band. For more details on the model of \mathcal{H}_{σ} see Ref.[25]. The results will be presented in terms of the following parameters:

$$\begin{aligned} V_1 &= \frac{\epsilon_s - \epsilon_p}{3} \\ V_2 &= \frac{2V_{pp\sigma} + 2\sqrt{2}V_{sp\sigma} + V_{ss\sigma}}{3}. \end{aligned} \quad (7.3)$$

The band structure for graphene is shown in Fig. (7.1).

7.1.1 Intra-atomic SO interaction

In a crystal, intra-atomic SO coupling arises from an interaction between electrons and atomic nuclei. It is given by expression $\mathcal{H}_{\text{SO}} = \Delta \vec{\mathbf{L}} \vec{\mathbf{s}}$ [25, 62, 110] where $\vec{\mathbf{L}}$ and $\vec{\mathbf{s}}$ are, the total atomic

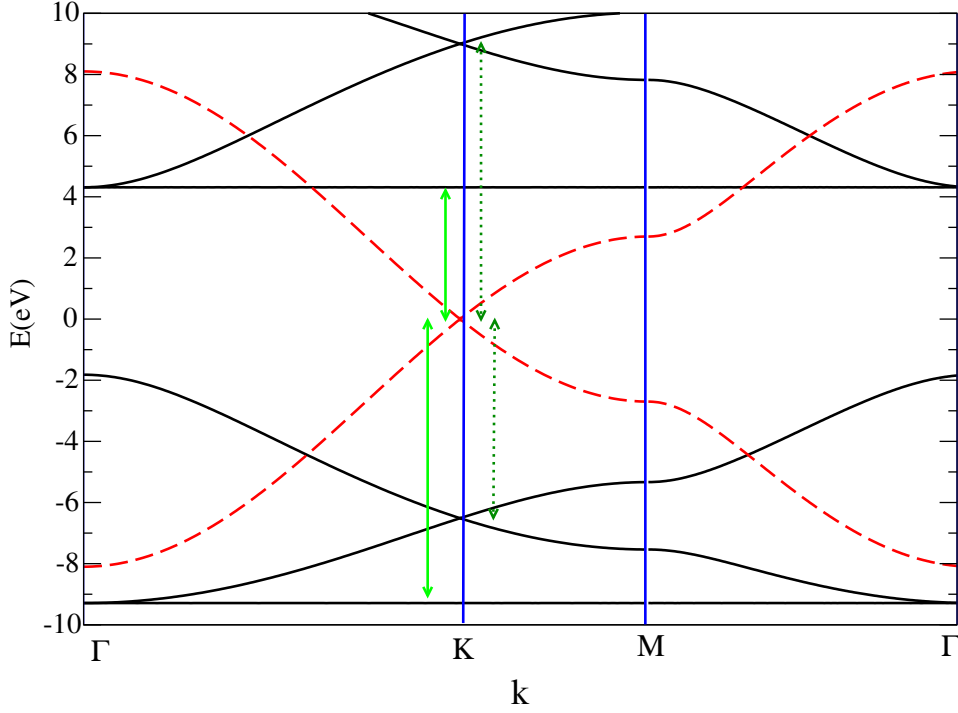


Figure 7.1: Black (full) curves: σ bands. Red (dashed) curves: π bands. The dotted and solid green arrows depict contributions to the up and down spins at the A sublattice in Eq.(7.4) respectively. The opposite contributions can be defined for the B sublattice. These interband transitions are equivalent to the processes depicted in Fig. 7.3, giving rise to the intra-atomic SO coupling. Adapted from [25].

angular momentum operator and total electronic spin operator respectively, and Δ is the intra-atomic SO coupling constant. In the second quantized form we come to [25]

$$\mathcal{H}_{\text{SO}} = \Delta \sum_{\kappa} \left(c_{z\uparrow}^{\kappa,\dagger} c_{x\downarrow}^{\kappa} - c_{z\downarrow}^{\kappa,\dagger} c_{x\uparrow}^{\kappa} + i c_{z\uparrow}^{\kappa,\dagger} c_{y\downarrow}^{\kappa} - i c_{z\downarrow}^{\kappa,\dagger} c_{y\uparrow}^{\kappa} + i c_{x\downarrow}^{\kappa,\dagger} c_{y\downarrow}^{\kappa} - i c_{x\uparrow}^{\kappa,\dagger} c_{y\uparrow}^{\kappa} + \text{H.c.} \right), \quad (7.4)$$

where the creation/annihilation operators $c_{z,x,y;s'}^{\kappa,\dagger}$ and $c_{z,x,y;s'}^{\kappa}$ refer to the corresponding p_z , p_x and p_y atomic orbitals of atom κ . The intra-atomic SO coupling Hamiltonian, Eq.(7.4), allows for transitions between states of the π band (p_z) near the K and K' points of the Brillouin zone, with states from the σ bands ($p_{x,y}$) at the same points. These transitions imply a change of the electronic degree of freedom, *i.e.* a “spin-flip” process (see Fig. 7.1). Next, we would like to consider two possibilities: (i) a curved graphene surface, (ii) the effect of a perpendicular electric field applied to flat graphene. In the latter case we will have to consider another intra-atomic process besides the intra-atomic SO coupling, the atomic Stark effect [25].

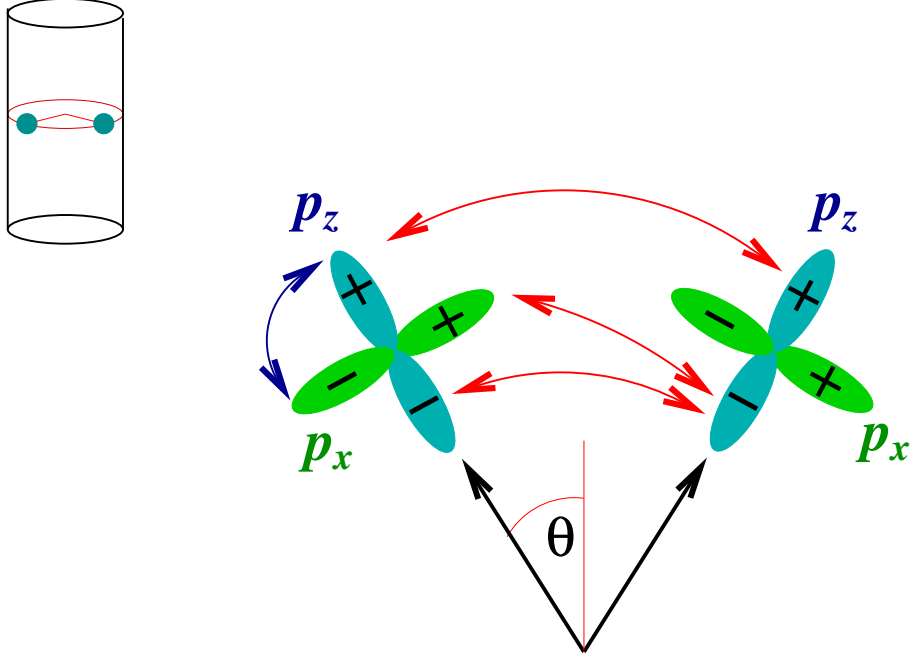


Figure 7.2: Sketch of the relevant orbitals, p_x and p_z needed for the analysis of spin-orbit effects in a curved nanotube. The arrows stand for the different hoppings described in the text (see Eq.(7.5)). Adapted from [25].

7.1.2 Effects of curvature

In a curved graphene sheet, a hopping between the orbitals in the π and σ bands is induced [105]. First, we will use a simple geometry to illustrate the effect of curvature between neighbouring atoms. This geometry is schematically shown in the left upper corner of Fig. 7.2. More specifically, we consider two atoms at the same height along the axis of the tube. In this geometry we consider that the p_z orbitals are oriented normal to the surface of the nanotube, the p_x orbitals are oriented along the surface circumference and the p_y orbitals are parallel to the nanotube axes. The curvature modifies the hopping between the two atoms compared to the flat surface for the p_z and p_x orbitals, but will not change, for this simple case, the hopping between p_y orbitals. The (reduced) p_z - p_x hopping Hamiltonian is the sum of three terms [25]:

$$\begin{aligned} \mathcal{H}_{\text{curv}} = & \sum_{s'} [V_{pp\pi} \cos^2(\theta) + V_{pp\sigma} \sin^2(\theta)] c_{zs'}^{1,\dagger} c_{zs'}^0 - [V_{pp\pi} \sin^2(\theta) + V_{pp\sigma} \cos^2(\theta)] c_{xs'}^{1,\dagger} c_{xs'}^0 \\ & + V_{sp\sigma} \sin^2(\theta) c_{zs'}^{1,\dagger} c_{ss'}^0 + \sin(\theta) \cos(\theta) (V_{pp\pi} - V_{pp\sigma}) (c_{zs'}^{1,\dagger} c_{xs'}^0 - c_{xs'}^{1,\dagger} c_{zs'}^0) + \text{H.c.} \quad (7.5) \end{aligned}$$

where 0 and 1 denote the two atoms considered and θ is the angle between the fixed z -axis and the direction normal to the curved surface (see Fig. 7.2). The angle θ , in the limit when the radius of curvature is much longer than the interatomic spacing, $a_{c-c} \ll R$, is given by $\theta \approx a_{c-c}/R$. The previous discussion can be extended to the case of general curvature when

the graphene sheet has two different curvature radii, R_1 and R_2 corresponding to the x and y directions in the plane. In that case, the factor R^{-1} has to be replaced by $R_1^{-1} + R_2^{-1}$. The hopping terms induced by (intrinsic) curvature discussed here break the isotropy of the lattice and lead to an effective anisotropic coupling between the π and σ bands in momentum space.

7.1.3 Effect of an electric field

Now we discuss the atomic Stark effect due to a perpendicular electric field \mathcal{E} . In this case, we need to consider the $|s\rangle$ orbital of the σ bands at each site, and the associated hopping terms. The Hamiltonian for this case includes the couplings [25]:

$$\mathcal{H}_{\mathcal{E}} = \sum_{\kappa=0,1; s'=\uparrow,\downarrow} \left(\lambda e \mathcal{E} c_{s;s'}^{\kappa,\dagger} c_{z;s'}^{\kappa} + \epsilon_s c_{s;s'}^{\kappa,\dagger} c_{s;s'}^{\kappa} + \text{H.c.} \right) + V_{sp\sigma} \sum_{s'=\uparrow,\downarrow} \left(a_x c_{x;s'}^{1,\dagger} c_{s;s'}^0 + a_y c_{y;s'}^{1,\dagger} c_{s;s'}^0 + \text{H.c.} \right) \quad (7.6)$$

where $\lambda = \langle p_z | \hat{z} | s \rangle$ is an electric dipole transition which induces hybridization between the s and p_z orbitals and where a_x and a_y are the x and y components of the vector connecting the carbon atoms 0 and 1. Note that this Hamiltonian mixes the states in the π band with states in the σ bands, just like the term responsible for curvature effects described above.

7.1.4 Low-energy expressions for SO interactions

It is often enough to consider low-energy properties of graphene in the vicinity of Dirac points (see Sec. 5.2). An effective mass model is then developed by writing the low-energy electronic wavefunction as in Eq.(5.29). The effective Hamiltonian acts on the components of the envelope function (5.28).

The effective mass Hamiltonian for SO interaction can be found by the second order degenerate perturbation theory treating the results of the previous subsections, Eqs.(7.4)–(7.6), as a perturbation [25, 106]. We can summarize the results as follows. If we consider the effects of curvature and electric field, we notice that they basically induce the same type of SO interaction, namely the Rashba-like SO interaction,

$$\mathcal{H}_R = \lambda_R (\sigma_x \tau_z s_y - \sigma_y s_x). \quad (7.7)$$

Here $\vec{\sigma}$, $\vec{\tau}$, and \vec{s} are Pauli matrices describing sublattice (A/B), valley (K/K'), and spin (\uparrow / \downarrow) degrees of freedom, respectively. Effective coupling constant λ_R can be expressed via previously

introduced parameters (7.3) in the limit $V_1 \ll V_2$ (widely separated σ bands) as [25]

$$\begin{aligned}\lambda_R &= \Delta_\varepsilon + \Delta_{\text{curv}}, \\ \Delta_\varepsilon &\simeq \frac{\sqrt{2}}{3} \frac{\Delta \lambda e \mathcal{E}}{V_2}, \\ \Delta_{\text{curv}} &\simeq \frac{\Delta(V_{pp\sigma} - V_{pp\pi})}{2V_1} \left(\frac{a_{c-c}}{R_1} + \frac{a_{c-c}}{R_2} \right) \left(\frac{V_1}{V_2} \right)^2.\end{aligned}\tag{7.8}$$

Thus, we recovered the effective form for the Rashba-type interaction expected from group-theoretical arguments by Kane and Mele in Ref. [23]. Even more importantly, this result shows that this effective spin-orbit coupling for the π bands in graphene to first order in the intra-atomic spin-orbit interaction Δ is given by two terms:

- Δ_ε : Corresponds to processes due to the intra-atomic spin-orbit coupling and the intra-atomic Stark effect between different orbitals of the π and σ bands, together with hopping between neighboring atoms. The mixing between the π and σ orbitals occurs between the p_z and s atomic orbitals due to the Stark effect λ and between the p_z and $p_{x,y}$ due to the atomic spin-orbit coupling Δ . This contribution is the equivalent, for graphene, to the known Rashba spin-orbit interaction [111] and it vanishes at $\mathcal{E} = 0$.
- Δ_{curv} : Corresponds to processes due to the intra-atomic spin-orbit coupling and the local curvature of the graphene surface which couples the π and σ bands, together with hopping between neighboring atoms. The mixing between the π and σ orbitals in this case occurs between p_z and $p_{x,y}$ atomic orbitals both due to the atomic spin-orbit coupling Δ and due to the curvature. This process is very sensitive to deformations of the lattice along the bond direction between the different atoms where the p part of the the sp^2 orbitals is important.

If we consider second order perturbation theory term quadratic in intra-atomic coupling (7.4), then we obtain another type of SO interaction, the so-called intrinsic SO coupling [25],

$$\mathcal{H}_{SO} = \Delta_{so} \sigma_z \tau_z s_z.\tag{7.9}$$

This term is completely determined from the symmetry properties of the honeycomb lattice and is similar to the Dresselhaus SO interaction in semiconducting heterostructures [25, 112]. Processes responsible for this type of SO coupling are depicted on Fig. 7.3. In terms of parameters $V_{1,2}$, $V_1 \ll V_2$ we have [25],

$$\Delta_{so} \simeq \frac{3}{4} \frac{\Delta^2}{V_1} \left(\frac{V_1}{V_2} \right)^4.\tag{7.10}$$

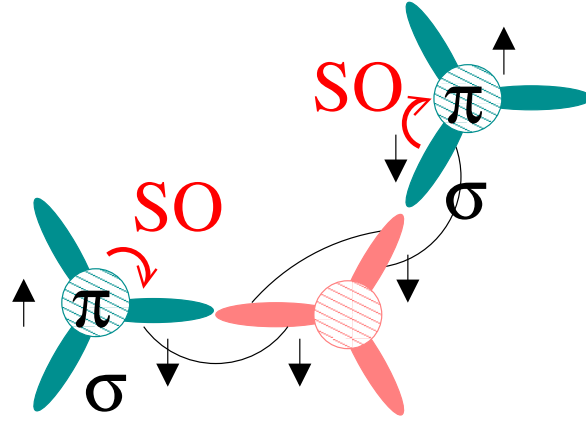


Figure 7.3: Sketch of the processes leading to an effective intrinsic term in the π band of graphene. Transitions drawn in red, and indicated by SO, are mediated by the intra-atomic spin-orbit coupling. Adapted from [25].

As one can see in contrast to the previous case, this term conserves z -projection of spin. We will see later that it is the intrinsic SO coupling term responsible for the quantum spin Hall (QSH) effect in graphene.

In the end of this section let us give numerical estimates of typical values for obtained SO interaction parameters. We summarize them in the Table 7.1 below. Estimates done by other authors are in agreement with these results [25, 106, 107], confirming that the effect of SO interaction in graphene is originally very weak.

Intrinsic coupling: Δ_{so}	$\frac{3}{4} \frac{\Delta^2}{V_1} \left(\frac{V_1}{V_2} \right)^4$	0.01K
Rashba coupling ($\mathcal{E} \approx 50\text{V}/300\text{nm}$): $\Delta_{\mathcal{E}}$	$\frac{\sqrt{2}}{3} \frac{\Delta \lambda \mathcal{E}}{V_2}$	0.04K
Curvature coupling: Δ_{curv}	$\frac{\Delta(V_{pp\sigma} - V_{pp\pi})}{2V_1} \left(\frac{a_{c-c}}{R_1} + \frac{a_{c-c}}{R_2} \right) \left(\frac{V_1}{V_2} \right)^2$	0.1K

Table 7.1: Dependence on band structure parameters, curvature, and electric field of the spin orbit couplings discussed in the text in the limit $V_1 \ll V_2$ (widely separated σ bands). The parameters used are $\lambda \approx 0.264 \text{ \AA}$ [110], $\mathcal{E} \approx 50 \text{ V}/300 \text{ nm}$ [23, 75], $\Delta = 12 \text{ meV}$ [113, 114], $V_{sp\sigma} \sim 4.2 \text{ eV}$, $V_{ss\sigma} \sim -3.63 \text{ eV}$, $V_{pp\sigma} \sim 5.38 \text{ eV}$ and $V_{pp\pi} \sim -2.24 \text{ eV}$ [115, 116], $V_1 = 2.47 \text{ eV}$, $V_2 = 6.33 \text{ eV}$, and $R \sim 50 - 100 \text{ nm}$. Adapted from [25].

7.2 Topological insulator in graphene: Kane-Mele model

In this section we will demonstrate how low-energy electronic and transport properties of graphene change if we consider the effects of spin-orbit interaction. From the previous sec-

tion we saw already which types of SO coupling could be present (in principle) in graphene, see equations (7.7) and (7.9). If one takes them into account, then interesting phenomena, such as the QSH effect, emerge. These effects were discovered in pioneer works by C. Kane and E. Mele [23, 24], who emphasized the importance of spin-orbital effects in graphene (however, they have not been observed experimentally yet due to small values of the SO coupling constants, see Table 7.1). Let us briefly review the Kane-Mele model as this is a background for our recent works [27, 60] discussed in the subsequent chapters.

In the continuous (Dirac) limit, graphene in presence of SO coupling is described by

$$\begin{aligned}\mathcal{H} &= \mathcal{H}_0 + \mathcal{H}_{SO} + \mathcal{H}_R, \\ \mathcal{H}_0 &= -i\hbar v_F(\sigma_x \tau_z \partial_x + \sigma_y \partial_y),\end{aligned}\tag{7.11}$$

where \mathcal{H}_{SO} and \mathcal{H}_R are defined in Eq.(7.7) and Eq.(7.9), while \mathcal{H}_0 is a usual graphene Hamiltonian (5.24). For $\lambda_R = 0$, Δ_{so} leads to an energy gap $2\Delta_{so}$ with $E(\mathbf{q}) = \pm\sqrt{(\hbar v_F q)^2 + \Delta_{so}^2}$. For $0 < \lambda_R < \Delta_{so}$ the energy gap $2(\Delta_{so} - \lambda_R)$ remains finite. For $\lambda_R > \Delta_{so}$ the gap closes, and the electronic structure is that of a zero gap semiconductor with quadratically dispersing bands [23]. In the following we will assume that $\lambda_R < \Delta_{so}$ and analyze the properties of the resulting gapped phase.

The gap generated by $\sigma_z \tau_z s_z$ (see Eq.(7.9)) is different from the gap that would be generated by the staggered sublattice potentials, σ_z or $\sigma_z s_z$. The ground states in the presence of the latter terms are adiabatically connected to simple insulating phases at strong coupling where the two sublattices are decoupled [23]. In contrast, the gap parameter $\sigma_z \tau_z s_z$ produces gaps with *opposite signs* at the K and K' points. This has no simple strong coupling limit. To connect smoothly between the states generated by σ_z and $\sigma_z \tau_z s_z$ one must pass through a critical point where the gap vanishes, separating ground states with distinct topological orders¹.

Let us consider in more details the gapped phase in graphene ($\lambda_R < \Delta_{so}$), see Fig. 7.4. For simplicity we will consider $\lambda_R = 0$ and $\Delta_{so} > 0$ since qualitatively it corresponds to the same physical picture. It turns out that the topological order in the gapped phase results in existence of gapless edge excitations in graphene with boundaries. As we know from Sec. 5.3, there are two major types of edges in finite graphene structures, *armchair* and *zigzag*. Edge states exist for both types of boundaries but are characterized by different length scales.

In order to plot the band structure, Fig. 7.4, in the full Brillouin zone, we employed a tight-binding version of Hamiltonian (7.11), which has the form [24],

$$\mathcal{H} = -t \sum_{\langle ij \rangle \alpha} c_{i\alpha}^\dagger c_{i\alpha} + i\lambda_{so} \sum_{\langle\langle ij \rangle\rangle \alpha\beta} \nu_{ij} s_{\alpha\beta}^z c_{i\alpha}^\dagger c_{j\beta} + i\lambda_R \sum_{\langle ij \rangle \alpha\beta} c_{i\alpha}^\dagger (\mathbf{s}_{\alpha\beta} \times \mathbf{d}_{ij})_z c_{j\beta},\tag{7.12}$$

¹Consider the following Hamiltonian: $\mathcal{H} = \mathcal{H}_0 + \mathcal{H}_1(\mu)$, where $\mathcal{H}_1(\mu) = \mu\mathcal{H}_{SO} + (1-\mu)\Delta_z\sigma_z$. The parameter μ varies in the interval $[0, 1]$. Then, there exists a critical value μ_c , at which the gap of Hamiltonian \mathcal{H} vanishes.

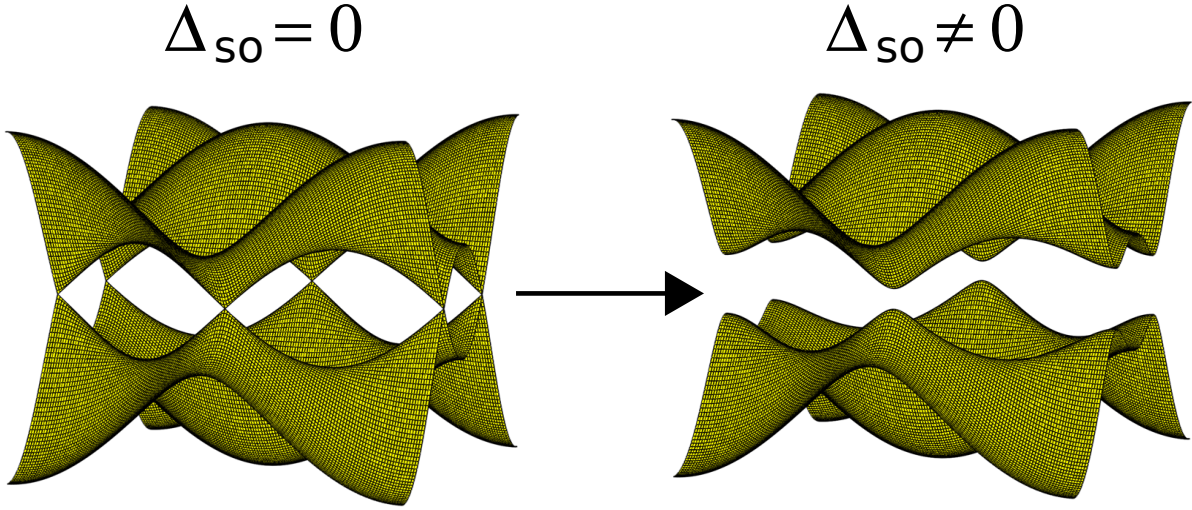


Figure 7.4: Comparison of the three-dimensional band structure of graphene in the case with (right) and without (left) the SO coupling. When the SO interaction is taken into account a bulk gap appears. Obtained with the help of Eq.(7.12) with parameters values $t = 2.7$ eV, $\lambda_{so} = 0.1t$ ($\Delta_{so} = 3\sqrt{3}\lambda_{so}$) and $\lambda_R = 0$.

where operator $c_{i\alpha}$ annihilates an electron on site i with a spin projection α ; single $\langle \rangle$ or double $\langle\langle \rangle\rangle$ brackets denote first and second nearest-neighbors on the lattice, respectively². \mathbf{s} is a vector of Pauli matrices in the spin space. The first term describes bare graphene first nearest-neighbors hopping and does not depend on spin. The second term is the mirror symmetric intrinsic SO coupling. In the tight-binding description this intrinsic SO coupling is represented by the second nearest neighbors hopping term with a spin-dependent amplitude, $\lambda_{so} = \Delta_{so}/(3\sqrt{3})$. $\nu_{ij} = \pm 1$ if the electron makes a counterclockwise (clockwise) turn to get to the second neighbor (see Fig. 7.5). The third term is the nearest neighbor Rashba term, which explicitly violates the $z \rightarrow -z$ mirror symmetry, $\mathbf{d}_{ij} = (\mathbf{r}_i - \mathbf{r}_j)/|\mathbf{r}_i - \mathbf{r}_j|$ is a unit vector connecting the two sites. But as we discussed above, we proceed assuming $\lambda_R = 0$.

7.2.1 Topologically protected edge modes

In this paragraph we will consider armchair and zigzag nanoribbons with SO coupling. We will summarize the main properties of the edge states in both ribbon types. To find analytical solutions we use the continuous model (7.11) with eigenstates of the form (5.28)-(5.29).

²Note that this is an effective Hamiltonian, which is written in terms of the creation/annihilation operators for π orbitals *only*. The effect of σ orbitals is already taken into account in the corresponding SO coupling constants.

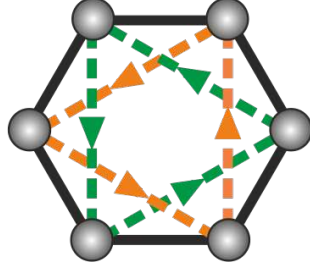


Figure 7.5: Single hexagon of graphene. Dashed arrows correspond to the second nearest neighbors hopping giving rise to the intrinsic SO interaction ($\sim \lambda_{so}$ in Eq.(7.12)). The direction of hopping is important in this case. If an electron hops counterclockwise, like on the cartoon, then $\nu_{ij} = +1$, otherwise $\nu_{ij} = -1$.

Armchair ribbons

Consider an armchair ribbon extending along the y -direction with boundaries at $x = 0$ and $x = W$ (see Fig. 5.8a). For simplicity, we consider that the ribbon is wide enough so that the two opposite boundaries can be treated independently. Then, we can write down the solution for envelope functions in a compact way,

$$\begin{pmatrix} \Phi_A^{(\prime)}(\mathbf{r}) \\ \Phi_B^{(\prime)}(\mathbf{r}) \end{pmatrix} = \left[A^{(\prime)} e^{ik_x x} \begin{pmatrix} 1 \\ \frac{\hbar v_F(\pm k_x + ik_y)}{E \pm \zeta \Delta_{so}} \end{pmatrix} + B^{(\prime)} e^{-ik_x x} \begin{pmatrix} 1 \\ \frac{\hbar v_F(\mp k_x + ik_y)}{E \pm \zeta \Delta_{so}} \end{pmatrix} \right] e^{ik_y y}, \quad (7.13)$$

where upper (lower) sign corresponds to K (K') points, and $\zeta = \pm 1$ distinguishes spin-up/spin-down solutions. This expression can be trivially obtained from a stationary Schrödinger equation with the Hamiltonian (7.11) (and $\lambda_R = 0$). Looking for a decaying solution for the edge states, we substitute $k_x = i\kappa$. To find an expression for κ one has to satisfy the armchair boundary conditions (5.30). It is a straightforward calculation which in the end leads to a very simple result. We will write the final expressions only.

For the upper boundary, $x = 0$ (see Fig. 5.8), we find: $\kappa = \Delta_{so}/(\hbar v_F)$, and the total wave function,

$$\Psi(\mathbf{r}) \propto e^{-\kappa x} e^{ik_y y} \begin{pmatrix} 1 \\ i\zeta \end{pmatrix} \sin Kx, \quad (7.14)$$

where $K = 4\pi/(3\sqrt{3}a_{c-c})$ is the x -coordinate of the K -point. The proportionality constant is to be found from a normalization condition. The eigenvalue corresponding to this solution is $E = \zeta \hbar v_F k_y$. We immediately observe that at this boundary there is a pair of edge states (with opposite spins, often referred to as Kramers doublet), which propagate in the opposite directions (see Fig. 7.6). This is a feature of the QSH effect. The name comes from the fact that there is no net charge current in a system with such a boundary, but there is a non-zero spin current [23].

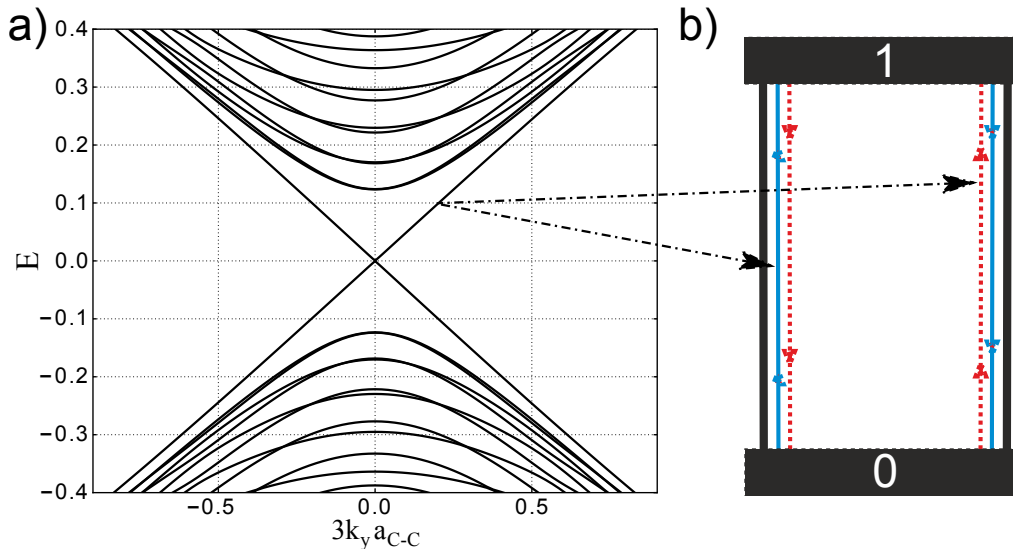


Figure 7.6: (a): Spectrum of the (metallic) armchair ribbon with $M = 80$ dimer lines in width in presence of the (intrinsic) SO coupling, $\lambda_{\text{so}} = 0.02t$ ($\Delta_{\text{so}} = 0.1t$), see Eq.(7.12). Linearly dispersing bands crossing at zero energy come from the edge states. (b): Cartoon of an armchair ribbon connected to two contacts. The blue solid (red dashed) arrows depict spin-up (spin-down) edge states at each boundary. The dashed-dotted arrow shows that at a given energy the edge states moving in the same direction are on the opposite boundaries of the ribbon and moreover have opposite spin projections.

At the lower boundary, $x = W$, we come to the solution: $\kappa = -\Delta_{\text{so}}/(\hbar v_F)$, and the total wave function reads,

$$\Psi(\mathbf{r}) \propto e^{\kappa(x-W)} e^{ik_y y} \begin{pmatrix} 1 \\ -i\zeta \end{pmatrix} \sin Kx. \quad (7.15)$$

In this case the corresponding eigenvalue is $E = -\zeta \hbar v_F k_y$, which means that on the opposite boundary (compared to $x = 0$), the direction of motion of electrons is reversed. Typical spectrum of an armchair ribbon in presence of the intrinsic SO coupling looks as on Fig. 7.6. A pair of linear bands crossing at $E = 0$ correspond to the helical edge states we have just discussed.

The features of the edge states described above led to a very naive and misleading picture of the QSH effect [82], according to which it can be looked at as two copies of a QH effect with opposite directions of an effective magnetic field for opposite spin projections. As we will see from the subsequent sections, this argument generally speaking is wrong.

To derive the results above we have assumed that the width of an armchair ribbon is much bigger than a characteristic length scale of an edge state $1/\kappa$. As we already know (see Section 5.3), armchair ribbons can be either metallic or semiconducting depending on their width. For semiconducting ribbons, energy gap decays as $1/W$ and becomes small for wide ribbons.

However if we consider ribbons of finite size, more detailed analysis shows that the QSH phase emerges as soon as the spin-orbit gap becomes larger than the confinement gap, $\Delta_{\text{so}} > \Delta_E(W)$. If this condition holds, it can be shown that the edge states (in semiconducting ribbons) have also a small energy gap which in turn decays exponentially with width [117, 118]. The effect of finite width also manifests itself on Fig. 7.6a, where the actual gap is slightly bigger than the bulk value, $2\Delta_{\text{so}}$, due to confinement.

Zigzag ribbons

This case was studied by Kane and Mele [23] and in more details by Metalidis and Prada [119]. The tight-binding version of graphene Hamiltonian with intrinsic SO interaction (7.12) contains the second nearest neighbors term. We remember from Section 5.3 that for zigzag ribbons the wave function has to vanish only on either A or B sublattice sites at the boundary. However, as spin-orbit coupling induces next-nearest neighbors hopping, the total wave function in our case has to vanish on both the A and the B sublattice sites at the edge [119]. It turns out that this results in appearance of two length scales which define the width of edge states. Qualitatively, the solution has a form [119],

$$\Psi(\mathbf{r}) = e^{ik_x x} \left[\alpha e^{-\kappa_1 y} \begin{pmatrix} \Phi_A(k_x, \kappa_1, s_z) \\ \Phi_B(k_x, \kappa_1, s_z) \end{pmatrix} + \beta e^{-\kappa_2 y} \begin{pmatrix} \Phi_A(k_x, \kappa_2, s_z) \\ \Phi_B(k_x, \kappa_2, s_z) \end{pmatrix} \right]. \quad (7.16)$$

It is interesting to note that in contrast to armchair ribbons, in zigzag ribbons, characteristic length scales $1/\kappa_{1,2}$ depend on energy, see Fig. 7.7. As we can see, in zigzag ribbons, $1/\kappa_2$ blows up when we reach the energies near the value of the SO gap. The edge state width increases and we can no longer distinguish it from bulk states. That is why in the next chapters we will concentrate on armchair ribbons. Typical spectrum of a zigzag ribbon with intrinsic SO coupling is depicted on Fig. 7.8. The bulk bandgaps at the one dimensional projections of the K and K' points are clearly seen. In addition, two bands traverse the gap, connecting the K and K' points. The wave functions corresponding to these bands are localized at the edges of the ribbon, see Eq.(7.16).

It is worth mentioning that in the case of irregular graphene edges (neither armchair nor zigzag), the edge states still persist, and their width depends on energy as it does in zigzag ribbons [119]. As we will see further, existence of the edge states is a bulk property and does not depend on boundary conditions.

In the end of this chapter we would like to discuss the topological nature of the edge states. It turns out that they are very robust to a big class of perturbations which conserve time-reversal symmetry (TRS). There is a special number, a topological invariant \mathbb{Z}_2 [24, 23], which is a characteristics of a bulk spectrum, that establishes the so-called *bulk-edge correspondance* [120, 121]. It takes only two values, 0 and 1, distinguishing trivial insulating phase from a topological phase. The latter possesses the edge states discussed above.

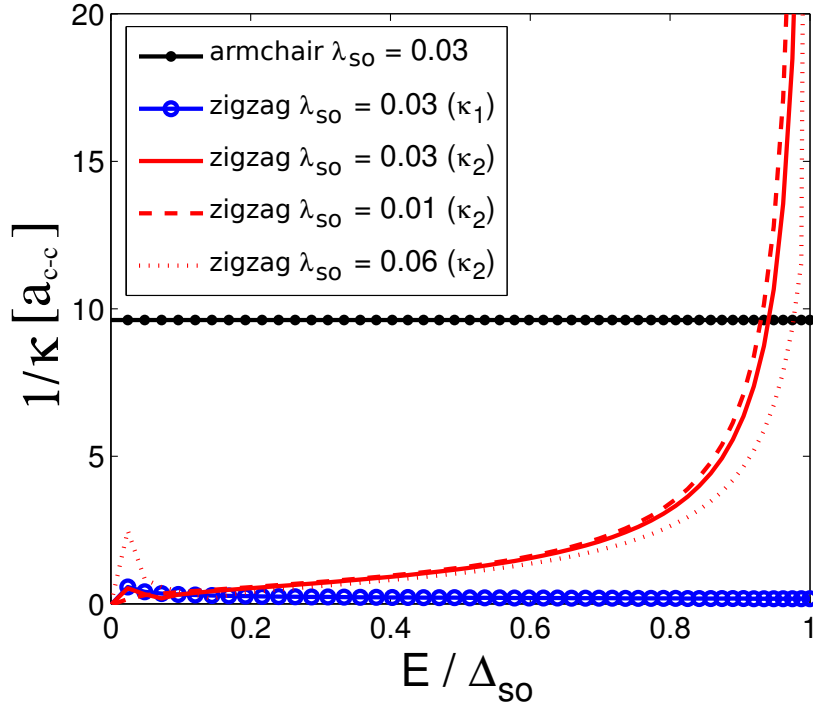


Figure 7.7: Comparison of the topological edge state width of armchair (closed black circles) and zigzag ribbons (solid red line for $1/\kappa_2$ and open blue circles for $1/\kappa_1$) as a function of Fermi energy. The spin-orbit coupling is $\lambda_{so} = 0.03t$. The dominant $1/\kappa_2$ contribution in the zigzag case is also plotted for different values of λ_{so} (0.01, 0.03, 0.06 for dashed, solid and dotted red lines respectively). Adapted from [119].

7.2.2 \mathbb{Z}_2 topological order

Let us discuss the topological properties of graphene with SO interaction. In order to characterize the gapped phase considered above, Kane and Mele proposed a method based on calculating the so-called \mathbb{Z}_2 topological invariant. It is a number characterizing the topology of a manifold mapping a (bulk) Hamiltonian onto the Brillouin zone (a torus in 2D). SO interaction allows a topological class of insulating band structures with TRS preserved [24, 23, 81]. In our case the time-reversal operator, which must be antiunitary, has the form [81]

$$\Theta = \exp(i\pi S_y/\hbar)K, \quad (7.17)$$

where S_y is the spin operator and K is complex conjugation. For spin 1/2 electrons, Θ has the property $\Theta^2 = -1$. This leads to an important constraint, known as Kramers' theorem, that all eigenstates of a time-reversal invariant Hamiltonian are at least twofold degenerate. This follows because if a non degenerate state $|\chi\rangle$ existed then $\Theta|\chi\rangle = c|\chi\rangle$ for some constant c . This would mean $\Theta^2|\chi\rangle = |c|^2|\chi\rangle$, which is not allowed because $|c|^2 \neq -1$. In the absence of spin

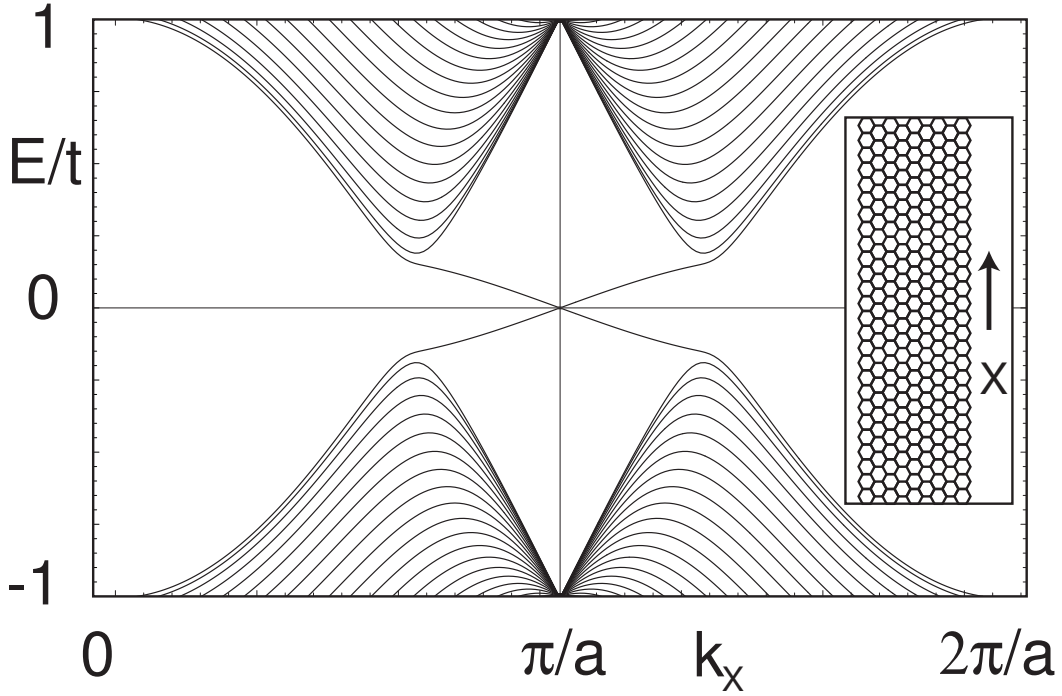


Figure 7.8: One dimensional energy bands for a zigzag ribbon (shown in inset) modeled by (7.12) with $\lambda_{\text{so}} = 0.03t$. The bands crossing the gap are spin filtered edge states. Adapted from [23].

orbit interactions, Kramers' degeneracy is simply the degeneracy between up and down spins. In the presence of SO interactions, however, it has nontrivial consequences.

A time-reversal invariant Bloch Hamiltonian must satisfy

$$\Theta \mathcal{H}(\mathbf{k}) \Theta^{-1} = \mathcal{H}(-\mathbf{k}). \quad (7.18)$$

One can classify the equivalence classes of Hamiltonians satisfying this constraint that can be smoothly deformed without closing the energy gap. In this case we can distinguish two different situations, $\nu = 0$ (trivial insulator) and $\nu = 1$ (topological insulator) with ν being the \mathbb{Z}_2 invariant. It can be understood as follows.

In Fig. 7.9 we show schematically plots of the electronic states associated with the edge of a time-reversal invariant 2D insulator as a function of the crystal momentum along the edge. Only half of the Brillouin zone $0 < k_x < \pi/a$ is shown because TRS requires that the other half $-\pi/a < k < 0$ is a mirror image. The shaded regions depict the bulk conduction and valence bands separated by an energy gap. Depending on the details of the Hamiltonian near the edge there may or may not be states bound to the edge inside the gap. If they are present, however, then Kramers theorem requires they be twofold degenerate at the time-reversal invariant momenta $k_x = 0$ and $k_x = \pi/a$ (which is the same as $-\pi/a$). Away from

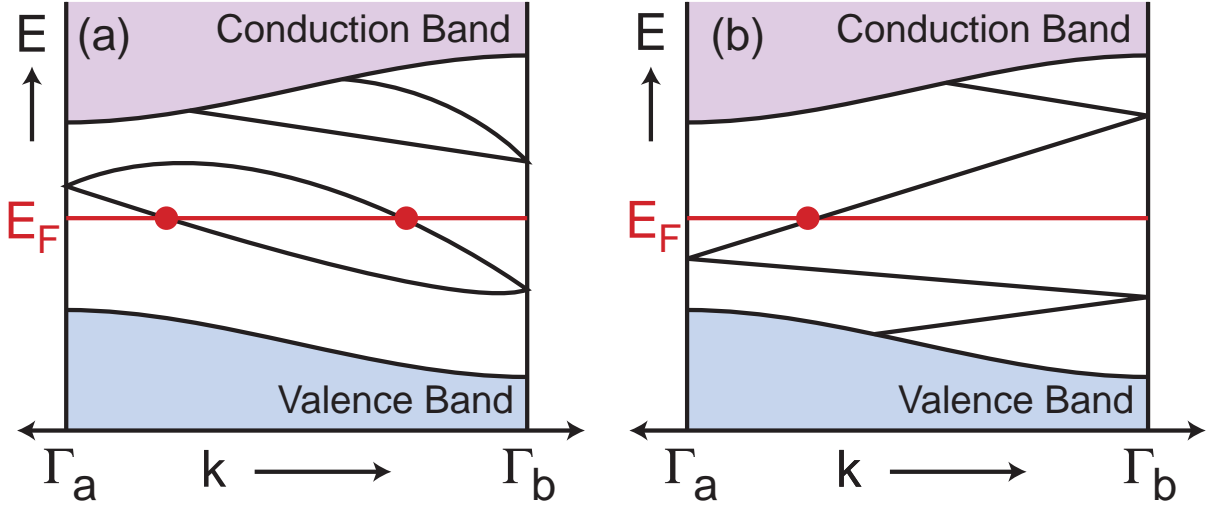


Figure 7.9: Electronic dispersion between two boundary Kramers degenerate points $\Gamma_a = 0$ and $\Gamma_b = \pi/a$. In (a) the number of surface states crossing the Fermi energy E_F is even, whereas in (b) it is odd. An odd number of crossings leads to topologically protected metallic boundary states. Adapted from [81].

these special points, labeled $\Gamma_{a,b}$ in Fig. 7.9, a spin orbit interaction will split the degeneracy. There are two ways the states at $k_x = 0$ and $k_x = \pi/a$ can connect. In Fig 7.9(a) they connect pairwise. In this case the edge states can be eliminated by pushing all of the bound states out of the gap. Between $k_x = 0$ and $k_x = \pi/a$, the bands intersect E_F an even number of times. In contrast, in Fig. 7.9b the edge states cannot be eliminated. The bands intersect E_F an odd number of times.

Which of these alternatives occurs depends on the topological class of the bulk band structure. Since each band intersecting E_F at k_x has a Kramers partner at $-k_x$, the bulk-boundary correspondence relates the number N_K of Kramers pairs of edge modes intersecting E_F to the change in the \mathbb{Z}_2 invariants across the interface,

$$N_K = \Delta\nu \bmod 2. \quad (7.19)$$

There are several mathematical formulations of the \mathbb{Z}_2 invariant ν [24, 122, 83, 123, 124, 125, 126, 127, 128]. We describe here only one approach [122]. First, we define a unitary matrix $w_{mn}(\mathbf{k}) = \langle u_m(\mathbf{k}) | \Theta | u_n(-\mathbf{k}) \rangle$ built from the occupied Bloch functions $|u_m(\mathbf{k})\rangle$. Since Θ is antiunitary and $\Theta^2 = -1$, $w^T(\mathbf{k}) = -w(-\mathbf{k})$. There are four special points Λ_a in the bulk 2D Brillouin zone where \mathbf{k} and $-\mathbf{k}$ coincide, so $w(\Lambda_a)$ is antisymmetric. The determinant of an antisymmetric matrix is the square of its Pfaffian, which allows us to define $\delta_a = \text{Pf}[w(\Lambda_a)] / \sqrt{\text{Det}[w(\Lambda_a)]} = \pm 1$. Provided $|u_m(\mathbf{k})\rangle$ is chosen continuously throughout the Brillouin zone (which is always possible), the branch of the square root can be specified globally,

and the \mathbb{Z}_2 invariant is

$$(-1)^\nu = \prod_{a=1}^4 \delta_a. \quad (7.20)$$

This formulation can be generalized to 3D topological insulators, and involves the 8 special points in the 3D Brillouin zone.

It is important to note that even if the z -component of spin is not conserved (as for a Rashba SO coupling, for example), as soon as the TRS is preserved one can always define a pair of states constituting a Kramers' doublet. In this case S_z is not a good quantum number and these states do not have particular spin polarization.

Chapter 8

Topological insulating phase in functionalized graphene

In this chapter we will propose a way how non-trivial topological phase can be induced in graphene. In previous chapter we saw that a certain type of spin-orbit interaction could turn graphene into a topological insulator. In practice, however, estimates done in the previous works [25] show that in a pristine graphene all types of SO coupling are extremely small to be visible. Namely, estimated value of the intrinsic SO gap induced as a consequence of mixing between σ and π orbitals due to intra-atomic SO coupling is ~ 10 mK (see Table 7.1). Similarly, Rashba SO interaction caused by a perpendicular electric field and a curvature of a graphene surface are too small to be observed [25].

Here, we propose a model which could provide a way to observe the quantum spin Hall effect in graphene in a controlled way even at quite high temperatures, ~ 100 K. Elaborating the initial idea by Weeks *et al.* [26] based on DFT calculations, we investigate the effective low-energy model of graphene functionalized with a special type of adatoms. In their work Weeks *et al.* have shown that Tl and In heavy atoms when deposited on a surface of graphene induce locally strong intrinsic SO interaction while keeping small spin mixing perturbations. Within this model we were able to show [27], that even at very low concentration of these adatoms it is possible to observe a perfectly homogeneous QSH phase with a renormalized SO coupling constant. We do multiterminal transport calculations which prove the validity of our arguments. The effect of on-site Anderson disorder on the QSH phase was also considered. It turns out that unrealistically big disorder strength is needed to destroy the phase, which proves its topological nature. In the end of the chapter we discuss a possible application of the peculiar transport characteristics of the QSH phase for thermopower applications.

8.1 Initial proposal

Here we give a review of the seminal work by Weeks *et al.* [26] which motivated our further research in this direction. Observing QSH effect in graphene is a difficult task since in a pristine structure it is expected to happen in an extremely small energy window close to a Dirac point. That is why it is obscured by the fluctuations in electrochemical potential or disorder (coming from a substrate, for example) which create electron-hole puddles [129, 130] washing away the effects we are interested in. So, in order to overcome this limitation one needs to enhance the initially weak SO interaction in graphene. Specifically, in the work [26] the authors investigate how graphene can "inherit" strong spin-orbit coupling from a dilute concentration of heavy adatoms (whose innate spin-orbit coupling strength can be on the electron-volt scale) deposited randomly into the honeycomb lattice.

The basic principle underlying their proposal can be understood by considering processes in which an electron from graphene tunnels onto an adatom – whereupon it "feels" enormous spin-orbit coupling – and then returns to the graphene sheet. Though the principle may seem to be quite simple, presence of adatoms might create several competing effects. For instance, adatoms often form local magnetic moments [131] which potentially spoil the time-reversal symmetry protecting the QSH effect. Moreover, adatoms generically mediate both intrinsic and Rashba spin-orbit coupling. The latter is believed to be detrimental to the QSH phase [24, 23], and previous work has indeed established that certain kinds of adatoms do generate substantial Rashba coupling in graphene that typically overwhelms the intrinsic contribution [108, 109, 132]. The adatoms may also favor competing, ordinary insulating states depending on their precise locations in the lattice. And finally, since spin-orbit coupling is generated non uniformly in graphene, the stabilization of a QSH phase even in an otherwise ideal situation is unclear *a priori*.

8.1.1 The setup

In order to investigate the influence of adatoms on electronic and transport properties of graphene, Weeks *et al.* have used a mixture of numerical methods and symmetry-based arguments. They considered three different occupations an adatom can in principle have when deposited on the surface of graphene, see Fig. 8.1. If heavy adatoms are to stabilize a more robust QSH phase in graphene, then, at a minimum, they should be nonmagnetic (to preserve time-reversal symmetry) and modify the physics near the Dirac points primarily by inducing large intrinsic spin-orbit coupling. The latter criterion leads us to focus on elements favoring the "hollow" (H) position in the graphene sheet indicated in Fig. 8.1a. Compared to the "bridge" (B) and "top" (T) positions, adatoms in the H position can most effectively mediate the spin-dependent second-neighbor hoppings present in the Kane-Mele model, while simultaneously

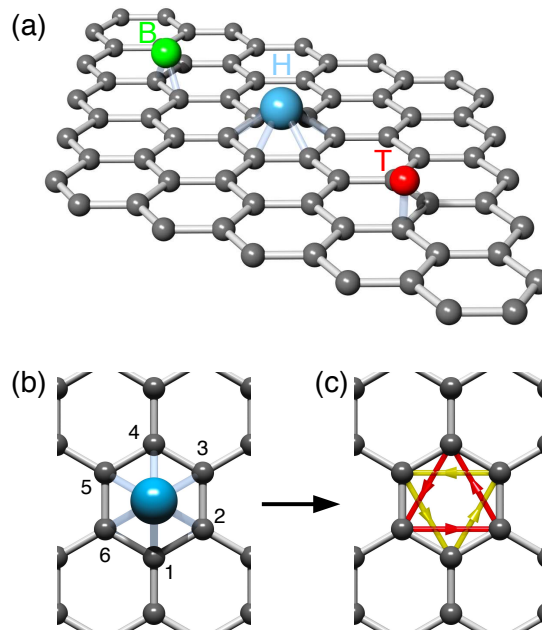


Figure 8.1: Adatoms in graphene. (a) Depending on the element, adatoms favor either the high-symmetry "bridge" (B), "hollow" (H), or "top" (T) position in the graphene sheet. (b) Detailed view of an H position adatom, which is best suited for inducing the intrinsic spin-orbit coupling necessary for stabilizing the topological phase. The desired spin-orbit terms mediated by the adatom are illustrated in (c). Red and yellow bonds represent the induced second-neighbor imaginary hopping, whose (positive) sign is indicated by the arrows for spin-up electrons. For spin-down electrons the arrows are reversed. Adapted from [26].

avoiding larger competing effects such as local sublattice symmetry-breaking generated in the T case.

Since H-position adatoms generically reside on one side of the graphene sheet, they will clearly mediate Rashba spin-orbit coupling as well, leading to a potentially delicate competition. If the adatoms' outer-shell electrons derive from p orbitals, however, the induced intrinsic spin-orbit terms always dominate over the induced Rashba interactions [26]. The latter arguments define the choice of the H-position adatoms for further considerations.

8.1.2 Numerical DFT simulations and effective TB description

As a first step in understanding the multiadatom case, authors in [26] examined a periodic system with one adatom residing in a large $N \times N$ supercell. This situation allowed them to utilize density functional theory (DFT) to ascertain suitable heavy elements and obtain a quantitative understanding of their effects on graphene. To ensure large spin-orbit coupling, they focused on elements in rows five and six of the periodic table, including In, Sn, Sb, Te, I,

La, Hf, Pt, Au, Hg, Tl, Pb and Bi. For each element, they calculated the total energy in the three adsorption geometries shown in Fig. 8.1a along with the adatom's spin moment. These calculations reveal that two elements—indium (atomic number $Z = 49$) and thallium ($Z = 81$)—satisfy the criteria of both favoring the high-symmetry H position and being nonmagnetic. Furthermore, both elements exhibit partially filled p shells, ensuring that the Rashba coupling they mediate in graphene is benign at the Dirac points.

For In and Tl heavy atoms Weeks *et al.* investigated thoroughly the band structure of graphene with one such atom per 4×4 supercell, see Fig. 8.2. On Figs. 8.2a,d they plot the band structure of graphene in the presence of adatoms assuming that *there is no SO coupling*. Though the translational invariance of the lattice is reduced, we still see a Dirac cone in the vicinity of zero-energy point. Other panels on Fig. 8.2 demonstrate the band structure *with non-zero SO coupling* where we clearly see a gap opening. This proves that the gap originates from the SO interaction and (as will be demonstrated below) has a non-trivial topological nature. Authors have also considered dependence of the induced gap as a function of adatom concentration (see Fig. 8.3), i.e. one adatom per 5×5 , 7×7 , and 10×10 supercells.

Quite naturally, the gap decreases as one reduces the coverage, as does the Fermi level since fewer electrons are donated to graphene at lower adatom concentrations. It is worth highlighting that the gap decreases sublinearly and that a sizable $\Delta_{so} \approx 10$ meV remains even with a mere 2.04% thallium concentration.

We move on to simplify the model further in order to investigate low-energy transport properties of the insulating phase in graphene. Weeks *et al.* considered first a full tight-binding model of functionalized graphene taking into account adatom's degrees of freedom. But it turns out that for the mentioned above In or Tl atoms (with partially filled p shells) it is possible to integrate out these degrees of freedom and derive an effective model of graphene with second nearest neighbors hopping in the vicinity of a Dirac point (encircled regions on Fig. 8.2),

$$H = H_t + \sum_I \delta H_I - \sum_{\mathbf{r}} \delta \mu_{\mathbf{r}} c_{\mathbf{r}}^{\dagger} c_{\mathbf{r}}. \quad (8.1)$$

Here $\delta \mu_{\mathbf{r}}$ represents a random on-site potential arising, *e.g.*, from the substrate (and not the adatoms), H_t is a usual first nearest neighbors Hamiltonian of graphene (5.16),

$$H_t = -t \sum_{\langle \mathbf{r}\mathbf{r}' \rangle} (c_{\mathbf{r}}^{\dagger} c_{\mathbf{r}'} + \text{H.c.}). \quad (8.2)$$

In the second term in Eq.(8.1), I labels the random plaquettes (hexagons) occupied by adatoms and

$$\delta H_I = -\delta \mu \sum_{\mathbf{r} \in I} c_{\mathbf{r}}^{\dagger} c_{\mathbf{r}} + \lambda_{so} \sum_{\langle \langle \mathbf{r}\mathbf{r}' \rangle \rangle \in I} (i\nu_{\mathbf{r}\mathbf{r}'} c_{\mathbf{r}}^{\dagger} s^z c_{\mathbf{r}'} + \text{H.c.}) + i\lambda_R \sum_{\mathbf{r}, \mathbf{r}' \in I} c_{\mathbf{r}}^{\dagger} (\mathbf{s} \times \mathbf{d}_{\mathbf{r}\mathbf{r}'})_z c_{\mathbf{r}'} \quad (8.3)$$

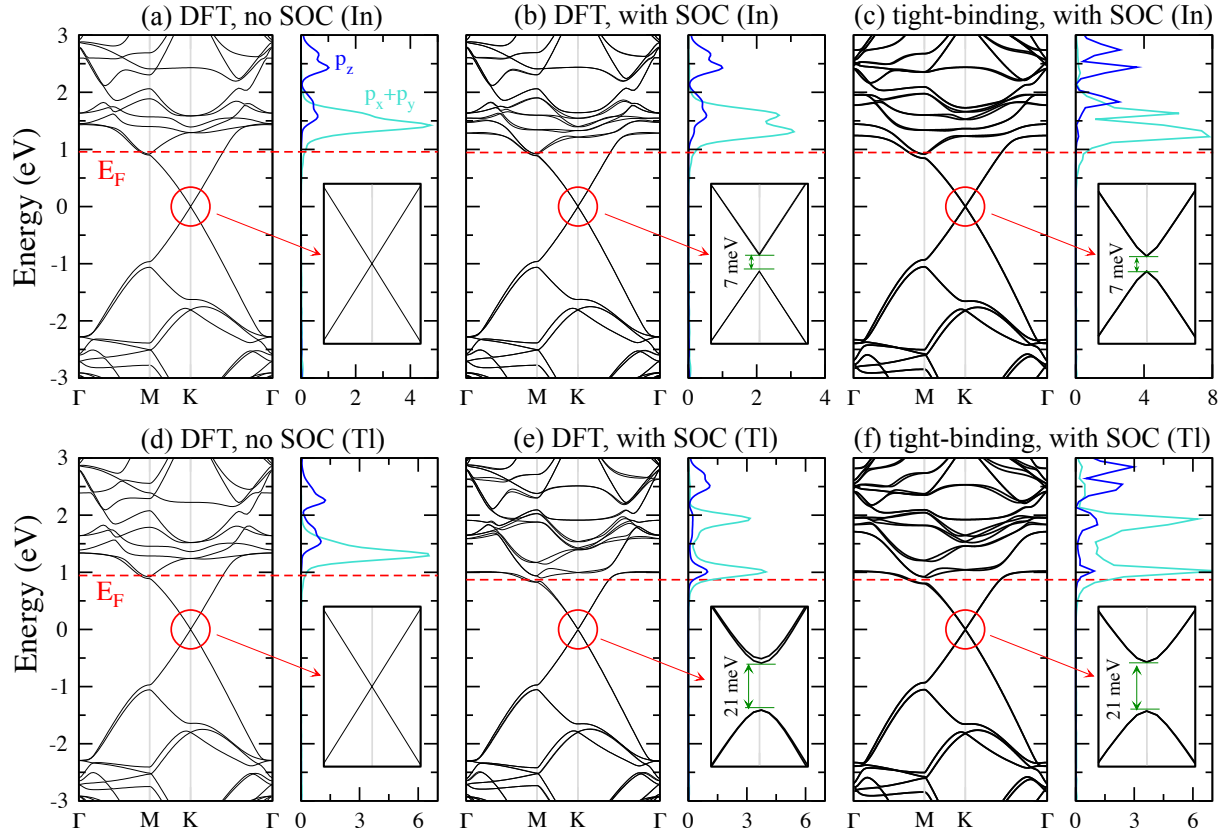


Figure 8.2: Band structure and the adatom local density of states (LDOS). All data correspond to one adatom in a 4×4 supercell, with the upper row corresponding to indium and the lower row corresponding to thallium. The left panels in (a) and (d) correspond to the band structure and LDOS computed using DFT *without* spin-orbit coupling. The horizontal dashed lines indicate the Fermi level (E_F), which shifts due to electron-doping from the adatoms. Insets zoom in on the band structure near the K point within an energy range -35 to 35 meV, showing that without spin-orbit interactions neither indium nor thallium open a gap at the Dirac points. The central panels in (b) and (e) are the corresponding DFT results including spin-orbit coupling. Remarkably, in the indium case a gap of 7 meV opens at the Dirac point, while with thallium the gap is larger still at 21 meV. Finally, the right panels in (c) and (f) were obtained using the tight-binding model taking into account the adatoms' degrees of freedom [26]. Adapted from [26].

with $\mathbf{d}_{\mathbf{r}\mathbf{r}'} = (\mathbf{r} - \mathbf{r}')/|\mathbf{r} - \mathbf{r}'|$. The first term in δH_I describes the chemical potential that screens charge from the adatoms, while the last two terms capture the local intrinsic (λ_{so}) and Rashba (λ_R) spin-orbit couplings induced by electrons hopping from graphene to an adatom and back. \mathbf{s} is a vector of Pauli matrices in the spin space, and $\nu_{\mathbf{r}\mathbf{r}'}$ are signs that equal $+1$, if an electron hops in the direction of the arrows in Fig. 8.1c, and -1 otherwise (see also Fig. 7.5). It is

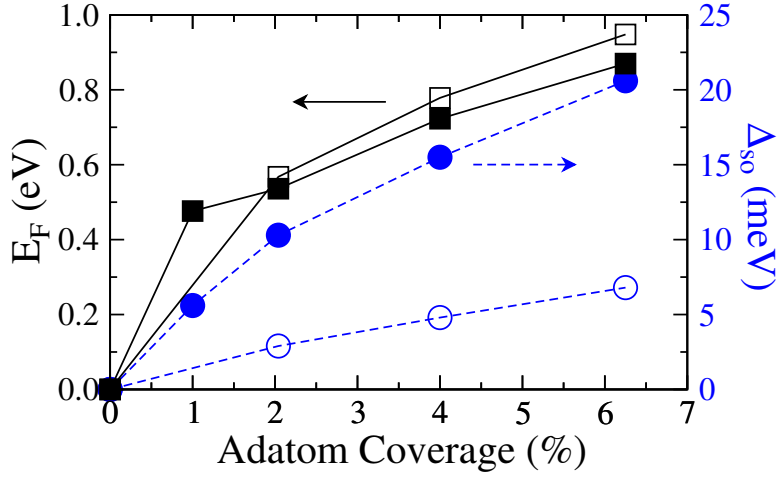


Figure 8.3: Coverage Effects. Spin-orbit-induced gap Δ_{so} opened at the Dirac points and Fermi level E_F (measured relative to the center of the gap) for different indium and thallium adatom coverages. The open and filled symbols represent data for indium and thallium, respectively. Adapted from [26].

important to notice that, unlike the conventional nearest-neighbor Rashba term considered in the Kane-Mele model (see Sec. 7.2) for pristine graphene [24], the adatom-generated Rashba term connects *all* sites in the hexagon. Such a "hexagon Rashba term" has the property of vanishing at the Dirac points. The latter is crucial for choosing this certain type of adatoms in order to induce a topological phase in graphene. The adatom also induces other symmetry-allowed terms, such as further-neighbor spin-independent hoppings, which we disregard because they either are weak or do not lead to qualitative changes in the results reported below [26].

8.1.3 Relation between the Kane-Mele model and adatoms' effective model

In this subsection we will show that the adatoms' effective model can be adiabatically continued to the Kane-Mele model [23, 24]. Since the Kane-Mele model is known to exhibit non-trivial topological properties of the insulating phase, this means that the gap induced by the presence of adatoms drives graphene to a topological insulator of the same kind. The latter is due to the fact that the properties of a topological insulator can change only abruptly. The possibility of adiabatic continuation from one model to another guarantees that a system is always in the same phase characterized by a certain topological invariant (in our case \mathbb{Z}_2 [24], see Sec. 7.2.2).

In order to prove this statement, Weeks *et al.* considered a model described by the Hamiltonian $H(\lambda) = (1 - \lambda)H_{N \times N} + \lambda H_{KM}$, which interpolates between the Hamiltonian of graphene with one adatom per $N \times N$ supercell ($\lambda = 0$) and the Kane-Mele Hamiltonian ($\lambda = 1$). The

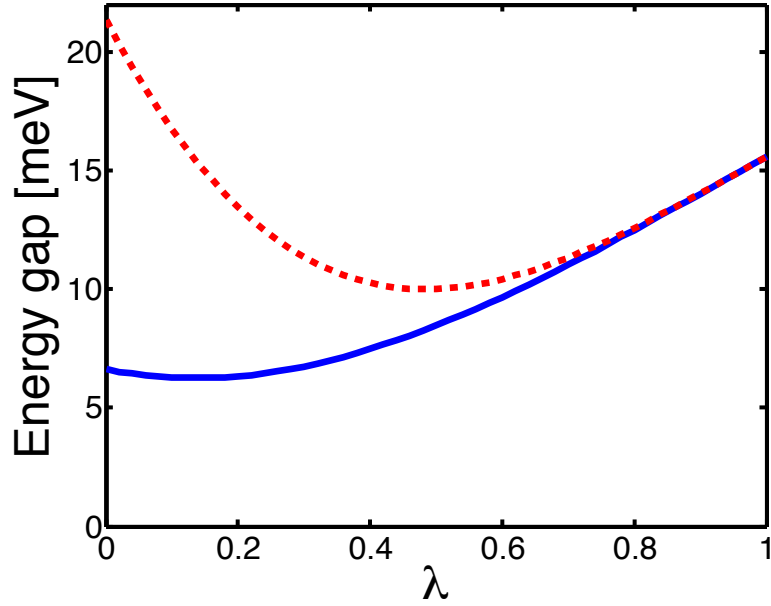


Figure 8.4: Adiabatic continuity. Energy gap at the Dirac point as the Hamiltonian adiabatically deforms from the periodic adatom Hamiltonian $H_{4\times 4}$ at $\lambda = 0$ to the Kane-Mele model at $\lambda = 1$. The solid blue and dashed red lines correspond to $H_{4\times 4}$ evaluated with parameters appropriate for indium and thallium, respectively. In both cases the gap remains finite as λ varies from 0 to 1, indicating that the Kane-Mele model and adatom Hamiltonian are adiabatically connected and thus support the same quantum spin Hall phase. Adapted from [26].

authors considered the case $N = 4$, but the result is general of course as changing N means changing the concentration of adatoms, which in turn can only vary the value of the SO gap (see Fig. 8.3) while keeping it different from zero. Then, varying parameter λ we extract the SO gap induced at the Dirac point, see Fig. 8.4. The curves on Fig. 8.4 illustrate that the Dirac-point gap computed for $H(\lambda)$ indeed remains finite for all λ between 0 to 1 with either indium (solid blue line) or thallium (dashed red line) parameters put into $H_{4\times 4}$. The QSH state known to be supported by H_{KM} and the insulating state stabilized by either type of adatom are, consequently, the same topological phase of matter.

8.1.4 Transport properties of graphene with randomly distributed adatoms

In the end of this section we briefly recall the results by Weeks *et al.* that motivated us to study the model of functionalized graphene in more details. In their work authors considered a two terminal setup, more specifically a graphene ribbon with a central region covered with adatoms and clean semi-infinite parts attached to it, which play a role of contacts (see Fig. 8.5a).

They investigate the robustness of the QSH phase in the presence of random adatoms and

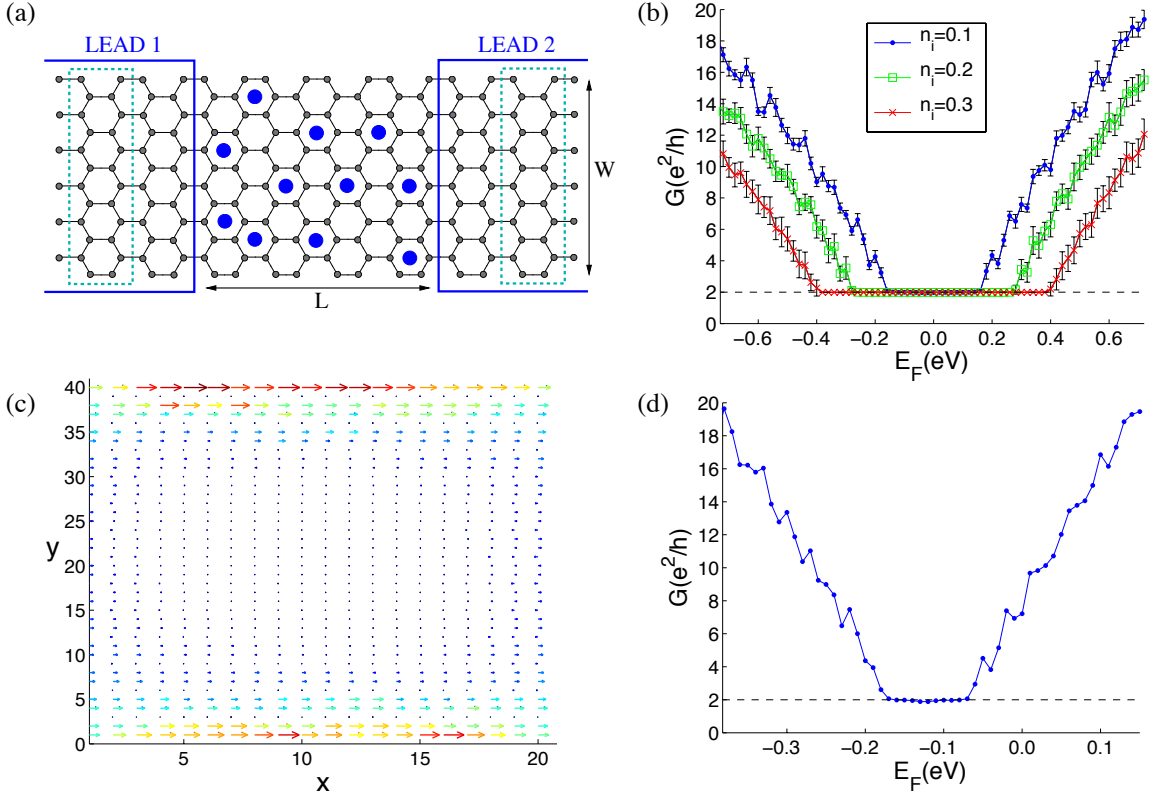


Figure 8.5: Transport. (a) Configuration used to determine the two-terminal conductance. Semi-infinite clean graphene leads are connected to the sample, which has adatoms distributed randomly across it. The length L of the system is set by the number of columns (indicated by dotted rectangles). The width W is set by the number of dimer lines. (b) Conductance G as a function of the Fermi energy E_F , averaged over 40 independent random adatom realizations at different concentrations $n_i = 0.1, 0.2, 0.3$ for a system of size $W = 80$ and $L = 40$ with $\lambda_{so} = 0.1t$. (c) Current distribution across a sample of size $W = 40$ and $L = 20$ at $n_i = 0.2$, $\lambda_{so} = 0.1t$ and $E_F = 0.15eV$. The magnitude of the current is represented by both the arrow size and color. (d) Conductance for the largest simulated system size using realistic parameters for thallium adatoms ($\lambda_{so} = 0.02t$ and $\delta\mu = 0.1t$) estimated from DFT data. Here $W = 200$, $L = 100$, and the coverage is $n_i = 0.15$. In all panels we take $t = 2.7$ eV. Adapted from [26].

disorder by simulating the classic two-terminal conductance measurement. Since zigzag edges are known to support gapless edge states (of a qualitatively different kind) even in pristine graphene [97, 133], to avoid complications we focus here on graphene strips with armchair edges. However, the results reported below remain valid for arbitrary edge configurations, as long as the bulk remains in the topological phase.

First, they consider the simplest setup which takes into account only intrinsic SO coupling λ_{so} and neglects the effects of disorder, $\delta\mu_{\text{r}} = 0$, as well as other adatom's terms, $\delta\mu = 0$ and $\lambda_{\text{R}} = 0$. Figure 8.5b illustrates the conductance for this case at several adatom concentrations n_i and model parameters indicated in the caption. A $2e^2/h$ plateau with width proportional to n_i clearly emerges, strongly suggesting the onset of a bulk mobility gap and quantized ballistic conduction by edge states. This picture is corroborated by Fig. 8.5c, which displays the current distribution for $E_{\text{F}} = 0.15$ eV across a smaller system size (chosen for clarity). These results establish that, in principle, adatoms' distribution need not be periodic to stabilize a QSH phase. To make contact with their DFT results, Weeks *et al.* also considered a system with $\lambda_{\text{so}} = 0.02t$ and $\delta\mu = 0.1t$, which would yield a similar bulk mobility gap to that seen in their thallium simulations if the adatom coverages were the same. While finite-size effects prevent them from studying the low-adatom coverages, Fig. 8.5d shows that, for $n_i = 0.15$, a robust conductance plateau indeed persists for these more realistic parameter values. They have also studied the effects of the hexagon Rashba term and residual on-site potential disorder on the stability of the QSH phase. Even a relatively large $\lambda_{\text{R}} \sim 2\lambda_{\text{so}}$ has a weak effect on the width of the conductance plateau. With uncorrelated on-site disorder $\delta\mu_{\text{r}}$, the topological phase is also remarkably robust – $\delta\mu_{\text{r}}$ can fluctuate on the scale of t while degrading the plateau only marginally. The topological phase is more sensitive, however, to correlated disorder which is likely more relevant experimentally. In this case, the conductance plateau survives only when $\delta\mu_{\text{r}}$ varies on a scale smaller roughly than the mobility gap for the clean case.

For one to observe the QSH phase experimentally, the chemical potential should therefore fluctuate on scales smaller than the 10 meV gaps predicted by Weeks *et al.* in [26]. This should be possible for certain substrates, as hexagonal boron nitride substrates [134] for example, which show disorder energy scales as low as 15 K.

8.2 Quantum spin Hall phase induced by randomly deposited adatoms

As we have seen from the previous chapter, there is a possibility (in principle) to enhance SO coupling in graphene by deposition of certain type of heavy atoms on its surface. In the work by Weeks *et al.* [26], they proposed an effective low-energy model of such a setup, as was discussed above. Two-terminal conductance simulations carried by the authors showed the signatures of the QSH phase. However, they did not try to investigate the properties of the phase itself and its dependence on the concentration of adatoms in finite-size samples.

In this chapter we present our recent work concerning this question [27]. We elaborate in more details the model proposed by Weeks *et al.* in order to identify effective parameters characterizing the QSH phase in a system with random distribution of adatoms. We make our

study based on transport simulations as well. But it turns out that one needs to have more than two terminals in order to extract more information about the QSH phase.

8.2.1 Parametric study of the QSH phase

Since the effects of disorder and Rashba SO coupling in most cases are not important if we study effects at energies within the SO gap as was discussed above, we concentrate on the model of graphene with intrinsic SO coupling only. This means that we take $\delta\mu_r = 0$, $\delta\mu = 0$, and $\lambda_R = 0$ in Eq.(8.1). The nearest-neighbor hopping $t = 2.7$ eV will set the energy scale: hereafter all energies are expressed in units of t while sizes are expressed in units of $\sqrt{3}a_{c-c}$.

In order to monitor the existence of the QSH phase, we focus on the signature of the associated edge modes on the conductance matrix of a multi-terminal sample. The latter is given by the multi-terminal Landauer-Büttiker formula (see Sec. 2.2), which expresses the current I_α flowing in the electrode α (see upper inset of Fig. 8.6 for a sketch of the sample) in presence of a potential V_β as

$$I_\alpha = \frac{e^2}{h} \sum_{\beta} T_{\alpha\beta} V_\beta, \quad (8.4)$$

where $T_{\alpha\beta}$ is the transmission coefficient between two electrodes. It can be computed numerically from the knowledge of the retarded Green's function G via the formula ($\alpha \neq \beta$) [52, 45]

$$T_{\alpha\beta} = \text{Tr}[\Gamma_\alpha G \Gamma_\beta G^\dagger], \quad (8.5)$$

with $\Gamma_\alpha = \text{Im}(\Sigma_\alpha)$, where Σ_α is the self-energy of lead α , and with the Green's function given by the expression

$$G(E) = (E - H - \sum_{\alpha} \Sigma_\alpha)^{-1} \quad (8.6)$$

(with the Hamiltonian H in its first quantization form). In the QSH phase the transmission between successive probes reads exactly $T_{\alpha,\alpha+1} = T_{\alpha,\alpha-1} = 1$, while all other transmission coefficients $T_{\alpha,\beta}$ ($\alpha \neq \beta$) vanish. In the following, we will use this unique characterization of the QSH phase in the 4-terminal cross geometry of Fig. 8.6. The 4-terminal geometry always provides an unambiguous characterization of this phase, as opposed to the two-terminal conductance where $g_{2T} = 2e^2/h$ can be observed at the Dirac point independently of the presence of SO interaction.

We also pay special attention to avoid the appearance of spurious effects in nano-ribbon geometries. Structural boundary conditions of graphene are of two types: armchair and zigzag. The latter features a zero-energy edge state, signatures of which have been shown to obscure the appearance of the QSH edge state [119]. Therefore we will henceforth consider armchair-terminated graphene systems in order to avoid confusion between different types of edge states. Armchair ribbons are themselves divided into two families [96]: they can be either metallic or

semiconducting depending on their width (see Sec. 5.3). In the following, we focus on metallic armchair ribbons to avoid the competition between the SO-interaction-induced gap and the finite-width-induced gap (see discussion in the end of Sec. 7.2.1). We use a cross-like geometry, with a fixed aspect ratio (see inset of Fig. 8.6) and smallest width W at contacts 1 and 3: the shape of the sample has been chosen such that most of the current is directly transmitted from 0 to 2 in the absence of SO interaction. The numerical calculations were performed using the KNIT package which implements a generalization of the recursive Green function algorithm to multi-terminal systems [22].

Fig. 8.6 shows the “longitudinal” T_{20} and “Hall” T_{10} , T_{30} transmission coefficients as a function of the strength of the SO interaction and for various concentrations n_{ad} of adatoms. One observes, as expected, that upon increasing the strength of λ_{so} for a fixed concentration n_{ad} of adatoms, one enters the QSH phase: the Hall coefficients tend to unity while the longitudinal one vanishes. The upper inset shows the actual up spin current density inside the sample in the QSH regime: we recover the expected edge state characteristics of the QSH phase, including an exponential decay of the current as a function of the distance to the edge but also oscillations with frequency $|\mathbf{K}|$ coming from the valley-mixing armchair boundary condition [119] (see equations (7.14) and (7.15)). The crucial point shown in Fig. 8.6 is that *all the results* are rescaled as a function of the effective SO interaction strength

$$\lambda_{\text{so}}^{\text{eff}} = \lambda_{\text{so}} n_{\text{ad}} . \quad (8.7)$$

In other words, the QSH phase, while originating from a very inhomogeneous sample, is perfectly described in *each sample* by an effective homogeneous phase with a uniform coverage but a reduced SO strength. In this phase, each adatom occupying one of the plaquettes spreads its coupling λ_{so} over a distance $\xi_{\text{ad}} = 1/\sqrt{n_{\text{ad}}}$, resulting in a weaker effective SO interaction strength $\lambda_{\text{so}}^{\text{eff}} = \lambda_{\text{so}}/\xi_{\text{ad}}^2$ but a uniform effective full coverage $n_{\text{ad}} = 1$. The surprising occurrence of this mean-field description in each disordered sample and down to very small concentrations can be attributed to the large localization length ξ of the QSH edge states (see below). This large value of ξ also explains why rather large values of $\lambda_{\text{so}}^{\text{eff}}$ are required to observe perfect “Hall” transmissions in the small samples considered in Figs. 8.6 and 8.7. In real, μm -sized samples, the required value of $\lambda_{\text{so}}^{\text{eff}}$ will be much smaller since deviations to perfect “Hall” effect are controlled by the ratio W/ξ between the width of the small arm W and the localization length ξ (see Fig. 8.9 below).

We have found that the above *effective homogeneous description* is very robust and applies for (i) a single realization of the adatom configuration, i.e. does not require disorder averaging, (ii) various sizes from wide samples deep into the QSH phase down to narrow samples where the edge states on both sides of the sample have a finite overlap, (iii) different energies, from the Dirac point up to the SO-interaction-induced gap. To illustrate this robustness, we performed some statistics and show in Fig. 8.7 how the transmission coefficients vary from one adatom

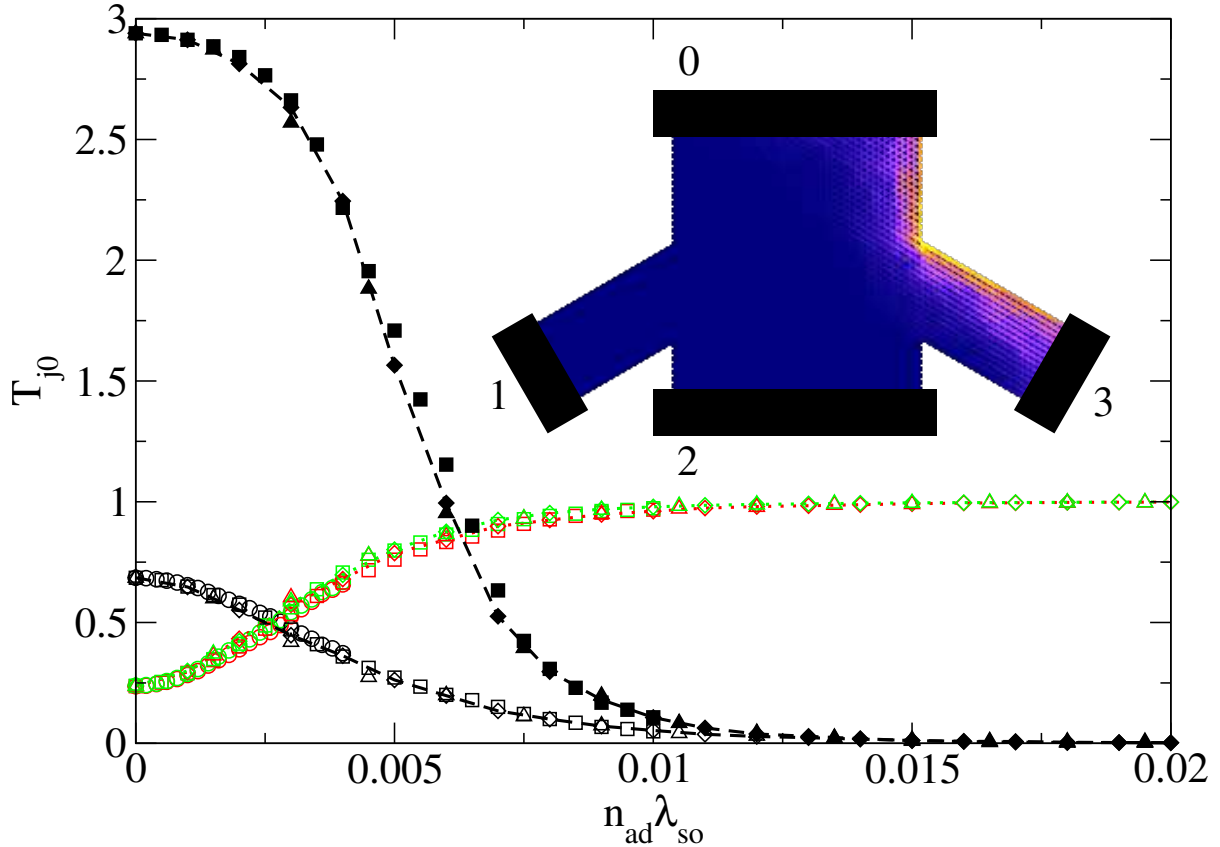


Figure 8.6: Upper inset: schematic of our setup: a 4-terminal graphene cross with armchair edges and width of the small arm $W = 21.5$. The different colors correspond to an actual calculation of the current density for spin-up electrons upon injection from contact 0. The existence of an edge state is manifest. Main figure: Scaling of the transmissions T_{j0} from contact 0 for various couplings λ_{so} and adatom densities n_{ad} , plotted as a function of the effective SO coupling strength $\lambda_{\text{so}}^{\text{eff}} = \lambda_{\text{so}} n_{\text{ad}}$. Dashed (black) lines correspond to “longitudinal” transmission T_{20} and dotted lines correspond to “Hall” transmissions T_{10} (red) and T_{30} (green). The two sets of curves correspond to an energy $E = 0$ (open symbols), and $E = 0.05$ (filled symbols). Different symbol shapes correspond to different values of SO coupling, respectively $\lambda_{\text{so}} = 0.02$ (circles), 0.05 (squares), 0.1 (diamonds) and 0.15 (triangles). Note that no averaging over adatom configurations has been performed here.

configuration to another. The “envelope” curves displayed in Fig. 8.7 correspond to the average transmission plus or minus one standard deviation (i.e. for a Gaussian distribution there is a 68% probability that the outcome will fall inside the envelope for a given adatom configuration). At small SO coupling, the system is essentially ballistic with very small (Gaussian) fluctuations. At large SO coupling, the system is deep in the QSH phase with small (log-normal) fluctuations (the inset of Fig. 8.7 shows the actual probability distributions). We find that, in the crossover

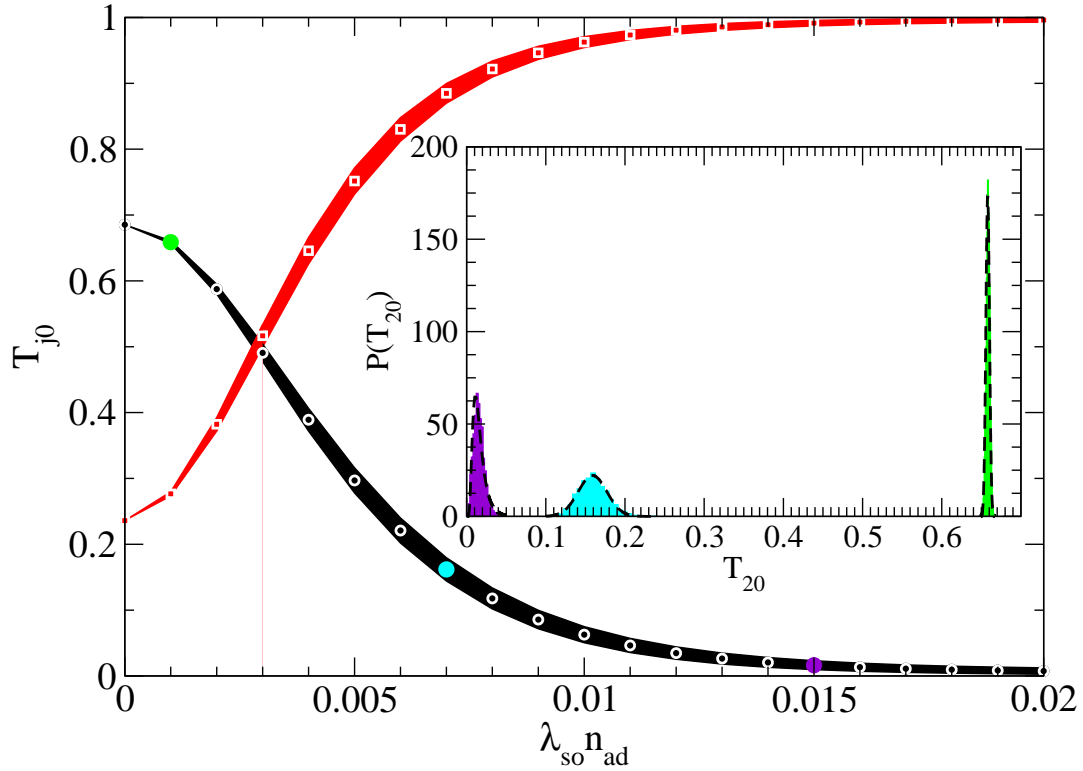


Figure 8.7: Statistics of the transmission coefficients T_{20} (lower curve, black) and T_{30} (upper curve, red) when averaged over 2500 adatom configurations, as a function of the effective SO coupling strength. The shaded regions represent one standard deviation from the mean value which is indicated by white symbols (circles for T_{20} and squares for T_{30}). The corresponding density of probability for 3 points (green, cyan and violet filled circles, from left to right) are given in the inset: as the SO coupling increases, the probability distribution $P(T_{20})$ shifts from a Gaussian (green and cyan) to a log-normal (violet). Fits are indicated by dashed lines. All data points were generated for an energy $E = 0$, a fixed adatom density $n_{ad} = 0.1$, and the same system sizes as in Fig. 8.6.

between these two limits, the fluctuations remain remarkably low for all values of the effective SO coupling strength. Additionally, we saw no evidence for a breakdown of our mean-field description, even down to very low adatom concentrations.

A celebrated property of a topological phase is its robustness with respect to the presence of disorder. The persistence of this property in the present context can easily be checked by

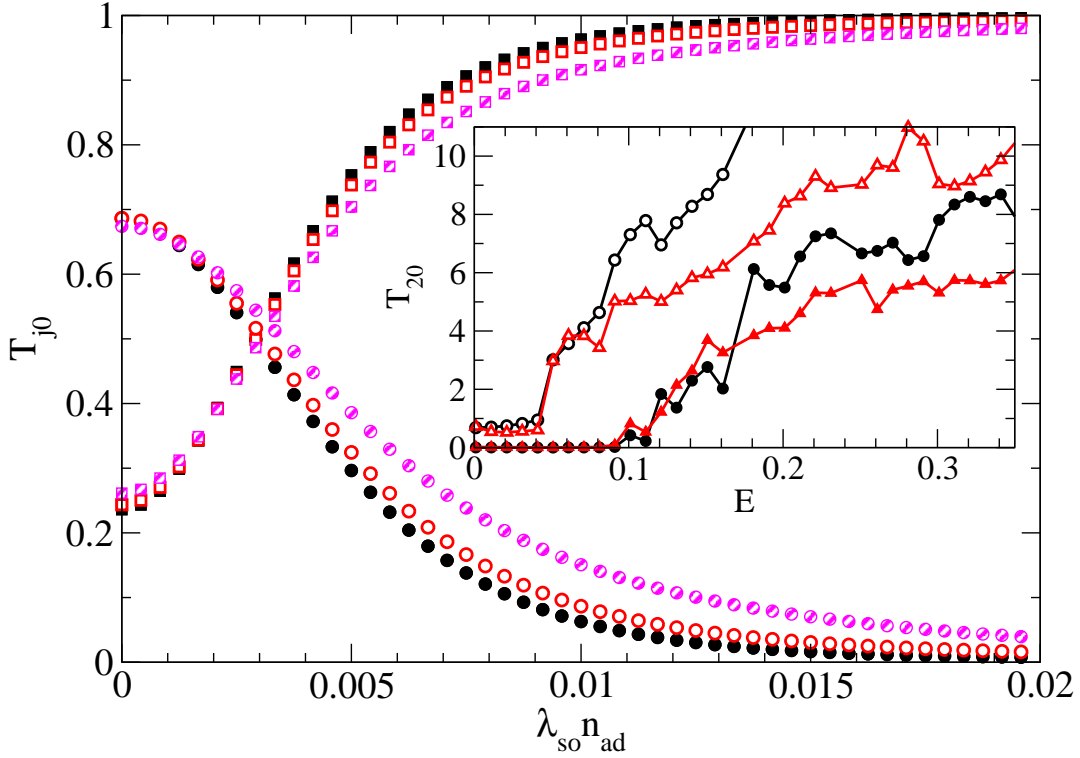


Figure 8.8: Transmission coefficients T_{20} (circles) and T_{30} (squares) as a function of the effective SO coupling strength, for various values of onsite disorder: $V = 0$ (filled black), $V = 0.4$ (empty red) and $V = 0.8$ (hashed magenta). No qualitative change is brought about by disorder, although some deviation from the $V = 0$ curve in the crossover region between the metal and the QSH phases starts to be visible at strong enough ($V = 0.8$) disorder. The data were averaged over 50 distinct realizations of disorder and adatom configuration for each value of $\lambda_{\text{so}}^{\text{eff}}$. The energy was kept at $E = 0$, and the system sizes as in Fig. 8.6. Inset: Longitudinal transmission T_{20} as a function of energy for $\lambda_{\text{so}}^{\text{eff}} = 0$ (empty symbols) and $\lambda_{\text{so}}^{\text{eff}} = 0.02$ (filled symbols). Circles are for $V = 0$ and triangles for a single disorder configuration with $V = 0.8$. Disorder has no effect on T_{20} in the QSH phase ($E < \Delta_{\text{so}} \approx 0.1$).

adding on-site disorder (on each site) to the Hamiltonian, following the standard prescription

$$H_{\text{dis}} = \sum_{i,\alpha} V_i c_{i,\alpha}^\dagger c_{i,\alpha}, \quad (8.8)$$

where V_i is a disorder strength randomly distributed in the interval $[-V/2, V/2]$. The transmission coefficients as a function of the effective spin-orbit coupling for several values of V are

shown in Fig. 8.8. As expected for a topological phase, the presence of disorder provides no qualitative (and hardly any quantitative) modification to the general picture described earlier. Deviations from the “clean” ($V = 0$) case remain small, unless the strength of disorder reaches (extremely strong) values of the order of the hopping parameter t . Note that, in the main panel of Fig. 8.8, the Fermi energy is very close to the Dirac point. It is well established that disorder has a very small effect on the metallic phase (at small λ_{so}) close to the Dirac point [135, 136]. This point can be understood from a semi-classical consideration: close to the Dirac point, the Fermi wave length diverges so that only very long range disorder affects the physics.

Away from the Dirac point, onsite disorder does affect the transport properties of graphene, but not of the QSH phase. This is best seen in the inset of Fig. 8.8 where we plot the longitudinal transmission T_{20} as a function of the Fermi energy in the presence/absence of spin-orbit coupling and disorder (for a typical sample). When spin-orbit coupling is present, adding disorder has no effect on T_{20} so long as $E < \Delta_{\text{so}} \approx 0.1$, i.e. inside the QSH phase. In the absence of spin-orbit coupling (or above the spin-orbit gap), however, disorder strongly affects T_{20} except at small energies close to the Dirac point. In short, we find that the QSH phase is very resilient to onsite disorder.

The above considerations lead us to predict that for the present system, the physics of the QSH phase is entirely described by the Kane-Mele model (i.e. the full coverage case, $n_{\text{ad}} = 1$) provided one performs the substitution $\lambda_{\text{so}} \rightarrow \lambda_{\text{so}} n_{\text{ad}}$. In particular, the known analytical expressions for the characteristic scales of the Kane-Mele model should apply here. We now explicitly check this for the gap Δ_{so} [23] of the QSH phase and the width ξ [119] of the edge states, whose expected expressions read

$$\Delta_{\text{so}} = 3\sqrt{3}\lambda_{\text{so}}^{\text{eff}}, \quad (8.9)$$

$$\xi = \frac{\hbar v_F}{2\Delta_{\text{so}}} = \frac{1}{12\lambda_{\text{so}}^{\text{eff}}}. \quad (8.10)$$

Fig. 8.9 shows the behavior of the longitudinal transmission T_{20} (averaged over several adatom configurations) as a function of the width W . Its exponential decrease $T_{20} \propto e^{-W/\xi}$ allows for an accurate determination of ξ : as the width increases, the overlap between two opposite edge modes and the associated backscattering decrease. An extremely good scaling of the data is obtained with an expression of the transmission deduced from Eq.(8.10), confirming the above effective homogeneous description.

As a last test, we now turn to a study of the two-terminal transmission $T(E)$ of a rectangular graphene ribbon as a function of the Fermi energy E_F . The results are shown in Fig. 8.10 (upper plot): for energies inside the topological gap ($E_F \leq \Delta_{\text{so}}$), the current is entirely carried by the edge states leading to $T = 2$. Above the gap ($E_F > \Delta_{\text{so}}$), one leaves the QSH phase and the transmission increases quickly, allowing for a precise extraction of the gap value. Note that as Δ_{so} gets smaller, wider samples must be used to keep the number of open channels at $E_F = \Delta_{\text{so}}$

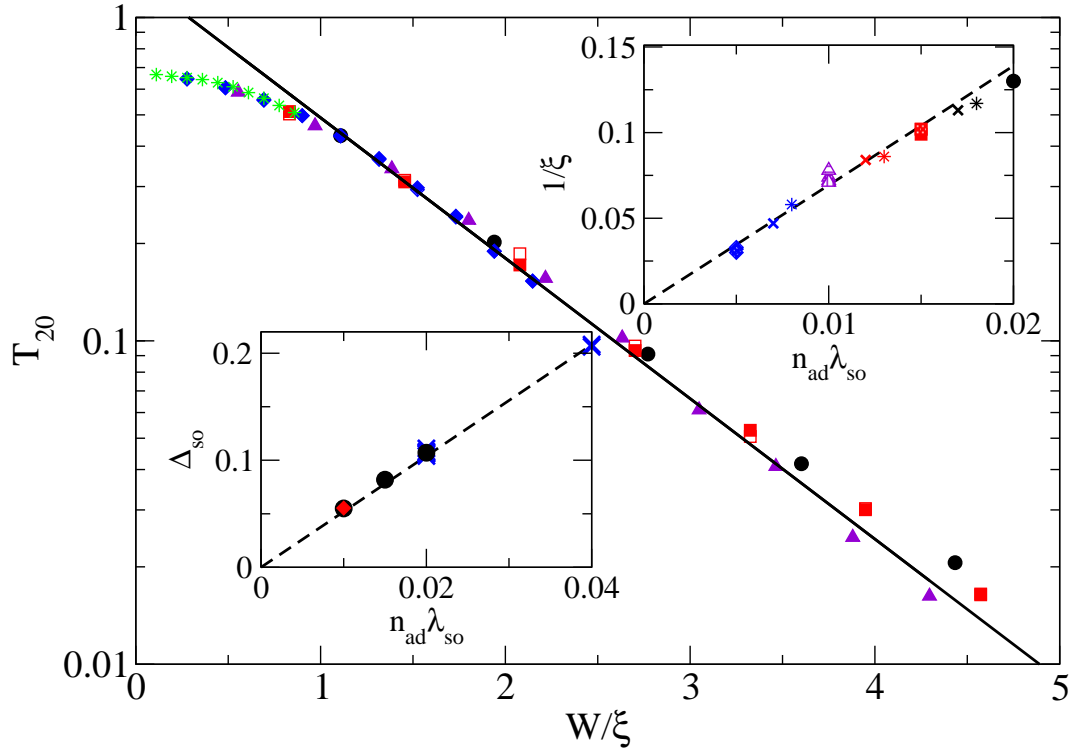


Figure 8.9: Averaged longitudinal transmission as a function of W/ξ for energy $E = 0$. Filled symbols: fixed $\lambda_{\text{so}} = 0.1$ with $n_{\text{ad}} = 0.2$ (circles), 0.15 (squares), 0.1 (triangles), 0.05 (diamonds). Open symbols: idem but the role of λ_{so} and fixed n_{ad} are exchanged, stars: $\lambda_{\text{so}} = 0.02$. Line: $Y \propto \exp -W/\xi$ where ξ is given by Eq.(8.10). Upper inset: $1/\xi$ (extracted from the data of the main plot) as a function of $\lambda_{\text{so}}^{\text{eff}}$ including additional points for different energy $E = 0.02$ (filled, dotted symbols), different aspect ratio of the sample (vertically and horizontally hashed triangles) and more values of n_{ad} (crosses, with fixed $\lambda_{\text{so}} = 0.1$) and λ_{so} (stars, with fixed $n_{\text{ad}} = 0.1$). Dashed line: Eq.(8.10). Lower inset: Δ_{so} as a function of $\lambda_{\text{so}}^{\text{eff}}$ for $\lambda_{\text{so}} = 0.02$ (diamonds), 0.05 (circles) and 0.1 (crosses). Dashed line: Eq.(8.9). In all cases, error bars due to sample-to-sample fluctuations are smaller than the symbol sizes.

larger than one. In the lower inset of Fig. 8.9, we plot the extracted Δ_{so} as a function of $\lambda_{\text{so}}^{\text{eff}}$ for various values of n_{ad} and find, again, a remarkable agreement with the effective homogeneous Kane-Mele description.

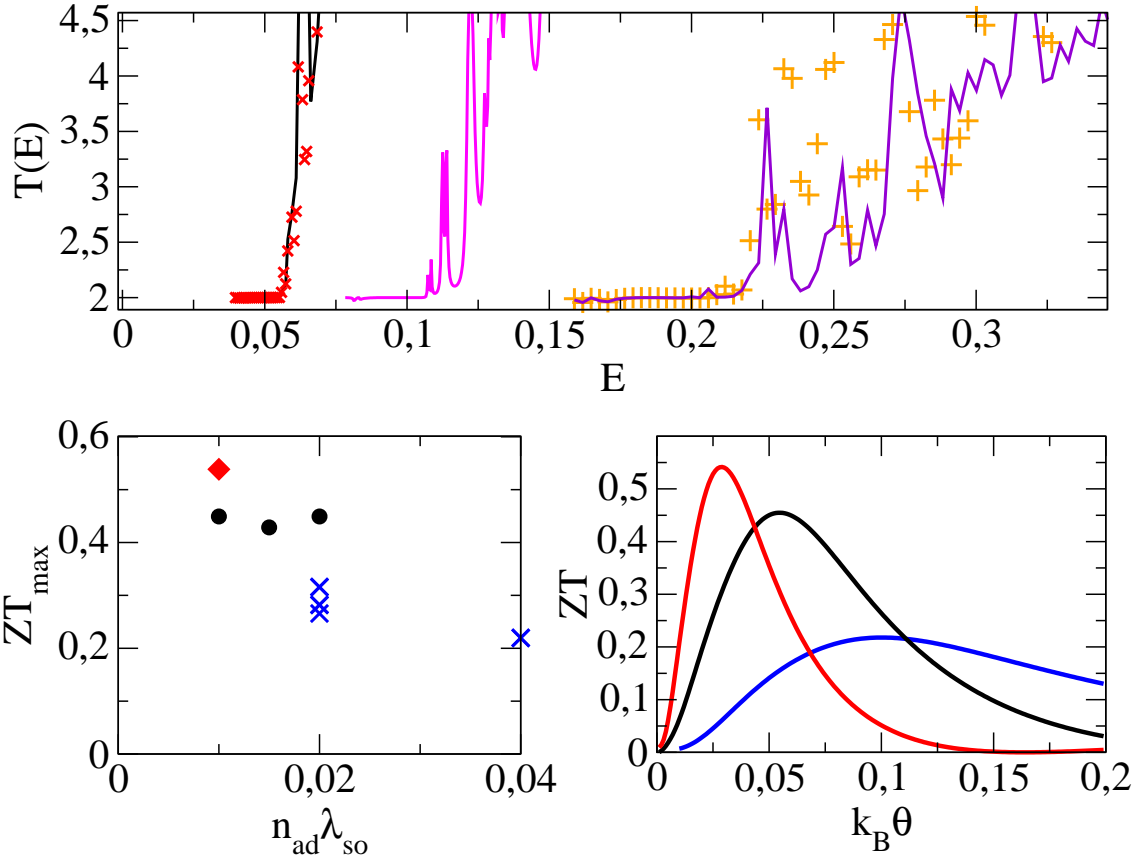


Figure 8.10: Upper plot: Transmission T as a function of the energy E in a simple armchair ribbon of width W , for $\lambda_{so}^{eff} = 0.01$ (black line: $n_{ad} = 0.2$, crosses: $n_{ad} = 0.5$) with $W = 130$, $\lambda_{so}^{eff} = 0.02$ (magenta) with $W = 65.5$, and $\lambda_{so}^{eff} = 0.04$ (violet and pluses: two different samples) with $W = 32.5$. Lower right: ZT as a function of temperature θ for $\lambda_{so}^{eff} = 0.01$, 0.02 and 0.04 from right to left. The Fermi energy was chosen to be equal to $1.5\Delta_{so}$. Lower left: peak value ZT_{max} of $ZT(\theta)$ as a function of λ_{so}^{eff} for $\lambda_{so} = 0.02$ (diamond), $\lambda_{so} = 0.05$ (circles) and $\lambda_{so} = 0.1$ (crosses).

8.2.2 Application to enhanced thermopower

We now turn to an analysis of a very peculiar feature of Fig. 8.10: the slope of the two-terminal transmission $T(E)$ above the gap is very steep, *and gets steeper* as the gap decreases. This property has strong implications in terms of thermopower generation. To discuss thermopower

at finite temperature within the Landauer-Büttiker framework, let us start by introducing

$$T_n = \int dE \left(-\frac{\partial f}{\partial E} \right) (E - E_F)^n T(E), \quad (8.11)$$

where $f(E) = 1/(e^{(E-E_F)/(k_B\theta)} + 1)$ is the Fermi function at temperature θ , from which we can express the conductance $g = (e^2/h)T_0$, the heat conductance $g_H = 1/(h\theta)T_2$ and the Seebeck conductance $g_S = -e/(h\theta)T_1$. The Seebeck coefficient $S = -\delta V/\delta\theta$ which characterizes the voltage δV across a sample produced by a difference of temperature $\delta\theta$ between sample edges is simply given by $S = g_S/g$. The dimensionless figure of merit which measures the efficiency of the thermopower generator is known as the $ZT = \theta S^2\sigma/\kappa$ parameter (we keep the standard notation ZT although we call the temperature θ and not T). σ (κ) is the electrical (thermal) conductivity. At low $ZT \ll 1$, a thermocouple has an efficiency equal to the fraction $ZT/4$ of the Carnot efficiency $\delta\theta/\theta$, while it tends to the Carnot value at large $ZT \gg 1$. Within the Landauer-Büttiker approach, we have [137]

$$ZT = \frac{(T_1)^2}{T_0T_2 - (T_1)^2} \quad (8.12)$$

which simplifies at low temperature into the so-called Mott formula [138]

$$ZT = \frac{\pi^2}{3}(k_B\theta)^2 \left(\frac{T'(E_F)}{T(E_F)} \right)^2. \quad (8.13)$$

Hence the key towards an efficient thermocouple lies in low values of the transmission and simultaneously a steep variation of this transmission with the energy. The shape of the transmission versus energy curve $T(E)$ presented in Fig. 8.10 possesses all the required properties: the low transmission value $T = 2$ accounts for the single edge state conducting channel (moreover it does not scale with the sample width W) while its derivative is typically of order $T' \approx 1/\Delta_{\text{so}}$. This results in very high values of $ZT \approx 1$ for temperatures $\theta \approx \Delta_{\text{so}}/k_B$.

To quantitatively describe the expected behavior, we have plotted the parameter ZT as a function of the temperature θ in the lower right of Fig. 8.10. We find well-defined maxima for $\theta \approx \Delta_{\text{so}}/(2k_B)$, while the optimal efficiency is reached for energy values $E_F \approx 3\Delta_{\text{so}}/2$. Note that the present material possesses the unique characteristics that the optimum temperature $\Delta_{\text{so}}/(2k_B)$ can be simply tuned by changing the concentration of adatoms while the Fermi level can be easily switched to the optimum value by *e.g.* a simple back gate. The lower left plot of Fig. 8.10 shows the value of the peak of $ZT(\theta)$ as a function of $\lambda_{\text{so}}^{\text{eff}}$: we find very high values, up to $ZT = 0.5$, which *tend to increase* upon decreasing the gap Δ_{so} . Hence, these graphene-based topological insulators appear as very good candidates for low-temperature thermocouples: for instance a 6% indium coverage is expected to give a gap of 80 K, hence an optimum working temperature of 40 K. At 1% coverage, the optimum temperature lies around 10 K, a target

temperature for *e.g.* radioisotope thermoelectric generators of spacecrafts for which a material with such high $ZT \approx 0.5$ would constitute a great improvement.

Finally, we note that the above estimate of ZT only takes into account the electron contribution to the thermal conductivity. Real values should renormalize by a factor $\kappa/(\kappa + \kappa_{ph})$ where κ_{ph} is the phonon contribution and should therefore be slightly smaller than predicted above. However, adding structural or extrinsic disorder to the ribbon or intentionally damaging the ribbon by making holes in it can drastically reduce the phonon-mediated thermal conductivity, while the *topologically protected* physics discussed above should remain largely unaffected.

8.2.3 Conclusions

One of the most important aspects associated with the discovery of graphene is the relative easiness (and low cost) of sample production. While very few groups can produce high mobility two-dimensional electron gases in semiconductor heterostructures, graphene physics requires lighter equipment and is being studied by an increasing number of groups. The same remark is even more applicable to the study of two-dimensional topological insulators. Hence, the proposal [26] discussed in this chapter for the realistic situation of inhomogeneous samples appears all the more promising.

We have shown that such a QSH phase, while originating from very inhomogeneous samples, can be described in *each sample* by the known results on the pure Kane-Mele model with an effective SO coupling strength accounting for the density of adatoms. This description should hold in the presence of disorder or charge-density fluctuations induced by the underlying substrate, as long as the magnitude of these effects remains smaller than the gap Δ_{so} . We have further demonstrated that this new material and its associated QSH phase provide a very efficient thermocouple at low temperature. Indeed, while important efforts have been made to improve the ZT parameter at room temperature (values of $ZT > 1$ can now be found), the existing materials are very inefficient at low temperature. For instance, existing thermocouples working around 10 K have $ZT < 0.01$. Moreover, the graphene-based thermocouples discussed here have a target temperature which can be tuned from a few hundred degrees Kelvin ($n_{ad} = 1$) down to 0 K ($n_{ad} = 0$) by simply changing the concentration of adatoms while retaining extremely high values of $ZT \approx 1$.

Chapter 9

From QH to QSH effect in graphene

In this chapter we will study the effect of a strong magnetic field on a QSH phase in graphene. It is well-known that a necessary condition for existence of a robust topological spin Hall phase is the time-reversal symmetry (TRS) in the system. If this symmetry is broken the edge states, which are the signature of the QSH phase, are no longer protected from backscattering. Application of a perpendicular magnetic field of course breaks explicitly TRS in the system. So, in general it is not clear what would happen to the QSH phase in this case.

Let us explain the problem in more details with the help of a simple schematic setup. Consider a four-terminal sample of Fig. 9.1. If we are in the QSH phase and no magnetic field is applied, we have a pair of edge states (Kramer's doublet) revealing the QSH effect. These edge states are helical, which implies that the direction of motion is coupled to the spin degree of freedom. On a given edge, electrons with opposite spin projections propagate in the opposite directions, see Fig. 9.1a. On the other hand, if we apply a strong magnetic field to a system in otherwise trivial phase (without SO interaction), one expects to see chiral edge states responsible for the QH effect, see Fig. 9.1b. Now the question we want to answer is what happens if we start from a system in the QSH phase and apply a (strong) magnetic field on top. At some point we naturally expect to see the QH effect, but in order to come from one phase to the other we need to reverse the direction of motion of one spin (see red dashed lines on Fig. 9.1).

Our calculations show that, surprisingly, in this case, when we have both SO coupling and a quantizing magnetic field in the system, one can observe features of both QH and QSH phases and this is determined by the position of the Fermi level. More precisely, if the Fermi level lies within the SO gap, we observe a pair of edge states for both spin species propagating (in the same direction) on the opposite edges, just like in the QSH phase, see Fig. 9.1a. On the other hand, when the Fermi level is outside the gap, both spin-up and spin-down electrons propagate on the same edge, just as expected in the QH phase (see Fig. 9.1b). This result is a direct consequence of the existence in graphene of a zero-energy Landau level. It is important to

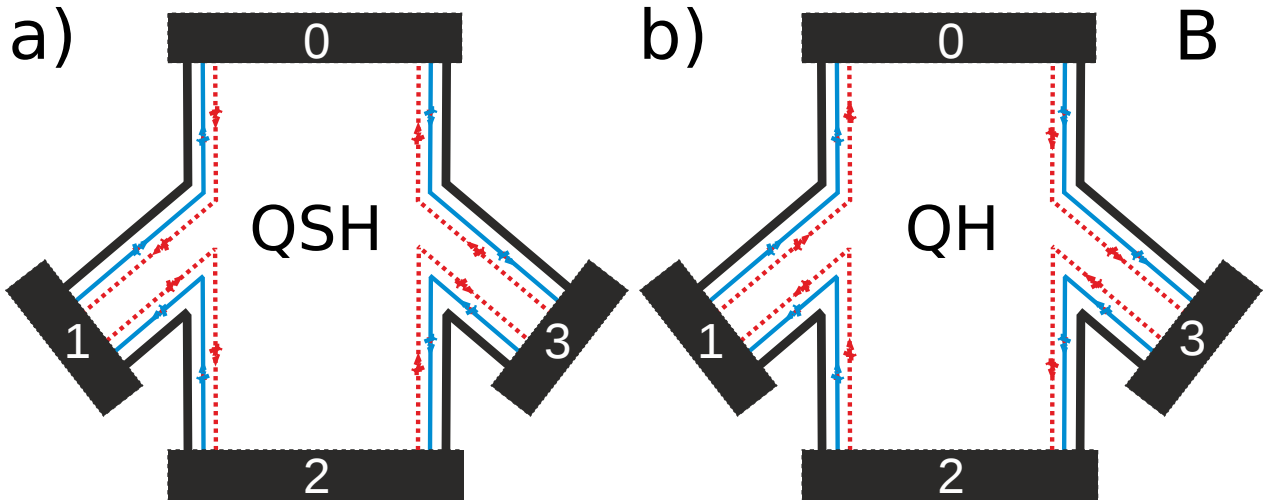


Figure 9.1: Cartoon of a 4-terminal conductor in a) QSH phase and b) QH phase. Blue solid and red dashed lines represent edge states for spin-up and spin-down electrons, respectively.

note that in the presence of spin-flipping perturbations (which conserve TRS), like Rashba SO coupling, though the edge states do not have specific spin polarization, they still form a Kramers doublet and the corresponding phase is characterized by a topological invariant [122, 81]. We also studied the effect of TRS-breaking perturbations, like magnetic impurities for example, on our results. It turns out that for finite size structures just as those used in experimental setups, we expect our results to be still valid. In this case though the edge states are no more protected by the TRS, one needs to apply an unrealistically strong magnetic disorder to destroy the QSH phase. Our estimates show that this happens on a characteristic length scale ~ 1 mm, which is far above the typical lengths of the samples used in experiments. Moreover, though in this case the (spin) Hall transmission is not e^2/h , the current is still confined to the edges of the sample, which distinguishes this phase from a trivial insulator.

9.1 Band structure

The issue of how time-reversal-symmetry breaking can affect the QSH phase has been addressed previously in the literature in different settings [139, 140, 28, 141]. To the best of our knowledge, however, transport signatures of the competition between QH and QSH phases in graphene have not been considered as of yet, with the exception of the work by Abanin et al. [142] where the QSH phase arose from a different mechanism (Zeeman splitting), which is extremely weak¹

¹It is so weak that it appears to be superseded by many-body effects in strong magnetic fields [143, 144]. If Zeeman splitting ϵ_Z were artificially enhanced, it would compete with SO coupling and lead to a phase transition when $\epsilon_Z = \Delta_{so}$, characterized by a reversal of the direction of spin current on a given edge [28].

and can therefore easily be destroyed by local fluctuations of the magnetic field. In contrast, we study the Kane and Mele model [23], to which we add the presence of a strong perpendicular magnetic field:

$$H = v_F(\hat{\Pi}_x\sigma_x\tau_z + \hat{\Pi}_y\sigma_y) + \Delta_{\text{so}}\sigma_z\tau_zs_z . \quad (9.1)$$

$\hat{\Pi} = \hat{\mathbf{p}} + e\mathbf{A}$ is the generalized momentum which accounts for the presence of the magnetic vector potential \mathbf{A} associated with a perpendicular magnetic field $\mathbf{B} = B\mathbf{z}$ ($\nabla \times \mathbf{A} = \mathbf{B}$), Δ_{so} is the SO-induced QSH gap, and $v_F = 3ta_{c-c}/2$ is the Fermi velocity (expressed as a function of the nearest-neighbor hopping amplitude t and the lattice constant a_{c-c} which we choose in the following as our working units of energy and length, respectively). $\{\sigma, \tau, s\}$ are Pauli matrices in, respectively, sublattice, valley and spin spaces.

The band structures of a graphene ribbon in the QSH and QH phases are quite different. In the QH phase, the perpendicular magnetic field gives rise to Landau levels $\epsilon_n = \pm(\hbar v_F/l_B)\sqrt{2|n|}$, with $l_B = \sqrt{\hbar/(eB)}$, which become dispersive close to the edges of the graphene ribbon (Fig. 9.2a). When the Fermi level is placed between two of these Landau levels, transport is characterized by spin-degenerate edge states as in Fig. 9.1b, which propagate in a direction imposed by the sign of the magnetic field. In the QSH phase, the band structure consists of hyperbolic bands above the QSH gap and a pair of linearly dispersing ones below it (Fig. 9.2b). These linear bands correspond to spin-polarized states, localized at the edges of the graphene ribbon on a characteristic length scale $\xi_{\text{so}} = \hbar v_F/\Delta_{\text{so}}$ (see Section 7.2). When the Fermi level is below the QSH gap, transport in the system can be described by counter-propagating edge states as shown in Fig. 9.1a. By comparing Figs. 9.1a and 9.1b, one observes that one spin species – hereafter referred to as the “unhappy” spin (dashed red in Fig. 9.1) – has to reverse its direction of propagation when going from one phase to the other. We will see how this reversal happens in two different setups: a homogeneous sample, where the quantum phase transition between QH and QSH phases is driven by electrostatic doping, and a heterojunction between the two phases.

The first insight is given by the spectrum of Eq.(9.1) in the presence of graphene edges. The energy spectrum for a bulk system described by Eq.(9.1) reads $\epsilon_n = \pm\sqrt{\Delta_B^2|n| + \Delta_{\text{so}}^2}$, with $\Delta_B = (\hbar v_F/l_B)\sqrt{2}$. The lowest level $n = 0$ stands out from the others, as each branch (\pm) can be shown to host only one of the two spin species [28] (Fig. 9.2c). Whereas $n > 0$ levels will all disperse in the same direction when confinement is taken into account, the fate of the lowest level is more subtle. To be more quantitative, we make use of a tight-binding model on the graphene hexagonal lattice, which in the presence of both Kane-Mele SO coupling and perpendicular magnetic field can be written as

$$H = -t \sum_{\langle i,j \rangle, \alpha} e^{i\phi_{ij}} c_{i,\alpha}^\dagger c_{j,\alpha} + i\lambda_{\text{so}} \sum_{\langle\langle i,j \rangle\rangle, \alpha, \beta} \nu_{ij} e^{i\phi_{ij}} c_{i,\alpha}^\dagger s_{\alpha\beta}^z c_{j,\beta} . \quad (9.2)$$

Indices (i, j) label lattice sites, (α, β) label spin indices, while symbols $\langle \rangle$ and $\langle\langle \rangle\rangle$ re-

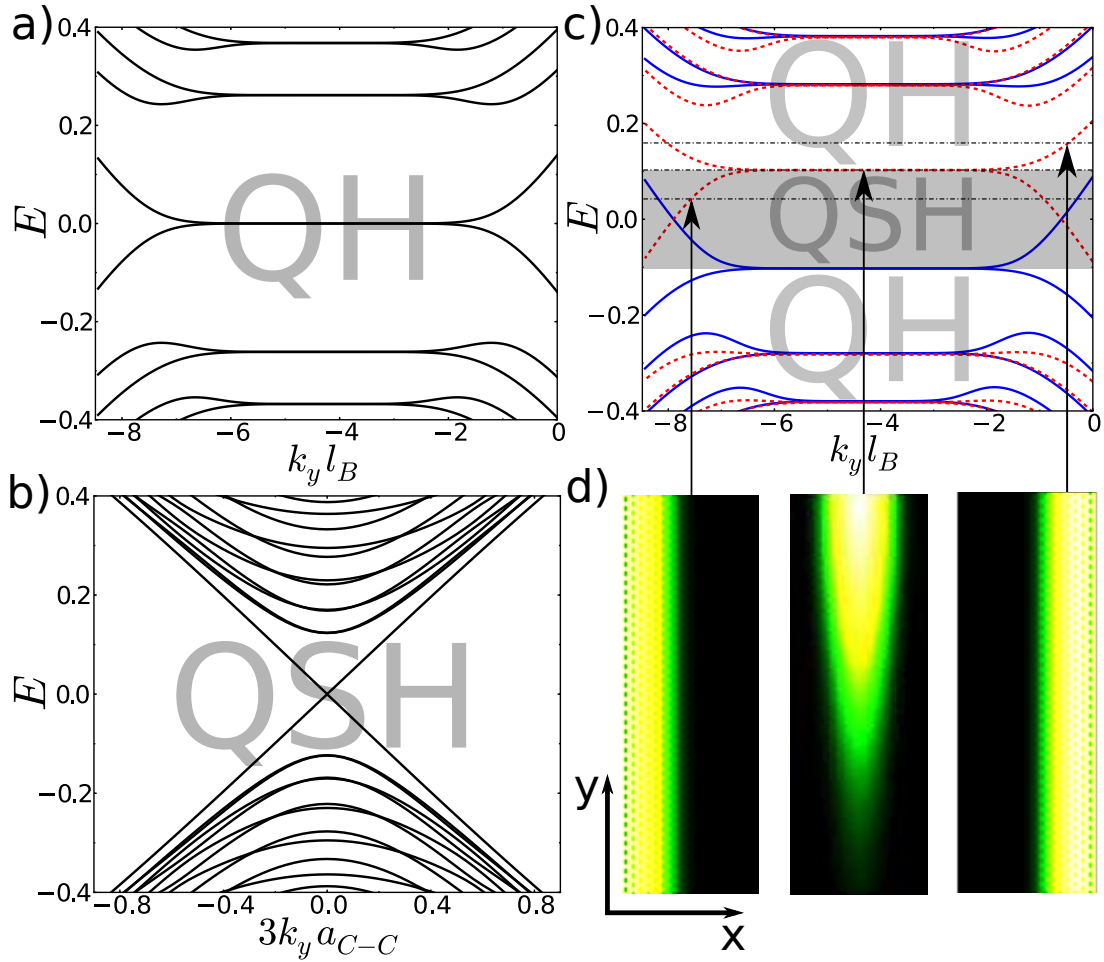


Figure 9.2: Band structure of a (semi-metallic armchair) graphene ribbon in the **a)** QH and **b)** QSH phase. When both magnetic field and SO coupling are present **c)**, the resulting band structure leads to a QSH phase for $|E_F| < \Delta_{\text{so}}$ (shaded region) and a QH phase for $|E_F| > \Delta_{\text{so}}$. Compared to the pure QH and QSH cases, the spin degeneracy is lifted (blue thick and red dashed lines), which is particularly prominent in the lowest band which consists of spin-polarized branches at $E = \pm\Delta_{\text{so}}$. As the Fermi energy crosses the SO gap, the localization of the “unhappy” spin (red dashed) shifts from one edge to the other, while it is fully localized in the bulk when $E_F = \Delta_{\text{so}}$. This is illustrated in the corresponding current-density plots **d)**. On the other hand, the “happy” spin (thick blue) gets increasingly localized on the same edge as the Fermi energy crosses the transition region (not shown). The parameters used are $\lambda_{\text{so}} = 0.02$, $l_B \simeq 8$, and a ribbon width $W = 40\sqrt{3}$.

spectively refer to nearest-neighbor coupling (with hopping amplitude t) and next-nearest-neighbor coupling (with SO-induced hopping amplitude $\lambda_{\text{so}} = \Delta_{\text{so}}/(3\sqrt{3})$ [23]). The Peierls phase $\phi_{ij} = (e/\hbar) \int_{\mathbf{r}_j}^{\mathbf{r}_i} \mathbf{A} \cdot d\mathbf{r}$ takes into account the contribution from the magnetic flux threading the lattice, and $\nu_{ij} = \pm 1$ depending on whether sites are coupled clockwise or counter-clockwise. Note that in order for the system to remain gauge invariant, Peierls substitution has to be done on all hopping matrix elements: nearest-neighbor *and* (SO) second nearest-neighbor. To compute transport properties numerically, we make use of the software KNIT, which is based on an advanced recursive Green's function technique [22], and works in the linear response regime. The numerical calculations are done with semi-metallic armchair boundary conditions, but our results are qualitatively unaffected by this choice. An important technical point is that the magnetic field should be present in the entire sample, including in the leads, in order to avoid spurious reflection at the lead-sample interface. The multi-terminal Peierls substitution prescription allowing to do that is described in the Appendix B.

The full tight-binding band structure of a semi-metallic armchair graphene ribbon described by the Hamiltonian in Eq.(9.2) is shown on Fig. 9.2c. It can be summarized in very simple terms: for Fermi energies inside the SO gap $|E_F| < \Delta_{\text{so}}$ (shaded region), the system is in the QSH phase, with opposite spin channels on a given edge propagating in opposite directions, while for energies $|E_F| > \Delta_{\text{so}}$, the system is in the QH phase, with opposite spin channels on a given edge propagating in the same direction. Hence for a given value of Δ_{so} , the transition between the two phases is governed solely by the Fermi energy and does not depend at all on the value of the magnetic field (once again neglecting Zeeman splitting, which is very small in graphene). This quite remarkable result is a direct consequence of the existence in graphene of a B -independent zero-energy Landau level: as soon as $\Delta_{\text{so}} \neq 0$, the spin degeneracy of the zero-energy Landau level is lifted, as opposed to all other Landau levels which remain spin degenerate [28]. This lifting leads to a QSH phase in the corresponding SO gap, as can be understood with the help of topological invariants.

9.2 Topological order

In this section, we discuss the topological order of the phases obtained by varying the chemical potential in the energy spectrum of Fig. 9.2c. In particular, we relate the unique transition between the QSH topological order and the QH topological order in presence of SO coupling to the specificities of the QH physics of Dirac fermions in graphene. Let us start by recalling the standard topological number characterization of Landau levels when $\Delta_{\text{so}} = 0$. Each Landau level n and its associated eigenfunctions over the first Brillouin zone are characterized by a topological invariant, the so-called Chern number [145]. This topological number takes a value $\mathcal{C}_{\tau,s}^{(n)} = +1$ for each Landau level, independently of the Landau n , valley τ or spin s indices. For

each value of the Fermi energy, we can characterize the corresponding phase by a topological number $\mathcal{C} = \sum_{\tau,s} \sum_{\epsilon_n < E_F} \mathcal{C}_{\tau,s}^{(n)}$ obtained by summing the Chern numbers of all filled energy bands [145]. For graphene and any Dirac system, however, this procedure would yield an ill-defined topological number \mathcal{C} due to the presence of an infinite number of filled Landau levels below E_F . As shown recently through the use of non-commutative Berry's connection [146], the correct topological number for a single Dirac cone takes a value $\mathcal{C}_{\tau,s} = -1/2$ for $\epsilon_{-1} < E_F < \epsilon_0$, and $\mathcal{C}_{\tau,s} = +1/2$ for $\epsilon_0 < E_F < \epsilon_1$, where ϵ_n are the usual Landau levels. In the discussion below, we will make use of the more convenient topological Chern number per spin species, $\mathcal{C}_s = \sum_{\tau} \mathcal{C}_{\tau,s}$ which takes values two-fold larger.

Let us now turn to the energy spectrum of Fig. 9.2c where $\Delta_{\text{so}} \neq 0$. The presence of the SO coupling does not modify any of the Chern numbers per Landau level, but it lifts the spin degeneracy of the $n = 0$ Landau level into the two levels at $E = \pm\Delta_{\text{so}}$. As the z component of spin is conserved, the topological Chern numbers per spin species introduced above turn out to be useful quantities to characterize the topological order in this new spectrum. They read

$$\mathcal{C}_{\uparrow} = -1, \mathcal{C}_{\downarrow} = -1 \text{ for } \epsilon_{-1} < E_F < -\Delta_{\text{so}} , \quad (9.3a)$$

$$\mathcal{C}_{\uparrow} = +1, \mathcal{C}_{\downarrow} = -1 \text{ for } -\Delta_{\text{so}} < E_F < \Delta_{\text{so}} , \quad (9.3b)$$

$$\mathcal{C}_{\uparrow} = +1, \mathcal{C}_{\downarrow} = +1 \text{ for } \Delta_{\text{so}} < E_F < \epsilon_1 , \quad (9.3c)$$

$$\mathcal{C}_{\uparrow} = +3, \mathcal{C}_{\downarrow} = +3 \text{ for } \epsilon_1 < E_F < \epsilon_2 , \quad (9.3d)$$

this time with ϵ_n the modified Landau levels introduced at the beginning of Sec. 9.1. The difference between \mathcal{C}_{\uparrow} and \mathcal{C}_{\downarrow} for $|E_F| < \Delta_{\text{so}}$ signals the appearance of a \mathbb{Z}_2 topological order characteristic of the QSH phase. Indeed, when the z component of spin is conserved, the \mathbb{Z}_2 topological index characterizing the QSH phase is defined as $\nu = (\mathcal{C}_{\uparrow} - \mathcal{C}_{\downarrow})/2 \pmod{2}$ [147, 81]. As all Landau levels $n \neq 0$ are still spin-degenerate, we have $\mathcal{C}_{\uparrow} = \mathcal{C}_{\downarrow}$ and thus $\nu = 0$ for all Fermi energies $|E_F| > \Delta_{\text{so}}$. For these values of E_F , the system lies in a QH phase characterized by the usual topological Chern number $\mathcal{C} = \mathcal{C}_{\uparrow} + \mathcal{C}_{\downarrow}$. However for $|E_F| < \Delta_{\text{so}}$, Eq.(9.3) leads to a non-trivial \mathbb{Z}_2 index $\nu = 1$, while the total Chern number simultaneously vanishes $\mathcal{C} = \mathcal{C}_{\uparrow} + \mathcal{C}_{\downarrow} = 0$. The system then lies in a different topologically insulating phase: the QSH insulator. This shows that as the Fermi energy crosses the values $\pm\Delta_{\text{so}}$, the system undergoes a quantum phase transition between two topological insulators – a QH phase and a QSH phase:

$$\nu = 0, \mathcal{C} = -2 \text{ for } \epsilon_{-1} < E_F < -\Delta_{\text{so}} : \text{QH} , \quad (9.4a)$$

$$\nu = 1, \mathcal{C} = 0 \text{ for } -\Delta_{\text{so}} < E_F < \Delta_{\text{so}} : \text{QSH} , \quad (9.4b)$$

$$\nu = 0, \mathcal{C} = 2 \text{ for } \Delta_{\text{so}} < E_F < \epsilon_1 : \text{QH} , \quad (9.4c)$$

$$\nu = 0, \mathcal{C} = 6 \text{ for } \epsilon_1 < E_F < \epsilon_2 : \text{QH} . \quad (9.4d)$$

This transition appears crucially tied to the Dirac physics of graphene and the presence of the $n = 0$ Landau level: in the present case, we do not need a SO coupling to overcome an energy

gap in order to drive this transition, as would be the case for non-relativistic fermions with Landau gap $\hbar\omega_c$ or if graphene had a trivial mass gap $m\sigma_z$. The spin degeneracy lifting of the $n = 0$ level is all that is required here. Let us note finally that while this argument formally uses the conservation of the S_z spin component, the robustness of topological numbers proves it to remain valid if non- S_z -conserving terms are included in the Hamiltonian, provided two branches of the $n = 0$ Landau level with opposite spins remain non-degenerate.

9.3 Transport signatures

9.3.1 Ballistic regime

Let us now study how this topological phase transition appears in transport. We will study the multi-terminal (dimensionless) differential conductance T_{ab} which expresses how much current dI_a is collected in lead a when the voltage in lead b is raised by dV_b ,

$$\frac{dI_a}{dV_b} = \frac{e^2}{h} T_{ab} . \quad (9.5)$$

Additionally, in order to observe the edge states directly, we also study (in color plots) the differential local current density $di(\vec{r})/dV_a$ which allows to clearly observe the edge states inside the sample. In Fig. 9.2d, we show local current-density plots which illustrate how the behavior of the “unhappy” spin changes as a function of the Fermi energy: it goes from propagating along one edge when $E_F < \Delta_{\text{so}}$ (left panel) to propagating along the other as $E_F > \Delta_{\text{so}}$ (right panel), while it gets localized in the bulk at the critical point $E_F = \Delta_{\text{so}}$ (middle panel). We find that the energy window where this localization is observed is extremely narrow and decays exponentially with the width of the sample. Note that this scenario is completely different from what one would expect starting from the naive toy model of SO coupling acting as a spin-dependent magnetic field $B_{\text{so}}\mathbf{z}s_z$. In this case, for a critical value of the real magnetic field $B = B_{\text{so}}$, the “unhappy” spin would feel no magnetic field at all and be fully delocalized. On the contrary, we observe that the QSH phase is virtually independent from the real magnetic field and that the “unhappy” spin actually gets localized when $E_F = \Delta_{\text{so}}$, illustrating the limitations of the toy model in this situation.

In the vicinity of the transition, the “unhappy” spin keeps propagating along a given edge but its classical cyclotron orbit center $x_c = -k_y l_B^2$ (with k_y the longitudinal wave vector component) is shifted inwards as the Fermi energy increases (see Fig. 9.2c). On the other hand, the “happy” spin gets increasingly localized on the same edge when the Fermi energy increases, which is qualitatively equivalent to the usual QH case. One can indeed show that the notion of a classical cyclotron orbit center remains well defined here, despite the presence of SO coupling, and that the corresponding eigenstates are very similar to those found in the pure QH regime [28].

Before presenting the rest of our numerical data on transport in the vicinity of the QSH-QH transition, a few words should be said about the shape of the spectrum corresponding to the non-zero Landau levels. While the branches corresponding to the “happy” spin seem basically unaffected by the SO coupling, the two branches of the “unhappy” spin display very different behaviors (Fig. 9.2c). In particular, one of them is significantly bent by the SO coupling, such that counter-propagating states along the same edge appear in a finite window of energy. This leads to the possibility of backscattering and therefore destroys the robustness of the QH phase in this energy window, the size of which can nevertheless be significantly reduced by increasing the width of the graphene ribbon². Note that at negative energies, $E_F < -\Delta_{\text{so}}$, “happy” and “unhappy” spin species exchange their roles (see Fig. 9.2c).

We proceed to investigate further how the transition between QSH and QH phases shows up in transport, and consider the 4-terminal Ψ -shape geometry depicted in the inset of Fig. 9.3a. In the core of Fig. 9.3a, we plot as a function of the Fermi energy the current collected in leads 1, 2 and 3 when injected from lead 0. Nothing unexpected happens away from the transition: the transmission coefficients feature characteristic signatures of current-carrying edge states (left and right panels of Fig. 9.2d). Around the critical value $E_F = \Delta_{\text{so}}$, however, we observe in Fig. 9.3a that the “unhappy” spin is fully transmitted in lead 2. This can be understood as follows. As the transition point is approached, the classical cyclotron orbit center is shifted (inwards) away from the edge (as discussed above) by a distance which can reach $2R_c$, where $R_c(B) = l_B^2/\xi_{\text{so}}$ is the classical cyclotron radius of the $n = 0$ level. When $2R_c > W_1/2$, where W_1 is the width of lead 1, then, somewhere in the vicinity of the transition, the incoming state cannot penetrate lead 1, hence leading to perfect direct transmission to lead 2 as observed in Fig. 9.3a. This feature could in principle be checked experimentally by simply varying the strength of the magnetic field close to the transition: for wider systems or at larger magnetic field, the width of the peak of direct transmission from 0 to 2 shrinks and eventually disappears.

A clear way to distinguish between QH and QSH phases in a transport measurement is to plot the “direct” dimensionless differential conductance from lead 0 to lead 2 as a function of the classical cyclotron radius $R_c \propto B^{-1}$. This is illustrated in Fig. 9.3b: below the QSH gap, the “direct” transmission is zero for any value of the magnetic field; on the other hand, above the QSH gap, transmission can become non-zero as the magnetic field weakens, due to the breakdown of the QH effect when R_c becomes larger than the width of the system. It thus interpolates between zero (in the QH regime) and a finite value which depends on the number of occupied bands at the Fermi level in the ribbon when $B = 0$. Of course, in the latter limit, the topological protection is lost and the value of the transmission will strongly depend on the disorder configuration.

²In fact, what happens is that in the energy window, in the dips (peaks) of the red dashed (blue solid) lines above $E = \Delta_{\text{so}}$ (below $E = -\Delta_{\text{so}}$), the counterpropagating edge states cancel out each other and play no role in transport. Therefore, one does not see any traces of these features in conductance simulations.

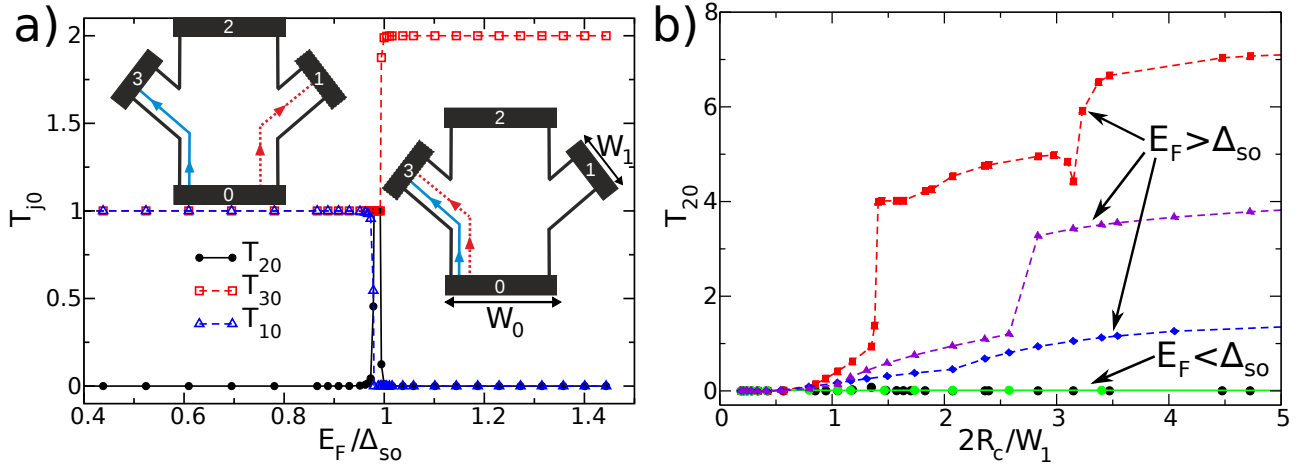


Figure 9.3: QSH-QH transition in a 4 terminal Ψ -shape geometry. **a)** Dimensionless differential conductance from lead 0, where the current is injected, to outgoing leads 1, 2 and 3 in the geometry depicted in the inset, as a function of the Fermi energy ($\lambda_{so} = 0.02$, $l_B \simeq 8$, and lead widths $W_0 = 64\sqrt{3}$, $W_1 = 22\sqrt{3}$). Below the SO gap, current is carried by QSH edge states, which propagate on different edges (left inset), while above the SO gap it is carried by QH edge states, which propagate on the same edge (right inset). **b)** Dimensionless differential conductance from lead 0 to lead 2 as a function of the classical cyclotron radius $R_c \propto B^{-1}$ (same values of λ_{so} , W_0 and W_1 as in **a**). Circular symbols (thick line) correspond to data with $E_F < \Delta_{so}$, while other symbols (dashed lines) correspond to data with $E_F > \Delta_{so}$, respectively $E_F/\Delta_{so} = 1.06$ (blue diamonds), $E_F/\Delta_{so} = 1.25$ (violet triangles), and $E_F/\Delta_{so} = 1.44$ (red squares). While this “direct” transmission is vanishingly small and independent of the magnetic field below the SO gap, it increases with both R_c and E_F above the SO gap. The latter situation arises because the QH phase is destroyed as $2R_c \gtrsim W_1$, and because the number of transmitting channels increases with l_B and E_F .

9.3.2 Effects of disorder

In this subsection, we study the robustness of the results described in the ballistic regime with respect to the presence of various types of disorder. In the absence of a magnetic field, the QSH phase is known to be very robust with respect to the presence of scalar disorder (i.e. disorder that breaks neither time reversal symmetry nor spin rotational symmetry), as introducing backscattering between edge states involves tunneling through the gapped bulk region. On the other hand, disorder that breaks both time reversal symmetry and spin rotational symmetry (such as magnetic impurities) leads to scattering between the two counter-propagating edge states of the same edge, which leads to intra-edge backscattering. If this intra-edge backscattering becomes strong (or the edges are very long), edge states may eventually get localized, such that no edge transport occurs anymore. In our case, as we explicitly break time reversal symmetry with a magnetic field, disorder that breaks only spin rotational symmetry (such as Rashba-like SO terms arising from adatoms) effectively behaves as magnetic impurities and could potentially lead to the same breakdown of the QSH phase.

In order to study these effects quantitatively, we add the general perturbation

$$H_{\text{dis}} = \sum_{i,\alpha,\beta} c_{i,\alpha}^\dagger \left(\sum_{\mu=0,x,y,z} V_{i,\mu} s_{\alpha\beta}^\mu \right) c_{i,\beta} \quad (9.6)$$

to our tight-binding Hamiltonian (9.2). The onsite potentials $V_{i,\mu}$ are independent random variables uniformly distributed inside a given interval on each site of the system (Anderson disorder). We study three different sorts of disorder with different symmetries: $V_{i,0} \in [-V_s/2, V_s/2]$ takes into account scalar (spin-independent) disorder, $V_{i,z} \in [-V_z/2, V_z/2]$ represents Zeeman-like (S_z conserving) impurities, and $\{V_{i,x}, V_{i,y}\} \in [-V_m/2, V_m/2]$ captures the influence of S_z non-conserving impurities.

The results are presented in Fig. 9.4 for the 4-terminal Ψ -shape geometry (depicted in the inset of Fig. 9.3a). Note that in order to obtain a significant effect of disorder, we used extremely (unrealistic) high values of disorder, much higher than the SO gap itself. A first general qualitative conclusion is that the ballistic results presented above are extremely robust with respect to all kinds of disorder. More precisely, we find, as expected, that extremely large values of V_s or V_z are needed to significantly affect the transport coefficients. ‘‘Magnetic’’ impurities (V_m), which can induce intra-edge backscattering, do affect the QSH phase at weaker values. We note, however, that the system remains topological (i.e. does not become a simple ordinary insulator) as transport is still dominated by edge contributions: for instance, at $V_m = 0.5$, the direct transmission probability T_{20} (from lead 0 to lead 2) remains many orders of magnitude smaller than T_{10} (from lead 0 to 1). The topological nature of the phase is encoded in the \mathbb{Z}_2 topological invariant, which cannot change unless the bulk gap is closed by the perturbations we consider. We checked (not shown) that the above results are essentially unaffected upon

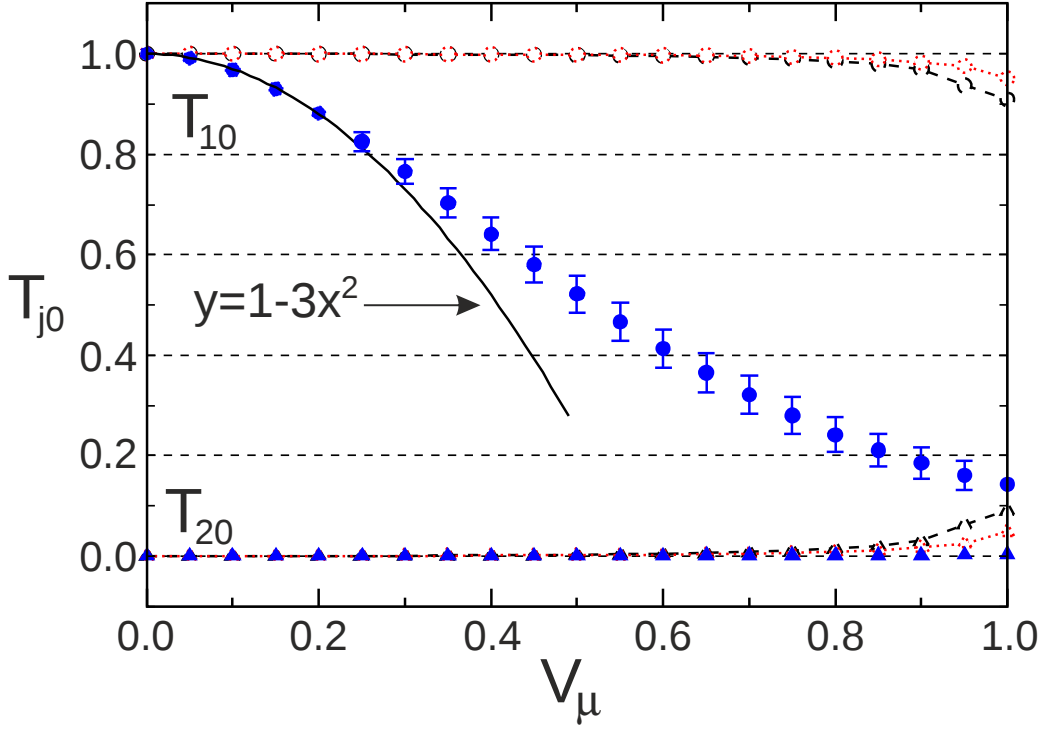


Figure 9.4: Effect of very strong disorder on the QSH phase in the 4-terminal Ψ -shape geometry. We plot the dimensionless differential conductance from lead 0 to leads 1 and 2 as a function of disorder strength for $\lambda_{\text{so}} = 0.02$, $l_B \simeq 8$, $E_F = 0.05$, and otherwise same system as in Fig. 9.3. Circular symbols stand for T_{10} and triangular symbols for T_{20} . The behavior for T_{30} (not shown) is the same as for T_{10} . Dashed black lines correspond to purely scalar disorder (V_s), dotted red lines correspond to purely Zeeman-like disorder (V_z), and filled blue symbols correspond to purely Sz non-conserving disorder (V_m). The latter is clearly the dominant effect on T_{10} , though unrealistically large values are required to quantitatively affect the edge state transmission (see main text for a mean free path estimate). Each data point has been averaged over 48 disorder configurations. Unless shown, error bars are smaller than symbol sizes. Full black line: fit $y = 1 - 3.0x^2$.

changing the SO gap by a factor of 2, putting all three sorts of disorder simultaneously or changing the Fermi energy (inside the SO gap).

To rule out any concerns raised by the intra-edge scattering due to V_m , the corresponding intra-edge mean free path l_e (or equivalently the localization length, as both are roughly equal for one-dimensional states) can be estimated using Fermi's golden rule: $l_e = v_d \tau_e$ where $v_d = \hbar^{-1}(dE/dk)$ is the drift velocity of the edge states (extracted for instance from Fig. 9.2), and $\tau_e \propto (V_m)^2 |dk/dE|$. Alternatively, one may extract it directly from the numerical calculations of Fig. 9.4, since $T_{10} \approx 1 - (L/l_e)$ (with L the length along the edge, roughly 5 nm in this

instance). Fitting the small V_m regime with $T_{10} \approx 1 - 3.0V_m^2$, we obtain (in nm)

$$l_e \approx (V_m/t)^{-2}, \quad (9.7)$$

where we have explicitly restored the hopping amplitude t (our energy unit) in order to get numbers. The ballistic results are essentially unaffected for systems smaller than l_e , while the edge states become localized for larger systems. In the context of a QSH phase induced by adatoms (using for instance the indium atoms proposed by Weeks *et al.* [26]), a possible source of V_m -like disorder comes from the SO coupling induced by the adatoms themselves. Typical values for V_m are smaller than 1 meV, which translates into extremely large intra-edge mean free paths $l_e > 1$ mm. Hence we estimate that this perturbation should be largely irrelevant in real size samples.

To summarize, all of our results are essentially unaffected by the presence of disorder, except when the Fermi energy lies in the vicinity of the QSH-QH transition, in which case strong disorder can give rise to a random network of QH and QSH regions through which a percolating cluster connecting opposite edges can therefore lead to backscattering³.

9.4 Topological heterojunction

We take advantage of the above described topological quantum phase transition as a function of the Fermi energy to propose a setup which allows for a direct junction between two different topological phases in the same sample. Let us consider the case in which an additional electrostatic gate enables to split the system in two parts, one in which the Fermi level is in the QSH phase, and the other in which the Fermi level is in the QH phase (Fig. 9.5). This constitutes a QSH-QH junction which shares some similarities with quantum Hall n - p junctions previously fabricated in graphene [148, 149]. Indeed, the incoming “unhappy” spin at the junction has no other choice but to propagate along the interface in order to reach the only other available channels which lie on the opposite edge. This is reminiscent of the situation both spin channels have to face in the QH regime when they must cross a n - p junction, since their direction of propagation on a given edge is reversed for negative energies. Various theoretical models have been proposed in the latter setup [150, 151, 152, 153] but they all fail to explain the experimental observations [148, 149], probably due to some dephasing mechanism taking place in the vicinity of the Dirac point which is obscured by charge-density fluctuations (so-called electron-hole puddles). The system we consider could therefore provide a new perspective to solve this puzzle, as the QSH-QH transition takes place at a value of energy which can be far away from

³This effect will be all the more potent for zigzag-terminated ribbons, as they feature energy-dependent QSH edge states, whose width is expected to strongly increase when the energy approaches the SO gap [119], see Fig. 7.7.

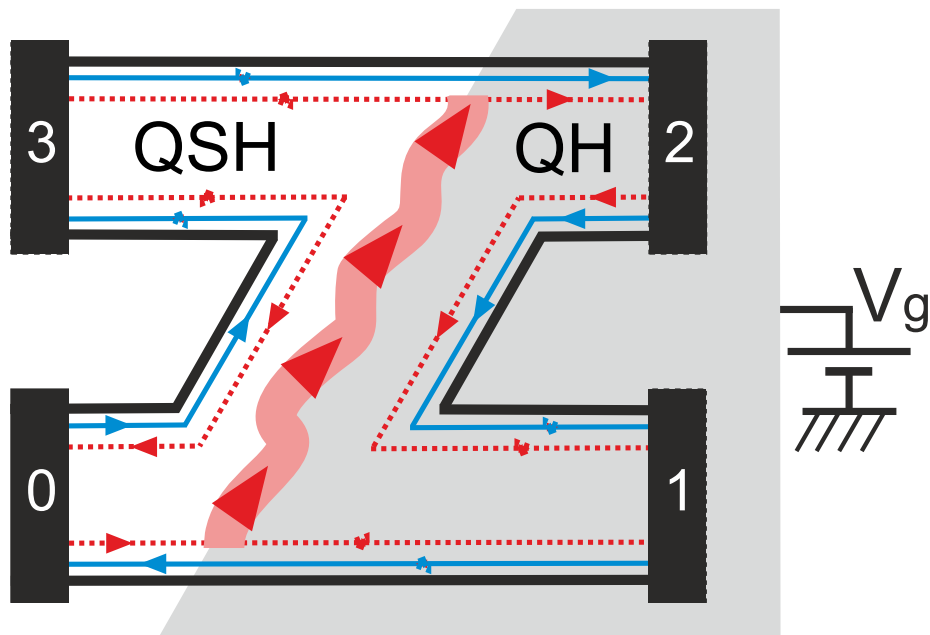


Figure 9.5: Topological heterojunction, with QSH edge states on the left and QH edge states on the right. This junction can be experimentally achieved by applying a top gate (grey shaded region) on the right half of the sample. While one of the spin species (thick blue) can propagate through this junction, the other one (red dashed) cannot and therefore gives rise to a chiral state, localized at the interface between QH and QSH phases, which connects both edges.

the Dirac point⁴ for realistic values of SO-induced QSH gap.

More generally, our proposal offers the possibility of studying the nature of the state that propagates at the interface between QSH and QH phases, which are characterized by different topological invariants [145, 24]. What we usually refer to as QSH (or QH) edge states are states propagating between QSH (or QH) insulators and a trivial insulator (the vacuum, typically). As the QSH insulator is characterized by a \mathbb{Z}_2 number, there is only one QSH topological phase: junctions between QSH phases with different Fermi energies (including n - p junctions) have no effect on transport, as the spin-polarized states can propagate through these junctions. On the other hand, the QH topological invariant is a \mathbb{Z} number, which counts the number of edge channels, and the notion of QH junctions therefore makes sense. In this case, one expects the existence of chiral propagating states, localized at the interface corresponding to the Landau level crossing. For QH n - n' junctions, these states are “bubbling” states [153], which simply follow the drifting Hall motion of charge carriers subjected to crossed electric and magnetic fields. For QH n - p junctions, these states are ambipolar “snake” states [154], which can be

⁴Far from the Dirac point, however, the adatoms which induce the QSH phase in graphene [26] may give rise to parasitic [23] Rashba-type SO couplings.

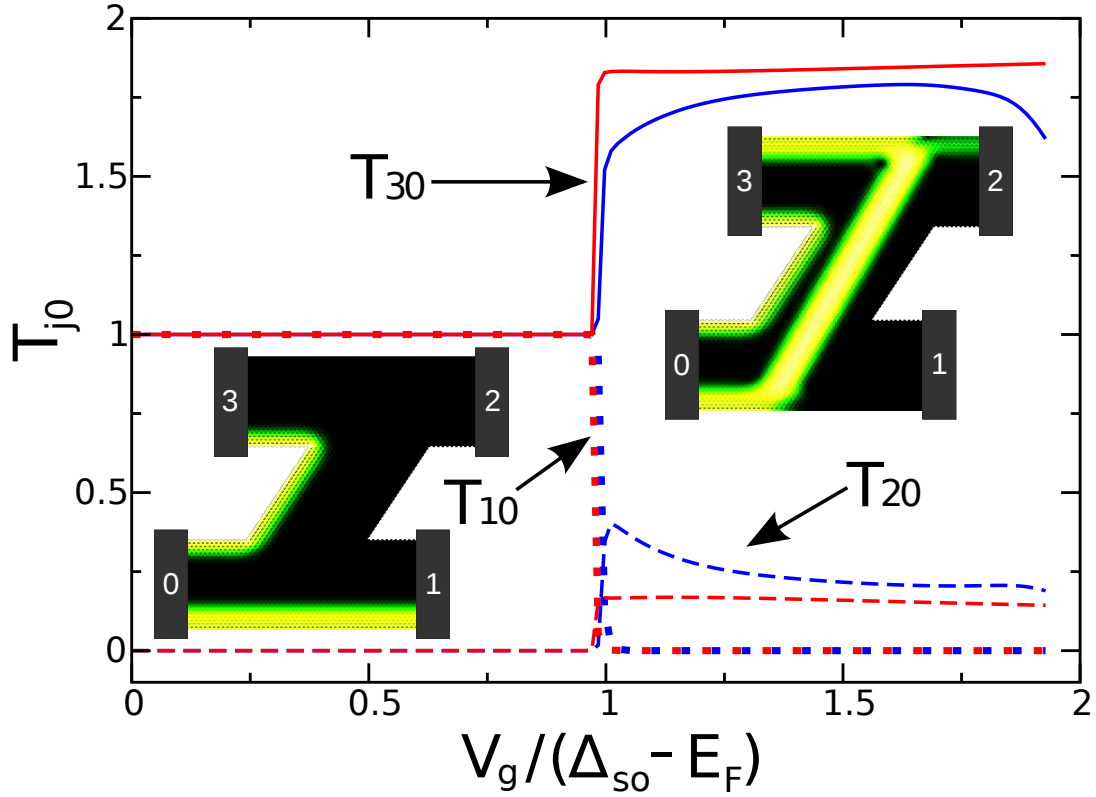


Figure 9.6: Heterostructure in a 4 terminal Z-shape sample as depicted in Fig. 9.5. Transmission probabilities from lead 0, where the current is injected, to outgoing leads 1 (dotted lines), 2 (dashed lines) and 3 (full lines) as a function of the top gate voltage V_g . When $V_g < (\Delta_{so} - E_F)$, such that left and right regions are in the QSH phase, current is perfectly transmitted by the QSH edge states, as shown in the current-density plot in the left inset. When V_g is high enough ($V_g > (\Delta_{so} - E_F)$) that the right part of the sample enters the QH phase, a QSH-QH junction is created, which is characterized by a chiral state propagating along the interface. This is illustrated in the current-density plot shown in the right inset. Once it has reached the opposite edge, this chiral state is partially transmitted in lead 2, partially transmitted in lead 3, with proportions shown in the main plot. The light red curves correspond to an abrupt voltage change across the junction region while the dark blue curves correspond to a smooth transition. Parameters are $E_F/\Delta_{so} = 0.58$ (in the left half of the sample), $\lambda_{so} = 0.02$, $l_B \simeq 8$, and widths $W_0 = W_c = 40\sqrt{3}$ for the leads and central region.

seen as classical skipping orbits of mixed electron-“hole” character. The characteristics of the state propagating at the interface between QSH and QH insulators, on the other hand, are still unclear as far as we know.

Our proposal is the following. Consider the Z-shape geometry shown in Fig. 9.5. It is split into two regions: the left half and the right half. A top gate is applied on the latter in order to tune the Fermi level in both regions independently. In Fig. 9.6, we plot, for a given value of the Fermi energy in the left half inside the QSH gap, the differential conductance T_{i0} from lead 0 to leads 1, 2 and 3 as a function of the gate voltage (which determines the value of the Fermi energy in the right half). While the Fermi energy in the right half remains below the value of Δ_{so} , transport characteristics remain unaffected by the gate (left inset of Fig. 9.6). However, as soon as the Fermi energy in the right half crosses the QSH gap, it gives rise to a QSH-QH junction characterized by a topological state at its interface (see right inset of Fig. 9.6). This chiral state propagates along the interface until it reaches the opposite edge, and then gets partially transmitted in lead 2, partially transmitted in lead 3, with proportions which depend on the microscopic details of the model (Fermi energies, the length of the interface, the smoothness of the potential step, the amount of disorder, the possible valley-space polarization of the edge states, etc), the study of which is left to subsequent work. This system constitutes a very efficient spin-polarized charge-current switching mechanism, as the current in lead 1 (respectively 2) can be reversibly switched from one (respectively zero) to zero (respectively non-zero) while simultaneously being spin-polarized (see Fig. 9.6). Additionally, this switching can be activated by simply tuning the voltage in the top gate over a very small energy range (whose lower bound will depend on the magnitude of the disorder in the vicinity of the transition), and should yield extremely sharp transitions with values of on/off current topologically protected from the presence of disorder⁵.

9.5 Conclusions

In summary, we showed that the transition between QSH and QH phases in graphene is independent of the value of the magnetic field (neglecting the weak effect of Zeeman splitting) and can be crossed simply by tuning the value of the Fermi energy across the SO-induced QSH gap. This unique property owes to existence of the zero-energy LL in graphene. In a heterojunction, one of the spin species gives rise to a chiral state propagating along the interface between QSH and QH phases. The nature of this special state is a fascinating issue which could bring new light concerning the unresolved mystery of conductance plateaus observed in quantum Hall n - p

⁵Note that a similar switching mechanism (without the spin polarization) could also be realized using a graphene quantum Hall n - p junction, provided the charge-density fluctuations close to the Dirac point can be reduced.

junctions [148, 149]. We also showed that the tunable transition between the QSH and QH topological phases could serve as a spin-polarized charge-current switch with potentially extremely high, topologically protected, on/off ratios. An interesting future direction of research could be to investigate whether this tunable topological phase transition can arise in bilayer graphene [155], which also possesses zero-energy Landau levels [156] and has very recently been shown to host a \mathbb{Z}_2 topologically insulating phase [157] for strong enough Rashba SO coupling.

Perspectives and future work

The thesis, as presented above, consists of two parts. So far there was no link between them and they appeared as completely separate. However, there is an interesting possibility of using the formalism developed in the first part of the thesis to make a new step in investigating the effects presented in the second part. Over the last two years, a series of works was done on the properties of various semiconducting materials irradiated by the high-frequency electromagnetic fields [158, 159, 160, 161, 162, 163]. It was shown that the band structure of these materials modified by the presence of radiation manifests itself in an intriguing behavior of DC conductance when a *stationary* bias is applied. Moreover, such systems as graphene and topological insulators (for example, HgTe/HgCdTe quantum wells) were shown to undergo a topological phase transition from a trivial (insulating) to a topological state when a circularly polarized laser field is applied [158, 159, 161, 163]. These proposals are based on the Floquet theory, and this is the Floquet Hamiltonian which possesses the topological edge states. The only difficulty is that the quasistationary states described by the Floquet Hamiltonian can be populated in a complicated way making it difficult to single out the effect of the (topological) edge states only [159, 161].

As a possible extension of the results presented in this thesis would be the investigation of the effect of external radiation on graphene with SO coupling. There are two regimes one could choose: off-resonant (when the frequency of light is bigger than the band width of a material, so that only virtual absorption/emission processes take place) [163] and resonant (low enough frequencies, enabling direct absorptions/emissions of light quanta) [159]. It was shown in Ref.[163], that in graphene the off-resonant light is enough to see the quantum Hall effect without a magnetic field. One interesting possibility would be to see whether one can observe any kind of topological transition, like the QSH/QH considered in this thesis, if we shine a high frequency light on graphene instead of applying a magnetic field. Moreover, in Ref.[159] authors showed that by an appropriate choice of the laser field parameters, it is possible to create both co- and counter-propagating helical edge states in an initially trivial (insulating) system (they considered HgTe/HgCdTe in this work).

Thus, the properties of various semiconducting materials in presence of an external radiation is a very promising line of research. Further investigations are needed to understand how one

can engineer in a controlled way the many interesting features potentially useful to design new optoelectronic nanodevices.

Appendix A

General results for AC observables given in Section 3.3

In this Appendix we present the formulae for AC observables beyond the WBL, see Section 3.3. Just as before we will split them in two parts: response to the internal and external perturbations.

A.1 External perturbation

First, we consider the situation when the AC voltage is applied to one of the contacts, say m' . Below we present various system response functions to such a perturbation assuming there is no DC bias in the system.

The AC conductance matrix is given by

$$\begin{aligned} \Upsilon_{m,m'}(\omega) = \frac{e^2}{h} \int \frac{dE}{\hbar\omega} \left\{ (f(E) - f(E + \hbar\omega)) \text{Tr} \left[\Lambda_m^{ar}(E; E + \hbar\omega) \mathcal{G}_2 \Lambda_{m'}^{ra}(E + \hbar\omega; E) \mathcal{G}_0^\dagger \right] \right. \\ + f(E + \hbar\omega) \text{Tr} \left[\Lambda_m^{aa}(E; E + \hbar\omega) \mathcal{G}_2^\dagger \Lambda_{m'}^{aa}(E + \hbar\omega; E) \mathcal{G}_0^\dagger \right] \\ - f(E) \text{Tr} \left[\Lambda_m^{rr}(E; E + \hbar\omega) \mathcal{G}_2 \Lambda_{m'}^{rr}(E + \hbar\omega; E) \mathcal{G}_0 \right] \\ \left. - f(E) \text{Tr} [D_1] + f(E + \hbar\omega) \text{Tr} [D_2] \delta_{m,m'} \right\}. \end{aligned} \quad (\text{A.1})$$

Functions $D_{1,2}$ in the diagonal part are defined as

$$D_1 = i \left(\mathcal{G}_2 - \mathcal{G}_0^\dagger \right) \Gamma(m'; E) + \left(\mathcal{G}_0 - \mathcal{G}_0^\dagger \right) \Lambda_{m'}^{rr}(E; E + \hbar\omega), \quad (\text{A.2})$$

$$D_2 = i \left(\mathcal{G}_2 - \mathcal{G}_0^\dagger \right) \Gamma(m'; E + \hbar\omega) + \left(\mathcal{G}_2 - \mathcal{G}_2^\dagger \right) \Lambda_{m'}^{aa}(E; E + \hbar\omega). \quad (\text{A.3})$$

The *stationary (DC) component of the current* to leading order in perturbation amplitude reads ($m \neq m'$)

$$\begin{aligned} \frac{d^2 I_m(0\omega)}{dV_{ac}^2} = & \frac{ie^3}{4\hbar^2\omega^2} \int \frac{dE}{2\pi\hbar} \left\{ \right. \\ & (f(E) - f(E + \hbar\omega)) \text{Tr} \left[\mathcal{G}_0 \Lambda_{m'}^{ra}(E; E + \hbar\omega) \mathcal{G}_2^\dagger \Lambda_{m'}^{aa}(E + \hbar\omega; E) \mathcal{G}_0^\dagger \Gamma_m(E) \right. \\ & \quad \left. - \mathcal{G}_0 \Lambda_{m'}^{rr}(E; E + \hbar\omega) \mathcal{G}_2 \Lambda_{m'}^{ra}(E + \hbar\omega; E) \mathcal{G}_0^\dagger \Gamma_m(E) \right] \\ & + (f(E - \hbar\omega) - f(E)) \text{Tr} \left[\mathcal{G}_0 \Lambda_{m'}^{rr}(E; E - \hbar\omega) \mathcal{G}_{-2} \Lambda_{m'}^{ra}(E - \hbar\omega; E) \mathcal{G}_0^\dagger \Gamma_m(E) \right. \\ & \quad \left. - \mathcal{G}_0 \Lambda_{m'}^{ra}(E; E - \hbar\omega) \mathcal{G}_{-2}^\dagger \Lambda_{m'}^{aa}(E - \hbar\omega; E) \mathcal{G}_0^\dagger \Gamma_m(E) \right] \\ & \left. - if(E) \text{Tr} \left[\mathcal{G}_0 \left(\Gamma_{m'}(E + \hbar\omega) + \Gamma_{m'}(E - \hbar\omega) - 2\Gamma_{m'}(E) \right) \mathcal{G}_0^\dagger \Gamma_m(E) \right] \right\}. \end{aligned} \quad (\text{A.4})$$

Adiabatic current. Assuming that the frequency of the perturbation is very small, to zeroth order in $\hbar\omega$ the current is ($m \neq m'$)

$$\begin{aligned} I_m^{ad}(t) = & \frac{e}{h} \int dE \left\{ f(E) \text{Tr} \left[i \left(F^0(t, E) - F^{0,\dagger}(t, E) \right) \Gamma_m(E) - F^0(t, E) \Gamma(E) F^{0,\dagger}(t, E) \Gamma_m(E) \right] \right. \\ & \left. + \text{Tr} \left[F^0(t, E) \left(\frac{\partial \Gamma_{m'}(E)}{\partial E} f(E) + \frac{\partial f}{\partial E} \Gamma_{m'}(E) \right) F^{0,\dagger}(t, E) \Gamma_m(E) \right] eV_{ac} \cos \omega t \right\}, \end{aligned} \quad (\text{A.5})$$

where the definition of the functions $F^{0,1}(t, E)$ is given in Section 4.3.2.

Correction to the adiabatic current. It is the leading order correction of the order $\sim \hbar\omega$ to Eq.(A.5). Note that it contains all orders in V_{ac} ,

$$\delta I_m^{ad}(t) = \delta I_m^1(t) + \delta I_m^2(t) + \delta I_m^3(t) + \delta I_m^4(t) + \delta I_m^5(t), \quad (\text{A.6})$$

where separate parts read,

$$\begin{aligned} \delta I_m^1(t) = e \int \frac{dE}{2\pi\hbar} \left\{ \text{Tr} \left[F^1(t, E) \left(\frac{\partial \Gamma_{m'}(E)}{\partial E} f(E) + \frac{\partial f}{\partial E} \Gamma_{m'}(E) \right) F^{0,\dagger}(t, E) \Gamma_m(E) \right. \right. \\ \left. \left. + F^0(t, E) \left(\frac{\partial \Gamma_{m'}(E)}{\partial E} f(E) + \frac{\partial f}{\partial E} \Gamma_{m'}(E) \right) F^{1,\dagger}(t, E) \Gamma_m(E) \right] \right. \\ \left. + f(E) \text{Tr} \left[i \left(F^1(t, E) - F^{1,\dagger}(t, E) \right) \Gamma_m(E) - F^1(t, E) \Gamma(E) F^{0,\dagger}(t, E) \Gamma_m(E) \right. \right. \\ \left. \left. - F^0(t, E) \Gamma(E) F^{1,\dagger}(t, E) \Gamma_m(E) \right] \right\}, \end{aligned} \quad (\text{A.7})$$

$$\delta I_m^2(t) = \frac{e\hbar}{2} \int \frac{dE}{2\pi\hbar} \text{Tr} \left[\frac{\partial(F^0(t, E) + F^{0,\dagger}(t, E))}{\partial t} \left(\frac{\partial \Gamma_m(E)}{\partial E} f(E) + \frac{\partial f}{\partial E} \Gamma_m(E) \right) \right], \quad (\text{A.8})$$

$$\begin{aligned} \delta I_m^3(t) = \frac{e\hbar}{2} \int \frac{dE}{2\pi\hbar} \frac{\partial}{\partial t} \left\{ \text{Tr} \left[F^0(t, E) \Gamma(E) F^{0,\dagger}(t, E) \frac{\partial}{\partial E} (\Sigma^r(m; E) + \Sigma^a(m; E)) \right] f(E) \right. \\ \left. - \text{Tr} \left[F^0(t, E) \left(\frac{\partial \Gamma_{m'}(E)}{\partial E} f(E) + \frac{\partial f}{\partial E} \Gamma_{m'}(E) \right) \right. \right. \\ \left. \left. \times F^{0,\dagger}(t, E) \frac{\partial}{\partial E} (\Sigma^r(m; E) + \Sigma^a(m; E)) \right] eV_{ac} \cos \omega t \right\}, \end{aligned} \quad (\text{A.9})$$

$$\begin{aligned} \delta I_m^4(t) = -\frac{ie\hbar}{2} \int \frac{dE}{2\pi\hbar} \left\{ \text{Tr} \left[F^0(t, E) \left(\frac{\partial \Gamma(E)}{\partial E} f(E) + \frac{\partial f}{\partial E} \Gamma(E) \right) \frac{\partial F^{0,\dagger}(t, E)}{\partial t} \Gamma_m(E) \right. \right. \\ \left. \left. - \frac{\partial F^0(t, E)}{\partial t} \left(\frac{\partial \Gamma(E)}{\partial E} f(E) + \frac{\partial f}{\partial E} \Gamma(E) \right) F^{0,\dagger}(t, E) \Gamma_m(E) \right] \right. \\ \left. + \text{Tr} \left[\frac{\partial F^0(t, E)}{\partial E} \Gamma(E) \frac{\partial F^{0,\dagger}(t, E)}{\partial t} \Gamma_m(E) - \frac{\partial F^0(t, E)}{\partial t} \Gamma(E) \frac{\partial F^{0,\dagger}(t, E)}{\partial E} \Gamma_m(E) \right] f(E) \right\}, \end{aligned} \quad (\text{A.10})$$

$$\begin{aligned} \delta I_m^5(t) = \frac{ie\hbar}{2} \int \frac{dE}{2\pi\hbar} \text{Tr} \left\{ \frac{\partial F^0(t, E)}{\partial E} \left(\frac{\partial \Gamma_{m'}(E)}{\partial E} f(E) + \frac{\partial f}{\partial E} \Gamma_{m'}(E) \right) \left[\frac{\partial}{\partial t} (F^{0,\dagger}(t, E) eV_{ac} \cos \omega t) \right] \Gamma_m(E) \right. \\ \left. - \left[\frac{\partial}{\partial t} (F^0(t, E) eV_{ac} \cos \omega t) \right] \left(\frac{\partial \Gamma_{m'}(E)}{\partial E} f(E) + \frac{\partial f}{\partial E} \Gamma_{m'}(E) \right) \frac{\partial F^{0,\dagger}(t, E)}{\partial E} \Gamma_m(E) \right\}. \end{aligned} \quad (\text{A.11})$$

The *generalized injectivity* [1, 6, 20], which is the density of particles on site i injected from the lead m' as a consequence of the oscillating electrochemical potential is

$$\begin{aligned} \frac{dn(i, 1\omega, m')}{dV_{ac}} = \frac{ie}{\hbar\omega} \int dE \left[(f(E) - f(E + \hbar\omega)) \mathcal{G}_2 \Lambda_{m'}^{ra}(E + \hbar\omega; E) \mathcal{G}_0^\dagger \right. \\ \left. - f(E) \mathcal{G}_2 \Lambda_{m'}^{rr}(E + \hbar\omega; E) \mathcal{G}_0 + f(E + \hbar\omega) \mathcal{G}_2^\dagger \Lambda_{m'}^{aa}(E + \hbar\omega; E) \mathcal{G}_0^\dagger \right]_{ii}. \end{aligned} \quad (\text{A.12})$$

A.2 Internal perturbation

Now we will present the results for the response to an internal potential. Again, we assume that there is no DC bias applied to the system.

Current response linear in V_{ac} is given by

$$\begin{aligned} \frac{dI_m(1\omega)}{dV_{ac}} = \frac{e^2}{h} \int dE \left\{ (f(E) - f(E + \hbar\omega)) \text{Tr} \left[\Lambda_m^{ar}(E; E + \hbar\omega) \mathcal{G}_2 W \mathcal{G}_0^\dagger \right] \right. \\ \left. - f(E) \text{Tr} \left[\Lambda_m^{rr}(E; E + \hbar\omega) \mathcal{G}_2 W \mathcal{G}_0 \right] + f(E + \hbar\omega) \text{Tr} \left[\Lambda_m^{aa}(E; E + \hbar\omega) \mathcal{G}_2^\dagger W \mathcal{G}_0^\dagger \right] \right\}. \quad (\text{A.13}) \end{aligned}$$

The *DC component of the current* caused by the rectification effect can be written (to leading order in V_{ac}) as

$$\begin{aligned} \frac{d^2 I_m(0\omega)}{dV_{ac}^2} = \frac{e^3}{4h} \int dE \text{Tr} \left[(f(E) - f(E + \hbar\omega)) \mathcal{G}_0 W \mathcal{G}_2 \Gamma(E + \hbar\omega) \mathcal{G}_2^\dagger W \mathcal{G}_0^\dagger \Gamma_m(E) \right. \\ \left. - (f(E - \hbar\omega) - f(E)) \mathcal{G}_0 W \mathcal{G}_{-2} \Gamma(E - \hbar\omega) \mathcal{G}_{-2}^\dagger W \mathcal{G}_0^\dagger \Gamma_m(E) \right]. \quad (\text{A.14}) \end{aligned}$$

Similarly, the *2nd harmonics of the current* is given by

$$\begin{aligned} \frac{d^2 I_m(2\omega)}{dV_{ac}^2} = \frac{e^3}{2h} \int dE \text{Tr} \left[(f(E) - f(E + \hbar\omega)) \mathcal{G}_2 W \mathcal{G}_0^\dagger W \mathcal{G}_{-2}^\dagger \Lambda_m^{ar}(E - \hbar\omega; E + \hbar\omega) \right. \\ \left. + (f(E - \hbar\omega) - f(E)) \mathcal{G}_2 W \mathcal{G}_0 W \mathcal{G}_{-2}^\dagger \Lambda_m^{ar}(E - \hbar\omega; E + \hbar\omega) \right. \quad (\text{A.15}) \end{aligned}$$

$$\begin{aligned} \left. + f(E + \hbar\omega) \mathcal{G}_2^\dagger W \mathcal{G}_0^\dagger W \mathcal{G}_{-2}^\dagger \Lambda_m^{aa}(E - \hbar\omega; E + \hbar\omega) \right. \quad (\text{A.16}) \\ \left. - f(E - \hbar\omega) \mathcal{G}_2 W \mathcal{G}_0 W \mathcal{G}_{-2} \Lambda_m^{rr}(E - \hbar\omega; E + \hbar\omega) \right]. \end{aligned}$$

The response function to perturbing the onsite potential on site i is the (*generalized emissivity*) [1, 6, 20] and it reads (note, that it differs from the original definition by Büttiker, where one has to multiply it by $1/(i\omega)$)

$$\begin{aligned} \frac{dI_m(1\omega)}{dV_{ii}} = \frac{e^2}{h} \int dE \left[(f(E) - f(E + \hbar\omega)) \mathcal{G}_0^\dagger \Lambda_m^{ar}(E; E + \hbar\omega) \mathcal{G}_2 \right. \\ \left. - f(E) \mathcal{G}_0 \Lambda_m^{rr}(E; E + \hbar\omega) \mathcal{G}_2 + f(E + \hbar\omega) \mathcal{G}_0^\dagger \Lambda_m^{aa}(E; E + \hbar\omega) \mathcal{G}_2^\dagger \right]_{ii}. \quad (\text{A.17}) \end{aligned}$$

Appendix B

Magnetic field in multi-terminal calculations

In this appendix, we explain how to compute the Peierls phase ϕ_{ij} between two atoms i and j in multi-terminal systems. It is given by

$$\phi_{ij} = \int_{\mathbf{r}_j}^{\mathbf{r}_i} \mathbf{A} \cdot d\mathbf{r} \quad (\text{B.1})$$

where $\mathbf{r}_i = (x_i, y_i)$ is the spatial position of site i . A common choice for \mathbf{A} is the Landau gauge (Lg)

$$\mathbf{A}_{Lg}(x, y) = -By \begin{pmatrix} 1 \\ 0 \end{pmatrix} \quad (\text{B.2})$$

which leads to

$$\phi_{ij}^{Lg} = -B(x_i - x_j) \frac{y_i + y_j}{2} \quad (\text{B.3})$$

(using linear paths between atoms). The numerical prescription follows simply: one calculates the real coordinates of the two atoms and uses the above equation to get ϕ_{ij} . An important aspect of the Landau gauge is that the phase depends on the x -coordinate only through the *difference* of x between the two atoms i and j . This is crucial for taking magnetic field into account in the leads: the leads are semi-infinite periodic systems made of layers. They are described by an intra-layer Hamiltonian H_0 and an inter-layer Hamiltonian V . Within the Landau gauge, we find that the matrices H_0 and V of *horizontal* leads are layer-independent, which allows the use of standard schemes to calculate their self-energies. However, general samples (such as the Ψ -shaped sample studied in this thesis) can have leads with an arbitrary angle θ with respect to the y -axis. For those leads, the corresponding gauge choice is

$$\mathbf{A}(\mathbf{r}) = -B(\mathbf{r} \cdot \mathbf{e}_2) \mathbf{e}_1 \quad (\text{B.4})$$

with

$$\mathbf{e}_1 = \begin{pmatrix} \cos \theta \\ \sin \theta \end{pmatrix}, \quad \mathbf{e}_2 = \begin{pmatrix} -\sin \theta \\ \cos \theta \end{pmatrix}, \quad (\text{B.5})$$

which leads to

$$\phi_{ij} = \phi_{ij}^{Lg} + \Phi_i - \Phi_j, \quad (\text{B.6})$$

where the potential

$$\Phi_i = B(1 - \cos 2\theta) \frac{x_i y_i}{2} + B \sin 2\theta \frac{x_i^2 - y_i^2}{4} \quad (\text{B.7})$$

is a pure gauge potential allowing to go from one choice of gauge to the other. A (possible) general prescription for an arbitrary system is now the following: one assigns a potential $\Phi_i = 0$ to all sites except those belonging to a lead. For the latter, one uses Eq.(B.7) with the appropriate angle θ . Then one calculates the phases ϕ_{ij} according to Eq.(B.6).

All the prescriptions above are given in real space. It is of course possible to calculate analytically the equivalent prescriptions in terms of the integer coordinates on the Bravais sublattices, as both are in one to one correspondance. However, for numerical purposes, it is more convenient to calculate the real space positions of the atoms numerically and then use Eqs. (B.3,B.6,B.7) in order to use a lattice-independent prescription.

Publication list

- M. H. D. Guimarães, O. Shevtsov, X. Waintal, and B. J. van Wees, "From quantum confinement to quantum Hall effect in graphene nanostructures", *Phys. Rev. B*, vol. 85, p. 075424, 2012.
- O. Shevtsov, P. Carmier, C. Groth, X. Waintal and D. Carpentier, "Tunable thermopower in a graphene-based topological insulator", *Phys. Rev. B*, vol. 85, p. 245441, 2012.
- O. Shevtsov, P. Carmier, C. Petitjean, C. Groth, D. Carpentier and X. Waintal, "Graphene-based heterojunction between two topological insulators", *Phys. Rev. X*, vol. 2, p. 031004, 2012.
- O. Shevtsov and X. Waintal, "Numerical cookbook for electronic quantum transport at finite frequency", submitted to *Phys. Rev. B*, 2012.

Bibliography

- [1] M. Buttiker, “Capacitance, admittance, and rectification properties of small conductors,” *Journal of Physics: Condensed Matter*, vol. 5, no. 50, p. 9361, 1993.
- [2] M. Büttiker, A. Prêtre, and H. Thomas, “Dynamic conductance and the scattering matrix of small conductors,” *Phys. Rev. Lett.*, vol. 70, pp. 4114–4117, 1993.
- [3] M. Büttiker, H. Thomas, and A. Prêtre, “Mesoscopic capacitors,” *Physics Letters A*, vol. 180, pp. 364 – 369, 1993.
- [4] M. Büttiker, A. Prêtre, and H. Thomas, “Admittance of small conductors,” *Phys. Rev. Lett.*, vol. 71, pp. 465–465, 1993.
- [5] M. Büttiker, H. Thomas, and A. Prêtre, “Current partition in multiprobe conductors in the presence of slowly oscillating external potentials,” *Zeitschrift für Physik B Condensed Matter*, vol. 94, pp. 133–137, 1994.
- [6] M. Büttiker, “Time-dependent current partition in mesoscopic conductors,” *Il Nuovo Cimento*, vol. 110B, pp. 509–522, 1995.
- [7] M. H. Pedersen and M. Büttiker, “Scattering theory of photon-assisted electron transport,” *Phys. Rev. B*, vol. 58, pp. 12993–13006, Nov 1998.
- [8] B. Wang, J. Wang, and H. Guo, “Current partition: A nonequilibrium green’s function approach,” *Phys. Rev. Lett.*, vol. 82, pp. 398–401, Jan 1999.
- [9] C. Roland, M. Buongiorno Nardelli, J. Wang, and H. Guo, “Dynamic conductance of carbon nanotubes,” *Phys. Rev. Lett.*, vol. 84, pp. 2921–2924, Mar 2000.
- [10] M.-K. Yip, W.-C. Kwok, J. Wang, and H. Guo, “Dynamic conductance of mesoscopic waveguides,” *Journal of Applied Physics*, vol. 89, no. 3, pp. 1777–1782, 2001.
- [11] B. Wang, J. Wang, and H. Guo, “Current plateaus of nonadiabatic charge pump: multiphoton assisted processes,” *Phys. Rev. B*, vol. 68, p. 155326, Oct 2003.

- [12] P. K. Tien and J. P. Gordon, “Multiphoton process observed in the interaction of microwave fields with the tunneling between superconductor films,” *Phys. Rev.*, vol. 129, pp. 647–651, Jan 1963.
- [13] A.-P. Jauho, N. S. Wingreen, and Y. Meir, “Time-dependent transport in interacting and noninteracting resonant-tunneling systems,” *Phys. Rev. B*, vol. 50, pp. 5528–5544, Aug 1994.
- [14] N. S. Wingreen, A.-P. Jauho, and Y. Meir, “Time-dependent transport through a mesoscopic structure,” *Phys. Rev. B*, vol. 48, pp. 8487–8490, Sep 1993.
- [15] M. P. Anantram and S. Datta, “Effect of phase breaking on the ac response of mesoscopic systems,” *Phys. Rev. B*, vol. 51, pp. 7632–7639, Mar 1995.
- [16] J. Q. You, C.-H. Lam, and H. Z. Zheng, “Landauer-büttiker formula for time-dependent transport through resonant-tunneling structures: A nonequilibrium green’s function approach,” *Phys. Rev. B*, vol. 62, pp. 1978–1983, Jul 2000.
- [17] G. Platero and R. Aguado, “Photon-assisted transport in semiconductor nanostructures,” *Physics Reports*, vol. 395, pp. 1–157, 2004.
- [18] S. Zhou, J. Jiang, and Q. Cai, “Small-signal ac response: a self-consistent non-equilibrium green’s function approach,” *Journal of Physics D: Applied Physics*, vol. 38, no. 2, p. 255, 2005.
- [19] C. Petitjean, D. Waltner, J. Kuipers, I. Adagideli, and K. Richter, “Semiclassical approach to the ac conductance of chaotic cavities,” *Phys. Rev. B*, vol. 80, p. 115310, Sep 2009.
- [20] Y. Wei and J. Wang, “Current conserving nonequilibrium ac transport theory,” *Phys. Rev. B*, vol. 79, p. 195315, May 2009.
- [21] D. Kienle, M. Vaidyanathan, and F. Léonard, “Self-consistent ac quantum transport using nonequilibrium green functions,” *Phys. Rev. B*, vol. 81, p. 115455, Mar 2010.
- [22] K. Kazymyrenko and X. Waintal, “Knitting algorithm for calculating green functions in quantum systems,” *Phys. Rev. B*, vol. 77, p. 115119, Mar 2008.
- [23] C. L. Kane and E. J. Mele, “Quantum spin Hall effect in graphene,” *Phys. Rev. Lett.*, vol. 95, p. 226801, 2005.
- [24] C. L. Kane and E. J. Mele, “ \mathbb{Z}_2 topological order and the quantum spin Hall effect,” *Phys. Rev. Lett.*, vol. 95, p. 146802, 2005.

- [25] D. Huertas-Hernando, F. Guinea, and A. Brataas, “Spin-orbit coupling in curved graphene, fullerenes, nanotubes, and nanotube caps,” *Phys. Rev. B*, vol. 74, p. 155426, 2006.
- [26] C. Weeks, J. Hu, J. Alicea, M. Franz, and R. Wu, “Engineering a robust quantum spin hall state in graphene via adatom deposition,” *Phys. Rev. X*, vol. 1, p. 021001, 2011.
- [27] O. Shevtsov, P. Carmier, C. Groth, X. Waintal, and D. Carpentier, “Tunable thermopower in a graphene-based topological insulator,” *Phys. Rev. B*, vol. 85, p. 245441, 2012.
- [28] A. De Martino, A. Hütten, and R. Egger, “Landau levels, edge states, and strained magnetic waveguides in graphene monolayers with enhanced spin-orbit interaction,” *Phys. Rev. B*, vol. 84, p. 155420, 2011.
- [29] S. Rotter, J.-Z. Tang, L. Wirtz, J. Trost, and J. Burgdörfer, “Modular recursive green’s function method for ballistic quantum transport,” *Phys. Rev. B*, vol. 62, pp. 1950–1960, Jul 2000.
- [30] P. Drouvelis, P. Schmelcher, and P. Bastian, “Parallel implementation of the recursive green’s function method,” *Journal of Computational Physics*, vol. 215, no. 2, pp. 741 – 756, 2006.
- [31] Y. Ji, Y. Chung, D. Sprinzak, M. Heiblum, D. Mahalu, and H. Shtrikman, “An electronic Mach-Zehnder interferometer,” *Nature*, vol. 422, no. 6930, pp. 415–418, 2003.
- [32] I. Neder, M. Heiblum, Y. Levinson, D. Mahalu, and V. Umansky, “Unexpected behavior in a two-path electron interferometer,” *Phys. Rev. Lett.*, vol. 96, p. 016804, 2006.
- [33] I. Neder, M. Heiblum, D. Mahalu, and V. Umansky, “Entanglement, dephasing, and phase recovery via cross-correlation measurements of electrons,” *Phys. Rev. Lett.*, vol. 98, p. 036803, Jan 2007.
- [34] I. Neder, F. Marquardt, M. Heiblum, D. Mahalu, and V. Umansky, “Controlled dephasing of electrons by non-gaussian shot noise,” *Nat. Phys.*, vol. 3, pp. 534–537, 2007.
- [35] P. Roulleau, F. Portier, D. C. Glattli, P. Roche, A. Cavanna, G. Faini, U. Gennser, and D. Mailly, “Finite bias visibility of the electronic mach-zehnder interferometer,” *Phys. Rev. B*, vol. 76, p. 161309, 2007.
- [36] P. Roulleau, F. Portier, P. Roche, A. Cavanna, G. Faini, U. Gennser, and D. Mailly, “Direct measurement of the coherence length of edge states in the integer quantum hall regime,” *Phys. Rev. Lett.*, vol. 100, p. 126802, 2008.

- [37] P. Roulleau, F. Portier, P. Roche, A. Cavanna, G. Faini, U. Gennser, and D. Mailly, “Noise dephasing in edge states of the integer quantum hall regime,” *Phys. Rev. Lett.*, vol. 101, p. 186803, 2008.
- [38] W. D. Oliver, J. Kim, R. C. Liu, and Y. Yamamoto, “Hanbury Brown and Twiss-Type Experiment with Electrons,” *Science*, vol. 284, no. 5412, pp. 299–301, 1999.
- [39] F. E. Camino, W. Zhou, and V. J. Goldman, “Aharonov-bohm electron interferometer in the integer quantum hall regime,” *Phys. Rev. B*, vol. 72, p. 155313, Oct 2005.
- [40] V. Kotimäki and E. Räsänen, “Aharonov-bohm effect in many-electron quantum rings,” *Phys. Rev. B*, vol. 81, p. 245316, Jun 2010.
- [41] P. W. Anderson, “Absence of diffusion in certain random lattices,” *Phys. Rev.*, vol. 109, pp. 1492–1505, 1958.
- [42] D. Vasileska and S. M. Goodnick, “Computational electronics,” *Synthesis Lectures on Computational Electromagnetics*, vol. 1, no. 1, pp. 1–216, 2006.
- [43] L. V. Keldysh, “Low frequency admittance of a quantum point contact,” *Sov. Phys. JETP*, vol. 20, pp. 1018–1026, 1965.
- [44] J. Rammer and H. Smith, “Quantum field-theoretical methods in transport theory of metals,” *Rev. Mod. Phys.*, vol. 58, pp. 323–359, Apr 1986.
- [45] S. Datta, *Electronic Transport in Mesoscopic Systems*. Cambridge Univ. Press, 1997.
- [46] J. Rammer, *Quantum field theory of non-equilibrium states*. Cambridge Univ. Press, 2007.
- [47] H. Haug and A.-P. Jauho, *Quantum Kinetics in Transport and Optics of Semiconductors*. Springer, 2010.
- [48] M. Buttiker, “Symmetry of electrical conduction,” *IBM Journal of Research and Development*, vol. 32, no. 3, pp. 317–334, 1988.
- [49] H. M. Pastawski, “Classical and quantum transport from generalized landauer-büttiker equations,” *Phys. Rev. B*, vol. 44, pp. 6329–6339, 1991.
- [50] Y. Imry and R. Landauer, “Conductance viewed as transmission,” *Rev. Mod. Phys.*, vol. 71, pp. S306–S312, Mar 1999.
- [51] R. Landauer, “Conductance from transmission: common sense points,” *Physica Scripta*, vol. 1992, no. T42, p. 110, 1992.

- [52] Y. Meir and N. S. Wingreen, “Landauer formula for the current through an interacting electron region,” *Phys. Rev. Lett.*, vol. 68, pp. 2512–2515, Apr 1992.
- [53] K. B. Kahen, “Recursive-green’s-function analysis of wave propagation in two-dimensional nonhomogeneous media,” *Phys. Rev. E*, vol. 47, pp. 2927–2933, Apr 1993.
- [54] D. Mamaluy, M. Sabathil, and P. Vogl, “Efficient method for the calculation of ballistic quantum transport,” *Journal of Applied Physics*, vol. 93, no. 8, pp. 4628–4633, 2003.
- [55] D. Mamaluy, D. Vasileska, M. Sabathil, T. Zibold, and P. Vogl, “Contact block reduction method for ballistic transport and carrier densities of open nanostructures,” *Phys. Rev. B*, vol. 71, p. 245321, 2005.
- [56] A. R. Akhmerov, C. W. Groth, J. Tworzydło, and C. W. J. Beenakker, “Switching of electrical current by spin precession in the first landau level of an inverted-gap semiconductor,” *Phys. Rev. B*, vol. 80, p. 195320, 2009.
- [57] H. Haugen, D. Huertas-Hernando, A. Brataas, and X. Waintal, “Crossed andreev reflection versus electron transfer in three-terminal graphene devices,” *Phys. Rev. B*, vol. 81, p. 174523, 2010.
- [58] H. Haugen, A. Brataas, X. Waintal, and G. E. W. Bauer, “Focused crossed andreev reflection,” *EPL (Europhysics Letters)*, vol. 93, p. 67005, 2011.
- [59] M. H. D. Guimarães, O. Shevtsov, X. Waintal, and B. J. van Wees, “From quantum confinement to quantum hall effect in graphene nanostructures,” *Phys. Rev. B*, vol. 85, p. 075424, Feb 2012.
- [60] O. Shevtsov, P. Carmier, C. Petitjean, C. Groth, D. Carpentier, and X. Waintal, “Graphene-based heterojunction between two topological insulators,” *Phys. Rev. X*, vol. 2, p. 031004, 2012.
- [61] Y. Blanter and M. Büttiker, “Shot noise in mesoscopic conductors,” *Physics Reports*, vol. 336, pp. 1 – 166, 2000.
- [62] L. D. Landau and E. M. Lifshitz, *Quantum Mechanics: Non-relativistic theory*, vol. 3. Pergamon Press, 1977.
- [63] M. Büttiker and T. Christen, “Basic elements of electrical conduction,” in *Quantum transport in semiconductor submicron structures* (B. Kramer, ed.), vol. 326 of *NATO Science Series E: (closed)*, 1996.

- [64] I. B. Levinson, “Potential distribution in a quantum point contact,” *Sov. Phys. JETP*, vol. 68, pp. 1257–1265, 1989.
- [65] D. S. Fisher and P. A. Lee, “Relation between conductivity and transmission matrix,” *Phys. Rev. B*, vol. 23, pp. 6851–6854, 1981.
- [66] L. Arrachea and M. Moskalets, “Relation between scattering-matrix and keldysh formalisms for quantum transport driven by time-periodic fields,” *Phys. Rev. B*, vol. 74, p. 245322, 2006.
- [67] E. N. Economou, *Green’s Functions in Quantum Physics*. Springer, 3rd ed., 2006.
- [68] R. Piessens, E. d. Kapenga, C. Uberhuber, and D. Kahaner, *QUADPACK: A Subroutine Package for Automatic Integration*. Springer–Verlag, 1983.
- [69] W. H. Press, S. A. Teukolsky, W. T. Vetterling, and B. P. Flannery, *Numerical Recipes: The Art of Scientific Computing*. Cambridge University Press, 3 ed., 2007.
- [70] T. Christen and M. Büttiker, “Low frequency admittance of a quantum point contact,” *Phys. Rev. Lett.*, vol. 77, pp. 143–146, Jul 1996.
- [71] I. E. Aronov, N. N. Beletskii, G. P. Berman, D. K. Campbell, G. D. Doolen, and S. V. Dudiy, “Frequency dependence of the admittance of a quantum point contact,” *Phys. Rev. B*, vol. 58, pp. 9894–9906, Oct 1998.
- [72] I. E. Aronov, G. P. Berman, D. K. Campbell, and S. V. Dudiy, “Wigner function description of a.c. transport through a two-dimensional quantum point contact,” *Journal of Physics: Condensed Matter*, vol. 9, no. 24, p. 5089, 1997.
- [73] P. Roulleau, F. Portier, P. Roche, A. Cavanna, G. Faini, U. Gennser, and D. Mailly, “Tuning decoherence with a voltage probe,” *Phys. Rev. Lett.*, vol. 102, p. 236802, 2009.
- [74] B. Trauzettel, Y. M. Blanter, and A. F. Morpurgo, “Photon-assisted electron transport in graphene: Scattering theory analysis,” *Phys. Rev. B*, vol. 75, p. 035305, 2007.
- [75] K. S. Novoselov, A. K. Geim, S. V. Morozov, D. Jiang, Y. Zhang, S. V. Dubonos, I. V. Grigorieva, and A. A. Firsov, “Electric field effect in atomically thin carbon films,” *Science*, vol. 306, p. 666, 2004.
- [76] K. S. Novoselov, A. K. Geim, S. V. Morozov, D. Jiang, M. I. Katsnelson, I. V. Grigorieva, S. V. Dubonos, and A. A. Firsov, “Two-dimensional gas of massless dirac fermions in graphene,” *Nature*, vol. 438, p. 197, 2005.

- [77] P. R. Wallace, “The band theory of graphite,” *Phys. Rev.*, vol. 71, pp. 622–634, 1947.
- [78] J. W. McClure, “Diamagnetism of graphite,” *Phys. Rev.*, vol. 104, pp. 666–671, 1956.
- [79] J. C. Slonczewski and P. R. Weiss, “Band structure of graphite,” *Phys. Rev.*, vol. 109, pp. 272–279, 1958.
- [80] G. S. Painter and D. E. Ellis, “Electronic band structure and optical properties of graphite from a variational approach,” *Phys. Rev. B*, vol. 1, pp. 4747–4752, 1970.
- [81] M. Z. Hasan and C. L. Kane, “Colloquium: Topological insulators,” *Rev. Mod. Phys.*, vol. 82, pp. 3045–3067, 2010.
- [82] B. A. Bernevig, T. L. Hughes, and S.-C. Zhang, “Quantum spin Hall effect and topological phase transition in HgTe quantum wells,” *Science*, vol. 314, pp. 1757–1761, 2006.
- [83] J. E. Moore and L. Balents, “Topological invariants of time-reversal-invariant band structures,” *Phys. Rev. B*, vol. 75, p. 121306, 2007.
- [84] R. Roy, “Topological phases and the quantum spin hall effect in three dimensions,” *Phys. Rev. B*, vol. 79, p. 195322, 2009.
- [85] M. O. Goerbig, “Electronic properties of graphene in a strong magnetic field,” *Rev. Mod. Phys.*, vol. 83, pp. 1193–1243, 2011.
- [86] J.-C. Charlier, X. Blase, and S. Roche, “Electronic and transport properties of nanotubes,” *Rev. Mod. Phys.*, vol. 79, pp. 677–732, 2007.
- [87] S. Reich, J. Maultzsch, C. Thomsen, and P. Ordejón, “Tight-binding description of graphene,” *Phys. Rev. B*, vol. 66, p. 035412, Jul 2002.
- [88] H. Hsu and L. E. Reichl, “Modeling graphene layers and single-walled carbon nanotubes with regularized δ -function potentials,” *Phys. Rev. B*, vol. 72, p. 155413, 2005.
- [89] A. Cresti, N. Nemeč, B. Biel, G. Niebler, F. Triozon, G. Cuniberti, and S. Roche, “Charge transport in disordered graphene-based low dimensional materials,” *Nano Research*, vol. 1, pp. 361–394, 2008.
- [90] R. Saito, G. Dresselhaus, and M. S. Dresselhaus, *Physical Properties of Carbon Nanotubes*. World Scientific Publishing, 1998.
- [91] E. Y. Andrei, G. Li, and X. Du, “Electronic properties of graphene: a perspective from scanning tunneling microscopy and magnetotransport,” *Reports on Progress in Physics*, vol. 75, p. 056501, 2012.

- [92] A. H. C. Neto, F. Guinea, N. M. R. Peres, K. S. Novoselov, and A. K. Geim, “The electronic properties of graphene,” *Rev. Mod. Phys.*, vol. 81, p. 109, 2009.
- [93] S. Weinberg, *The Quantum Theory of Fields I*. Cambridge University Press, 1995.
- [94] N. H. Shon and T. Ando, “Quantum transport in two-dimensional graphite system,” *Journal of the Physical Society of Japan*, vol. 67, pp. 2421–2429, 1998.
- [95] M. I. Katsnelson, K. S. Novoselov, and A. K. Geim, “Chiral tunnelling and the Klein paradox in graphene,” *Nature Physics*, vol. 2, pp. 620–625, 2006.
- [96] L. Brey and H. A. Fertig, “Electronic states of graphene nanoribbons studied with the dirac equation,” *Phys. Rev. B*, vol. 73, p. 235411, 2006.
- [97] K. Wakabayashi, M. Fujita, H. Ajiki, and M. Sigrist, “Electronic and magnetic properties of nanographite ribbons,” *Phys. Rev. B*, vol. 59, pp. 8271–8282, 1999.
- [98] H. Zheng, Z. F. Wang, T. Luo, Q. W. Shi, and J. Chen, “Analytical study of electronic structure in armchair graphene nanoribbons,” *Phys. Rev. B*, vol. 75, p. 165414, 2007.
- [99] J. Wurm, M. Wimmer, I. Adagideli, K. Richter, and H. U. Baranger, “Interfaces within graphene nanoribbons,” *New Journal of Physics*, vol. 11, p. 095022, 2009.
- [100] Y. Zhang, Y.-W. Tan, H. L. Stormer, and P. Kim, “Experimental observation of quantum hall effect and berry’s phase in graphene,” *Nature*, vol. 438, p. 201, 2005.
- [101] Z. Jiang, E. A. Henriksen, L. C. Tung, Y.-J. Wang, M. E. Schwartz, M. Y. Han, P. Kim, and H. L. Stormer, “Infrared spectroscopy of landau levels of graphene,” *Phys. Rev. Lett.*, vol. 98, p. 197403, 2007.
- [102] G. Li and E. Y. Andrei, “Observation of landau levels of dirac fermions in graphite,” *Nat. Phys.*, vol. 3, pp. 623–627, 2007.
- [103] V. P. Gusynin, V. A. Miransky, S. G. Sharapov, and I. A. Shovkovy, “Edge states, mass and spin gaps, and quantum hall effect in graphene,” *Phys. Rev. B*, vol. 77, p. 205409, 2008.
- [104] V. P. Gusynin, V. A. Miransky, S. G. Sharapov, I. A. Shovkovy, and C. M. Wyenberg, “Edge states on graphene ribbons in magnetic field: Interplay between dirac and ferromagnetic-like gaps,” *Phys. Rev. B*, vol. 79, p. 115431, 2009.
- [105] T. Ando, “Spin-orbit interaction in carbon nanotubes,” *Journal of the Physical Society of Japan*, vol. 69, pp. 1757–1763, 2000.

- [106] H. Min, J. E. Hill, N. A. Sinitsyn, B. R. Sahu, L. Kleinman, and A. H. MacDonald, “Intrinsic and rashba spin-orbit interactions in graphene sheets,” *Phys. Rev. B*, vol. 74, p. 165310, 2006.
- [107] Y. Yao, F. Ye, X.-L. Qi, S.-C. Zhang, and Z. Fang, “Spin-orbit gap of graphene: First-principles calculations,” *Phys. Rev. B*, vol. 75, p. 041401, 2007.
- [108] A. H. Castro Neto and F. Guinea, “Impurity-induced spin-orbit coupling in graphene,” *Phys. Rev. Lett.*, vol. 103, p. 026804, 2009.
- [109] S. Abdelouahed, A. Ernst, J. Henk, I. V. Maznichenko, and I. Mertig, “Spin-split electronic states in graphene: Effects due to lattice deformation, rashba effect, and adatoms by first principles,” *Phys. Rev. B*, vol. 82, p. 125424, 2010.
- [110] B. H. Braensden and C. J. Joachain, *Physics of Atoms and Molecules*. Longman Scientific Technical, 1984.
- [111] Y. A. Bychkov and E. I. Rashba, “Oscillatory effects and the magnetic susceptibility of carriers in inversion layers,” *Journal of Physics C: Solid State Physics*, vol. 17, p. 6039, 1984.
- [112] G. Dresselhaus, “Spin-orbit coupling effects in zinc blende structures,” *Phys. Rev.*, vol. 100, pp. 580–586, 1955.
- [113] J. Serrano, M. Cardona, and T. Ruf, “Spin-orbit splitting in diamond: excitons and acceptor related states,” *Solid State Communications*, vol. 113, pp. 411 – 414, 2000.
- [114] F. Hermann and S. Skillman, *Atomic Structure Calculations*. Prentice Hall, Englewood Cliffs, NJ, 1963.
- [115] D. Tománek and S. G. Louie, “First-principles calculation of highly asymmetric structure in scanning-tunneling-microscopy images of graphite,” *Phys. Rev. B*, vol. 37, pp. 8327–8336, 1988.
- [116] D. Tománek and M. A. Schluter, “Growth regimes of carbon clusters,” *Phys. Rev. Lett.*, vol. 67, pp. 2331–2334, 1991.
- [117] B. Zhou, H.-Z. Lu, R.-L. Chu, S.-Q. Shen, and Q. Niu, “Finite size effects on helical edge states in a quantum spin-hall system,” *Phys. Rev. Lett.*, vol. 101, p. 246807, 2008.
- [118] Y. Ohyama, H. Tsuchiura, and A. Sakuma, “Finite size effects on the quantum spin hall state,” *Journal of Physics: Conference Series*, vol. 266, p. 012103, 2011.

- [119] G. Metalidis and E. Prada, “Transport through quantum spin Hall insulator/metal junctions in graphene ribbons,” 2011.
- [120] Y. Hatsugai, “Chern number and edge states in the integer quantum hall effect,” *Phys. Rev. Lett.*, vol. 71, pp. 3697–3700, 1993.
- [121] T. Fukui and Y. Hatsugai, “Topological aspects of the quantum spin-hall effect in graphene: z_2 topological order and spin chern number,” *Phys. Rev. B*, vol. 75, p. 121403, 2007.
- [122] L. Fu and C. L. Kane, “Time reversal polarization and a Z_2 adiabatic spin pump,” *Phys. Rev. B*, vol. 74, p. 195312, 2006.
- [123] L. Fu and C. L. Kane, “Topological insulators with inversion symmetry,” *Phys. Rev. B*, vol. 76, p. 045302, 2007.
- [124] T. Fukui and Y. Hatsugai, “Quantum spin hall effect in three dimensional materials: Lattice computation of z_2 topological invariants and its application to bi and sb,” *Journal of the Physical Society of Japan*, vol. 76, p. 053702, 2007.
- [125] T. Fukui, T. Fujiwara, and Y. Hatsugai, “Topological meaning of z_2 numbers in time reversal invariant systems,” *Journal of the Physical Society of Japan*, vol. 77, p. 123705, 2008.
- [126] X.-L. Qi, T. L. Hughes, and S.-C. Zhang, “Topological field theory of time-reversal invariant insulators,” *Phys. Rev. B*, vol. 78, p. 195424, 2008.
- [127] R. Roy, “ Z_2 classification of quantum spin hall systems: An approach using time-reversal invariance,” *Phys. Rev. B*, vol. 79, p. 195321, 2009.
- [128] Z. Wang, X.-L. Qi, and S.-C. Zhang, “Equivalent topological invariants of topological insulators,” *New Journal of Physics*, vol. 12, p. 065007, 2010.
- [129] E. H. Hwang, S. Adam, and S. Das Sarma, “Carrier transport in two-dimensional graphene layers,” *Phys. Rev. Lett.*, vol. 98, p. 186806, 2007.
- [130] J. Martin, N. Akerman, G. Ulbricht, T. Lohmann, J. H. Smet, K. von Klitzing, and A. Yacoby, “Observation of electron-hole puddles in graphene using a scanning single-electron transistor,” *Nat. Phys.*, vol. 4, p. 144, 2008.
- [131] K. T. Chan, J. B. Neaton, and M. L. Cohen, “First-principles study of metal adatom adsorption on graphene,” *Phys. Rev. B*, vol. 77, p. 235430, 2008.

- [132] Z. Qiao, S. A. Yang, W. Feng, W.-K. Tse, J. Ding, Y. Yao, J. Wang, and Q. Niu, “Quantum anomalous hall effect in graphene from rashba and exchange effects,” *Phys. Rev. B*, vol. 82, p. 161414, 2010.
- [133] K. Nakada, M. Fujita, G. Dresselhaus, and M. S. Dresselhaus, “Edge state in graphene ribbons: Nanometer size effect and edge shape dependence,” *Phys. Rev. B*, vol. 54, pp. 17954–17961, 1996.
- [134] C. R. Dean, A. F. Young, I. Meric, C. Lee, L. Wang, S. Sorgenfrei, K. Watanabe, T. Taniguchi, P. Kim, K. L. Shepard, and J. Hone, “Boron nitride substrates for high-quality graphene electronics,” *Nature Nanotechnology*, vol. 5, p. 722, 2010.
- [135] A. Schuessler, P. M. Ostrovsky, I. V. Gornyi, and A. D. Mirlin, “Analytic theory of ballistic transport in disordered graphene,” *Phys. Rev. B*, vol. 79, p. 075405, 2009.
- [136] J. Wurm, M. Wimmer, and K. Richter, “Symmetries and the conductance of graphene nanoribbons with long-range disorder,” *Phys. Rev. B*, vol. 85, p. 245418, 2012.
- [137] U. Sivan and Y. Imry, “Multichannel Landauer formula for thermoelectric transport with application to thermopower near the mobility edge,” *Phys. Rev. B*, vol. 33, pp. 551–558, 1986.
- [138] M. Cutler and N. F. Mott, “Observation of Anderson localization in an electron gas,” *Phys. Rev.*, vol. 181, pp. 1336–1340, 1969.
- [139] G. Tkachov and E. M. Hankiewicz, “Ballistic quantum spin hall state and enhanced edge backscattering in strong magnetic fields,” *Phys. Rev. Lett.*, vol. 104, p. 166803, 2010.
- [140] Y. Yang, Z. Xu, L. Sheng, B. Wang, D. Y. Xing, and D. N. Sheng, “Time-reversal-symmetry-broken quantum spin hall effect,” *Phys. Rev. Lett.*, vol. 107, p. 066602, 2011.
- [141] N. Goldman, W. Beugeling, and C. M. Smith, “Topological phase transitions between chiral and helical spin textures in a lattice with spin-orbit coupling and a magnetic field,” *EPL*, 2011.
- [142] D. A. Abanin, P. A. Lee, and L. S. Levitov, “Spin-filtered edge states and quantum hall effect in graphene,” *Phys. Rev. Lett.*, vol. 96, p. 176803, 2006.
- [143] Y. Zhang, Z. Jiang, J. P. Small, M. S. Purewal, Y.-W. Tan, M. Fazlollahi, J. D. Chudow, J. A. Jaszczak, H. L. Stormer, and P. Kim, “Landau-level splitting in graphene in high magnetic fields,” *Phys. Rev. Lett.*, vol. 96, p. 136806, 2006.

- [144] Z. Jiang, Y. Zhang, H. L. Stormer, and P. Kim, “Quantum hall states near the charge-neutral dirac point in graphene,” *Phys. Rev. Lett.*, vol. 99, p. 106802, 2007.
- [145] D. J. Thouless, M. Kohmoto, M. P. Nightingale, and M. den Nijs, “Quantized hall conductance in a two-dimensional periodic potential,” *Phys. Rev. Lett.*, vol. 49, pp. 405–408, 1982.
- [146] H. Watanabe, Y. Hatsugai, and H. Aoki, “Manipulation of the dirac cones and the anomaly in the graphene related quantum hall effect,” *Journal of Physics: Conference Series*, vol. 334, p. 012044, 2011.
- [147] D. N. Sheng, Z. Y. Weng, L. Sheng, and F. D. M. Haldane, “Quantum spin-hall effect and topologically invariant chern numbers,” *Phys. Rev. Lett.*, vol. 97, p. 036808, 2006.
- [148] J. R. Williams, L. DiCarlo, and C. M. Marcus, “Quantum Hall effect in a graphene p-n junction,” *Science*, vol. 317, p. 638, 2007.
- [149] B. Ozyilmaz, P. Jarillo-Herrero, D. Efetov, D. A. Abanin, L. S. Levitov, and P. Kim, “Electronic transport and quantum Hall effect in bipolar graphene p-n-p junction,” *Phys. Rev. Lett.*, vol. 99, p. 166804, 2007.
- [150] D. A. Abanin and L. S. Levitov, “Quantized transport in graphene p-n junctions in magnetic field,” *Science*, vol. 317, p. 641, 2007.
- [151] J. Tworzydło, I. Snyman, A. R. Akhmerov, and C. W. J. Beenakker, “Valley-isospin dependence of the quantum Hall effect in a graphene p-n junction,” *Phys. Rev. B*, vol. 76, p. 035411, 2007.
- [152] A. R. Akhmerov, J. H. Bardarson, A. Rycerz, and C. W. J. Beenakker, “Theory of the valley-valve effect in graphene nanoribbons,” *Phys. Rev. B*, vol. 77, p. 205416, 2008.
- [153] P. Carmier, C. Lewenkopf, and D. Ullmo, “Semiclassical magnetotransport in graphene n - p junctions,” *Phys. Rev. B*, vol. 84, p. 195428, 2011.
- [154] J. R. Williams and C. M. Marcus, “Snake states along graphene p - n junctions,” *Phys. Rev. Lett.*, vol. 107, p. 046602, 2011.
- [155] K. S. Novoselov, E. McCann, S. V. Morozov, V. I. Fal’ko, M. I. Katsnelson, U. Zeitler, D. Jiang, F. Schedin, and A. K. Geim, “Unconventional quantum hall effect and berry’s phase of 2π in bilayer graphene,” *Nature Physics*, vol. 2, p. 177, 2006.
- [156] E. McCann and V. I. Fal’ko, “Landau level degeneracy and quantum Hall effect in a graphite bilayer,” *Physical Review Letters*, vol. 96, p. 086805, 2006.

- [157] Z. Qiao, W.-K. Tse, H. Jiang, Y. Yao, and Q. Niu, “Two-dimensional topological insulator state and topological phase transition in bilayer graphene,” *Phys. Rev. Lett.*, vol. 107, p. 256801, 2011.
- [158] J. Inoue and A. Tanaka, “Photoinduced transition between conventional and topological insulators in two-dimensional electronic systems,” *Phys. Rev. Lett.*, vol. 105, p. 017401, 2010.
- [159] N. H. Lindner, G. Refael, and V. Galitski, “Floquet topological insulator in semiconductor quantum wells,” *Nat. Phys.*, vol. 7, pp. 490–495, 2011.
- [160] H. L. Calvo, H. M. Pastawski, S. Roche, and L. E. F. Foa Torres, “Tuning laser-induced band gaps in graphene,” *Applied Physics Letters*, vol. 98, p. 232103, 2011.
- [161] Z. Gu, H. A. Fertig, D. P. Arovas, and A. Auerbach, “Floquet spectrum and transport through an irradiated graphene ribbon,” *Phys. Rev. Lett.*, vol. 107, p. 216601, 2011.
- [162] T. Ojanen and T. Kitagawa, “Photoinduced helical metal and magnetization in two-dimensional electron systems with spin-orbit coupling,” *Phys. Rev. B*, vol. 85, p. 161202, 2012.
- [163] T. Kitagawa, T. Oka, A. Brataas, L. Fu, and E. Demler, “Transport properties of nonequilibrium systems under the application of light: Photoinduced quantum hall insulators without landau levels,” *Phys. Rev. B*, vol. 84, p. 235108, 2011.

Rapidly changing market of electronic devices sets up a lot of challenges for the manufacturing and design technologies. When electronic circuit elements get smaller, the device behavior becomes increasingly complicated as new physical phenomena due to quantum interference effects come into play. Understanding of the latter necessitates development of advanced theoretical tools. In this thesis we investigate quantum electron transport in multiterminal devices.

In the first part making use of the Keldysh Green's functions we develop a general framework for electron quantum transport in multi-terminal systems in the presence of oscillating fields. We are able to express any AC observable in terms of stationary Green's functions and leads self-energies, which makes our formalism a practical numerical tool for a variety of possible finite-frequency perturbations.

In the second part we investigate theoretically a proposal to induce strong spin-orbital coupling in graphene by functionalizing its surface with certain type of heavy adatoms. In this case graphene becomes a topological insulator. Then we investigate the evolution of this topological phase in external magnetic field. We were able to see a unique transition between quantum Hall and quantum spin Hall phases in the same system by only varying the position of the Fermi level. A heterojunction between these two phases was shown to give rise to a new type of a chiral state at the interface between the latter.

Keywords: quantum transport, finite frequency, graphene, spin-orbit coupling, Hall effects.

Les évolutions rapides du marché des composants électroniques font apparaître de nombreux challenges pour la conception et la fabrication de ces derniers. Lorsque ces éléments deviennent plus petits, leur comportement se complexifie à mesure que de nouveaux phénomènes, liés aux effets d'interférence, entrent en jeu. Comprendre ces derniers nécessite le développement d'outils théoriques avancés. Dans ce contexte cette thèse est consacrée au transport électronique quantique dans des systèmes multi-terminaux.

Dans la première partie on développe un formalisme général, utilisant les fonctions de Green de Keldysh, pour le transport électronique quantique dans des systèmes multi-terminaux en présence de perturbations oscillantes. Nous sommes capable d'exprimer toute observable AC en termes de fonctions de Green à l'équilibre et des self-énergies des contacts. Ceci fait de notre formalisme un outil pratique pour toute une variété de perturbations à fréquence finie.

Dans la seconde partie on présente l'idée d'induction d'un fort couplage spin-orbite dans le graphène en déposant à sa surface un certain type d'atomes lourds. Le graphène devient alors un isolant topologique. Nous avons ensuite étudié l'évolution de la phase topologique avec un champ magnétique externe. Une transition entre la phase de Hall quantique et la phase de Hall quantique de spin a été identifiée dans le même système en variant seulement la position du niveau de Fermi. Nous avons montré qu'une hétérojonction entre ces deux phases donnait lieu à un nouveau type d'état chiral à l'interface.

Mots clés: transport quantique, fréquence finie, graphène, couplage spin-orbite, effets Hall.